UNIVERSIDADE D
COIMBRA

Nuno Filipe Viseu Duarte

PROPORTIONAL COUNTERS EQUIPPED WITH THIN B_4C CONVERSION LAYERS FOR THE DETECTION OF SLOW NEUTRONS

Tese no âmbito do Doutoramento em Engenharia Física, Instrumentação, orientada pelo Doutor Fernando Domingues Amaro e pelo Doutor Carlos Davide da Rocha Azevedo e apresentada ao Departamento de Física da Faculdade de Ciências e Tecnologia da Universidade de Coimbra.

Outubro de 2021

1 2  9 0 UNIVERSIDADE D COIMBRA

Faculty of Sciences and Technology
Department of Physics

Proportional counters equipped with thin B_4C conversion layers for the detection of slow neutrons

Nuno Viseu Duarte

Ph.D. thesis in Engineering Physics, in the field of Instrumentation, performed under scientific guidance of Dr. Fernando Amaro and Dr. Carlos Azevedo, presented to the Physics Department of the Faculty of Sciences and Technology of the University of Coimbra.

October, 2021

The research reported in this thesis was performed with financial support from the following institutions and programs:

- Research project PTDC/NAN-MAT/30178/2017, funded by national funds through FCT/MCTES and co-financed by the European Regional Development Fund (ERDF) through the Portuguese Operational Program for Competitiveness and Internationalization, COMPETE 2020.
- Doctorate in Applied and Engineering Physics (DAEPHYS) program and Fundação para a Ciência e Tencologia (FCT), through a PhD grant with reference PD/BD/128268/2016.

Abstract

Because of their unique properties, neutrons are an ideal probe to study the structure and dynamic processes that occur at an atomic scale in matter. In recent years, significant investments in neutron science have been made, which materialized in the construction of large-scale research facilities that only recently started operating or that are expected to do so in a near future. These modern facilities provide high neutron beam fluxes, and are pushing the performance limits of neutron detectors. Additionally, in the last two decades, neutron detectors have been massively deployed for homeland security, to control the illicit transportation of special nuclear materials across international borders. At the same time, the neutron research community was struck by a severe shortage of ^{3}He, the gas that was considered the golden standard for neutron detection. The search for technological alternatives to ^{3}He-based detectors is mostly constrained by the fact that only a few isotopes have a relevant interaction probability when traversed by neutrons. In most cases, the physical mechanism involved in their detection is the neutron capture reaction, in which a neutron is absorbed by a nucleus that subsequently breaks into two heavy charged particles, easily detectable due to their high ionizing power. In practice, other than ^{3}He, the only isotopes that have a significant probability of interacting with neutrons via the described reaction are ^{6}Li and ^{10}B.

In this work, two novel neutron detectors were developed, both based on the deployment of micrometric boron carbide (B_4C) layers. One of these is the fine powder aerosol detector, which consists of a gaseous proportional counter with B_4C microparticles in suspension, small enough to allow for both secondary particles from the neutron capture reaction to escape it and deposit a large fraction of their initial energy in the surrounding gas, extending the energy spectrum of the detector response to higher energies. Strategies for the optimization of particle dispersion were investigated, and neutron irradiation measurements were carried to access the feasibility of this detection concept. Results indicated that the simultaneous detection of both reaction products from neutron captures occurring in suspended particles is possible. However, keeping a homogeneous and continuous suspension of the fine powder for long periods is technically challenging. A similar aerosol detector was also developed for the detection of hard x-rays, replacing B_4C with high-Z nanoparticles to increase the photoelectric effect probability, converting high energy photons into photoelectrons, characteristic x-rays and Auger electrons, which have a higher probability of being detected in the gas volume. Using Bi_2O_3 nanoparticles, an efficiency increase by a factor of 3.6 was observed for 59.5 keV photons.

The second neutron detector presented is the coincidence detector, aimed at applications that require fine spatial resolution. This foresees the use of a detection layer composed of a thin B_4C film deposited on a thin Mylar substrate, surrounded by a counting gas, and two MWPCs on each side of the layer. Because both secondary products from the neutron capture reaction can simultaneously escape the conversion

layer, the position of the neutron interaction site can be pinpointed when both particles are detected in coincidence by each MWPC. Through GEANT4 simulations, it was verified that even for a substantially inferior number of detected neutrons, spatial resolution can be significantly improved when compared to conventional detectors that employ thick detection layers. For the same neutron exposure, and considering only the limitation of spatial resolution impinged by the range of the secondary particles of the neutron capture reaction in the gas at atmospheric pressure, simulation results indicate an improvement of spatial resolution by a factor of 8.25.

Resumo

Devido às suas propriedades únicas, a irradiação com neutrões é uma ferramenta ideal para estudar a estrutura e os processos dinâmicos que ocorrem na escala atómica da matéria. Nos últimos anos, foi feito um investimento considerável na ciência de neutrões, que se materializou na construção de novas instituições de investigação que apenas recentemente iniciaram a sua operação, ou que serão iniciadas num futuro próximo. Estas instituições modernas fornecem feixes de neutrões de elevado fluxo, aumentado os limites de desempenho de detetores de neutrões. Adicionalmente, nas últimas duas décadas, detetores de neutrões foram massivamente instalados em aplicações de segurança interna, para controlar o transporte ilícito de materiais nucleares especiais entre fronteiras internacionais. Ao mesmo tempo, a comunidade científica ligada à ciência de neutrões foi abalada por uma grave escassez de ^{3}He, o gás considerado como o padrão de referência na deteção de neutrões. A procura por alternativas tecnológicas aos detetores baseados em ^{3}He, é maioritariamente restringida pelo fato de que apenas alguns isótopos têm uma probabilidade de interação relevante ao atravessados por neutrões. Na maioria dos casos, o mecanismo físico envolvido na sua deteção é a reação de captura nuclear de neutrões, na qual um neutrão é absorvido por um núcleo que posteriormente se divide em dois iões pesados, facilmente detetáveis devido ao seu alto poder ionizante. Na prática, para além do ^{3}He, os únicos isótopos que têm uma probabilidade significativa de interagir com neutrões pela reação descrita são o ^{6}Li e o ^{10}B.

Neste trabalho, dois novos detetores de neutrões foram desenvolvidos, ambos baseados no uso de camadas micrométricas de carboneto de boro (B_4C). Um deles é o detetor aerossol, que consiste num contador proporcional gasoso com micropartículas de B_4C em suspensão, com dimensões suficientemente reduzidas para permitir que ambas as partículas secundárias emitidas na reação de captura dos neutrões escapem e depositem grande parte da sua energia inicial no gás envolvente, estendendo assim o espectro de energias do detetor para energias mais altas. Foram investigadas estratégias para a otimização da dispersão das partículas, e feitas medidas com irradiação de neutrões para analisar a viabilidade deste conceito de deteção. Os resultados indicaram que a deteção simultânea de ambos os produtos de reação da captura de neutrões em partículas suspensas é possível. No entanto, manter uma suspensão homogénea e contínua das micropartículas por longos períodos de tempo é tecnicamente difícil. Um detetor aerossol semelhante foi também desenvolvido para a deteção de raios-X duros, substituindo o B_4C por nanopartículas com elevado Z, de modo a aumentar a probabilidade de ocorrência do efeito fotoelétrico, convertendo fotões de alta energia em fotoeletrões, raios-X característicos e eletrões de Auger, que têm maior probabilidade de serem detetados no volume gasoso. Usando nanopartículas de Bi_2O_3, um aumento de eficiência por um fator de 3.6 foi observado para fotões de 59.5 keV.

O segundo detetor de neutrões apresentado é o detetor de coincidência, direcionado a

aplicações que requerem boa resolução espacial. Este baseia-se numa camada de deteção composta por um filme fino de B_4C depositado num substrato fino de Mylar, envolvido por um gás de deteção, e duas câmaras multifios em cada lado da camada. Como ambos os produtos da reação de captura de neutrões podem escapar simultaneamente da camada de conversão, o ponto de interação dos neutrões pode ser identificado quando ambas as partículas são detetadas em coincidência por cada uma das câmaras multifios. Através de simulações em GEANT4, verificou-se que mesmo com um número substancialmente inferior de neutrões detetados, a resolução espacial pode ser significativamente melhorada em comparação com detetores convencionais que usam camadas espessas de deteção. Para a mesma irradiação de neutrões, e considerando apenas a limitação de resolução espacial provocada pelo alcance das partículas secundárias da reação de captura de neutrões no gás, os resultados de simulação indicam uma melhoria de resolução espacial por um fator de 8.25.

Acknowledgments

These pages are meant to provide a scientific contribution to the field of neutron detection. Nonetheless, they also mark (and celebrate) the end of a long journey that would not be possible to walk alone. Many people were by my side during these years to help and guide me, technically and emotionally, to whom I am thankful.

For starters, Professor Joaquim Santos. I perfectly remember, back when I was on a small trip visiting a friend in Azores, the moment I opened his email suggesting me to apply for a doctoral fellowship to work in the LIBPhys-UC group. Looking back now, that was the day that marked the beginning of a life-changing path, which I am very glad I took. Thank you for believing in me, for encouraging me to pursue this PhD., and for your continuous concern and involvement in the progress and success of my work.

I thank my supervisor Fernando Amaro, for introducing me to the world of radiation detectors, for sharing his knowledge of detector development and operation, for his ideas on the approach to achieve our goals, for our discussions on the results obtained and for the detailed manuscript revision. As importantly, thank you for the trusting and friendly relation we built.

I thank Carlos Azevedo, my co-supervisor, for the insights and teachings on specific technicalities of computer simulations developed over the course of this thesis. Also, for his readiness to help me whenever solicited and for his endless cheerfulness.

A special acknowledgement to João Marcos, who came on board of this project in its final year, and provided meaningful assistance in the experimental campaigns.

A sincere thanks to Dr. Bruno Guérard for facilitating the experimental work at ILL and for his valuable inputs.

I gratefully acknowledge the willingness of Sérgio Carmo to try out the detector irradiation with neutrons "accidentally" produced by the cyclotron at ICNAS, and his support during this measurements.

Access to TAIL-UC facility funded under QREN-Mais Centro Project ICT/2009/02/012/1890 is acknowledged. I particularly thank Dr. Pedro Sidónio for the time spent in the acquisition of the SEM images presented in Chapters 4 and 5 of this dissertation.

To my labmates and fellow doctoral students/recent doctors who shared the boat with me, thank you for the comradeship and for making LIBPhys a pleasant and fun place to work in.

To my parents, who since the day I was born supported me and granted all the opportunities and conditions I needed to succeed. I recognize what a big privilege this is and the effort it took, for which I am eternally grateful.

I am also grateful to my parents-in-law, Fernanda and José, for welcoming me to their home, where a big part of this dissertation was written. Particularly Fernanda, who took care of a million time-consuming everyday chores, which allowed me to have more time and energy for writing.

Thank you, my dear sister, for shaping the person I am today, and for always being available to offer me your advice, which I take into high consideration.

Thank you Rosa, for inspiring me to think big since I was a kid.

To Anita, my nuclear family, thank you for making me look forward to an amazing future, come what may.

Contents

List of Abbreviations

B_4C	Boron Carbide
Bi_2O_3	Bismuth(III) Oxide
BN	Boron Nitride
BNC	Bayonet Neill–Concelman
BoPET	Biaxially-oriented Polyethylene Terephthalate
CF	ConFlat
CFD	Computational Fluid Dynamics
CH_4	Methane
CNSC	China Spallation Neutron Source
CO_2	Carbon Dioxide
CSDA	Continuous Slowing Down Approximation
CSNS	China Spallation Neutron Source
CVD	Chemical Vapor Deposition
DAQ	Data Acquisition System
e	Elementary charge
ESS	European Spallation Source
FRM-II	Research Neutron Source Heinz Maier-Leibnitz
FWHM	Full Width at Half Maximum
GEM	Gas Electron Multiplier
GHS	Globally Harmonized System
HV	High Voltage
IBA	Ion Beam Applications
ICNAS	Institute for Nuclear Sciences Applied to Health
ILL	Institute Laue-Langevin
J-PARC	Japan Proton Accelerator Research Complex
LIBPhys	Laboratory for Instrumentation, Biomedical Engineering and Radiation Physics
LiF	Lithium Fluoride
MCA	Multichannel Analyser
MWPC	Multi Wire Proportional Chamber
P5	Ar:CH_4 gas in 95%:5% proportion
P10	Ar:CH_4 gas in 90%:10% proportion
PHS	Pulse Height Spectrum
PC	Proportional Counter
PLA	Polylactic Acid
PNNL	Pacific Northwest National Laboratory
POM	Polyoxymethylene

PSF	Point Spread Function
PSI	Paul Scherrer Institute
PSND	Position Sensitive Neutron Detector
RMS	Root Mean Square
RPC	Resistive Plate Chamber
RPM	Radiation Portal Monitor
SI	International System of Units
SANS	Small-Angle Neutron Scattering
SEM	Scanning Electron Microscope
SHV	Safe High Voltage
SNR	Signal-to-Noise Ratio
SNS	Spallation Neutron Source
SRIM	Stopping and Range of Ions in Matter
TPC	Time Projection Chamber
UCN	Ultracold Neutrons
UHV	Ultra-High Vacuum
WIMP	Weakly Interacting Massive Particle
Z	Atomic Number

List of Tables

List of Figures

1 Introduction

1.1 Motivation and Outline

The discovery of the neutron is attributed to James Chadwick in 1932 [1]. Less than a century later, neutrons play an important role in scientific research. The physical properties of neutrons make them an ideal probe for the investigation of matter in different scientific fields, such as physics, chemistry and biology as well as for specific medical and industrial applications. A variety of techniques use neutron irradiation on a sample to analyse it, such as neutron imaging, diffraction, reflectometry, spectroscopy, and small angle scattering. All these have a common need: the detection of neutrons that are transmitted or scattered by the sample. Neutron detectors are equally fundamental in homeland security applications that monitor the illicit transportation of special nuclear materials across international borders.

Neutrons are deeply penetrating particles, that can travel long distances in most materials without interacting. Indeed, on account of their neutral charge, neutrons do not undergo Coulomb interactions with atomic electrons, so their principal means of interaction is with the nuclei of atoms. Their detection is usually achieved via nuclear capture reactions, in which the neutron is absorbed by a nucleus, which becomes unstable and decays into two highly ionizing charged particles. These reactions only occur with significant cross-section for a few isotopes and the ones with the most practical interest for detection applications are, by decreasing cross-section ^{3}He, ^{10}B and ^{6}Li. Until recent years, proportional counters filled with ^{3}He gas were considered the golden standard for neutron detection, due to their high efficiency, good gamma-ray discrimination, and non-toxicity. However, when a severe shortage of this gas was acknowledged, prices skyrocketed and heavy acquisition restrictions were implemented. With no possibility of a sustainable supply and demand scenario for the amount of neutron detectors required worldwide, scientists were forced to urgently

find alternatives to ^{3}He-based detectors, while meeting the requirements of the new detectors to be installed in neutron research facilities. Another additional motivation was the fact that ^{3}He detectors were already at the limit of their performance capabilities, namely regarding counting rate and position resolution, which fell short of the requirements of instruments in modern research facilities.

Consequently, over the last decade, great effort and investment was put into the development of ^{3}He-free neutron detectors, and for a wide range of applications, gaseous detectors that rely on the ^{10}B nuclear capture reaction are the most promising alternatives. Because boron is a solid at standard temperature and pressure conditions, these detectors

employ a thin coating of elemental boron or a boron-containing mixture, surrounded by a counting gas for charge amplification. These materials are not self-supporting, hence they are generally deposited directly on the inner walls of the detector or in substrates that are then inserted inside it.

Due to momentum and energy conservation, the reaction products of the ^{10}B neutron capture (an alpha particle and ^{7}Li nucleus) are emitted in the same line of action, in opposite directions. In conventional boron coated gaseous detectors, for each neutron capture, only one of the reaction products can travel towards the gas to generate a detectable signal in the detector, while the other is absorbed by the boron layer or the substrate. Furthermore, depending on the depth in which the nuclear capture occurs and the consequent energy lost to collisions inside the boron layer, the range of the ^{7}Li and alpha particles in conventional counting gases at atmospheric pressure can extend up to several millimetres, which intrinsically limits the spatial resolution of such detectors.

This thesis is centred on the development of two novel neutron detection techniques, both of them based on the deployment of micrometric boron-based conversion layers in gaseous detectors, with the aim of simultaneously detecting both secondary particles that are emitted in a single ^{10}B neutron capture reaction.

In Chapter 2, the fundamental principles of the interaction of radiation with matter are discussed, which is essential for the comprehension of the physical processes involved in the functioning of neutron detectors. This chapter also includes an overview of the different possible mechanisms to produce the free neutrons that are used in irradiation experiments, as well as of specific concepts related to their detection, such as neutron moderation, conversion and gamma-ray discrimination. Finally, an overview of the basic parameters of general gaseous radiation detection are also addressed.

To contextualize the research that has been carried roughly over the last decade in the development of new neutron detectors, Chapter 3 begins by exposing their most relevant applications, and how the ^{3}He shortage crisis shaped their evolution, as well as the reasons that led to this shortage. Subsequently, the state of the art of ^{3}He-free detectors will be focused, specifically boron-based alternatives (as the ones developed in this thesis), presenting some of the detectors currently in use or planned to be used in neutron research facilities.

In Chapter 4, the first neutron detector developed in the aim of this thesis is introduced: the fine powder aerosol detector, which consists of a gaseous proportional counter filled with a ^{10}B-containing fine powder for neutron conversion, thus forming an aerosol in which the nanoparticles are suspended by a continuous gas flow in the detector. By selecting nanoparticles with a diameter smaller than the range of the neutron capture reaction products in that material, it is possible for both products to escape it and deposit a large fraction of their initial energy in the gas, extending the energy spectrum of the detector response to higher energies, which is an attractive feature to improve gamma-ray discrimination. This chapter begins by presenting the simulation results carried to validate the detector concept and optimize its efficiency, followed by the experimental determination of the operational properties (gas gain and energy resolution) of a detector prototype. To optimize the performance of the aerosol detector, it is fundamental to minimize the attachment of fine particles to the inner walls, since only for neutron captures occurring in suspended particles can both the ^{7}Li and the alpha particles escape the fine particle to ionize the surrounding gas. Considering this, it is also presented in this chapter a detailed study about the effectiveness of applying a high degree of surface polishing to the detector inner walls to reduce particle attachment. After this, the experimental

campaigns for the detector irradiation with thermal neutrons are described. At last, the potential of using the same concept to detect hard x-rays by using high-Z nanoparticles is examined.

The neutron coincidence detector, the second one developed, is described in Chapter 5, which is based on the same strategy of simultaneously detecting both secondary products of each neutron capture reaction, this time by using thin a boron-based converter coated on a thin substrate. Its working principle is based on the idea that by using independent readout systems to detect each particle that emerges from opposite sides of the detection layer, and by combining the information from these two signals, it is possible to reconstruct the neutron interaction site with greater precision than in conventional boron-based detectors, which employ detection layers with a combined thickness of converter and substrate with at least hundreds of microns, and consequently can only detect one of the secondary particles per neutron capture. The spatial resolution of such detectors is intrinsically limited by the range of the ^{7}Li and alpha particles in the gas, which can extend up to several millimetres at atmospheric pressure. However, by taking advantage of the fact that these particles are emitted in-line with opposite directions, it is possible to pinpoint the interaction site of each neutron detection if both escape the detection layer and are detected by independent readouts on each side of it, leading to an improvement of spatial resolution. Monte Carlo simulations with GEANT4 were developed to optimize the materials, geometry and layer thicknesses of the coincidence detector, as well as to compare it with conventional boron-based detectors in terms of spatial resolution, by considering the position reconstruction uncertainty that arises from the range of the secondary products of the neutron capture reaction.

Finally, Chapter 6 reports some general conclusions and future work directions.

1.2 Scientific Contributions

The work developed for this thesis resulted, so far, in the following publications in international peer-reviewed journals:

- *Operational properties of fine powder aerosol as radiation detection medium in gaseous proportional counters*, Nucl. Instr. and Meth. A, 942 (2019): 162392. N.V. Duarte, C.M.B. Monteiro, C.D.R. Azevedo, A. Antognini and F.D. Amaro.

  Personal contributions: Assembly of the experimental setup, participation in measurements, data analysis (analysis of pulse height spectra and evaluation of detector gain and energy resolution) and manuscript preparation and submission.

- *Operation of a novel large area, high gain, single stage gaseous electron multiplier*, Journal of Instrumentation 16.01 (2021): P01033. F.D. Amaro, R. Roque, N.V. Duarte, A. Cortez and J.A. Mir.

  Personal contributions: Participation in the experimental measurements and manuscript revision (the micro-pattern gaseous detector presented in this paper (COBRA_125) was initially intended to be used as the readout mechanism of the detector described in Chapter 5, although it was eventually decided to use MWPCs).

And also produced the patent:

- *A gaseous detector and a method for the determination of the position of at least one neutron*, European Patent Request and Portuguese Patent Request (Patents Pending). F.D. Amaro, C.M.B. Monteiro, N.V. Duarte and J.S. Marcos.

The results obtained over the course of this thesis were also presented through oral communications in the following international conferences and scientific meetings (presenting author underlined):

- *Nanoparticle aerosol as radiation detection medium in gaseous proportional counters: an alternative solution for neutron detection*, 19$^{\text{th}}$ International Workshop on Radiation Imaging Detectors, 2017. J.M.F. dos Santos, F.D. Amaro, N.V. Duarte, C.M.B. Monteiro and A. Antognini.

- *Fine particle aerosol as radiation detection medium in gaseous proportional counters*, Materials Science and Nanotechnology Conference, 2021. F.D. Amaro, N.V. Duarte, C.M.B. Monteiro, J.M.F. dos Santos and A. Antognini.

- *Using neutron capture coincidence to improve spatial resolution in neutron detectors*, Neutrons and Muons in Portugal Workshop, 2021. N.V. Duarte, J.S. Macros and F.D. Amaro.

- *Fine powder aerosol proportional counters for neutron detection*, 4$^{\text{th}}$ Doctoral Congress in Engineering of the University of Porto, 2021. N.V. Duarte, J.S. Macros and F.D. Amaro.

As well as via several poster presentations:

- *Proportional counter filled with fine powder aerosol*, European Conference on X-ray Spectrometry, 2018. N.V. Duarte, C.M.B. Monteiro, C.D. Azevedo, J.M.F dos Santos, A. Antognini and F. D. Amaro.

- *Neutron detection using a fine powder aerosol proportional counter*, Science and Technology in Portugal Summit, 2019. N.V. Duarte, C.M.B. Monteiro, C.D. Azevedo, J.M.F dos Santos, A. Antognini and F. D. Amaro.

- *Development of large area, high gain, thick gaseous electron multiplier: from GEM_100 to COBRA_125.*, Iberian Joint Meeting on Atomic and Molecular Physics, 2019. A. Cortez, F.D. Amaro, R. Roque, N.V. Duarte.

- *Optimizing the performance of fine powder aerosol neutron detectors*, Quasielastic Neutron Scattering and Inelastic Neutron Spectrometers, 2021. N.V. Duarte, J.S. Marcos and F.D. Amaro.

- *Improving spatial resolution of neutron detectors with submicrometric B_4C layers*, Particles and Nuclei International Conference, 2021. N.V. Duarte, J.S. Marcos and F.D. Amaro.

2 Scientific Background

2.1 Interaction of Radiation with Matter

Before addressing the specifics of neutron detectors, it is essential to have a comprehension of the physical processes involved in their operation. This requires an understanding of the fundamentals of the interaction of radiation with matter, not only of neutrons, but also of other particles involved in the neutron detection process, namely heavy charged particles, electrons and photons.

2.1.1 Heavy Charged Particles

This class of particles ranges from protons, the fundamental heavy charged particle, and alpha particles (^{4}He nuclei, composed by two protons and two neutrons) to heavier ions. The proton (as the neutron, although the latter has neutral charge) belongs to a family of particles designated as hadrons, composed by 2 up quarks, each with charge $+\frac{2}{3}\ e$ and 1 down quark, with charge $-\frac{1}{3}\ e$, making for a total charge of $+1\ e$. As hadrons, they experience not only atomic interactions, through electromagnetic force, but also nuclear interactions through strong force.

Heavy charged particles interact primarily through Coulomb forces with the orbital electrons of the absorber atoms. Depending on the transferred energy, an interaction can lead to the excitation of the absorber atom, in which the electron moves to a higher energy electronic shell, or to its ionization, in which the electron is stripped from the atom.

When traversing matter, these particles interact with many orbital electrons simultaneously, losing a fraction of their energy in each interaction. Due to this high interaction rate, the path of heavy charged particles in matter tends to be straight, as these particles are not significantly influenced by each single collision. Instead, energy is evenly lost along a great number of small collisions that only slightly deflect the trajectory of the incoming particle, and evenly in all directions. It is only at the end of their trajectory, after losing most of their energy, that more abrupt path deviations are observed. As a result, heavy charged particles are characterized by a precise range, which indicates the average thickness of a given material required to bring a particle to rest. It is important to clarify that the range of a particle differs from its path length, which quantifies the total distance travelled. However, for heavy charged particles these values are approximately the same, since they tend to follow straight paths [2].

Range is inversely proportional to the density of the absorbing material, since a higher concentration of atoms means a higher interaction probability and consequently a lower range. Consequently, the range of a given heavy charged particle varies significantly between gases and solids, being much shorter for the latter. For the same medium, the range of heavy charged particles depends on their kinetic energy, mass and charge. While

higher energies make for a higher range, both mass and charge are inversely proportional to it. An example of this is shown in Fig. 2.1, comparing the range of protons and alpha particles in dry air, as a function of their energy. This plot was calculated using the PSTAR (Stopping-Power and Range Tables for Protons) and ASTAR (Stopping-Power and Range Tables for Helium Ions) software [3].

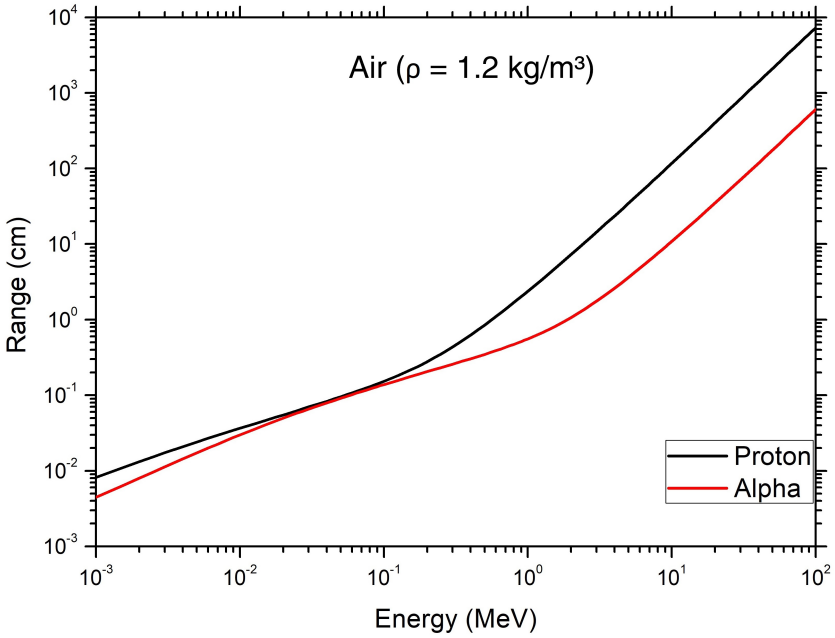

Figure 2.1: Range of protons (black plot) and alpha particles (red plot) in dry air ($\rho = 1.2$ kg/m^3). Because alpha particles are heavier and have a greater charge than protons ($+2$ e vs. $+1$ e), they have a higher interaction probability and consequently a lower range. Calculated from [3].

The stopping power (dE/dx) is used to formally describe the effect of resistance to the movement of a heavy charged particle through a material. It is defined as the average energy lost by the particle per distance travelled in the absorber, and is given by the Bethe formula [4]:

$$-\frac{dE}{dx} = \frac{4\pi n z^2 e^4}{m_e v^2}\left[\ln\left(\frac{2m_e v^2 E}{2I^2(1-\frac{v^2}{c^2})}\right) - \ln\left(1-\frac{v^2}{c^2}\right) - \frac{v^2}{c^2}\right] \tag{2.1}$$

where n and I represent respectively the electron density and the mean excitation energy of the absorber material, v and z the velocity and charge number of the incoming particle, c the speed of light in vacuum and m_e the electron rest mass. The term in brackets is a dimensionless parameter called the stopping number (L).

The dependence of equation (2.1) on z^2/v^2 results in a large multiplicative factor for low energy charged ions. Thus, the rate at which a heavy charged particle loses energy is not constant, but rather varies as the particle is slowed down in matter. Above a given initial energy threshold, more energy per unit length is deposited at the end of the particle trajectory than at its beginning. As a result, a plot of the stopping power along the travelled path results in a maximum immediately followed by an abrupt drop, known as the Bragg peak. This effect is depicted in Fig. 2.2, for 10 MeV alpha particles traversing argon at atmospheric pressure. This plot was calculated using the Stopping and Range of Ions in Matter (SRIM) software [5].

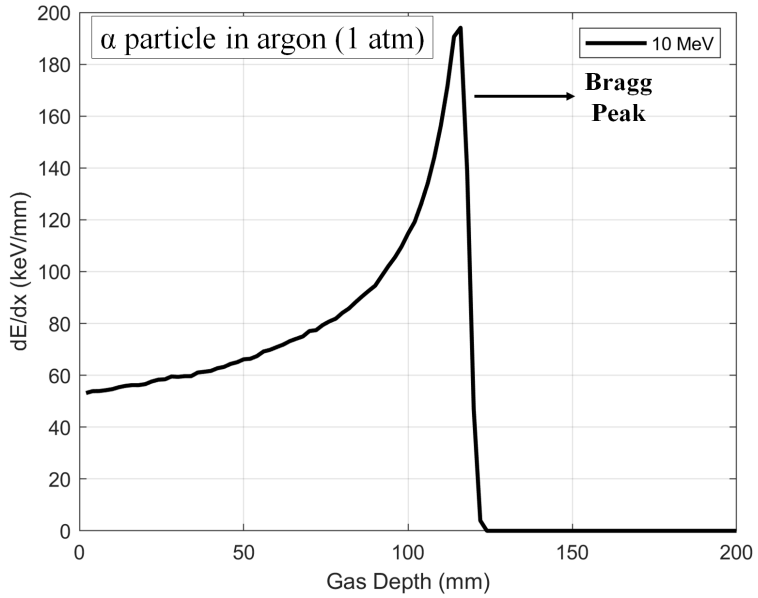

Figure 2.2: Stopping power of a 10 MeV alpha particle traversing argon at atmospheric pressure as a function of the travelled path length, showing a Bragg peak. Derived from SRIM simulation [5].

After losing all kinetic energy, the particle will stop and pick up the necessary number of electrons from the surrounding matter to become neutral. For protons and alpha particles the following reactions occur:

$$p^+ + e^- \rightarrow {}^1_1\mathrm{H} \tag{2.2}$$

$$\alpha^{2+} + 2e^- \rightarrow {}^4_2\mathrm{He} \tag{2.3}$$

Although rarer, the interaction of heavy charged particles with nuclei of absorber atoms is also possible. If a heavy charged particle approaches a nucleus closely enough, it may be scattered or captured by the nucleus. The particle may either be elastically scattered, in which case the kinetic energy of the system is conserved, or inelastically scattered, leaving the nucleus in an excited state. In general, little energy is transferred in these collisions, since the nuclei of the absorber material are usually much heavier than the incoming charged particle [6]. In the case of nuclear capture, a nuclear reaction occurs in which the heavy charged particle is captured by an absorber nucleus, forming an unstable isotope that decays until it reaches a stable form [7].

2.1.2 Electrons and Positrons

Free electrons and positrons, also referred to as β radiation, generally travel much faster than heavy charged particles across matter, since they weigh only a small fraction of a proton ($^{m_{e^-}}/_{m_{p^+}} \approx 5 \times 10^{-4}$). They interact mainly by two mechanisms: inelastic collisions with orbital electrons, and elastic scattering of the nuclei of absorber atoms. In the first case, particles are slowed down by collisional losses due to the ionization and excitation of absorber atoms. When electrons are deflected by the nucleus, an additional energy loss mechanism occurs: the emission of electromagnetic radiation in a process

known as bremsstrahlung. The total energy loss of electrons and positrons, therefore, is composed of two parts [6]:

$$\left(\frac{dE}{dx}\right)_{\text{total}} = \left(\frac{dE}{dx}\right)_{\text{coll}} + \left(\frac{dE}{dx}\right)_{\text{rad}} \tag{2.4}$$

The energy loss by radiative and collisional mechanisms for electrons in dry air is plotted in Fig. 2.3. This plot was calculated using the ESTAR (Stopping-Power and Range Tables for Electrons) software [3].

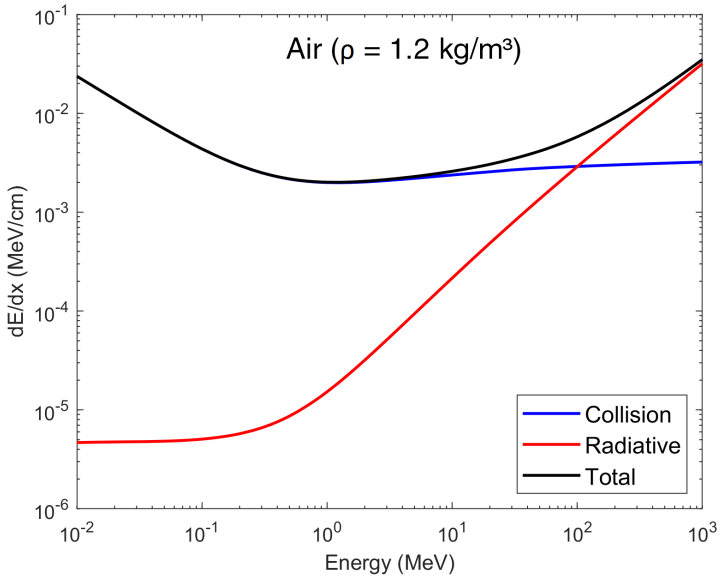

Figure 2.3: Contributions of collision (blue plot) and radiative (red plot) energy loss to the stopping power of electrons in dry air ($\rho = 1.2$ kg/m^3). Calculated from [3].

At energies of a few MeV or less, the energy loss by radiative processes is negligible. However, as energy increases, the relevance of this mechanism rises, becoming greater than collisional energy loss.

Both interaction mechanisms are responsible for the very irregular path of fast electrons when traversing matter. The slowing down process is less gradual in collisions with orbital electrons, which have the same mass and consequently a larger fraction of energy is transferred. Additionally, collisions with nuclei that are much heavier can abruptly deviate the trajectory of the particle. Because of this tortuous path, in contrast with heavy charged particles, their path length is generally considerably larger than their range in a given material [8].

Collision Loss

An expression similar to that of equation (2.1) has also been derived by Bethe to describe the specific energy loss due to ionization and excitation (the collisional losses) for fast electrons:

$$-\frac{dE}{dx} = \frac{4\pi n z^2 e^4}{m_e v^2}\left[\ln\left(\frac{m_e v^2 E}{2I^2(1-\beta^2)}\right) - (\ln 2)\left(2\sqrt{1-\beta^2} - 1 + \beta^2\right) + (1-\beta^2) + \frac{1}{8}\left(1-\sqrt{1-\beta^2}\right)^2\right] \tag{2.5}$$

where the symbols have the same meaning as in equation (2.1) and $\beta \equiv v/c$.

Radiative Loss

Bremsstrahlung consists of the production of electromagnetic radiation arising from the acceleration of the electron as it is deviated from its straight-line course by the electrical attraction of the nucleus [6]. The conversion from kinetic energy to electromagnetic radiation is predicted by the energy conservation law. Bremsstrahlung radiation consists of photons with energies from zero up to a maximum value equal to the kinetic energy of the particle. The intensity of the emitted Bremsstrahlung (I) is given by the expression [2]:

$$I \propto \left(\frac{q \cdot Z}{m} \right)^2 \tag{2.6}$$

where q and m represent the charge and mass of the moving particle, respectively, and Z the atomic number of the atom involved in the interaction. In the light of this equation, we can understand why bremsstrahlung is not particularly relevant when considering the passage of heavy charged particles through matter: their much greater mass implies that the intensity of the emitted Bremsstrahlung radiation is negligible. From equation (2.6) we can also conclude that the emitted radiation is greater for heavier (higher Z) materials.

Another possible interaction mechanism of fast electrons that can be used as a detection principle is Cherenkov radiation, which occurs when a charged particle travels at a superior velocity than light in the same medium. Therefore, to emit Cherenkov radiation, a particle must have a velocity:

$$v > \frac{c}{n} \tag{2.7}$$

where n is the medium refraction index and c the speed of light in vacuum. In such cases, an electromagnetic shock wave is created (Fig 2.4), with a conical wavefront emitted at a well-defined angle.

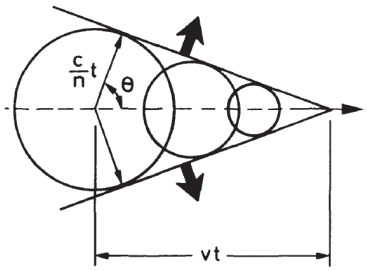

Figure 2.4: Emission of Cherenkov radiation. Image from [6].

The velocity threshold and the dependence of the emission angle on the particle velocity are attractive properties of Cherenkov radiation for detection applications [6]. Although in these detectors it is the electrons travelling faster than light in that medium that are responsible for producing Cherenkov radiation, this detection technique is often used for indirect detection of other particles, such as neutrinos. In most Cherenkov detectors, water is used as the detection medium and the emitted radiation is generally detected by photomultipliers tubes (PMTs).

2.1.3 Photons

Photons constitute electromagnetic radiation, from low energy radio waves to high energy gamma-rays. Considered as particles, they travel with the speed of light c and they have zero rest mass and charge. The relation between the energy of a photon (E) and its frequency (ν) or wavelength (λ) is given by:

$$E = h\nu = h\frac{c}{\lambda} \tag{2.8}$$

where h is the Planck constant ($h = 6.626 \times 10^{-34}\text{m}^2\text{kg/s}$).

Four mechanisms dominate photon interactions with matter: photoelectric effect, elastic scattering, inelastic (or Compton) scattering and pair production. The occurrence probability of these interactions is strongly depend on the photon energy, each dominating in a specific energy range. Figure 2.5 shows this dependence, plotting the photon linear attenuation coefficient (μ) of the different interaction mechanisms in argon as a function of the incoming photon energy, calculated with the XCOM software [9].

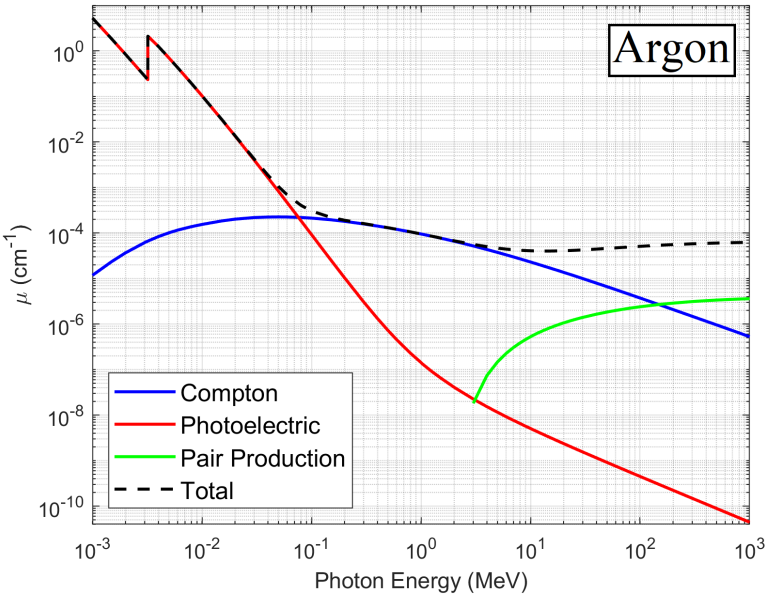

Figure 2.5: Linear attenuation coefficients of the several photon interaction mechanisms on argon. Calculated from [9].

High energy photons, namely x-rays and gamma-rays, are much more penetrating than charged particles. Additionally, a beam of photons is not degraded in energy while traversing matter, being instead only attenuated in intensity. This attenuation is quantified by the linear attenuation coefficient (μ), which is related to the photon cross-section (σ):

$$\mu = \sigma n_a \tag{2.9}$$

where n_a is the number of atoms per volume of the absorber.

The attenuation of a beam of photons in a material as a function of distance travelled (x) is given by:

$$I(x) = I_0 e^{-\mu x} \tag{2.10}$$

where I_0 is the initial number of emitted photons and $I(x)$ is the number of photons transmitted (i.e. not attenuated) after travelling a distance x in the absorber.

The total probability for a photon to interact with matter is given by the sum of the linear attenuation coefficients for each process shown in Fig. 2.5:

$$\mu_{\text{total}} = \mu_{\text{photoelectric}} + \mu_{\text{Compton}} + \mu_{\text{pair-production}} \tag{2.11}$$

The elastic scattering of photons is generally not accounted in this equation, for the reasons discussed immediately below.

Elastic Scattering

Elastic scattering of photons is caused by two processes: Thomson scattering from single atomic electrons, and Rayleigh scattering, which occurs from strongly bound electrons acting cooperatively [6].

Thomson scattering is the scattering of free electrons in the classical limit. This process happens in the low-energy limit, when the electric field of the incident photon accelerates the electron, causing it, in turn, to emit radiation at the same frequency as the incident photon.

Rayleigh scattering, on the other hand, is the scattering of photons by atoms as a whole. In this process, all the electrons in the atom participate in a coherent manner, and therefore it is also called coherent scattering.

In both processes, the direction of the incoming photon is changed, but virtually no energy is transferred to the medium, which is why in most practical purposes the elastic scatter of photons can be neglected. Additionally, the cross-section of Thomson and Rayleigh scattering for high energy x-rays and gamma-rays is very small.

Photoelectric Effect

For low energy x-rays, photoelectric absorption is the most relevant form of interaction. In this process, a photon is absorbed by an atom which ejects an inner shell electron (designated photoelectron), with kinetic energy equal to the difference between the photon incoming energy ($h\nu$) and the binding energy (E_b) of the corresponding atomic shell:

$$E_{e^-} = h\nu - E_b \tag{2.12}$$

The shell vacancy from the photoelectron is filled by an electron from an outer shell, which in term results in the emission of either a photon (fluorescence) or of another outer shell electron (Auger electron). In this process, and as long as the incoming photon energy is higher than the binding energy of the K shell, most interactions will occur with electrons from this shell.

In case of fluorescence, the energy of the emitted photon is given by the difference between the energy levels of the shell from which the photoelectron is ejected and the original shell of the electron which filled the vacancy. For instance, if we consider a photon being absorbed in the K shell, and the electron which fills the vacancy jumping from the L_3 shell, the energy of the emitted photon is given by:

$$h\nu = E_K - E_{L_3} \tag{2.13}$$

where E_K and E_{L_3} are respectively the electron binding energies in the K and L_3

shells. Because these photons are emitted with fixed energies that depend on the atomic energy levels which are different for each element, they are designated as "characteristic x-rays", and can be used to study the atomic composition of materials.

Alternatively to fluorescence, while one electron jumps down to fill the vacancy a second electron from an outer shell may be emitted, designated as the Auger electron. If we consider the example of the photoelectron being ejected from the K shell, the electron to fill the vacancy jumping from the L_3 shell and the Auger electron emitted from the M_5 shell, its kinetic energy is given by:

$$E_{\text{Auger}} = E_K - E_{L_1} - E_{M_5} \tag{2.14}$$

Several characteristic x-rays and/or Auger electrons can be emitted in a single photoelectric absorption, until the atoms reaches its lower energy state.

Inelastic Scattering

Inelastic, or Compton scattering occurs with loosely bound electrons, to which a fraction of the incident photon energy is transferred. Although electrons in matter are bound, if their binding energy is much inferior to the energy of the incoming photon, i.e, $E_b << h\nu$, they can essentially be treated as free electrons. Fig. 2.6 show the kinematic scheme of the Compton interaction.

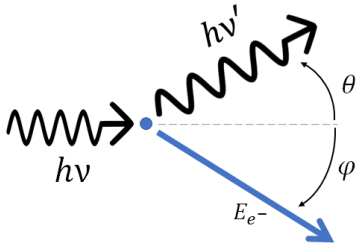

Figure 2.6: Kinematics of Compton scattering.

The energy transferred to the recoil electron depends on the incoming photon energy ($h\nu$) and the photon scattering angle (θ) [8]:

$$E_{e^-} = h\nu - h\nu' = h\nu\left(1 - \frac{1}{1 + \frac{h\nu}{m_e c^2}(1 - \cos\theta)}\right) \tag{2.15}$$

where $h\nu'$ is the energy of the scattered photon and $m_e c^2$ the electron rest mass. As evidenced by this equation, the energy transferred to the recoil electron is maximum for backscattering emissions, i.e., $\theta = \pi$. This is known as the Compton edge, with energy:

$$E_{e^-_{\max}} = \frac{2h\nu\left(\frac{h\nu}{m_e c^2}\right)}{1 + 2\left(\frac{h\nu}{m_e c^2}\right)} \tag{2.16}$$

Finally, the probability of Compton scattering depends on the number of electrons available as scattering targets, and therefore increases linearly with Z.

Pair production

Pair production involves the transformation of a photon into an electron-positron pair. Consequently, only photons that carry an energy greater than the rest mass of an electron-positron pair, i.e., 2×0.511 MeV $= 1.022$ MeV, can suffer this interaction. This mechanism is therefore only relevant for gamma-rays of several MeV. All the excess energy carried by the photon above the pair production threshold goes into kinetic energy shared by the positron and the electron.

To conserve momentum, a third body is required for this interaction to occur, which is usually a nucleus. Because the positron will subsequently annihilate after slowing down in the absorbing medium, two annihilation photons are normally produced as secondary products of the interaction.

2.1.4 Neutrons

Although neutrons have neutral charge, as hadrons, they are composed by quarks that carry charge: 2 down quarks, each with charge $-\frac{1}{3}\ e$ and 1 up quark, with charge $+\frac{2}{3}\ e$. Therefore, the quarks individual charges cancel out to generate a neutral particle. Nonetheless, neutrons have spin ($+\frac{1}{2}\hbar$) and a magnetic moment ($\mu_n = -1.913\mu_N$, where μ_N is the nuclear magneton) [10]. Consequently, they are affected by magnetic fields.

Another particularity of neutrons is that they are unstable when not bound in a nucleus by the strong force, with a half-life of $\tau_{1/2} = 611$ s (~ 10 minutes) [10], undergoing β^- decay:

$$n \rightarrow p^+ + e^- + \overline{\nu_e} \tag{2.17}$$

Despite being massive, with a rest mass of 939.56 MeV, slightly higher than the proton, neutrons have the particularity of interacting very little with matter when compared to the other types of particles/radiation discussed above. As uncharged particles, they do not interact with atomic electrons by means of Coulomb force, so their principal means of interactions is through the strong force with nuclei. Only when a nuclei of the absorbing atoms intercepts the neutron trajectory (within $\sim 10^{-15}$ m, the range of the strong force) will an interaction occur, which is a very low probability occurrence accounting to the tiny size of the nucleus in relation to the atom. Because of this, neutrons can generally travel long distances through matter without suffering any interaction. When it does happen, four main mechanisms may occur, depending on its energy and on the absorbing material: elastic scattering, inelastic scattering, neutron capture reactions and nuclear fission. The first two are considered neutron scattering interactions, while the latter two are considered neutron absorption interactions.

The total probability for a neutron to interact in matter is given by the sum of the individual cross-sections listed above:

$$\sigma_{\text{total}} = \sigma_{\text{elastic}} + \sigma_{\text{inelastic}} + \sigma_{\text{capture}} + \sigma_{\text{fission}} \tag{2.18}$$

Another relevant parameter is the neutron macroscopic cross-section (Σ), obtained by multiplying the cross-section (σ) by the density of the target material (N, number of nuclei per unit volume):

$$\Sigma_{\text{total}} = N\sigma_{\text{total}} = \frac{N_A \cdot \rho}{M}\sigma_{\text{total}} \tag{2.19}$$

where ρ is the material density, M its molar mass and N_A the Avogadro number. This parameter quantifies neutron interaction probability per unit of path length. Analogously with photos, a beam of neutrons will be exponentially attenuated by an absorber:

$$I(x) = I_0 e^{-\Sigma x} \tag{2.20}$$

where I_0 is the initial number of emitted neutrons and $I(x)$ is the number of neutrons transmitted after travelling a distance x in the absorber.

One additional parameter directly related to neutron cross-section is the neutron mean free path ($\lambda = 1/\Sigma$), which gives the average distance travelled by a neutron between interactions.

Elastic Scattering

When a neutron suffers an elastic collision, a fraction of its energy is transferred to the recoiling nucleus (which remains in the ground state) and in the process the neutron is slowed down. This is the principal mechanism of energy loss for fast neutrons. The kinematics of this interaction is depicted in Fig. 2.7, considering the lab coordinate system.

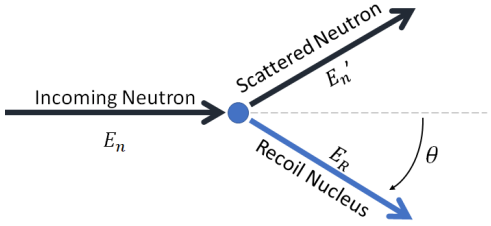

Figure 2.7: Elastic scatter of a neutron with a target nucleus at rest, in the lab coordinate system.

At energies of several MeV, this collision may be treated nonrelativistically. In this case, by considering the conservation of total energy and momentum of the system, the following relation is derived for the energy of the recoil nucleus [8]:

$$E_R = \frac{4A}{(1+A)^2}(\cos^2\theta)E_n \tag{2.21}$$

where E_n and E_R are respectively the energies of the incoming neutron and the recoil nucleus, A is the atomic mass number of the absorber and θ is the scattering angle of the recoil nucleus in the lab coordinate system.

From equation 2.21, we see that the energy transferred to the recoil nucleus is uniquely determined by the mass number of the target material and the scattering angle. For grazing angles, the neutron is only slightly deflected, and the recoil nucleus is emitted almost perpendicularly to the incoming neutron direction ($\theta \approx 90°$), with minimal energy being transferred. The other extreme case, a head-on collision, results in the maximum possible energy transfer, with the recoil being emitted in the same direction as the incoming neutron ($\theta \approx 0°$). In this case, we can write equation (2.21) as:

$$\left.\frac{E_R}{E_n}\right|_{\max} = \frac{4A}{(1+A)^2} \tag{2.22}$$

From this, we can conclude that the energy of a neutron is reduced more efficiently in collisions with nuclei of low atomic mass. In particular, the maximum possible energy transfer from the neutron to the recoil nuclei occurs when A = 1, i.e., when hydrogen is the absorber.

Inelastic Scattering

One additional mechanism that contributes to neutron moderation, although with less preponderance, is inelastic scattering. In an inelastic scattering collision between a neutron and a nucleus, the latter is left in an excited state. Therefore, the total kinetic energy of the system is not conserved, since part of the energy transferred is used to excite the nucleus. The excited nucleus will usually emit characteristic gamma rays upon de-excitation and the neutron loses a greater fraction of its energy than it would in an equivalent elastic collision [8].

Inelastic neutron scattering is only possible if the neutron energy exceeds a characteristic threshold of the absorber element, usually on the order of 1 MeV or more [6]. Below this energy, only elastic scattering may occur. Because elements of lower mass number have higher nuclear excitation energies, this interaction is more probable to occur with heavier nuclei [11].

Neutron Capture Reactions

On neutron capture reactions, the neutron is absorbed by the nucleus of the target material, which becomes unstable and decays producing secondary radiation, such as heavy charged particles, gamma-rays and conversion electrons. The slower the neutron is, the more time it will spend in the proximity of a nucleus, increasing the probability of being absorbed. In general, the cross-section for neutron capture reactions are roughly proportional to $\sim 1/v$, where v is the neutron velocity. Therefore, neutron absorption is more likely to occur at low energies [6].

Reactions of type (n, γ), i.e., in which the only secondary particle produced are gamma-rays, are designated as radiative neutron captures, which occur, for instance, with the isotopes $^{135}\mathrm{Xe}(n,\gamma)^{136}\mathrm{Xe}$, $^{147}\mathrm{Sm}(n,\gamma)^{148}\mathrm{Sm}$ or $^{151}\mathrm{Eu}(n,\gamma)^{152}\mathrm{Eu}$ [12].

For slow neutrons, their initial kinetic energy can be neglected in comparison to the much higher energy released by the reaction, i.e. the Q-value (usually hundreds of keV up to a few MeV). In this approximation, energy and momentum conservation laws dictate that the neutron capture fragments are emitted back-to-back in the cases of the (n, p), (n, t) or (n, α) reactions, which respectively result in the emission of a proton, a triton and an alpha particle, along with the ion that is formed by the remaining neutrons and protons of the nucleus. At the moment of the creation of the two fragments, the atomic electrons are dispersed, and thus the two fragments carry a net electric charge [13]. Additionally, the emission angles are isotropically distributed and do not depend on the energy/velocity of the incoming neutrons, information which is lost after the neutron capture.

The production of secondary radiation through neutron capture reactions is the fundamental mechanism used in the detection of cold and thermal neutrons. However, only a few isotopes are susceptible to neutron-induced reactions with a sufficiently high cross-section, which is a major restriction in the development of detection techniques. Ahead in this chapter, a discussion of the most common nuclear capture reactions used in detectors will be presented.

Nuclear Fission

In the neutron induced fission reactions, the neutron is absorbed by the target nucleus, creating a compound nucleus that is unstable and splits into smaller nuclei releasing two or more neutrons and gamma-rays. The smaller nuclei emitted are called fission products or fission fragments, and they are usually radioactive, undergoing β^- decay [11]. Fission reactions typically release an energy of several hundred MeV, which is hundreds of times greater than the typical Q-values of neutron capture reactions. As with neutron capture reaction, nuclear fission cross-section varies with $\sim 1/v$, and therefore is more likely to occur at low energies.

Nuclides that are capable of capturing neutrons and undergoing fission (with cross-section in order of thousands of barns) are designated as "fissile". Some examples are heavy isotopes such as ^{233}U, ^{235}U and ^{239}Pu.

Spontaneous fission can also occur naturally as a type of radioactive decay, but this phenomenon is very rare, occurring only for a few isotopes, such as ^{240}Pu and ^{252}Cf.

2.2 Neutron Production, Moderation and Detection

2.2.1 Neutron Sources

The activity of a radioisotope source is defined as its rate of decay, given by [8]:

$$A(t) = \left|\frac{dN(t)}{dt}\right| = |\lambda N(t)| \rightarrow N(t) = N_0 e^{-\lambda t} \tag{2.23}$$

where N and N_0 are the number of radioactive nuclei at the time t and $t = 0$, respectively, and λ is the decay constant, which translates the probability per unit time for a nucleus to decay. The SI unit of activity is the *becquerel* (Bq), corresponding to 1 decay per second, although historically the *curie* (Ci) is more widely used, corresponding to 3.7×10^{10} decays per second (the activity of one gram of pure ^{226}Ra). Thus, 1 Bq $= 2.703 \times 10^{-11}$ Ci.

By knowing the activity of a radioactive source at a time $t = 0$ (A_0), the decay constant λ can be used to calculate its activity at any given time:

$$A(t) = \lambda N(t) = \lambda N_0 e^{-\lambda t} = A_0 e^{-\lambda t} \tag{2.24}$$

Some radioactive decays can occur through different decay reactions. The branching ratio is defined as the fraction of particles that decay through a specific decay channel in relation to the total number of possible channels. Thus, the emission rate of a specific particle by a radioactive source is not given by its activity, which indicates only the source disintegration rate. It is necessary to know the decay scheme of the particular isotope and its branching ratios to infer the emission rate of any given particle.

When it comes to neutron sources, the only isotopes that naturally emit neutrons are those that undergo spontaneous fission as a radioactive decay mode. However, such nuclei are rare and their decay rate is very low [11]. For every other case, neutrons are tightly bound to the nucleus by the strong force, so energy above a certain binding threshold must be given to the nucleus to eject them. This energy transfer may be given by collision from a heavy particle, such as a proton or a neutron, or by photon absorption.

To produce neutrons in controlled conditions for scientific or medical purposes, three types of sources can be differentiated: isotopic sources, nuclear reactors and spallation sources.

Isotopic Sources

A neutron isotopic source may be composed by a single radioisotope, if it decays by spontaneous fission, or by mixing together two radioisotopes, in which the decay product of the first (an alpha particle or a gamma-ray) induces a nuclear reaction in the second that results in the ejection of a neutron.

By far, the most commonly used spontaneous fission source is ^{252}Cf, which decays by spontaneous fission with 3% probability, while the remaining decay mode is by emission of an alpha particle to form ^{248}Cm, with 97% probability. The neutron energy spectrum of this source is similar to a fission reactor spectrum, shown in Fig. 2.8, and has a peak around ~ 2 MeV.

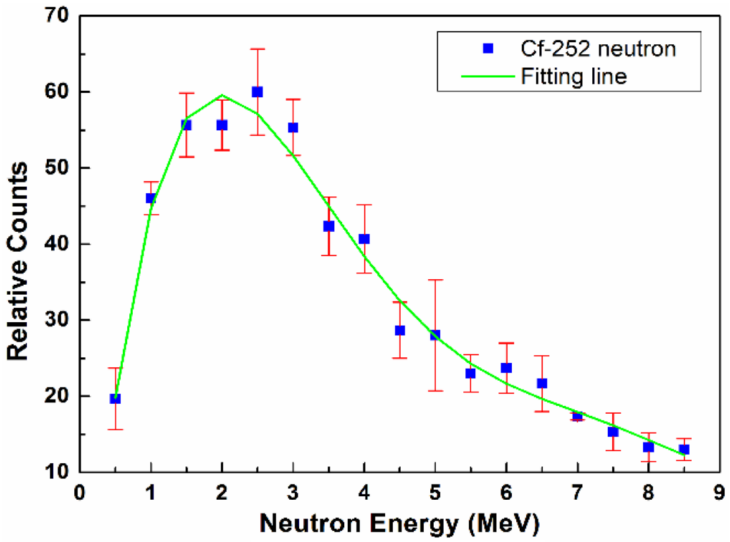

Figure 2.8: ^{252}Cf fission neutron energy spectrum. Image from [14].

3 to 4 neutrons are emitted per decay of ^{252}Cf, depending on the two fission fragments generated. Although ^{252}Cf has a high activity, which means that a small amount of material is sufficient to achieve high neutron emission rates, it also has a short half-life, of just 2.6 years, and consequently it quickly weakens and must be replaced in relatively short times.

Neutron sources can also be produced by bombarding alpha particles on light elements. These are (α, n) reactions, and can be used to build a neutron source by mixing a radioisotope that emits alpha particles with a low atomic weight isotope, usually by blending powders of the two materials, in variable proportions. The most common source of this type is Americium-Beryllium, typically designated as an AmBe source. The decay reaction of ^{241}Am is given by:

$$^{241}\mathrm{Am} \rightarrow {}^{237}\mathrm{Np} + {}^{4}\alpha + \gamma \tag{2.25}$$

with the most probable energies of the alpha particles of 5.54 MeV (84.5%) and 5.44 MeV (13.2%), while the most intense gamma-ray emission occurs at 59.54 keV. Beryllium is the most commonly used material in conjunction with an alpha source because its

nucleus has a loosely bound neutron. By striking that neutron with an alpha particle of sufficient energy, a nuclear reaction takes place that produces a free neutron [11]:

$$\alpha + {}^{9}\mathrm{Be} \rightarrow {}^{12}\mathrm{C} + n \qquad (\mathrm{Q} = 5.75\ \mathrm{MeV}) \tag{2.26}$$

Because alpha particles from the ^{241}Am decay are emitted with several energies and can be differently attenuated before colliding with a ^{9}Be nucleus, the neutron energy spectrum from an ^{241}AmBe source is complex, as shown in Fig. 2.9.

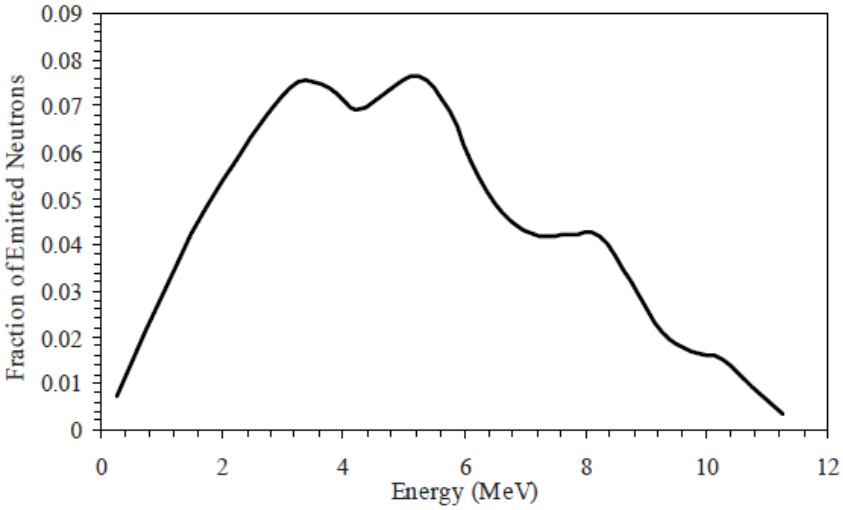

Figure 2.9: Neutron energy spectrum of an AmBe source. Image adapted from [11].

This process to produce neutrons is very inefficient, with only 1 in about 10^4 alpha particles from the ^{241}Am decay interacting with a ^{9}Be nucleus to produce neutrons. About 70 neutrons are produced per MBq of ^{241}Am [13]. Additionally, an AmBe source has a gamma-ray emission rate which is orders of magnitude higher than the neutron yield.

Neutrons can also be produced in the reaction of gamma-ray with light targets, most commonly made of beryllium or deuterium (for example, heavy water). These are (γ, n) reactions, and sources that produce neutrons through this mechanism are referred to as photoneutron sources. The nuclear reactions for the mentioned isotopes are [11]:

$$^{9}\mathrm{Be} + \gamma \rightarrow {}^{8}\mathrm{B} + n \qquad (\mathrm{Q} = \text{-}1.63\ \mathrm{MeV}) \tag{2.27}$$

$$^{2}\mathrm{H} + \gamma \rightarrow {}^{1}\mathrm{H} + n \qquad (\mathrm{Q} = \text{-}2.23\ \mathrm{MeV}) \tag{2.28}$$

These have a negative Q-value (endothermic reactions), meaning that they require an energy input to occur, due to the need of overcoming the binding energy of the neutron in the nucleus. As a consequence, the kinetic energy of the system is inferior after the reaction occurs. An attractive feature of photoneutron sources is the fact that they produce nearly monoenergetic neutrons (if monoenergetic photons are used). The most common gamma-ray sources used to form this sources are ^{24}Na ($\mathrm{E}_\gamma = 2.8$ MeV, $\tau_{1/2} = 15$ hours) and ^{124}Sb ($\mathrm{E}_\gamma = 1.7$ MeV, $\tau_{1/2} = 60$ days) [11]. Similarly to (α, n) sources, only a small fraction of photons actually interact with the source material to produce a neutron, typically around 10^{-6} [15].

The main advantages of isotopic sources, in general, are the fact that they are small, compact, portable and easy to handle. However, these have a very low neutron emission

rate, which severely restricts their use in scientific applications, which generally require a high flux of neutrons incident on the sample. Another disadvantage is the fact these sources cannot be "turned off", being continuously emitting neutrons. As such, their activity will progressively decrease over time until eventually wearing out, typically with the vast majority of neutrons being emitted when the source is not being put into practical use.

Nuclear Reactors

Several neutron research facilities, which require high neutron fluxes for irradiation experiments, produce neutrons through nuclear reactors using ^{235}U as fuel. Although its spontaneous fission decay is only vestigial, this isotope is fissile by thermal neutron absorption, forming an unstable compound nucleus which breaks by fission:

$$^{235}\mathrm{U} + n \rightarrow {}^{236}\mathrm{U}^* \rightarrow \text{fission} \tag{2.29}$$

^{236}U can split up in more than 40 different ways and consequently generate over 80 different fission fragments. In each fission, two fission fragments are emitted along with 2-4 neutrons. The most probable fission fragments and their respective fission yield are ^{95}Zr (6.3%), ^{137}Cs (6.2%), ^{141}Ce (6.0%), ^{144}Ce (6.0%), ^{90}Sr (5.8%) and ^{91}Y (5.4%). Fig. 2.10 shows a plot of the energy spectrum of neutrons released by this reaction.

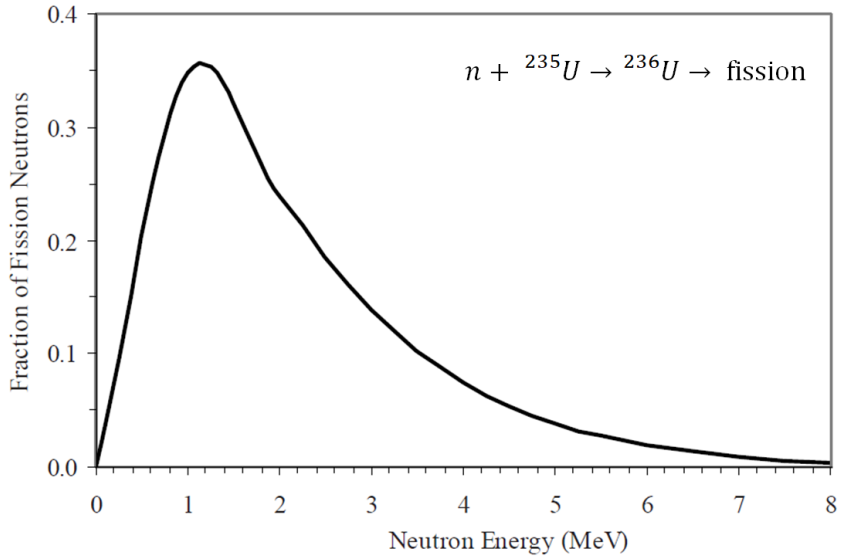

Figure 2.10: Neutron energy spectrum for thermal fission of ^{235}U. Image from [11].

The spectrum shows a peak at $\sim$ 1 MeV and an average value of $\sim$ 2 MeV. Consequently, neutrons require thermalisation before being guided to the beam lines. For this purpose, the ^{235}U fuel is immersed in a "reactor pool", typically filled with demineralised or heavy water, which additionally cools the reactor core and provides shielding from the gamma radiation produced.

^{235}U has a natural abundance of only 0.72%, while ^{238}U makes up for 99.274%. However, the latter is not fissile by thermal neutron absorption. Therefore, nuclear reactions use highly enriched ^{235}U ($> 90\%$) to generate high neutron fluxes.

Nuclear reactors for research typically operate in 1-2 months cycles, followed by a shutdown period to change the fuel element. During operation cycles, neutrons are

produced in steady flux.

Examples of neutron research facilities that use nuclear reactors with enriched ^{235}U as fuel are the Institute Laue Langevin (ILL) [16] in Grenoble, France, the Research Neutron Source Heinz Maier-Leibnitz (FRM II) [17] in Munich, Germany and the PIK reactor [18] in Saint Petersburg, Russia.

Spallation Sources

One additional method to produce neutrons consists of accelerating heavy charged particles up to very high energies and colliding them with a heavy metal. Dozens of neutrons can be stripped from the target by a single collision, in a process known as neutron spallation.

Unlike nuclear reactors, which emit a continuous flux of neutrons, the ions that produce spallation are accelerated in bunches, which typically results in a pulsed neutron source. These, however, can achieve peak intensities 1-2 orders of magnitude higher than nuclear reactors.

Neutron research facilities that produce neutrons through spallation accelerate protons up to relativistic speeds using either a linear accelerator, a cyclotron or a synchrotron, and collide them with heavy metal targets such as tungsten, lead or liquid mercury. The very high energies involved in this reaction require a target cooling mechanism, which is typically achieved with a water circulation system. The European Spallation Source (ESS) [19], currently being constructed in Lund, Sweden, will employ the first wheel-shaped rotating tungsten target, to evenly distribute the energy from proton collisions across it.

The increasing regulatory costs of nuclear reactors due to safety concerns has been driving a shift towards spallation sources. Other examples of neutron spallation sources for scientific research are the SINQ spallation source at PSI (Paul Scherrer Institute) [20] in Villigen, Switzerland, the ISIS Neutron and Muon Source [21] in Oxfordshire, United Kingdom, the Spallation Neutron Source (SNS) [22] in Oak Ridge, United States, the China Spallation Neutron Source (CSNS) [23] in Dongguan, China and the Japan Proton Accelerator Research Complex (J-PARC) [24] in Tokai, Japan. Table 2.1 lists the targets and accelerators used for neutron spallation in these facilities, along with the proton beam power, which can be associated with neutron flux production.

Facility	Target	Accelerator	Proton Beam Power (MW)
ESS	Tungsten	Linear	5 (planned) [25]
SINQ	Lead	Cyclotron	0.75 [26]
ISIS	Tungsten	Synchrotron	0.18 [27]
SNS	Liquid Mercury	Linear	1.4 (2.8 upgrade planned)[28]
CSNS	Tungsten	Synchrotron	0.1 (0.5 upgrade planned)[29]
J-PARC	Liquid Mercury	Synchrotron	0.51 (1.3 upgrade planned)[30]

Table 2.1: Characteristics of the main neutron spallation research facilities.

The PSI accelerator system consists of two isochronous cyclotrons, producing a proton beam with only 20 ns between pulses, which is a delay irrelevant for the production of thermal neutrons [31]. Therefore, the SINQ spallation source is a continuous neutron source, which makes it an exception among spallation sources.

2.2.2 Neutron Energy Ranges

Neutrons are typically classified according to their energy, since their cross-sections for a given type of interaction vary greatly as a function of it. There is no standard classification, and different limits for each energy category can be found across literature. Although some are very exhaustive, discriminating up to 10 different energy ranges [32], here we will account for a simpler common terminology, presented in Table 2.2:

Category	**Energy**	**Wavelength (Å)**	**Velocity (m/s)**	**Temperature (K)**
Ultracold	< 200 neV	> 640	< 6	< 0.002
Very Cold	200 neV $\leq E < 50$ μeV	$40 < \lambda \leq 640$	$6 \leq v < 100$	$0.002 \leq T < 0.6$
Cold	50 μeV $\leq E < 25$ meV	$1.8 < \lambda \leq 40$	$100 \leq v < 2200$	$0.6 \leq T < 290$
Thermal	25 meV	1.8	2200	290
Epithermal	25 meV $< E \leq 500$ keV	$0.0004 \leq \lambda < 1.8$	$2200 < v \leq 10^7$	$290 < T \leq 6 \times 10^9$
Fast	> 500 keV	< 0.0004	$> 10^7$	$> 6 \times 10^9$

Table 2.2: Categories of neutrons according to their energy [33].

Note that in Table 2.2 neutrons are categorized not only by their energy, but also by their wavelength (λ), velocity (v), and temperature (T). These are essentially different descriptions of the same physical property, and can all be related to the neutron energy (E) through equations:

$$E = \frac{1}{2} m_n v^2 \iff v = \sqrt{\frac{2E}{m_n}} \tag{2.30}$$

$$\lambda = \frac{2\pi\hbar}{m_n v} \iff \lambda = \frac{h}{\sqrt{2 m_n E}} \tag{2.31}$$

$$v_p = \sqrt{\frac{2 k_B T}{m_n}} \iff T = \frac{E}{k_B} \tag{2.32}$$

The first term of equation (2.30) is simply the classic definition of kinematic energy, where m_n is the neutron mass, from which velocity is derived. The first term of equation (2.31) identifies the De Broglie relationship, where h is the Planck constant, from which the neutron wave length is derived. Finally, the first term of equation (2.32) is the most probable speed (v_p) of an atom or molecule following a Maxwellian distribution, in which k_B is the Boltzmann constant, from which temperature is derived by replacing the v_p with the classic expression of kinetic energy as used in equation (2.30).

In one extreme of the neutron energy range we have ultracold neutrons (UCN), which are characterized by the unique feature of being totally reflected by most materials under any incident angle, by virtue of their neutron optical potential. This offers the possibility of storing them in "neutron bottles" for hundreds of seconds to study their fundamental characteristics [34]. However, their production is much more technically challenging than thermal or cold neutrons, requiring an additional moderation mechanism beyond what can be achieved using cryogenic moderators, which consists of transferring the neutron energy to a crystal lattice in the form of a phonon [35].

Thermal and cold neutrons are easier to produce, and are the most frequently used in neutron scatter facilities to study samples in irradiation experiments. The energy of thermal neutrons is defined as the most probable energy at room temperature considering

a Maxwell–Boltzmann distribution of temperatures. Therefore, it is given by $k_B T$, with $k_B = 8.617 \times 10^{-5}$eV/K, which yields ~ 0.0253 eV for a temperature of 293 K (20°C).

The energy range of fast neutrons correspond to the original energy carried when they are released from the nucleus to which they were bound, before undergoing moderation.

The interaction of neutrons with matter depend critically on their energy, which makes it impractical to develop detector suitable for use with neutrons of all energies. Instead, neutron detectors are optimized to be deployed in the detection of neutrons of a predetermined energy category, often within an even more specific energy range.

2.2.3 Neutron Moderation

Whichever type of source is used to produce neutrons, they are always originally emitted as fast neutrons, typically with energies the MeV order of magnitude. Because the neutron capture cross-section is inversely proportional to the incoming neutron energy, by a factor of roughly $1/\sqrt{E}$, neutrons used in irradiation experiments undergo a moderation process by which their energy is dissipated, mostly through successive elastic scattering interactions with a moderator medium, until reaching thermal equilibrium with the surrounding atoms, around an energy of 0.025 eV. At this point, neutrons diffuse through matter until being captured or undergoing other type of nuclear reaction. To obtain cold neutrons, more energy needs to be dissipated, which can be achieved using cryogenic moderators such as liquid helium.

Referring back to equation (2.22), it was concluded that hydrogen is the most efficient moderator, since the incoming neutron can lose up to all of its energy in case of a head-on collision with an absorber nucleus. For heavier materials, only successively smaller energy transfers are possible, as evidenced by the plot of Fig. 2.11, calculated from equation (2.22). For this reason, hydrogenous materials such as water, paraffin or polyethylene are the most common moderators to produce thermal neutrons.

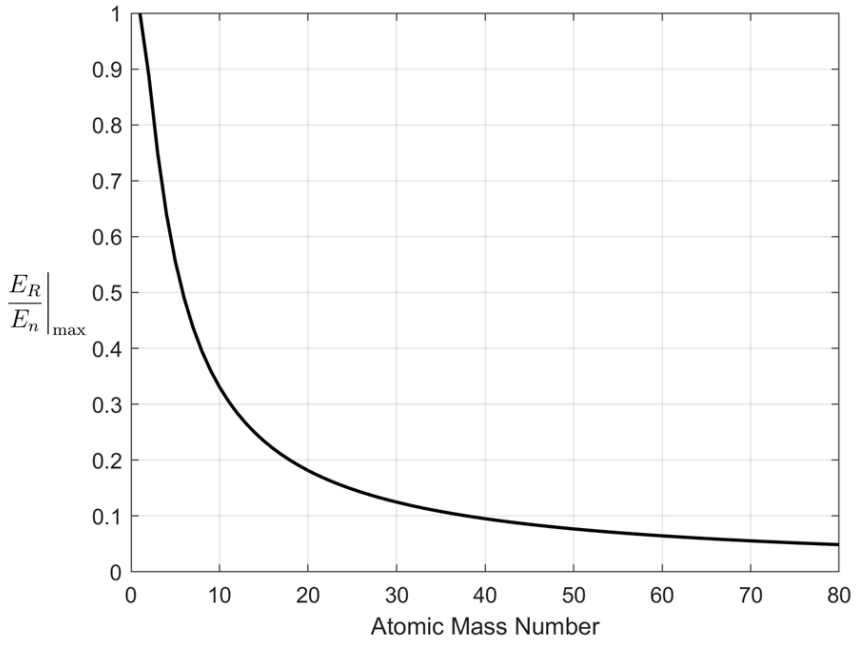

Figure 2.11: Maximum fraction of energy transferred from the neutron to the recoil neutron in an elastic scatter as a function of the atomic mass number.

After hydrogen ($A = 1$), a rapid drop of the neutron energy transferred to the recoil nucleus in a head-on collision ($\frac{E_R}{E_n}|_{\max}$) is observed. Table 2.3 shows this parameter for a variety of absorber materials, calculated from equation (2.22). As an example, if we considering 1 MeV neutrons being moderated by ^{12}C, it would require on average 111 collisions to reach thermal equilibrium. In contrast, this would be achieved after only about 17.5 collisions using hydrogen as moderator [6].

Target Nucleus	$\frac{E_R}{E_n}\|_{\max}$
$^{1}_{1}$H	1
$^{2}_{1}$H	0.889
$^{3}_{1}$H	0.750
$^{4}_{2}$He	0.640
$^{12}_{6}$C	0.284
$^{16}_{8}$O	0.221

Table 2.3: Neutron energy transferred to the recoil nucleus in a head-on collision for several absorber materials.

2.2.4 Neutron Conversion and Detection

As seen in section 2.1.4, neutrons can travel long distances without interacting in most materials, due to their neutral charge. Furthermore, they do not interact directly with atomic electrons, as photons do. Therefore, mechanisms for neutron detection are based on indirect methods [36].

All four neutron interaction mechanisms (elastic and inelastic scatter, neutron capture reactions and fission) can be exploited in the development of neutron detectors. Nonetheless, there is a common factor between them: it is the secondary radiation produced in these interactions that initiates the detection processes. This radiation might be protons, electrons, alpha-particles, gamma-rays or fission fragments. The process of producing secondary radiation with the purpose of identifying the passage of a neutron is designated as neutron conversion, and it is the fundamental principle of neutron detectors. The detection of neutrons is, therefore, a two-step process. Although some exceptions exist, which will be presented ahead, most neutron detectors employ different materials for neutron conversion and for the amplification and detection of the secondary radiation produced. These can be solid, liquid, gaseous, or a combination of different states for neutron conversion and secondary radiation detection.

As already explained, all neutrons are originally produced as fast neutrons, and their detection is typically achieved through neutron capture reactions after being thermalized. Although this is the most deployed technique, the detection of fast neutrons is also possible by exploiting scatter interactions. In such cases, they are designated as fast neutron detectors, and most of them rely on the elastic scattering of a neutron with a hydrogen nucleus, where the recoiling proton acquires sufficient kinetic energy to ionize the surrounding material, creating electron-ion pairs that are collected by an electrode to generate an electrical signal [37]. An alternative strategy is based on using PMTs to detect the 2.22 MeV gamma-ray emitted in the inelastic scattering of a neutron with a hydrogen nucleus [38].

Neutron detection through nuclear fission reaction is also possible. Detectors that

employ this mechanism are designated as fission chambers, which consist of a gaseous detector with a thin ^{235}U coating on the inner walls. The two fission fragments are emitted in opposite directions and one of them is emitted towards the gas where electron-ion pairs are created. Fission chambers are operated in ionization mode because the ionization caused by the high energy fission fragments is sufficient to generate a measurable signal, without further charge multiplication being necessary [36]. Neutron gaseous detectors that employ other conversion materials operate in the proportional regime. The differences between these regions of operation will be addressed in section 2.3.2.

Despite the possibility of using the above-mentioned mechanisms, the vast majority of neutron detectors rely on nuclear capture reactions to detect the charged particles or gamma-rays produced in this interaction. When selecting the conversion material to use in a detector, the first property to consider is the thermal neutron capture cross-section, which should be high enough in order to achieve a high detection efficiency. This is a major restriction, since only a few isotopes have relevant thermal neutron capture cross-section. Table 2.4 shows some of the highest cross-sections for the capture of thermal neutron (σ_{th}) found in natural and stable isotopes (not considering isotopes that react via nuclear fission), and a plot of the cross-sections of the listed isotopes as a function of the incoming neutron energy in depicted in Fig. 2.12.

Isotope	**Isotopic Abundance**	$\boldsymbol{\sigma_{th}}$ **(barn)**	**Reaction Products**	**Q-value (MeV)**
^{3}He	0.000137%	5 330	p^+, t	0.764
^{6}Li	7.6%	940	t, α	4.78
^{10}B	19.9%	3 840	α, ^{7}Li, γ	2.31 (94%) 2.79 (6%)
^{113}Cd	12.2%	20 600	γ, e^-	9.04
^{155}Gd	14.8%	60 900	γ, e^-	8.54
^{157}Gd	15.7%	254 000	γ, e^-	7.94

Table 2.4: Thermal neutron capture cross-sections (σ_{th}) and type of neutron capture reaction for relevant stable isotopes.

Different reaction products are produced depending on the isotope used for the neutron capture reaction. This is a vital aspect to regard in the development of neutron detectors, and the adequacy of each reaction depends on the specific conditions and environment in which the detector is expected to be deployed. Generally, although not necessarily, reactions that produce heavy charged particles (^{3}He, ^{6}Li and ^{10}B) are the most convenient to be used in neutron detectors. Apart from the cross-section and type of secondary particles produced, other important aspects must be considered when selecting a neutron conversion material for a detector, such as their isotropic abundance in nature (or availability in enriched formats), material toxicity, robustness or acquisition cost. In Fig. 2.12 it can be seen that the neutron capture cross-section is strongly dependent on energy of the incoming neutron, roughly by the factor $1/\sqrt{E}$ (or $1/v$). For cadmium and gadolinium, this dependence is broken at defined energies by the presence of nuclear resonances. Some characteristics of the neutron capture reactions of the isotopes listed in Table 2.4 will now be addressed.

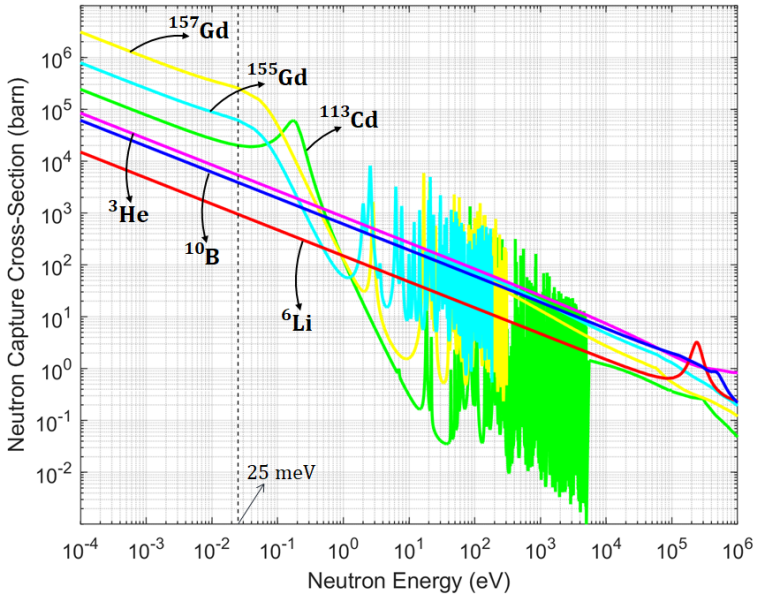

Figure 2.12: Neutron capture reaction cross-sections as a function of incident neutron energy for ^{3}He, ^{6}Li, ^{10}B, ^{113}Cd, ^{155}Gd and ^{157}Gd. Plotted with data from [39].

^{3}He(n,p)^{3}H Reaction

Gaseous at room temperature, ^{3}He is currently the most deployed material in neutron detectors, in the form of gaseous proportional counters (PCs) [40]. This isotope has the highest cross-section ($\sigma(^{3}He) = 5330$ barn) among those in which the neutron capture reaction leads to the production of heavy charged particles. The reaction that occurs when a neutron is captured by a ^{3}He nucleus results in the production of a triton and a proton:

$$^{3}\text{He} \; + \; n \; \rightarrow \; ^{3}\text{t (191 keV)} \; + \; ^{1}\text{p (573 keV)} \quad \text{(Q = 764 keV)} \tag{2.33}$$

The thermal neutron energy is very small when compared to the reaction Q-value. As a consequence of this, it is impossible to extract any information on the incoming neutron energy. Another consequence is that, because the incoming linear momentum is essentially zero, the conservation of momentum dictates that the two reaction products will be emitted in opposite directions. Basing on the energy and momentum conservation principles, we can calculate the individual energies of the triton and proton produced:

Energy Conservation:

$$E_t + E_p = Q \tag{2.34}$$

Momentum Conservation:

$$\begin{aligned} |\overrightarrow{p_t}| = |\overrightarrow{p_p}| \implies m_t v_t = m_p v_p &\iff m_t \sqrt{\frac{2E_t}{m_t}} = m_p \sqrt{\frac{2E_p}{m_p}} \\ &\iff m_t E_t = m_p E_p \end{aligned} \tag{2.35}$$

Combining equations (2.34) and (2.35), we obtain the relations:

$$\begin{cases} E_\alpha = \dfrac{Q}{\frac{m_p}{m_t} + 1} \\ \\ E_t = Q\left(1 - \dfrac{1}{\frac{m_p}{m_t} + 1}\right) \end{cases} \tag{2.36}$$

which can be used to determine the energies of each of the reaction products. Therefore, the energy released in the ^{3}He reaction, $Q = 764$ keV is distributed with $E_t = 191$ keV and $E_p = 573$ keV.

The same principles can be used to calculate the energies of the reaction products emitted in neutron capture reactions that originate heavy charged particles, namely the ^{6}Li and the ^{10}B reactions.

The main drawback of ^{3}He as a neutron conversion in detectors is the fact that it is extremely scarce in nature (with an isotopic abundance of $\sim 0.000137\%$), which led to an unsustainable supply and demand scenario that will be further discussed in section 3.2.

^{6}Li(n,t)^{4}He Reaction

Neutron capture by the ^{6}Li isotope, a solid at room temperature, results in the reaction:

$$^6\text{Li} \; + \; n \; \rightarrow \; ^3\text{t (2.73 MeV)} \; + \; ^4\alpha \text{ (2.05 MeV)} \quad \text{(Q = 4.78 MeV)} \tag{2.37}$$

Similarly to the ^{3}He reaction, the alpha particle and triton are emitted in opposite directions due to energy and momentum conservation. Among the neutron capture reactions that produce heavy charged particles, this is the one with a larger Q-value (4.78 MeV). On the other hand, its cross-section is the lowest, with a value of $\sigma(^6Li) = 940$ barn for thermal neutrons.

Although ^{6}Li has a low natural isotopic abundance (7.6%), with the remaining fraction attributed to ^{7}Li, high levels of ^{6}Li enrichment ($\sim$ 95%) are easily achievable. ^{6}Li is most often found in neutron detectors combined with scintillating materials such as ZnS [41–43]. The heavy charged particles released in the neutron capture reaction interact with the scintillating material, exciting its atoms which subsequently emit light in the de-excitation process. This light is then detected, typically with PMTs. The light yield of the triton from the ^{6}Li reaction is about an order of magnitude higher than that of the alpha particles from the ^{10}B reaction [44]. Additionally, boron-loaded detectors are more expensive, which tends to make scaling to larger-volume detectors cost-prohibitive [45]. These factors make ^{6}Li a particularly attractive material for neutron scintillator detectors.

^{10}B(n,α)^{7}Li Reaction

Another very common material in neutron detectors is solid boron, which has a relatively high neutron capture cross-section for the ^{10}B isotope ($\sigma(^{10}B) = 3840$ barn),

and decays into an α-particle and a ^{7}Li nucleus upon a neutron capture:

$$^{10}\mathrm{B} \; + \; n \; \rightarrow \; \begin{cases} ^{7}\mathrm{Li}^{*} \; (0.84 \text{ MeV}) \; + \; \alpha \; (1.47 \text{ MeV}); & \mathrm{Q} = 2.31 \text{ MeV } (94\%) \\ \\ ^{7}\mathrm{Li} \; (1.01 \text{ MeV}) \; + \; \alpha \; (1.78 \text{ MeV}); & \mathrm{Q} = 2.79 \text{ MeV } (6\%) \end{cases} \tag{2.38}$$

When a thermal neutron is captured by ^{10}B two possible outcomes can follow, with 94% chances of producing ^{7}Li in the first excited state and 6% in the ground state. When the excited ^{7}Li nucleus is produced, it quickly returns to the ground state ($\tau_{1/2} = 10^{-13}$ s) by emitting a 0.48 MeV gamma-ray. The two branches result in different energies of the secondary particles produced, as identified in reaction 2.38. Again, energy and momentum conservation dictates that the charged particles are emitted in opposite directions.

^{113}Cd(n,γ)^{114}Cd Reaction

The ^{113}Cd(n,γ)^{114}Cd reaction leads to the emission of gamma-ray cascades from ^{144}Cd with a sum energy of 9.043 MeV [46], along with conversion electrons with energies from 70 keV to 535 keV [47].

Both have low stopping power, and consequently this is not a converter commonly found in neutron detectors. However, exceptions exist, particularly aimed at homeland security applications where there is interest in simultaneously detecting neutrons and gamma-rays. Detection is achieved by using plastic scintillators covered by a cadmium film. While the latter absorbs the neutrons, the scintillator can simultaneously moderate them and detect the gamma-rays emitted in the ^{113}Cd neutron capture reaction as well as those present in the environment originating from other sources. Discrimination between these signals is possible due to the characteristic behaviour of fast neutrons inside the detector, producing recoil protons in the thermalisation process and losing their energy quickly. These protons also produce a signal in the scintillator, and the short delay time between the thermal neutron capture signal after the recoil proton signal allows using the time coincidence to confirm it is a neutron signal and thus discriminate from gamma-ray interactions from other sources [48].

^{155}Gd(n,γ) and ^{157}Gd(n,γ) Reaction

Gadolinium has the largest neutron capture cross-section of all isotopes, which is why this isotope is favoured in certain detection applications. Natural gadolinium contains only 14.80% of ^{155}Gd and 15.65% of ^{157}Gd, with the remaining isotopes having an insignificant cross-sections for thermal neutron capture. Nonetheless, due to the very high cross-sections of these isotopes, especially ^{157}Gd, natural gadolinium has a thermal neutron capture cross-section of $\sigma(^{\mathrm{nat}}\mathrm{Gd}) = 48800$ barn, which is still about 12.7 times higher that ^{10}B [32].

However, it is not a common neutron converter, mostly because neutrons and gamma-rays produce a similar signature in the detector. The neutron capture reaction results in the emission of a gamma-ray cascade with energies up to 7.94 MeV for ^{157}Gd and 8.5 MeV for ^{155}Gd, along with conversion electrons with energies ranging from 29 keV to 250 keV. Additionally, it is a high-Z ($Z = 64$) material, which also increases its sensitivity to gamma background [49].

Gadolinium is used in experiments for the direct detection of dark matter such

as XENONnT and LUX-ZEPLIN, to absorb and tag background neutrons, vetoing neutron induced events from potential dark matter interactions. Both experiments essentially consist of a two-phase (liquid-gas) time projection chamber (TPC) filled with xenon, surrounded by several layers of shielding, to detect interactions from dark matter candidates such as WIMPs. In the XENONnT experiment, gadolinium is used as a dopant in the water shielding that surrounds the TPC, and the gamma-rays emitted in the ^{155}Gd and ^{157}Gd reactions are directly detected by PMTs distributed across the walls of the water tank [50]. In the LUX-ZEPLIN experiment, gadolinium is loaded in a liquid scintillator (linear alkylbenzene) placed inside acrylic vessels inside a water tank, surrounding the TPC, and it is the scintillation induced by the gamma-rays of the Gd neutron capture reaction that is detected, also using PMTs on the walls of the water tank [51].

2.2.5 Gamma-ray Discrimination

Gamma-rays are naturally present in the same environments where neutrons are produced, whether considering portable isotopic sources, spallation facilities or nuclear reactors. Their energy extends over a wide range, from a few hundred keV up to a few MeV [52], and they can originate from a multitude of sources. For one, the nuclear decay or nuclear reaction that generates neutrons also emits energy in the form of high energy photons. Also, although elastic scattering is the dominant mechanism in neutron moderation, inelastic scattering may also occur, in which case the nucleus is left in an excited state which quickly de-excites by emitting a gamma-ray. Furthermore, as neutrons are moderated by scattering with hydrogen atoms of conventional moderators such as water, paraffin or polyethylene, they may also undergo a radiative neutron capture reaction with a hydrogen atom, which leads to the emission of a 2.22 MeV gamma-ray [38]. Additionally, after long irradiation periods, detector components can undergo neutron activation [52], inducing radioactivity in the materials which may decay via gamma-ray emission. Finally, in the case of boron-based detectors, the neutron capture reaction itself results in the emission of a 0.48 MeV photon with 94% probability (reaction (2.38)).

When traversing the detector, gamma-rays can interact with the gas volume or the surrounding walls (the probability of interaction with the thin anode wire(s) is negligible due to its small dimensions). Photons are detected after being converted into electron-ion pairs when interacting in the detector (the exception to this are scintillator detectors, that use photomultiplier tubes or other photosensors to detect light directly). Low energy photons are more likely to interact in the gas by photoelectric effect, while high energy photons interact mostly via Compton scattering with the detector walls and only generate a signal if the recoil electron reaches the gas [53, 54]. Overall, gamma-ray interactions on the walls are the most prevalent effect. Because the high energy electrons emitted from the walls in the Compton effect have a low stopping power in the gas, they will only deposit a fraction of its energy. Consequently, the detection of a single gamma-ray results in a low-amplitude pulse that can be separated from neutron induced signals. However, for high gamma interaction rates, a pileup effect occurs, in which pulses from several individual gamma-ray interactions are superimposed and the resulting peak amplitude extends to higher energies, increasing the overlap with the neutron spectrum. This phenomenon is represented in Fig. 2.13, which shows the response of a ^{3}He detector at 5 bar irradiated with gamma-rays emitted by a ^{137}Cs source, which decays mainly by emitting a 662 keV photon. The gamma-ray exposure rate was varied from 100 mR/h to 5 R/h by

using sources with different activities and by varying the distance from the source to the detector, for equal acquisition times [55].

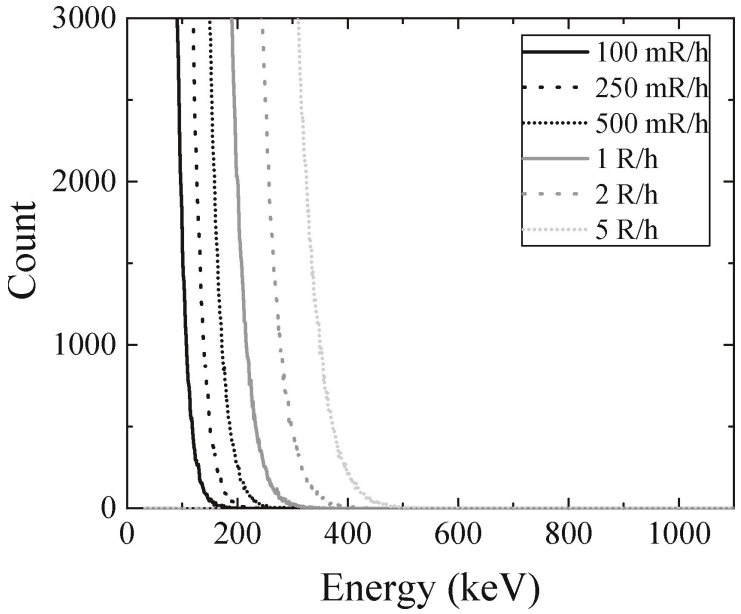

Figure 2.13: Gamma-ray energy spectrum from a ^{3}He neutron detector for several exposure rates (units of Roentgen per hour). Image from [55].

Because gaseous detectors are not efficient in the detection of high-energy gamma-rays, their signature is a pulse height distribution decreasing exponentially with increasing energy. Discrimination is usually achieved by setting a cut-off energy in the pulse height distribution and discarding signals that fall below that threshold. More complex discrimination methods consist of analysing each signal pulse. Because gamma-ray interactions typically result in longer electron-ion pairs tracks in the gas compared to those induced by the heavy-charged particles emitted in neutron capture reactions, the latter generates pulses with faster rise times, as all electrons reach the anode almost simultaneously. By looking at the rise times of each pulse, the slower ones can be assumed to come from gamma-rays and be rejected [2].

Seeing that gamma-ray interaction cross-section increases with the atomic number of the material, proportionally to Z^n where n varies between 4 and 5 over the photon energy range [8], the choice of aluminium for the detector walls ($Z = 13$) over stainless-steel, which is mainly composed by iron ($Z = 26$), can have a relevant positive impact on gamma-ray discrimination [56].

2.3 Gaseous Radiation Detectors

Gaseous detectors were the first electrical devices developed for radiation detection [6], and are still widely used. They are generally cheap to produce, relatively simple to operate, require low maintenance and can cover large volumes. In their simplest format, they consist of a gas-filled chamber with two electrodes: a cathode and an anode. By applying an electric potential difference between them and using a proper charge collection system, it is possible to count the number of particles crossing the detector, identify them, measure their energy, and track their trajectories in the gas in two or three dimensions.

A type of gaseous detector widely used in the detection of low energy x-rays and neutrons is the proportional counter, the kind of detectors developed in the aim of this thesis, as will be presented in Chapters 4 and 5. Introduced in the 1940s [8], their most common geometry is a cylindrical cathode with a thin anode wire centred on its axis, creating an electrical field with an intensity that varies inversely with radius.

The general concepts of gaseous detectors, and some relevant characteristics specific to proportional counters will now be discussed.

2.3.1 Filling Gas

When an ionizing radiation traverses a gas, it causes the excitation and ionization of the gas atoms. Associated with these processes, are the excitation and ionization potentials, which give the minimum energy necessary to either excite or remove an electron from the atom. Gaseous detectors work by collecting the electron-ion pairs generated when incident radiation traverses the gaseous volume of the detector, generating an electronic output signal. These electron-ion pairs are denoted as the primary ionization or primary charges. The average energy required to produce one electron-ion pair in a gas is defined as its w-value. This number is not equal to the ionization potential, but rather a bit superior, due to the fact that some of the energy is lost in excitation processes, which do not contribute to the formation of electron-ion pairs. It is also relatively independent of the type of incident radiation. Table 2.5 shows the properties of some of the most common filling gases.

Gas	**Excitation Potential (eV)**	**Ionization Potential (eV)**	**w-value (eV)**
H_2	10.8	15.4	37
He	19.8	24.6	41
N_2	8.1	15.5	35
O_2	7.9	12.2	31
Ne	16.6	21.6	36
Ar	11.6	15.8	26
Kr	10.0	14.0	24
Xe	8.4	12.1	22
CO_2	10.0	13.7	33
CH_4		13.1	28

Table 2.5: Excitation and ionization potential, and mean energy for electron-ion pair creation of common filling gases [6].

Gases with low w-value are preferred to employ in detectors, since that results in a greater number of electron-ion pairs produced when interacting with radiation of a given energy. To convert these electron-ion pairs into an electrical signal, it is essential that they (or at least the electrons) reach the electrodes for their charge to be collected. However, during the drift of these charge carriers, three types of interaction with the gas molecules can occur that causes the original charge to be lost and consequently to not contribute to the signal formation. These are charge transfer, electron attachment and recombination. Charge transfer consists of a positive ion colliding with a neutral gas molecule and receiving an electron from it, turning into a neutral particle, while the gas molecule becomes ionized. Electron attachment occurs when a free electron is captured by

a neutral molecule during its diffusion, forming a negative ion, that shares many properties with the original positive ion formed in the ionization process, but with opposite charge. Some gases, such as oxygen, have a high tendency to form negative ions by attachment of free electrons. Collisions between the positive ions and the free electrons can also occur, in a process designated as recombination, which restores the state of charge neutrality [8].

Another important aspect in detector operation is maintaining the purity of the gas. The filling gas can be either sealed in the detector or circulating in continuous flow. In the first case, a purification system must be deployed to remove traces of oxygen and other electronegative impurities. It is common to have a sealed detector in which the gas is circulating, in such a way that the purifying system is separated from the detection volume. In the case of detectors operating in continuous flow, there is no need for a gas purification system because new gas is constantly being injected into the detector, while the exiting gas is vented to the atmosphere. The latter is commonly used when working with cheap filling gases, since it avoids potential problems involving gas purity. An additional advantage is the flexibility of changing the filling gas when desired.

Most gaseous detectors use a noble gas because of their low chemical reactivity, relatively low electron attachment coefficient, they can be easily purified and require the lowest electric field intensities for avalanche multiplication of charges. Argon is the most widely used filling gas, mostly because of its affordability. However, argon or other noble gases are typically used in a mixture with a molecular gas such as CH_4 (methane) or CO_2 (carbon dioxide), designated as the quenching gas, which serves the purpose of reducing the detector dead time and maintaining the proportionality between the deposited energy and the collected charge (these concepts will be explained in further sections). As already mentioned, when the incoming radiation interacts with the gas, a fraction of the energy transfer results in the excitation of the gas molecules, rather than in ionizations. In the de-excitation process, these emit photons (in the visible or ultraviolet region) capable of originating new ionizations, either in the filling gas or in the cathode walls of the detector. These new free electrons will then drift towards the anode and can trigger another avalanche multiplication, potentially increasing the detector dead time and causing a proportionality loss between the energy of the incoming radiation and the collected charge. To prevent this effect, a polyatomic quenching gas is added, which absorbs the de-excitation photons and dissipates their energy through molecular dissociation or elastic collisions. A small concentration of a quenching gas (5%-10%) is sufficient to produce a significant change in the detector operation.

Finally, it should be emphasized that the choice of gas is completely application dependent, and potentially influenced by a compromise between effectiveness and affordability. For instance, in detectors that require high efficiency for the detection of gamma-ray photons, higher Z-number gases such as krypton or xenon are beneficial. In contrast, for applications in which energy resolution is not a particular concern, virtually any affordable gas can be used, even ambient air [6].

2.3.2 Regions of Operation

The charge generated in a single detection event depends heavily on the voltage applied between the cathode and the anode. According to this, different regions of operation can be identified, depicted in Fig. 2.14

Detectors do not operate in the recombination region, because the electric field is too low to overcome the electron-ion recombination effects and consequently the collected

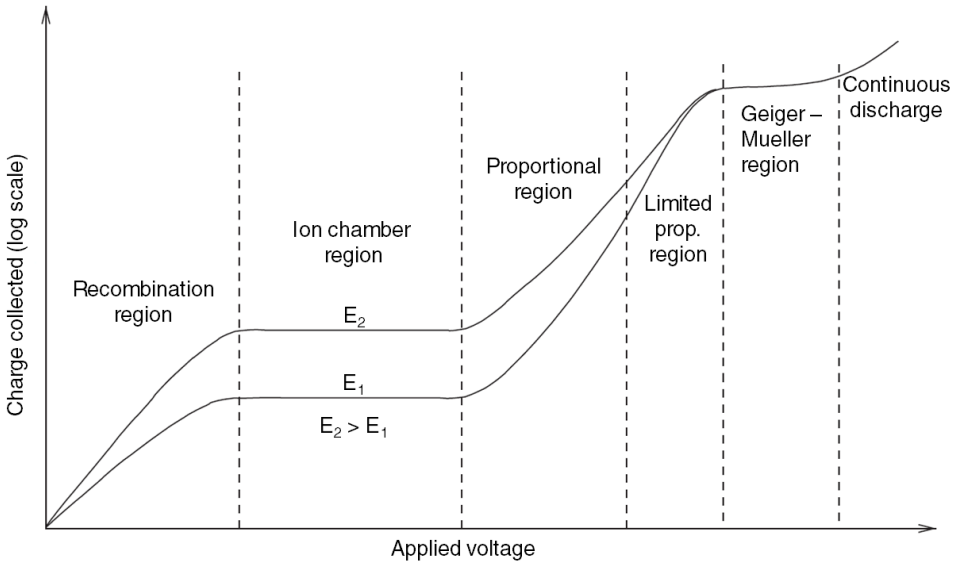

Figure 2.14: Variation of the pulse height produced by different types of detectors with respect to the applied voltage. The two curves correspond to two different energies of incident radiation ($E_2 > E_1$).

charge does not accurately reflect the energy deposited by the incoming radiation.

Increasing the applied voltage, the operation region for ionization chambers is reached. In this region, the recombination effects are negligible, and consequently the collected charge is proportional to the energy deposited in the gas by the incoming radiation, which makes its measurement possible. Because there is no charge multiplication in this region, increasing the anode voltage does not affect the measured current, which is designated as the saturation current. The signal derived only from the primary charges is small, so ionization chambers are generally used in the detection of highly ionizing particles in current mode.

Further increasing the electric field magnitude, the threshold value for charge multiplication in the gas is reached, and we enter the proportional region. This designation derives from the fact that the collected charge is proportional to the primary charge generated. If the electrons from the primary ionization gain enough energy from the electric field, they can induce an additional production of electron-ion pairs in the gas. The electrons liberated in this secondary ionization will also be accelerated by the electric field, and collide with other gas molecules, thus creating additional ionizations. This process goes on, generating a cascade of secondary ionizations known as the Townsend avalanche. This multiplication of charges allows for the amplification of the detector signal, and is fundamental to detect less ionizing particles. In this region, the total charge collected by the detector grows exponentially with the increase of the applied voltage.

If the bias voltage is further increased, nonlinearities will begin to be observed, as more and more secondary charges are produced in the detector. This corresponds to the region of limited proportionality, and occurs because the positively charged ions move much slower than the electrons, on account of their higher mass. As a result, a cloud of positive charges is formed between the anode and the cathode, inducing the so-called space charge effects, which distort and reduce the effective electric field experienced by the electrons. The consequence of this is the loss of proportionality between the primary charge and the collected charge, and therefore this is an operation region to avoid when

the energy information of the detected particles is intended.

Finally, Geiger-Muller counters operate in the highest voltage region, where the space charge effect created by the positive ions is so high that it manages to eventually reduce the electric field below the threshold for gas multiplication. Therefore, avalanche multiplication of charges occurs in a self-limiting process, terminating when a fixed number of secondary positive ions have been formed, regardless of the initial number of electron-ion pairs. This is known as a Geiger discharge. The collected charge is not proportional to the deposited energy, and consequently this information, as well as particle identification, cannot be accessed with Geiger-Muller counters. On the positive side, these detectors provide a signal so strong that each particle creates a pulse above the noise level, which allows to accurately count the number of particles traversing the detector, although with the disadvantage of relatively long dead times, since it is only after most of the slow moving positive ions being collected by the cathode that the detector can start working again.

If the applied voltage is increased beyond this point, the positive ions will be accelerated with sufficient energy to violently strike the cathode walls and strip electrons from it. These electrons will then drift towards the anode and trigger another avalanche, giving rise to successive Geiger discharges, in a cycle that cannot be controlled unless the applied voltage is lowered. In this region, electric arcs can be produced between the anode and the cathode, eventually damaging the detector.

2.3.3 Gas Multiplication Factor

As it was seen, when a gaseous detector operates in the proportional region, the multiplication of electrons occurs. In these conditions, the total charge Q generated in the detector is expressed by:

$$Q = n_0 e M \tag{2.39}$$

where n_0 is the number of primary electron-ion pairs, e the elementary charge and M is defined as the average gas multiplication factor, also commonly designated as the detector gain or gas gain.

The number of primary electron-ion pairs generated in an ionization event can be derived from the w-value, which is considered as an empirical value:

$$n_0 = \frac{E}{w} \tag{2.40}$$

where E is the energy deposited in the gas by the incident radiation.

Electron multiplication in a gas is a threshold process, that can only occur if the accelerated electrons acquire an energy superior to the ionization potential of the neutral gas molecules between collisions. In that case, collisions between the electrons and gas molecules generate further electron-ion pairs. The fractional increase in the number of electrons ($\frac{dn}{n}$) per path length (dr) is, therefore, a cascade process given by the Townsend equation:

$$\frac{dn}{n} = \alpha dr \tag{2.41}$$

where α is the Townsend coefficient of the gas. Its value is zero below a threshold and then rises with increasing electric field magnitude. Solving this equation, considering a

uniform electric field, gives an electron density that grows exponentially with distance as the avalanche progresses:

$$n(x) = n_0 e^{\alpha r} \tag{2.42}$$

If we consider a cylindrical field with a central wire anode surrounded by cathode walls, the most common geometry of proportional counters, the gas multiplication factor (M) is obtained by integrating equation (2.41) in terms of the electrical field $\mathcal{E}(r)$:

$$\ln M = \int_{\mathcal{E}(a)}^{\mathcal{E}(r_c)} \alpha \frac{\partial r}{\partial \mathcal{E}} d\mathcal{E} \tag{2.43}$$

where a is the anode radius and r_c the critical radius, above which the electric field falls below the threshold value for charge multiplication.

Assuming linearity between the α and $\mathcal{E}$, Diethorn derived the widely used expression for M [57]:

$$\ln M = \frac{\mathrm{HV}}{\ln(b/a)} \frac{\ln 2}{\delta V} \left(\ln \frac{\mathrm{HV}}{pa \ln(b/a)} - \ln K \right) \tag{2.44}$$

where HV is the applied voltage, b is the cathode radius, p the gas pressure and the two parameters δV and K are empirical constants for a given gas. δV corresponds to the potential difference through which an electron moves between successive ionizations, and K represents the threshold value of $\mathcal{E}/p$ below which electron multiplication is no longer energetically possible.

Expression (2.44) is valid for uniform electric fields, assuming the absence of multiplications induced by excitation photons from the gas molecules and a negligible space charge effect in the multiplication region.

2.3.4 Detection Efficiency

Detection efficiency is one of the most relevant parameters of a radiation detector, as it essentially quantifies the probability of a particle with a given energy being detected. Depending on the application, it is common to differentiate between absolute and intrinsic efficiency. Absolute efficiency is defined as:

$$\epsilon_{\mathrm{abs}} = \frac{\text{number of pulses detected}}{\text{number of radiation quanta emitted by the source}} \tag{2.45}$$

Consequently, it is not only dependent on the detector properties but also on the geometrical characteristics of the experimental setup, such as the distance between the source and the detector. To know the detector efficiency independently of the experimental setup disposition, intrinsic efficiency is used:

$$\epsilon_{\mathrm{int}} = \frac{\text{number of pulses detected}}{\text{number of radiation quanta incident on the detector}} \tag{2.46}$$

This expression for efficiency is only dependent on the detector and source characteristics, and not on their relative positions, neglecting small changes in the path length of the radiation through the detector that may come by increasing the distance between them. The intrinsic and absolute efficiencies can be related to each other by the probability of radiation incidence on the detector. For isotropic sources, this probability

is given by the solid angle (Ω) of the detector seen from the source position, and the mentioned relation is given by $\epsilon_{\text{int}} = \epsilon_{\text{abs}} \times (4\pi/\Omega)$ [8].

Among other factors, detection efficiency is mostly dependent on the type and energy of the incident radiation, and on the detector size and materials. In general terms, charged particles (such as electrons, protons and heavy ions) interact more easily than electrically neutral ones (such as photons, neutrons and neutrinos). Also, large detectors allow for increased detection volumes, and consequently for greater efficiency. But naturally, detectors can be optimized for the detection of any given particle.

One relevant detector characteristic that affects detection efficiency is dead time, which is the minimum time required for a detector to separate two events in order for them to be recorded as two separate pulses. This time depends on the detector itself, related to the collection time of the electron-ion pairs, and on the associated electronics, such as the preamplifier peaking time and the remaining pulse-processing units. During dead time period, a detector may either be insensitive, i.e., any events arriving are lost, or, in case the detector is sensitive during this period, an arriving event will pile-up on the first event and cause a distortion of the signal, and subsequent loss of information of both events [6]. In gaseous detectors, dead time can be reduced by increasing the electric field in the drift region (which allows a faster collection of the electron-ion pairs in the gas), or by choosing a filling gas with high stopping power and high electron drift velocities.

When determining the efficiency of a detector, a minimum energy threshold is defined to separate the signal from the interactions of the radiation being measured from electronic noise or other sources of background.

2.3.5 Energy Resolution

Due to the statistical nature of ionization reactions, the number of ion pairs produced by two identical incident particles with the same energy will not necessarily be the same. These statistical fluctuations limit the achievable energy resolution of detectors. As a consequence, when a detector is exposed to a monoenergetic source of radiation, its pulse height spectrum (PHS) will not exhibit a perfectly defined peak, but rather a distribution around an average value, which follows a Gaussian distribution. This effect is depicted in Fig. 2.15 for two detectors with different energy resolution.

The energy resolution (R) of a peak at energy E and with width ΔE is defined as $\frac{\Delta E}{E}$. Its value is given as a percentage, and is determined through the full width at half maximum (FWHM) divided by the peak centroid (A_0) of the Gaussian distribution obtained when a detector is irradiated by a monoenergetic source:

$$R = \frac{\text{FWHM}}{A_0} \tag{2.47}$$

Because the FWHM of a Gaussian distribution is related to its standard deviation (σ) by $\text{FWHM} = 2\sqrt{2\ln 2}\,\sigma \approx 2.355\,\sigma$, energy resolution can also be written in terms of the collected charge (Q) as:

$$R = 2.355\left(\frac{\sigma_Q}{Q}\right) \tag{2.48}$$

Energy resolution in detectors is limited by several factors, such as random noise, either within the detector or from the associated electronics, or by fluctuations of the electric field, for instance due to instabilities of the HV supply or space charge effects. Even if the operating characteristics of the detector remain perfectly stable over the course

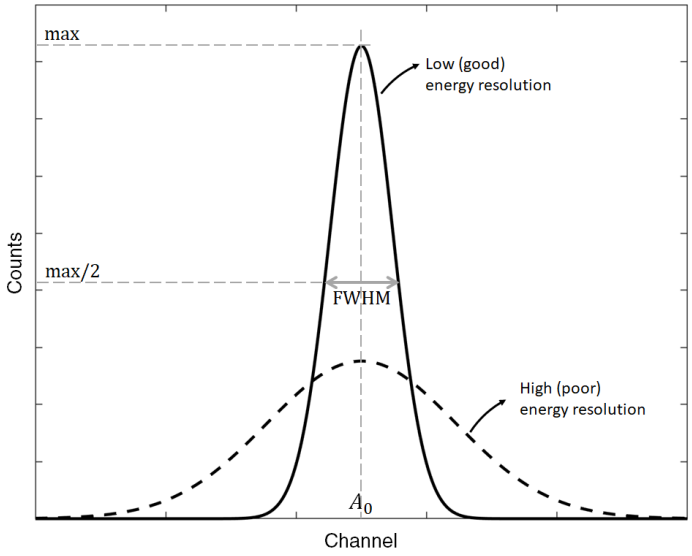

Figure 2.15: Comparison of a hypothetical PHS of two detectors, showing a good and a poor energy resolution.

of measurements, energy resolution is still limited by the statistical fluctuations of charge production that arise from the discrete nature of the measured signal itself, which can be considered as the minimum statistical limit of energy resolution (R_{min}). In the simplest model, this limit can be estimated assuming that they follow a Poisson distribution. In this scenario, the standard deviation of the primary charges is $\sigma_{n_0} = \sqrt{n_0}$, and the statistical limit for energy resolution is given by:

$$R_{\text{min}} = 2.355\frac{\sqrt{n_0}}{n_0} = 2.355\sqrt{\frac{w}{E}} \tag{2.49}$$

However, the Poisson distribution assumption is an over simplification that assumes that ionization events are all independent from each other, which is not realistic. This is specially true when the radiation is fully absorbed in the gas, since in this case the energy deposited has a fixed value and consequently the total number of ionizations that can occur and the energy lost in each ionization is constrained by this value. Indeed, measurements of energy resolution have shown inferior values then R_{min} when calculated through equation (2.49) [6]. The Fano factor (F) has been introduced to quantify the observed variance from the pure Poisson statistics: $\sigma_{n_0} = \sqrt{Fn_0}$. Taking this parameter into consideration, equation (2.49) is rewritten as:

$$R_{\text{min}} = 2.355\sqrt{\frac{Fw}{E}} \tag{2.50}$$

The Fano factor has a value between $0 < F \leq 1$, and is substantially low for noble gases (for instance, $F = 0.17$ for argon [8]), which greatly increases the achievable energy resolution.

2.3.6 Spatial Resolution

In some applications, there is the need to know not only the energy and intensity of the incident radiation (or of the capture reaction products, in the case of neutrons),

but also the spatial coordinates of the position where the incident particle entered the detector, or even tracking its trajectory across the detection volume. Detectors with this capability are designated as position sensitive detectors, and are characterized by their spatial resolution, which is defined as the ability for a detector to distinguish between two events that occur at a distance Δx, with a given confidence level [13]. A popular strategy to achieve position sensitivity in proportional counters is to use an array of anode wires separated by a fixed distance, forming a multi-wire proportional chamber (MWPC). Each wire acts as an individual detector, which gives information about the position where a particle was detected.

The point spread function (PSF) is defined as the response of a position sensitive system to an input point source. A widely used criterion to quantify spatial resolution is through the FWHM of the reconstructed position distribution of a perfectly punctiform beam, i.e., the PSF of the detector, which is assumed to follow a Gaussian distribution (Fig. 2.16-left). Considering the detector has a linear PSF, the reconstructed position distribution of an incident beam is given by the convolution of the beam dimensions with its PSF (Fig. 2.16-right).

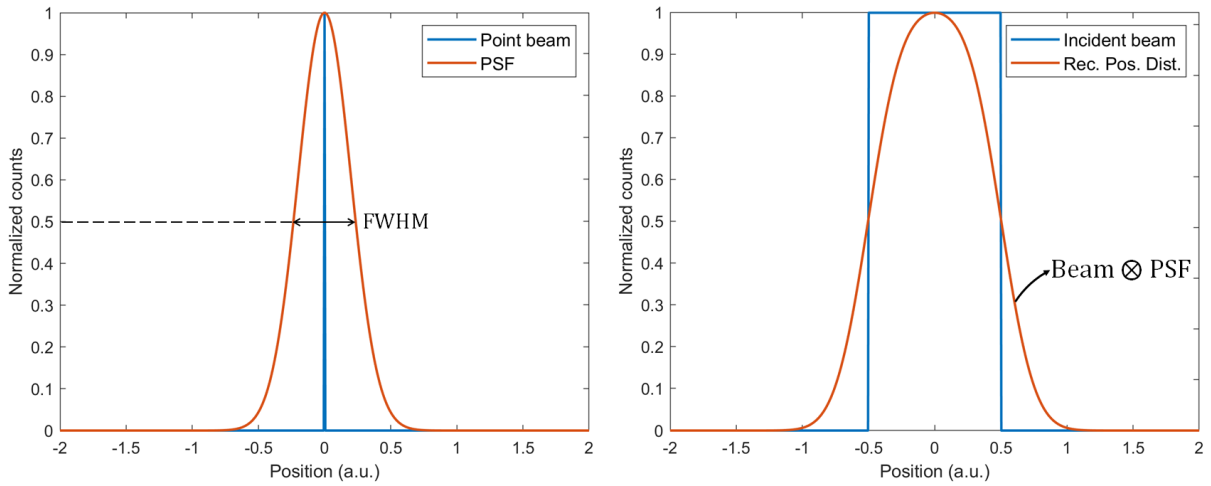

Figure 2.16: Left: FWHM of a point spread function, which defines the spatial resolution of a detector. Right: Reconstructed position distribution of a beam with arbitrary width, obtained from the convolution of the incident source with the PSF of the detector.

To measure the spatial resolution of the detector by its PSF, it is necessary to irradiate it with a punctiform beam, which, in practice, is impossible. Although masks with narrow slits can be used to produce highly collimated beams of very small dimensions, these will inevitably have a non-negligible width. However, if the beam is sufficiently narrower than the spatial resolution of the detector, its width does not significantly alter the spatial resolution measured [58]. This is evidenced by the calculations presented in Fig. 2.17, which show the reconstructed position distribution of a detector for a punctiform beam (i.e., its PSF), compared against beams of variable dimensions. The width of each beam is given as a fraction of the spatial resolution of the detector (SR), determined by the FWHM of the PSF.

A beam with width corresponding to 50% of the spatial resolution results in a difference of ∼6% between the measured spatial resolution and the real one. For narrower beams, this percentage would be even smaller. For a 2D position sensitive detector, the spatial resolution of each coordinate can be measured separately, and therefore only one beam

dimension needs to be sufficiently narrow.

In contrast, when the beam width is comparable or greater than the spatial resolution, a considerable difference between the measured and the real spatial resolution is obtained. For a beam width equal to the spatial resolution, the difference is of ∼25%, and this value increases to ∼102% when the width is double.

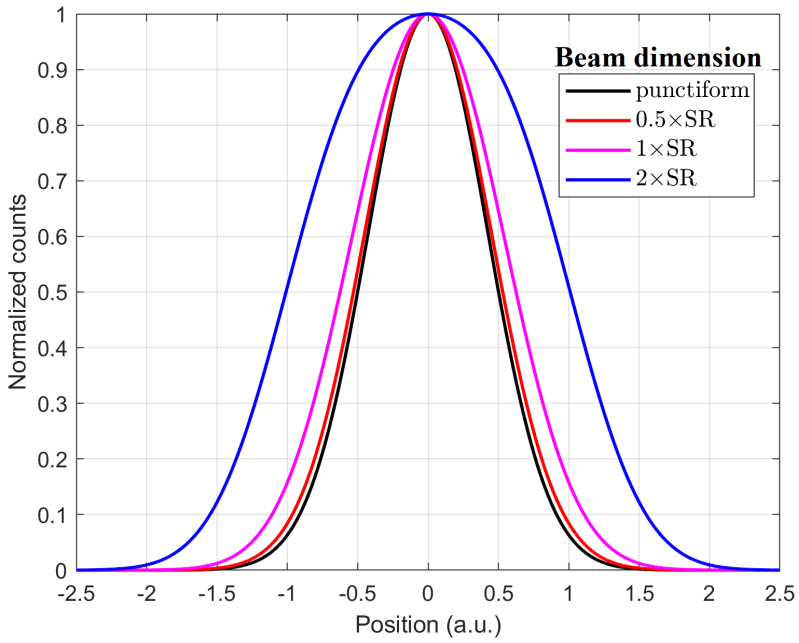

Figure 2.17: Reconstructed position distribution of a detector for beams of variable dimensions, given as a fraction of spatial resolution (SR). The spatial resolution is defined as the FWHM of the distribution obtained for the punctiform beam.

3 Neutron Detectors: State of the Art

Soon after the discovery of the neutron in 1932 by James Chadwick [1], experiments to use this particle as a probe to study materials were idealized, similarly to what had already been achieved with x-rays. However, while x-ray sources suitable for scattering experiments were at the time relatively easy to construct and manage, producing an intense and steady flux of neutrons was a much harder task. This scenario changed between 1939-1943 with the discovery of nuclear fission by Lise Meitner and Otto Hahn, and the subsequent demonstration of a self-sustained and controlled neutron producing chain reaction by Enrico Fermi. In 1946, the first neutron diffraction patterns were obtained by Ernest Wollan, by installing a diffractometer in a nuclear reactor in Oak Ridge, USA [59].

Less than one hundred years after the discovery of the neutron, we find dozens of scientific facilities around the world dedicated to the production of neutrons to use in scattering experiments in a variety of fields, such as nuclear and particle physics [33], materials characterization [60], molecular dynamic studies [61], crystallography [62] and medical therapy [63], to name a few. Over the course of decades, the production, moderation and guiding of neutrons have been constantly evolving, resulting in neutron beams with increasing intensities and covering a wider energy range, with progressively colder neutrons obtained through innovative moderation techniques. Along with the evolution of neutron beams, came the evolution of neutron detectors, improving their performance in parameters such as detection efficiency, counting rate, spatial resolution and time resolution.

Another factor that contributed to the evolution of neutron detectors is their deployment in homeland security applications. The fact that nuclear fission reactions can be exploited to create weapons of mass destruction led to a very tight monitoring of fissile materials that can potentially be used in the production of nuclear bombs. Because a signature of some of these materials is the emission of neutrons, several countries have detection systems equipped with neutron detectors to flag their illicit transportation.

In this chapter, we will focus on the state of the art of neutron detectors. However, before analysing the operating principles and characteristics of current detectors, we will frame their evolution by presenting the most relevant applications in which they are used, as well as the associated requirements. To understand the evolution of neutron detectors, it is also fundamental to discuss the role and consequences of the ^{3}He shortage crisis which, as will be seen, was a major cause for a technological shift in their development.

Neutron detectors can be developed in a wide variety of designs, regarding the selection of neutron converter and the material used for the collection of the secondary particles from the neutron capture reaction. However, in this chapter we will focus on detectors

that follow the same format as the ones developed in the aim of this thesis: gaseous detectors based on solid boron converters. These are categorized as thermal/cold neutron detectors with basis on their operation principle. Nevertheless, in some applications they might be used to detect fast neutrons, which is achievable by surrounding the detector with a moderator material. In other words, neutron moderation and neutron detection are regarded as separate processes.

3.1 Applications and Requirements

Neutron detectors cover a variety of applications in different areas, such as radiation protection, nuclear energy, reactor instrumentation, nuclear decommissioning and nuclear waste, to name a few [64]. However, two applications stand out: homeland security and neutron scattering facilities for scientific research, on which we will focus. This emphasis is attributed not only due to the number of detectors deployed, but mostly because these applications have driven the evolution of neutron detectors the most, particularly after the acknowledgement of the ^{3}He shortage crisis that will be discussed in section 3.2.

3.1.1 Homeland Security

The deployment of neutron detectors in homeland security applications is associated with the prevention of the illicit transportation of radioactive materials, particularly those classified as Special Nuclear Materials (SNM), such as ^{239}Pu, ^{233}U and ^{235}U [65]. These are fissile materials that can be used in the construction of nuclear weapons and consequently their transportation is heavily monitored. Depending on the specific SNM, they can be detected either by their gamma-ray or neutron signatures. While plutonium emits both a significant gamma and neutron radiation, enriched uranium emits lower energy gamma-rays and has a very low emission rate of neutrons, which makes it easier to shield and consequently harder to detect. Detection of SNM through their gamma-ray signature has some limitations, such as the high variability of natural background, the natural gamma-ray emission of radioactive materials transported in authorized commerce and the presence of individuals undergoing medical radionuclide treatments, which can be overcome by detecting the neutron emission instead. Neutron detection has the advantage of having a lower natural background, and fewer neutron sources, which must be licensed, are carried in the normal flow of commerce [66].

The control of these radioactive materials is done by Radiation Portal Monitors (RPMs), which are large area detectors composed of separate units sensitive to gamma-rays, fast neutrons and thermal neutrons. When vehicles and cargo containers go through these portals, they are triggered in case the detectors signal an abnormal level of radioactivity. If that happens, the cargo container or vehicle is directed to a secondary inspection area for further inspection [67]. An illustration of a RPM installed in a land border is presented in Fig. 3.1.

Although RPMs are currently installed in several countries, the greatest stockholder is, by far, the USA, where a massive deployment of RPMs across land borders, airports, seaports and ferries took place after 2001, in response to the 9/11 terrorist attacks. As of August 2016, a total of 1386 RPMs were installed and in operation in the USA, with 320 additional ones in storage. As a result of this impressive campaign, nearly 100% of

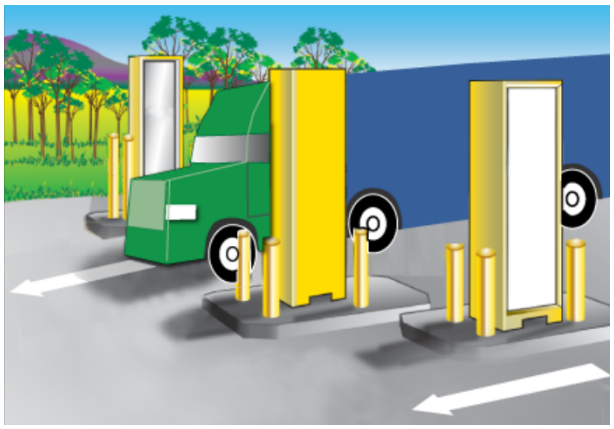

Figure 3.1: Illustration of a Radiation Portal Monitor. Image from [67].

the over 100 million vehicles and 20 million cargo containers entering either through land borders or seaports are scanned by RPMs [67].

The fundamental performance requirements for neutron detectors in RPMs are a high detection efficiency, low intrinsic gamma-ray sensitivity and maintaining neutron detection efficiency when simultaneously exposed to a high gamma-ray intensity [68]. These requirements are notably fulfilled by ^{3}He proportional counters, the neutron detectors utilized in the vast majority of RPMs, mounted in a polyethylene moderator enclosure to thermalize the fast neutrons emitted by the SNMs. Besides their high efficiency and intrinsic low gamma-ray sensitivity, ^{3}He detectors are relatively simple in design, mechanically robust and do not degrade over years of operation [66]. Additionally, up to recent times ^{3}He was an affordable and easily available material. The combination of these factors made of ^{3}He PCs the indisputable best option for the neutron detection requirements of RPMs.

However, a little over a decade ago, a critical shortage of ^{3}He changed the paradigm for the development and maintenance of neutron detectors in RPMs. Their massive deployment played a crucial role in this shortage, as will be discussed further in section 3.2. In fact, depending on the manufacturer, a single RPM requires at least 44 litres of ^{3}He, with some exceptions going over 130 litres [66]. Seeing that thousands of RPMs were built over a short period of time, it is no surprise that this caused a disruption of the supply and demand balance of ^{3}He. These circumstances motivated a great amount of research for ^{3}He-free neutron detectors compatible with the current performance requirements, to allow for a direct replacement of ^{3}He PCs.

3.1.2 Neutron Scattering Facilities

Neutrons are sensitive to all four fundamental forces, are typically non-damaging when used in sample irradiation, deeply penetrating and influenced by magnetic fields due to their spin. This makes them a "complete laboratory" [69], and a powerful probe to study matter and reveal the structure and behaviour of materials at an atomic and molecular scale [70], since their wavelength is comparable to the dimensions of the atomic structures.

When compared to x-rays, which have an attenuation cross-section roughly proportional to the atomic number (Z) of the traversed material, neutrons do not show any systematic relation, but rather an apparently random cross-section variation with Z. This effect is plotted in Fig. 3.2, which shows the total cross-section for thermal

neutrons and for 60 keV photons as a function of the atomic number. In both cases, the cross-section values account for the processes of absorption (removal of the incoming particle) and scattering (deflection of the incoming particle).

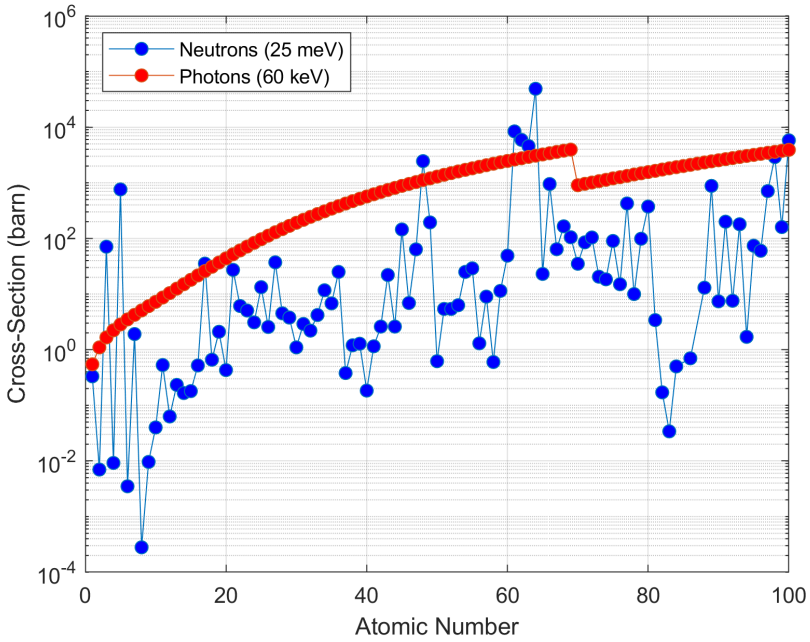

Figure 3.2: Total cross-section plotted against the atomic number for thermal neutrons and 60 keV photons. Plotted with data from [9] and [71].

The discontinuity of the photon cross-section at $Z = 70$ is due to the binding energy of the K-shell of ytterbium (61.332 keV), which is the first element with binding energy superior to the considered photon energy (60 keV), and consequently allows for a new interaction mechanism via photoelectric effect with electrons of the K-shell. While the interaction of x-rays with electrons gives rise to a near-monotonic increase of the cross-section, the nuclear interaction of neutrons with the different elements is not a regular function of the atomic number and can also differ greatly for different isotopes of the same element. For instance, the isotopes of hydrogen have cross-sections of $\sigma(^1\mathrm{H}) = 20.768$ barn, $\sigma(^2\mathrm{H}) = 3.395$ barn and $\sigma(^3\mathrm{H}) = 1.664$ barn. These properties make neutrons much more sensitive to light elements and to different isotopes of the same element. Through neutron irradiation it is possible to gain information on a given sample that would be inaccessible using x-rays, while the opposite is also true. Therefore, neutron and x-ray scattering can be considered complementary techniques.

In recent times, significant investments in neutron science have been made, which materialized in new large-scale research facilities that only recently have finished construction, such as the China Spallation Neutron Source (CSNS) [23], or that are currently still under construction, such as the PIK reactor in Russia [18] or the European Spallation Source (ESS) in Sweden [19]. When constructed, ESS will be equipped with the most powerful neutron source in a neutron scattering facility, providing a neutron beam up to one hundred times brighter than currently available in any other facility [72]. Fig. 3.3 shows the single-pulse brightness as a function of time at a neutron wavelength of 5 Å for ESS, ILL [16], SNS [22], J-PARC [24] and ISIS [21] (Target Stations 1 and 2). For SNS, J-PARC and ISIS, different moderator designs are shown, to illustrate the compromise

between resolution and achievable intensity. For ESS, two pulses are shown, corresponding to the pulse brightness of the design announced in the initial technical design report (full blue) [25] and the current design (blue line) [73]. The brightness increase was achieved through the optimization of the neutron moderation system.

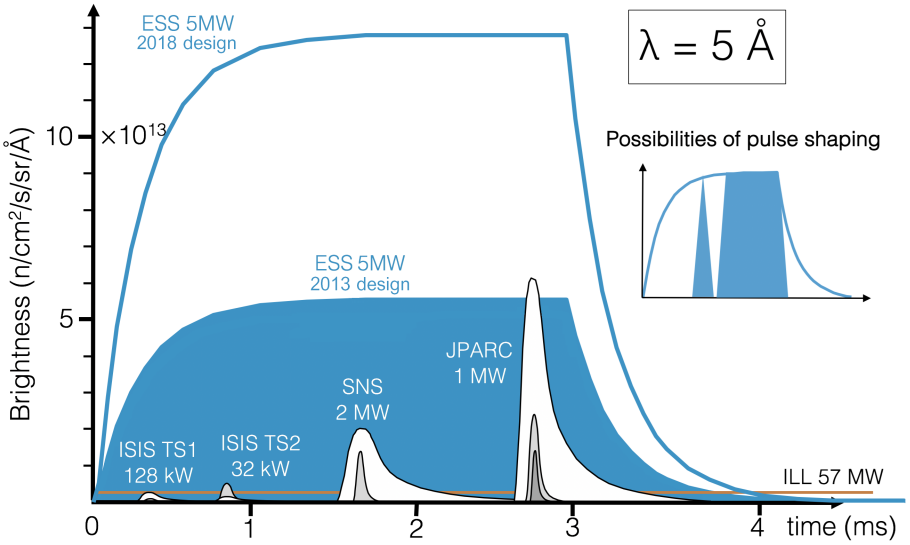

Figure 3.3: Comparison of the brightness of a single neutron at a wavelength of 5 Å for some of the leading neutron sources around the world. Image from [72].

Some of the neutron scattering techniques used in these facilities for the study of samples include neutron imaging, small-angle neutron scattering (SANS), neutron reflectometry, neutron spectroscopy, and neutron diffraction. All of these techniques have the common need of detecting the neutrons that are either transmitted or scattered by the sample. Therefore, for each neutron beam, there is the need to deploy at least one neutron detector, which is developed according to predetermined performance goals, that depend on the neutron energy, beam flux, and scattering technique to be used.

3.2 The ^{3}He Shortage Crisis

The majority of neutron detectors currently in use are ^{3}He gaseous proportional counters. In the 1970s and ever since, this instrument became the golden standard for neutron detection because of the exceptional properties of ^{3}He, in terms of its thermal neutron capture cross-section, pulse resolution, gamma rejection, physical robustness and non-toxicity [74]. As a consequence, increasing demand for this gas has been observed while its supply has not followed the same trend. When the scientific community became aware of this shortage crisis, a little over a decade ago, prices skyrocketed and heavy acquisition restrictions were implemented [66, 75, 76]. A major cause of this crisis was the massive deployment of RPMs, which use ^{3}He neutron detectors, across the United States borders after the 2001 terrorist attacks [74]. Fig. 3.4 correlates the evolution of the ^{3}He reserves levels with the deployment of RPMs.

Ultimately, the Radiation Portal Monitor Project ended with any possibility of having a sustainable supply and demand scenario, which caused ^{3}He reserves to diminish abruptly right after 2002. Its scarcity is such that it is not freely sold in a conventional market

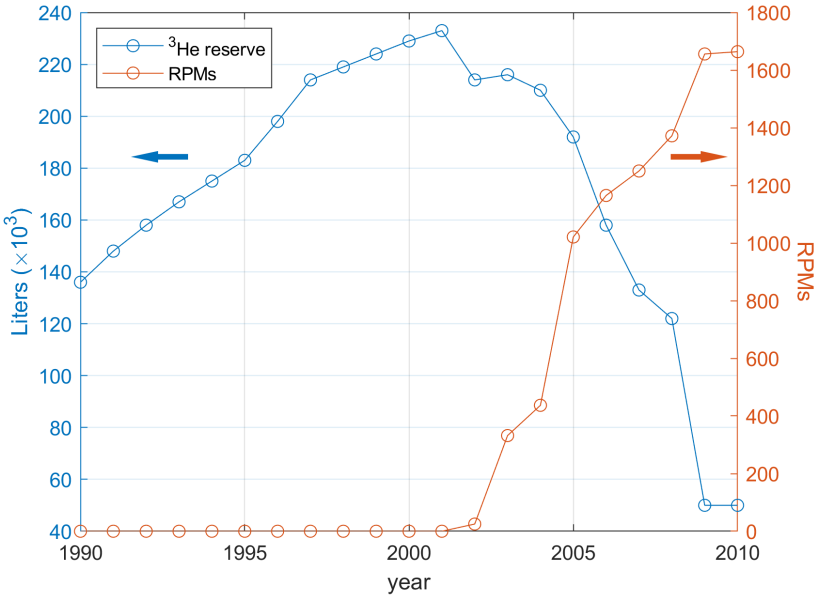

Figure 3.4: Chronological evolution of ^{3}He reserves and deployment of Radiation Portal Monitors in the United States. Data from [67, 77].

approach. Instead, its distribution is highly regulated by the U.S. Department of Energy, which assesses national needs and allocates it accordingly [77]. The consequence of this was a continuous and rapid increase in price, from 100 $/litre in 2008 to 2000 $/litre in 2010 and to a minimum of 2750 $/litre in 2014 which was only possible to acquire through public auction of limited amounts [78].

While security programs in the United States have soaked up 85% of its supply, the remaining fraction is left to be shared between a wide range of applications, affecting several scientific and industrial areas which depend on ^{3}He, as listed in Table 3.1 [79].

Application	**^{3}He Quote**
Neutron detectors for security	84.5%
Neutron-scattering facilities	10%
Oil & gas detectors	2.5%
Medical imaging	1.7%
Low-temperature physics	1.3%

Table 3.1: Usage of ^{3}He by different industries and scientific areas. Data from [79].

For some specific scientific fields, there is no substitute for the unique characteristics of ^{3}He, as are the cases of dilution refrigeration and quantum fluids research [77], which makes it crucial for neutron detectors to be replaced by ^{3}He-free alternatives. The long term operation of the RPMs already in use also depends on developing these alternatives, since the current ^{3}He availability is not enough to ensure their maintenance in the future. In fact, recent studies account that RPMs operation can only be ensured until 2030 [67].

The difficulty with restocking ^{3}He comes from the fact that its natural isotopic abundance is only 0.000137% of natural helium (roughly 1 ppm), making it unprofitable to extract it from air, rocks or water by separation from ^{4}He [80]. Commercialized ^{3}He currently comes almost entirely from the decay of tritium reserves existent in the USA

and Russia (a few other countries contribute with only a small amount) [66]. The natural radioactive decay of tritium to ^{3}He has a half-life time of 12.3 years [81]:

$$^3\mathrm{H} \rightarrow {}^3\mathrm{He} + \mathrm{e}^- + \overline{\nu} \tag{3.1}$$

Tritium is used as an ingredient in nuclear bombs, and large reserves were kept by the United States and Russia. With the end of the Cold War and the adoption of non-proliferation treaties, the production of tritium dropped significantly [79].

Seeing that tritium production is prohibitively expensive and it would take many years before an appreciable quantity would become available, it is extremely unlikely that the extraction of ^{3}He from tritium stockpiles could ever again be a viable means of meeting the demand for this gas [82].

Therefore, the only viable solution for this scarcity problem is to massively replace neutron detection technologies that rely on ^{3}He.

An additional motivation for the development of ^{3}He-free alternatives is the fact that ^{3}He detectors do not meet the current requirements of modern instruments, namely in what regards position resolution and counting rate [83]. For instance, to take full advantage of the beam brightness of ESS, which will be the most powerful pulsed neutron source to date [25], detector features must be improved to a point beyond the performance capability limits of ^{3}He detectors.

3.3 Gaseous Neutron Detectors

3.3.1 ^{3}He Proportional Counter

The most attractive features of ^{3}He proportional counters are the high thermal neutron detection efficiency and good gamma-ray discrimination. In a ^{3}He proportional counter, ^{3}He can work simultaneously as the conversion material, converting neutrons into heavy charged particles, and as the proportional gas in which the charged particles deposit their energy. For the second purpose, additional filling gases such as CO_2 or CF_4, cheaper and with greater stopping power, are added to reduce the w-value of the gas mixture and to act as a quencher [84].

The neutron capture reaction in ^{3}He results in the back-to-back emission of a triton and a proton, with energies of 191 keV and 573 keV, respectively (reaction 2.33). If the detector is large enough, both reaction products deposit their total energy in the proportional counter, and a full energy deposition peak with a Gaussian shape centred at 764 keV is obtained in the response of the detector, as depicted in Fig. 3.5. However, for neutron captures occurring near the detector wall, one of the reaction products can be emitted towards it and escape the gas before depositing all its energy. This is known as the wall-effect and originates a low continuum of energies in the detector response, also visible in Fig. 3.5. This feature in the detector response can be marginally reduced by increasing the detector diameter, which maximizes the number of neutron captures occurring far from the walls, or by increasing the stopping gas pressure, which reduces the reaction products range.

The detection efficiency of a single ^{3}He proportional counter depends on its volume and the ^{3}He gas pressure. ^{3}He proportional counters can operate at gas pressures as high as 15 bar [86], although pressures around 10-12 bar are more usual [87, 88]. For such

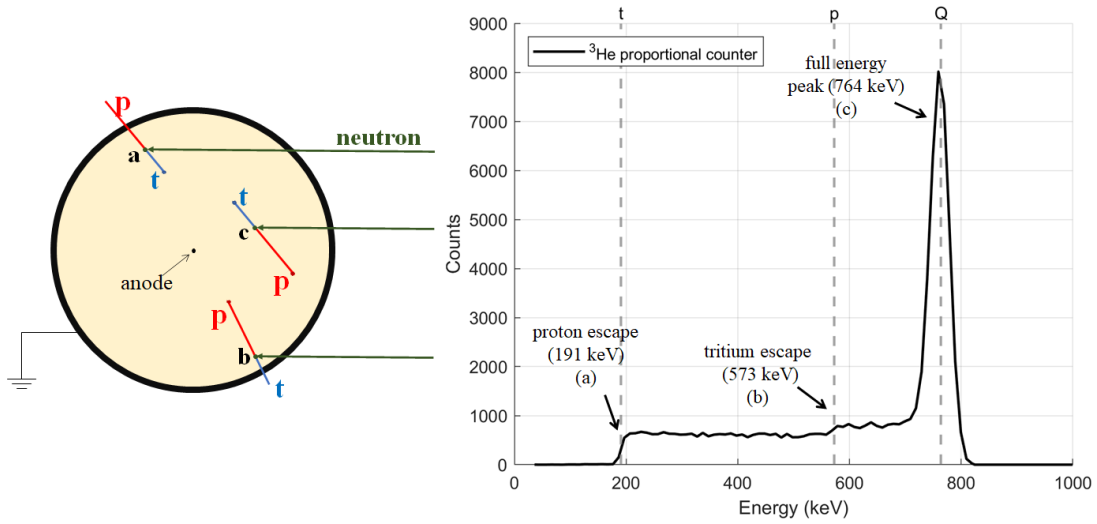

Figure 3.5: Left – Three possible neutron interactions in a ^{3}He PC (cases a, b, and c). Right - Typical pulse height distribution of a 1 inch diameter ^{3}He PC at atmospheric pressure irradiated by thermal neutrons, obtained by the GEANT4 simulation [85]. The main peak corresponds to events in which all the energy released in the neutron capture reaction is deposited, i.e., both the triton and the proton are stopped in the gas (c). The proton escape is recorded when the proton is not detected (a), leaving only the energy of the tritium (191 keV) while complementarity, the tritium escape originates in events where only the proton (573 keV) is detected (b).

pressures, maximum efficiencies for thermal neutrons in the order of 80%-90% are reached [36, 58].

Despite its high efficiency, an insurmountable drawback of this detector is the fact that ^{3}He has become extremely scarce. The high price and limited availability of this gas make it imperative to shift the development of neutron detectors towards ^{3}He-free alternatives, particularly for large area applications. Seeing that ^{3}He PCs unfolded as the dominant neutron detector, replacing it on a global scale does not come without tremendous effort. The dimension of this endeavour is such that although more than a decade of intensive research and development for ^{3}He-free neutron detectors has gone by, 80% of neutron detectors currently used in neutron scattering applications worldwide are still based on ^{3}He [40].

However, positive outcomes are starting to materialize on larger scales. This is evident when looking at new neutron research facilities like ESS. Among the 15 user instruments to be installed in the first development stage, only 3 of them will deploy ^{3}He, which would not be feasible without the recent developments on ^{3}He-free neutron detection technologies [73].

3.3.2 BF_3 Proportional Counter

Boron trifluoride (BF_3) is the only alternative gas converter to ^{3}He. BF_3 proportional counters, first referred in 1939 [89], were the most popular instrument for neutron detection before the rise of the ^{3}He proportional counter [90]. This detector is similar in design and construction to ^{3}He detectors, with the simple difference of being filled with a different gas, containing the neutron sensitive isotope ^{10}B. Boron trifluoride also works

simultaneously as neutron conversion material and proportional gas, although it is a rather poor working gas for charge multiplication, especially when operating at higher pressures, due to its slight electronegativity [91]. Because of this, BF_3 fill pressure is limited to approximately 2 atm [92], which, along with the fact that the neutron capture cross-section of ^{10}B is only 72% of that of ^{3}He, substantially limits its achievable efficiency in comparison to ^{3}He PCs, which can operate at much higher pressures. To compensate for the low natural abundance of the neutron sensitive isotope (of 20%), there are commercially available options for ^{10}B enriched boron trifluoride, which can inherently increase detection efficiency up to a factor of five.

When irradiated by a neutron source, the pulse height spectrum of a BF_3 detector (Fig. 3.6) is similar to that of a ^{3}He PC, showing a full energy peak. A shift to higher energies is obtained, due to the higher Q-value of reaction (2.38). The full energy peak is centred at approximately 2.31 MeV, corresponding to the 94% probability reaction branch with both the ^{7}Li nuclei (0.84 MeV) and alpha particle (1.47 MeV) being fully stopped in the gas.

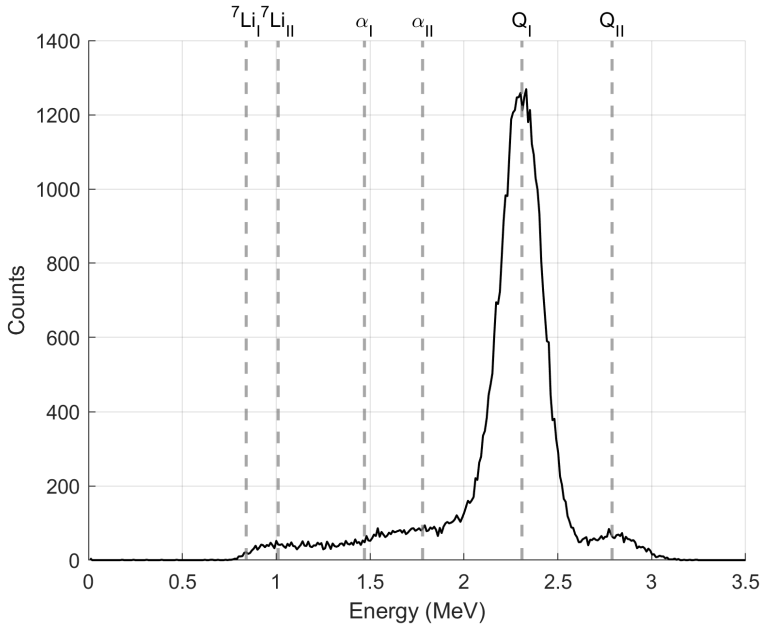

Figure 3.6: Typical pulse height distribution of a 1 inch diameter BF_3 proportional counter at atmospheric pressure irradiated by thermal neutrons, obtained by GEANT4 simulation. Two full peaks are visible at energies 2.31 MeV and 2.79 MeV, respectively corresponding to the 94% and 6% probability branches of reaction (2.38). Additionally, the wall-effect causes a low energy tail at the left of the full energy peaks.

The higher reaction Q-value increases gamma-ray discrimination capability [92]. This factor, along with gas affordability are the advantageous aspects of this detector. On the downside, BF_3 PCs have only managed to report between 30% and 50% of the efficiency of the ^{3}He PCs [93]. Also, BF_3 is corrosive, and tubes filled with it can show ageing effects over short times. Yet, the main reason why the use of BF_3 has been nearly abandoned since the early 1980s regards safety restrictions [94]. BF_3 is highly toxic, requiring delicate handling and strict storage and shipping regulations. The event of a gas leakage in this detector could bring a serious outcome in matter of public safety. Thus, the use of such detectors in the ample homeland security market would imply considerable additional costs in hazard prevention by adding multiple layers of containment, material to absorb

the toxic gas in case of leakage and an improved detector housing to minimize its likelihood [93]. Because of this, BF_3 detectors have failed to establish as a reliable ^{3}He-free solution for neutron detection.

3.4 Boron-Coated Gaseous Neutron Detectors

In response to the ^{3}He shortage crisis, research for alternative solutions has intensified significantly over the course of the last decade.

Suitable neutron converters to be deployed in detectors must have a relevant thermal neutron capture cross-section, which is the first restriction of material selection, since only a handful of isotopes fulfil this requirement, as was discussed in section 2.2.4. Due to the characteristics of the neutron capture reaction, only lithium, boron and gadolinium can, in practice, be considered as potential candidates to be used in thermal/cold neutron detectors for the applications discussed in section 3.1, which make for the vast majority of the market for neutron detectors. Among these, the properties of ^{10}B make it, in general, a better candidate for the replacement of ^{3}He detectors in most applications. This is evidenced, for instance, by the planned instrument suite of ESS: of the initial 15 neutron beam instruments that will be installed, 3 of them will continue to use ^{3}He PCs (in instruments that require a small detection area), 1 will use lithium scintillators, 1 will use gadolinium foils, while the remaining 10 will rely on gaseous detectors using solid boron converters [73]. For the remainder of this chapter, a review of the most relevant neutron detectors of the latter kind will be focused.

For the sake of brevity, only detectors that are either already being used or planned to be used in concrete applications will be addressed. However, additional boron-based neutron detection technologies currently still under development exist, with potential to be employed in future applications, such as detectors based on resistive plate chambers (RPCs) [95–97], coated macrostructured cathodes [98, 99] and time projection chambers (TPCs) [100, 101].

3.4.1 Boron-lined Proportional Counter

The boron-lined (commonly abbreviated as B-lined) proportional counter is the simplest geometry among gaseous neutron detectors based on solid boron neutron converters. The differentiating characteristic between this detector and the purely gaseous ^{3}He and BF_3 PCs is the fact the conversion material, ^{10}B, is present as a solid layer, coated on the inner walls of the detector (Fig. 3.7-left). The evident advantage of this approach is the fact that any suitable counting gas can now be freely chosen for charge multiplication, since it no longer serves the purpose of converting neutrons into heavy charged particles. Thus, a non-toxic and inexpensive proportional gas can be selected, which typically consists of a gaseous mixture between argon and a quenching gas, such as Ar:CO_2, in various proportions.

Naturally, this neutron detection technique also brings disadvantages compared to ^{3}He or BF_3 detectors. Because the ^{7}Li and alpha particle from the neutron capture reaction are emitted in-line with opposite directions, it is geometrically impossible for both of them to simultaneously deposit their energy in the gas. Since neutrons are captured near the detector wall, at least one of the reaction products will be absorbed either in the converter or in the wall, while the other might reach the gas only after losing a significant

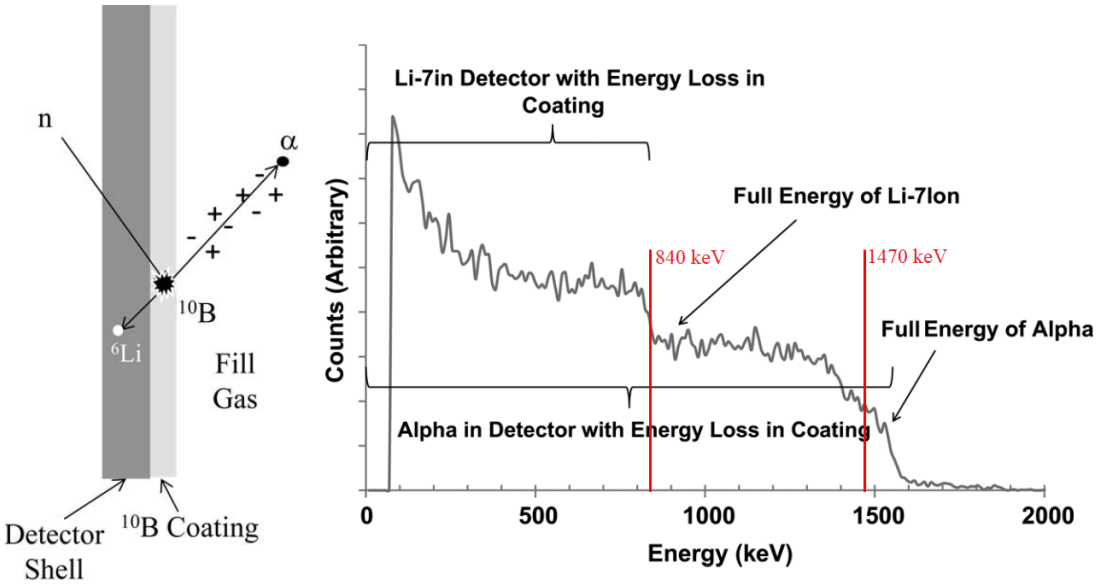

Figure 3.7: Left: Illustration of the B-lined proportional counter detection principle, in which neutrons are captured by the solid boron layer in the inner walls of the detector. Right: Typical pulse height spectrum of a B-lined proportional counter irradiated by thermal neutrons, exhibiting the wall-effect. Image from [102].

fraction of its initial emission energy, due to interactions in the boron layer. There is also a small probability of neither particle escaping the converter, if the reaction products are emitted aligned or roughly so in respect to the detector wall. This compromises detection efficiency, and also causes the wall-effect on the detector response (represented in Fig. 3.7-right), compromising the capacity to discriminate against gamma-ray induced events.

As was seen with the BF_3 and ^{3}He PCs, detection efficiency can be increased by simply increasing the filling gas pressure. An analogous principle can be applied to the B-lined detector, but only up to a certain extent, by increasing the thickness of the solid boron layer. While this brings a greater neutron capture efficiency, this is only verified up to a thickness limit. After this limit, as more neutrons are captured, more secondary reaction products are absorbed in the solid layer before reaching the gas. Consequently, there is an optimal coating thickness below which neutrons are not efficiently captured, whereas above it the reaction products cannot reach the gas. This artefact is represented in Fig. 3.8, which shows a simulation-based modeling of the relationship between coating thickness, thermal neutron capture efficiency, and detection efficiency for an individual B-10 lined detector [102]. The coating thickness is expressed as areal density, i.e., ^{10}B mass per area, because the range of the reaction products in the conversion material is dependent on the number of atoms per length, which determines interaction probability. Conversion between areal density (ρ_A) and material thickness (t) can be done by knowing the material density (ρ): $t = \frac{\rho_A}{\rho}$.

The vertical line in Fig. 3.8 indicates the optimal coating thickness, imposing an efficiency limit for a single boron-lined tube of approximately 12% (using ^{10}B enriched boron), significantly lower than ^{3}He PCs. This is the main limitation of B-lined detectors. Nonetheless, the principle of using solid boron-coatings for neutron conversion in a gaseous detector can be applied in combination with strategies to increase detection efficiency, as will be presented in the following detectors of this chapter.

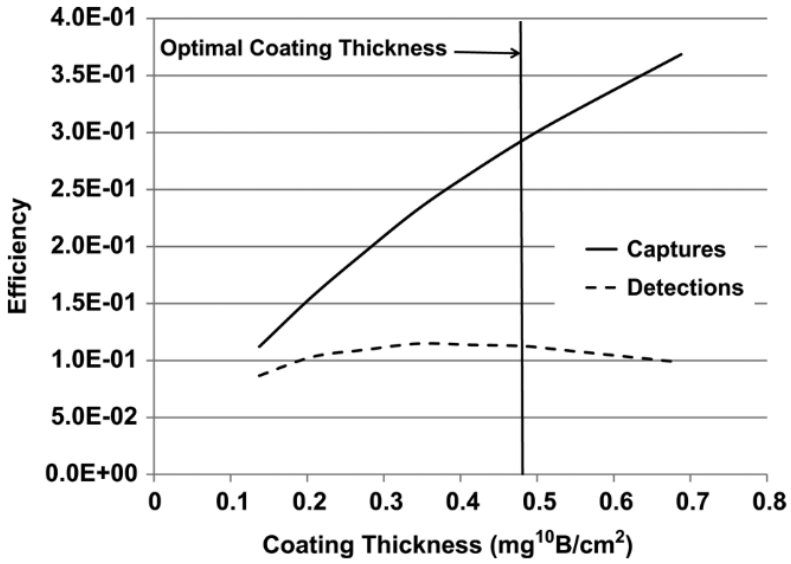

Figure 3.8: Neutron capture and detection efficiency as a function of ^{10}B areal density. Below the optimal thickness neutrons are not efficiently captured, whereas above it more neutrons are captured, but also more reaction products are absorbed in the coating layer. Image from [102].

3.4.2 Boron-Coated Straws

Boron-coated straws are a position sensitive ^{10}B-based gaseous neutron detector developed by Proportional Technologies Inc., consisting of an array of boron-lined proportional counters, arranged to increase detection efficiency by incrementing the wall surface area and consequently the amount of conversion material traversed by incoming neutrons, rather than increasing the coating thickness, which worsens the ratio between converted and detected neutrons. Thus, it is essentially composed of many individual smaller diameter B-line detectors, as shown in Fig. 3.9. The material used for neutron conversion in each straw is ^{10}B enriched boron carbide ($^{10}B_4C$).

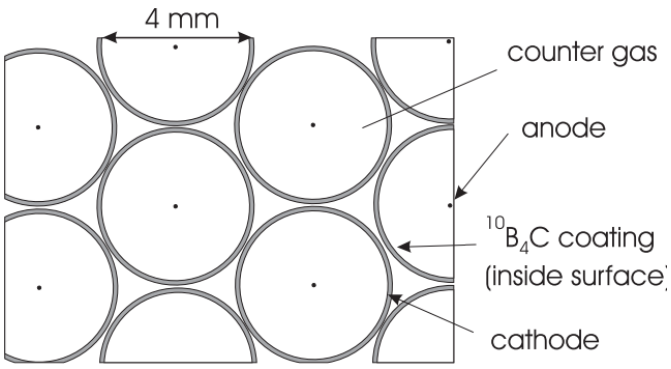

Figure 3.9: Boron-coated straws for thermal neutron detection. Image from [103].

This ^{3}He-free alternative has been in development for roughly two decades, originally directed towards large-area detectors in neutron scattering facilities requiring high counting rates [103]. However, when the ^{3}He shortage was acknowledged, it was optimized to be deployed in homeland security as a direct substitute of ^{3}He PCs in RPMs [104].

Using a reasonably deep stack of straws, elevated neutron detection efficiencies can

be achieved. This efficiency depends not only on the number, but also on the shape of the straws. Instead of cylindrical tubes, using irregular shaped walls leads to an efficiency increase, due to the superior wall surface area, which makes for an increase in the path travelled by the neutron inside the converter and consequently a superior capture probability. This is the same basic principle used by macrostructured cathodes in other detectors with different geometries [98, 99]. Fig. 3.10 shows a comparison between cylindrical and star-shaped tubes. Each detector consists of an array of 31 boron-coated straws bundled inside a 1.15 inch diameter tube. The optimal coating thickness to maximize detection efficiency for each geometry was determined through Monte Carlo simulations, with the respective values presented in Fig. 3.11, along with their comparison with a 1.15 inch (2.92 cm) ^{3}He PC at different gas pressures.

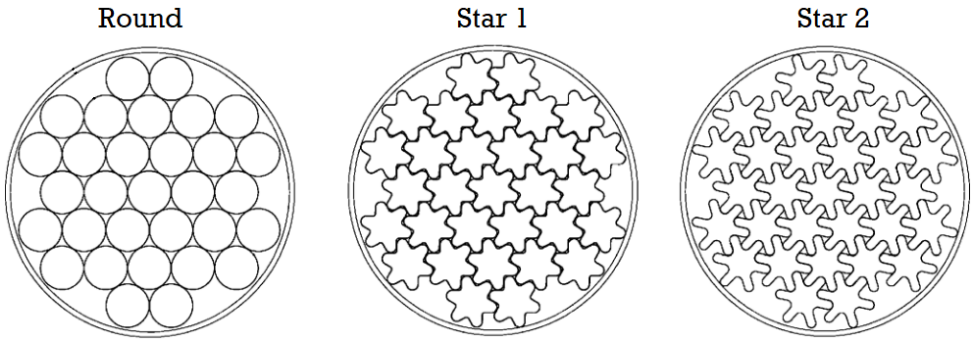

Figure 3.10: Array of 31 boron-coated straws bundled inside a 2.92 cm diameter tube, with design variations with round and star-shaped straws, identified as Star 1 and Star 2. Image from [105].

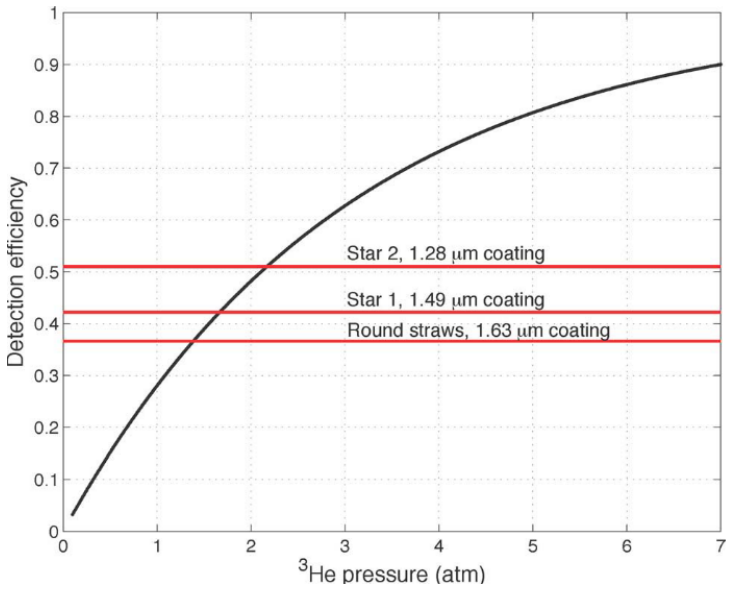

Figure 3.11: Intrinsic thermal neutron efficiency calculated for a 2.92 cm ^{3}He proportional counter as a function of filling gas pressure. The horizontal red lines mark the efficiency calculated for the 3 detector configurations of Fig. 3.10. Image from [105].

The maximum efficiency theoretically achievable with this concept was obtained with the Star 2 detector, yielding 50.9% for thermal neutrons with a 1.28 μm coating. Star

1 detector showed an efficiency of 42.1% for a 1.49 μm coating, and the round-shaped achieved the lowest efficiency of 36.5% efficiency with a 1.63 μm coating [105].

Prototypes were developed in accordance to the geometries simulated. A Star 1 detector configuration with 31 straws and a 0.85 μm thick $^{10}B_4C$ coating is presented in Fig. 3.12-left. Experimental results with neutron and gamma-ray irradiation produced the response shown in Fig. 3.12-right. A moderated ^{252}Cf source was used for thermal neutron irradiation, and a ^{137}Cs source at different exposure levels for gamma-ray irradiation.

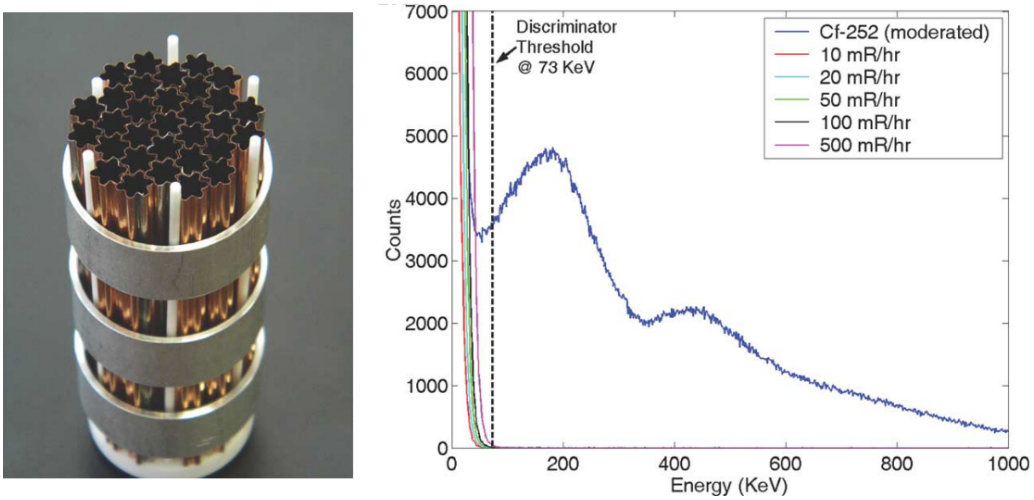

Figure 3.12: Left: Prototype of the Star 1 configuration, employing 31 straws with a 0.85 μm thick $^{10}B_4C$ (enriched) coating. Right: PHS obtained by irradiation with a moderated ^{252}Cf neutron source and a ^{137}Cs gamma-ray source at different exposure levels. Image from [105].

Boron-coated straws are already commercially available in 1 inch star straws format, for direct replacement of ^{3}He tubes in RPMs, with their use approved by the USA government in 2016 [106]. The commercialized product consists of 37 star-shaped copper straws with a 1 μm thick $^{10}B_4C$ coating, filled with Ar:CO_2, at a low pressure of 0.7 atm, to make it safer to transport and handle. Tests held at the Pacific Northwest National Laboratory (PNNL), showed an intrinsic efficiency for thermal neutrons of 54%, equivalent to a 1 inch ^{3}He detector operating at 3.4 atm.

This detector has been tested to be used for SANS applications at CSNS [107], and it is planned to be used in LoKi, also a SANS instrument at ESS [73].

3.4.3 Multi-Grid Detector

The Multi-Grid detector has been developed by a collaboration between ILL, ESS and Linköping University, in order to provide an alternative for ^{3}He detectors in neutron scattering facilities, particularly large-area applications where the cost and availability of this gas would be prohibitive. Its fundamental principle consists of improving the efficiency of ^{10}B-based gaseous detectors by stacking successive thin boron layers to increase the path travelled by neutrons in the conversion material, without increasing the thickness of each boron layer. Analogously to the boron-coated straws, this results in a bundle of individual detectors, although arranged in a different geometry.

The geometry of the Multi-Grid, depicted in Fig. 3.13, is composed of several small rectangular sections (voxels) stacked together, forming rectangular counter tubes with anode wires through their centres, operating as a MWPC.

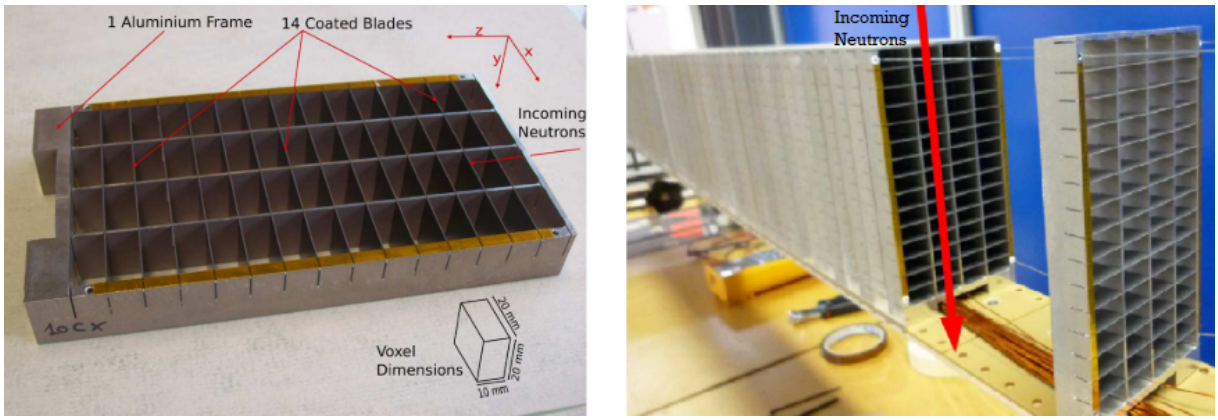

Figure 3.13: Left: Detector frame with 14 enriched $^{10}B_4C$ coated aluminium blades. Right: Grids stacked to create rectangular tubes, with anode wires placed in the middle of each tube, creating 60 individual proportional counters. Image from [108].

This prototype consists of 96 grids, covering an active surface of 8×200 cm^2. Each grid is made of 14 double-side coated blades, adding up to a total of 28 conversion layers. The blades are coated with ^{10}B enriched B_4C, with a thickness of 1 μm per layer. The grids are stacked with 0.5 mm spacing in order to reduce dead zones, while keeping electrical insulation between each cathode grid. After mounted, the whole structure depicted in Fig. 3.13-right is inserted inside a sealed gas vessel, filled either with CF_4 or Ar:CO_2 (90%:10%) mixture at atmospheric pressure [108].

The detector readout is formed by 60 anode wires: 4 rows of 15 wires each. An anode wire reads out each tube, thereby giving the position of where the neutron conversion occurred in one of the lateral coordinates, as well as in detector depth. Position resolution in the remaining coordinate is obtained by the segmented cathode grids, which are read in coincidence with the anode [108].

The pulse height spectrum is characterized by typical plateaus of the wall-effect, where it is possible to distinguish the contributions of the ^{7}Li and alpha particles in the detector response, visible in Fig. 3.14.

The efficiency measured for this prototype was 47.9% for 2.5 Å neutrons [109]. It is useful to characterize a detector in terms of its efficiency for thermal neutrons (1.8 Å), which is a standard to easily compare efficiency between different detectors. Assuming that the impact of the neutron wavelength on detection efficiency is limited to its influence on the neutron capture probability, and that the neutron capture cross-section of ^{10}B follows a $1/\sqrt{E}$ dependence with the neutron wavelength (as discussed in section 2.2.4), which in term implies a direct proportionality between cross-section and the neutron wavelength (as given by equation (2.31)), the detection efficiency can be estimated as ~34.5% for thermal neutrons (1.8 Å).

This detector has 3D imaging capability, with the best achievable spatial resolution being defined by the dimensions of each voxel: $1 \times 2 \times 2$ cm^3. However, for applications in which the spatial resolution in a lateral dimension can be relaxed, the anode wires can be connected 2 by 2 to reduce the number of readout channels, and consequently also the complexity and the cost of the detector [109].

A Multi-Grid detector has been installed and tested at the Cold Neutron Chopper Spectrometer (CNCS) at the SNS in Oak Ridge, USA, with encouraging results, fulfilling the requirements that were previously achieved with ^{3}He detectors, and performing better

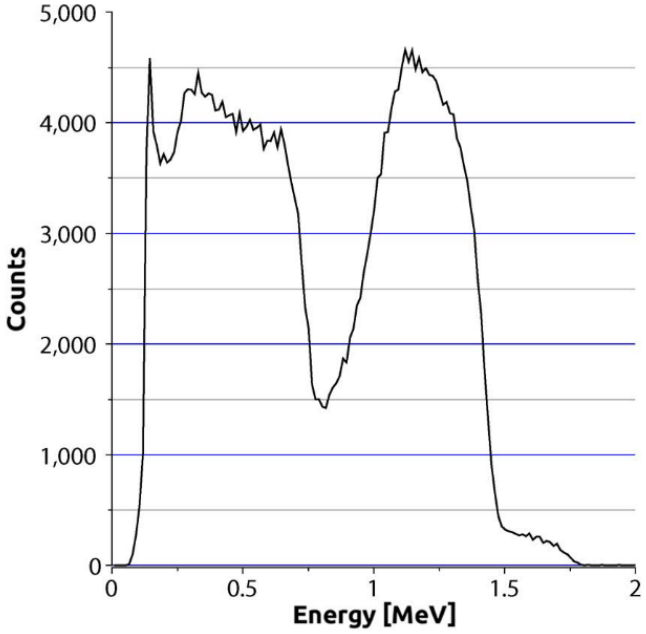

Figure 3.14: Pulse height spectrum of the Multi-Grid detector irradiated by monochromatic ($\lambda = 2.5$ Å) neutrons at the CT2 beam line of ILL (an energy threshold at 100 keV was applied). Image from [108].

in some parameters, namely at handling higher counting rates and showing less sensitivity to fast neutrons which constitute a background source [110]. Additionally, the Multi-Grid is planned to be used in the neutron spectroscopy instruments CSPEC and T-REX at ESS [73].

3.4.4 Grazing Angle Detectors (Multi-Blade and Jalousie)

While boron-coated straws and the Multi-Grid detectors use successive conversion layers for the incoming neutrons to traverse, another strategy for increasing detection efficiency consists of tilting the conversion layer, so that neutrons enter it at a grazing angle, typically between 5° and 10°. This way, neutrons travel a longer path near the surface of the layer than they would for a perpendicular incidence angle, which maximizes the probability of one of the secondary neutron capture reaction products escaping the converter to reach the surrounding counting gas. Two detectors based on this principle can be highlighted: the Multi-Blade and the Jalousie, which differ mostly in geometrical aspects and readout details.

Multi-Blade

The Multi-Blade is a small area detector aimed at neutron reflectometry applications. Its development was motivated not only by the ^{3}He scarcity problem, but also to overcome the limitations of ^{3}He PCs, namely in terms of spatial resolution and counting rate [111]. It consists of a MWPC using Ar:CO_2 (80%:10%) gas at atmospheric pressure and in continuous flow, equipped with $^{10}B_4C$ conversion layers oriented at a 5° angle in respect to the direction of the incoming neutrons. The first Multi-Blade prototype was built in 2012, developed at ILL [112], and several prototype optimizations have since then been carried. The geometry of the most recent version is shown in Fig. 3.15.

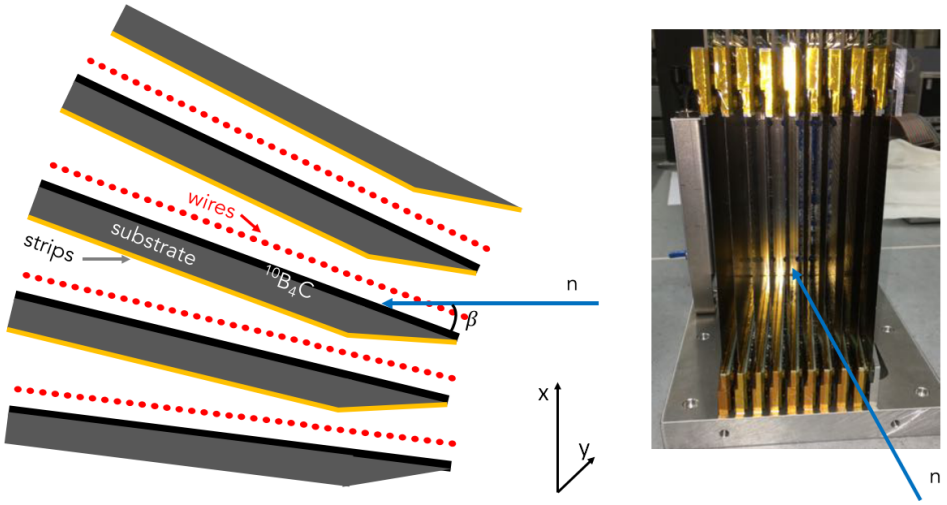

Figure 3.15: Left: Sketch of the cross-section of the Multi-Blade detector composed of identical units (cassettes) arranged over a circle and placed adjacent to each other. Right: A picture of the Multi-Blade detector made up of 9 cassettes. Image from [113].

The Multi-Blade detector has a modular design arranged over a circle, composed by several identical units, designated as cassettes, which consist of a substrate coated on one side with enriched $^{10}B_4C$, and with a cathode strip plane attached to the other, formed by 32 copper strips 4 mm wide on a Kapton substrate. Each cassette is also equipped with an anode wire plane, placed 4.6 mm above the converter, composed of 32 tungsten 15 μm diameter wires with a pitch of 4 mm, oriented orthogonally to the strips. The Multi-Blade is consequently divided into several MWPC, each one formed by the wire plane of a cassette and the strip plane of the cassette immediately above. The disposition and shape of the cassettes ensures that, unless scattering occurs, every incoming neutron always crosses exactly one cassette, entering from the converter side.

Both the wires and the strips are read individually, rather than in groups or by charge division. Although this requires a considerable number of electronic channels, this effort is required in order to improve linearity and reach higher counting rates. The signal amplitudes measured on the wires and on the strips are strongly correlated, because they are induced by the same avalanche, which allows for them to be read in coincidence. Due to the pitch of the wires and their distance from the conversion layer, 70% of times a single wire is involved in the detection process, about 30% two wires are triggered and the probability to see a signal in three or more wires in a single neutron detection is below 1% [111].

Each blade is coated on one side with a 7.5 μm thick enriched $^{10}B_4C$ layer. Although neutron detection efficiency saturates at a $\sim$3 μm coating thickness, due to the fact that the secondary neutron capture reaction products can no longer reach the gas, a high thickness is desired to absorb neutrons, even if they are not detected. The justification for this consists of reducing the probability of neutrons reaching the substrate, and potentially being scattered and detected in a position that would not accurately reflect the direction at which it was emitted from the sample. A 7.5 μm thick $^{10}B_4C$ layer is calculated to have neutron absorption probability of 99% for 2.5 Å neutrons incident at a 5° angle.

While the first versions of the Multi-Blade used 2 mm thick aluminium substrates for depositing the neutron conversion material, the most recent version uses titanium substrates instead. This is because aluminium slightly bends due to the mechanical stress

of the coating, whereas titanium has shown to be more robust.

This detector has 2D position reconstruction capability of the neutron interaction site, with the x-coordinates given by the wire plane and the y-coordinate by the strips plane [113]. Its spatial resolution (FWHM) in these coordinates is respectively 0.54×2.5 mm^2, which serves the purpose of reflectometers which typically require only submillimetric position resolution in one coordinate. The position resolution of the wire plane is immediately improved by a factor of $1/\sin(5°) = 11.5$ due to the inclination of the cassettes, which corresponds to the projection of the x-coordinate (identified in Fig. 3.15) in the wire planes. This inclination also improves the counting rate capability, because the neutron flux is spread over a 11.5 times wider surface. The detection efficiency reported is of 44% for 2.5 Å neutrons, which can be estimated as 32% for thermal neutrons.

The Multi-Blade is planned to be installed in several neutron research facilities, namely at ESS (Estia and FREIA reflectometers) [73], at PSI (AMOR reflectometer) [113], and for reflectometers at the PIK reactor.

Jalousie

Turning attention now to the Jalousie detector, it follows the same principle of tilting the conversion layers to improve detection efficiency. However, unlike the Multi-Blade which was arranged so that every neutron traversed only one conversion layer, the Jalousie detector makes use of stacking conversion layers to achieve an even higher detection efficiency. Independently of where they enter from, neutrons can traverse up to 8 conversion layers when traversing the detector. Analogously to the Multi-Blade, this detector follows a modular design with each detection segment composed by two anode wire planes on each side of a cathode plane, coated with enriched boron (^{10}B) on both sides and structured in strips for cathode signal readout. The cathode and wire planes are enclosed by a 300 μm aluminium cover to seal the gas, which is also boron-coated on both sides, making for a total of 4 conversion layers in each detection segment [114], which are arranged in a circular shape around the sample. Fig. 3.16-left shows a section of the Jalousie detector with 4 detection segments, and Fig. 3.16-right illustrates the complete detector.

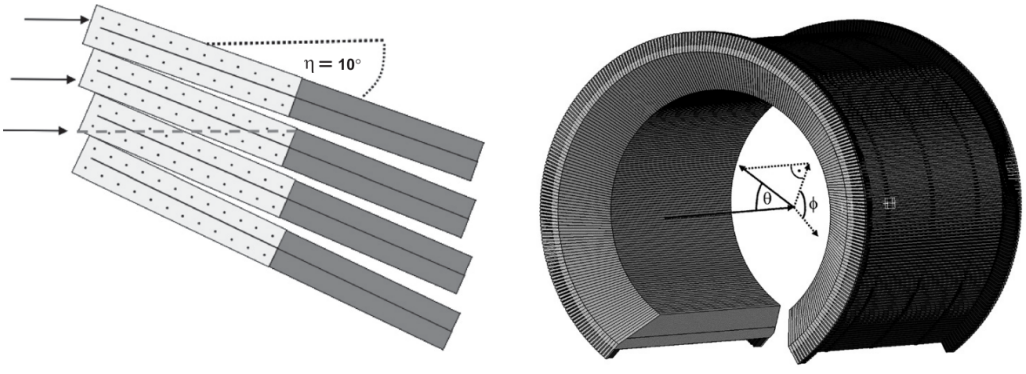

Figure 3.16: Left: Section of the Jalousie detector showing 4 detection segments, each one with two planes of wires represented as dots and a strip-structured boron-coated cathode between them represented as a line. Right: Arrangement of many detection segments to form a cylindrical detector with both length and inner diameter of 160 cm, covering a big solid angle. Images from [114].

The detector is designed to operate in proportional mode in a continuous flow of

Ar:CO_2 in variable proportions at atmospheric pressure. The Jalousie segments are mounted on frames forming a 10° angle between the incoming neutron and the boron layers. This angle was found to be the best compromise between efficiency improvement and mechanical design, which becomes more challenging for decreasing incidence angles [115].

The anode wires and the cathode strips are perpendicular to each other, each one connected to an individual electronic channel, to allow for 2D position reconstruction of the neutron capture site. Between every two anode wires, a field-shaping wire is additionally allocated to help in charge extraction (not represented in Fig. 3.16-left). The intrinsic spatial resolution (FWHM) was calculated to be 3.4×4.9 mm^2. The optimal ^{10}B coating was calculated to be 1 μm, which results in a 68% detection efficiency for thermal neutrons [114].

Although this detector was initially developed to replace the ^{3}He detectors of the POWTEX diffractometer at FRM II, it is currently also planned to be installed in the neutron diffraction instruments of ESS: DREAM, HEIMDAL and MAGiC [73].

3.4.5 GEM-based Detectors

Different detectors use gas electron multipliers (GEMs) along with padded anodes or strip planes instead of wires for charge multiplication and signal readout. GEMs were developed in the 90s at CERN [116], and their most conventional design consists of a 50 μm insulating Kapton foil coated on both sides with conductive copper, perforated to form a high density and uniform matrix of holes, with 70 μm diameter and 140 μm pitch (Fig. 3.17-left).

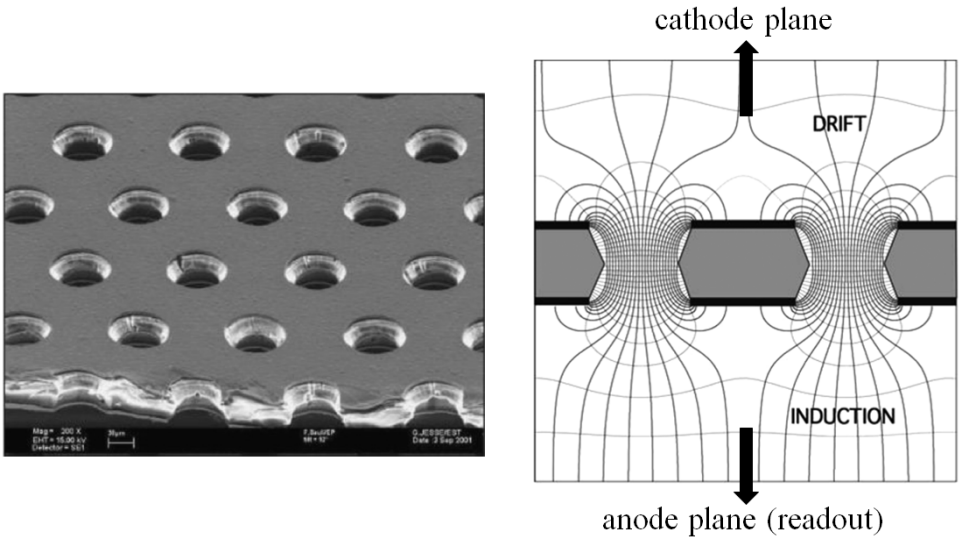

Figure 3.17: Left: SEM image of a typical GEM foil. Right: Computed electric field lines in the drift, holes and induction regions. Images adapted from [117].

By applying a potential difference between the copper surfaces on each side of the foil, an intense electric field is created in the holes, which forces the ionization electrons to drift through the holes, to be multiplied and transferred to a collection region. The space between the cathode and the GEM foil is called the drift region, which represents the sensitive volume where the primary charges are created, and consequently its length must be adjusted to the range of the ionizing primary particles. The region between the GEM

foil and the anode is designated as the induction region, where the multiplied charges induce a signal on the anode plane, which is typically segmented in strips or pads for spatial resolution capability. These regions are represented in Fig. 3.17-right.

To achieve higher gains, it is common to use a cascade of several GEM foils to add more multiplication stages while requiring lower voltages on each GEM, thus reducing the probability of discharges.

An attractive particularity of GEM-based detectors, in opposition to MWPCs, is the fact that the multiplication stage is separated from the charge collection stage. This allows for higher counting rate capability, since most of the positive ions do not reach the induction field and therefore do not affect the gain of the GEM foil due to space charge effects [118, 119]. In fact, this is the main motivation for the development of the GEM-based thermal neutron detectors here presented, since the high neutron beam brightness expected at the instruments of modern research facilities make it imperative to have detectors with high counting rate capability.

bGEM Detector

The bGEM detector geometry consists of a 0.4 mm aluminium cathode coated on its inner side with a 1 μm thick layer of B_4C (not enriched), using a triple GEM cascade at a distance of 13 mm from the cathode (drift gap), followed by a padded anode plane for signal readout. A schematic representation of this detector is presented in Fig. 3.18.

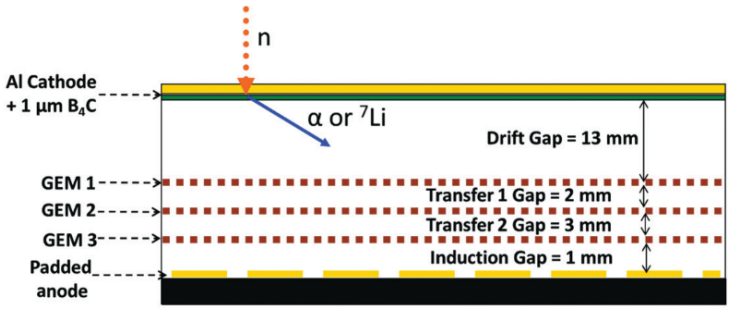

Figure 3.18: Schematic of the bGEM detector. Image from [120].

The detector is operated with a gas mixture of Ar:CO_2 (70%:30%) at atmospheric pressure in continuous flow. As neutrons are converted in the B_4C layer, one of the reaction products may reach the gas. The drift gap of 13 mm is sufficient to guarantee that the ionizing particles from the neutron capture reaction are fully stopped before reaching the GEM foils. The electrons from the primary ionizations are then accelerated towards the GEM cascade, where they undergo 3 multiplication stages, which results in a gain of ~100 when the sum of potential difference over the 3 GEM foils is $V_{GEM} = 870$ V. This was found to be the ideal working voltage, and comes from a compromise between increasing counting rate (which increases with V_{GEM}, but plateaus between 825 V and 925 V), while minimizing gamma-ray sensitivity, which also increases with V_{GEM}. Because the gamma-ray induced signals come mostly from fast electrons stripped from the solid material of the detector through Compton effect, which deposit much less energy in the gas, keeping the GEM gas gain not superior to about 100 guarantees that gamma-ray induced signals fall below the threshold set for noise rejection [121].

The signal is induced on an anode plane connected to the front-end electronics chain. The padded anode consists of a 2D gold-plated copper readout structure segmented with

132 pads of 8×8 mm^2, plus 4 L-shapped pads with 192 mm^2 on its corners, making for an active area of 100×100 mm^2. A photograph of it is shown in Fig. 3.19.

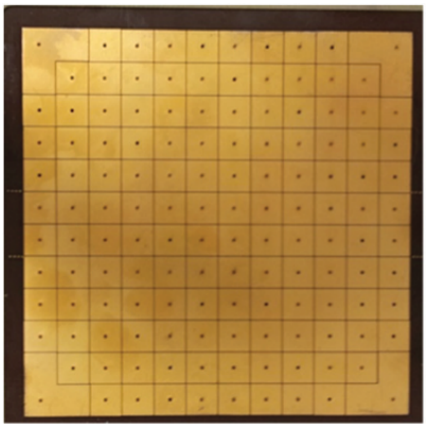

Figure 3.19: Photograph of the bGEM padded anode readout, composed of 132 pads with dimensions 8×8 mm^2 plus 4 L-shaped pads with an area of 192 mm^2, covering a total area of 100×100 mm^2. Image from [120].

Each pad is individually read, and its dimensions set a physical limit to spatial resolution. The achievable spatial resolution, however, is greater than the pad dimensions, because even in an ideal scenario, one neutron capture can generate a signal in several pads [118]. The spatial resolution (FWHM) was determined to be 31×37 mm^2 [121].

Because the bGEM deploys only one relatively thin conversion layer, its detection efficiency for thermal neutrons is only of $\sim$1% [122]. Therefore, its application is limited to beam monitors, which are essential for the continuous diagnose of a neutron beam, measuring the neutron flux and its spatial distribution. Beam monitors must have high time and space resolution, but a low detection efficiency to minimize the neutron beam attenuation.

Although it was specifically the bGEM detector that was highlighted here, several groups around the world have developed similar solutions. For instance, a detector has been developed with an efficiency of 0.027% to use as beam monitor in the diffractometers of J-PARC, using a ^{10}B coated aluminium cathode, a double GEM structure and anode strips with 0.8 mm pitch, which allows for a 1.2 mm spatial resolution [123].

BAND-GEM Detector

The BAND (Boron Array Neutron Detector)-GEM idea comes from the need of improving the performance of the bGEM in terms of efficiency, to be applied in other applications beyond beam monitors, specifically the LoKI SANS instrument at ESS [118, 119]. To improve detection efficiency, this detector deploys several conversion layers stacked and oriented at a grazing angle in respect to the incoming neutron beam. A scheme of the BAND-GEM detector is given in Fig. 3.20-right.

The cathode consists of a 0.4 mm thick aluminium foil. Unlike the bGEM, the conversion material is not deposited on the cathode, but rather distributed over 24 aluminium coated grids (only 6 are represented in the scheme of Fig. 3.20-right). Each grid, shown in Fig. 3.20-left, is composed by 11 strips 200 μm thick, 10 cm long, 3 mm high and with a pitch of 4 mm, coated on both sides with a 1 μm thick enriched $^{10}B_4C$ layer. The grids are vertically stacked, separated by a 1 mm thick insulator frame and

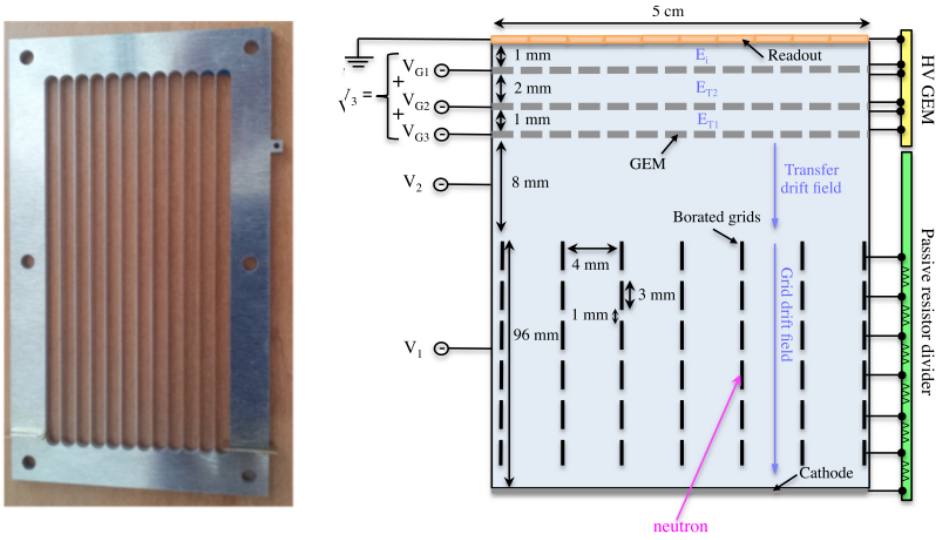

Figure 3.20: Left: Aluminium grid to be coated with 1 μm of $^{10}B_4C$, composed by 11 strips 10 cm long, 3 mm high and 200 μm thick, with a pitch of 4 mm. Right: Schematic of the BAND-GEM detector. Image from [124].

fed with a bias voltage through a passive voltage divider, so that a suitable electric field is generated into the grids stack, to transport the primary charges to the gas region close to the GEM surface. Above the converter grids, there is an 8 mm drift region followed by a triple GEM cascade and a padded anode readout, similarly to the bGEM. The padded anode, however, has a different geometry, shown in Fig. 3.21, composed of small (4×3 mm^2), medium (4×6 mm^2), and large (4×12 mm^2) pads [124].

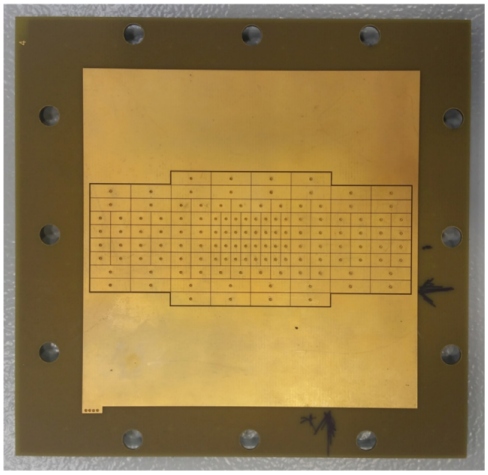

Figure 3.21: Photograph of the BAND-GEM padded anode readout, composed of pads with variable dimensions. Images from [124].

The detector is tilted so that the coated grids form a 5° angle in relation to the neutron beam direction to maximize detection efficiency, measured with a value of 40% for 4 Å neutrons, which can be estimated to correspond to 18% for thermal neutrons. This inclination also brings a spatial resolution improvement, due to the reason explained for the Multi-Blade detector, which is of ∼7 mm (FWHM) for the mentioned angle [118].

CASCADE Detector

Another strategy to combine boron neutron converters with GEMs is to perform the coating directly on the surface of the GEM foils, as is the case of the CASCADE detector, first developed at Heidelberg University in the early 2000s, and in continuous development and adaptation to various applications [125, 126]. Unlike all the above-exposed detectors, this results in a charge transparent substrate, which allows to explore different detector geometries and charge readout methods.

The most recent version of the CASCADE detector uses 6 layers of conversion material. These are divided into two mirrored half-spaces that, apart from differences in the coating thickness of each layer, result in a symmetric detector. Whereas the first and last layers of neutron converter are respectively coated on the top and bottom drift electrodes, followed by a regular GEM, the in-between stages are single-sided boron-coated GEMs. Fig. 3.22 shows a schematic representation of one half-space of the detector.

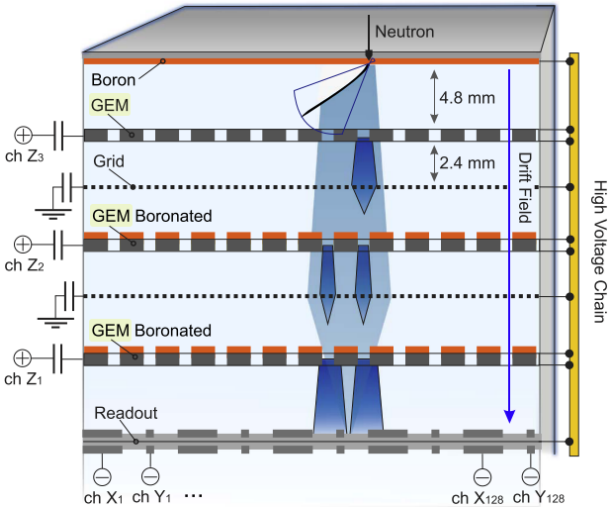

Figure 3.22: Schematic of one half-space of the CASCADE detector. Image from [126].

The coating material is 99% enriched boron (^{10}B). The individual thicknesses of each layer are, from top to bottom, 1.5 μm, 0.8 μm, 0.99 μm, 0.95 μm, 0.8 μm, and 1.0 μm.

The charge is projected towards a double-sided microstructured anode, which consists of a printed circuit board of perpendicular stripes with an active area of 20 $\times$ 20 cm^2. Each side is divided into 128 strips with a pitch of 1.56 mm, each connected to an individual electronic channel. In addition to the signal from the collection of electrons in the microstructured anode, which gives 2D spatial information (x and y), the induction signal caused by the movement of electrons traversing the GEM foils is also read through the copper surface of each GEM. This gives spatial information on a third coordinate (z), allowing the identification of the origin of the neutron conversion reaction as charge can be tracked while traversing the stacked GEMs.

The detector operates in a continuous flow of Ar:CO_2 in variable proportions, at atmospheric pressure or beyond. Increasing the filing gas pressure leads to an improvement of spatial resolution due to the shortening of the tracks of the primary particles [127].

The measured efficiency for 0.8 Å neutrons was of 7.8%, which can be extrapolated to approximately 23.4% for thermal neutrons. The intrinsic detector resolution (FWHM) was determined to be 3.4 mm at atmospheric pressure in both x and y coordinates, and is limited by three factors: the resolution of the readout strips themselves, the track lengths

of the primary ^{7}Li and alpha particles, and the scattering of neutrons, mostly by the hydrogen present in the detector material, such as the Kapton in the GEM foils.

The CASCADE detector is currently installed at the Spin-Echo instruments RESEDA and MIRA at FRM II in Germany [101].

4 Fine Powder Aerosol Detector

Finding adequate ^{3}He-free neutron detection alternatives has become an imperative that motivated a great deal of research and development over the last decade. With the exception of BF_3, which is toxic and therefore not suitable for most applications, no other gas exists that can be used for neutron detection in gaseous detectors. The principal consumer of ^{3}He gas, by a large scale, are neutron detectors deployed in homeland security applications, namely RPMs. Therefore, finding an adequate alternative solution for these devices would bring a significant relief to the demand for ^{3}He. As was exposed in section 3.1.1, RPMs are equipped with large area neutron detectors, which have as main requirements high detection efficiency and good gamma-ray discrimination capability. ^{3}He proportional counters (PCs) fulfil these requirements and consequently, alternative detection technologies must do so as well.

^{3}He PCs provide a thermal neutron detection signature easy to identify, by depositing the full energy of the neutron capture reaction 2.33 in the gas, and producing output pulses with amplitudes that follow a Gaussian distribution with a centroid proportional to this energy. This is not possible using solid coating alternatives, such as boron-lined detectors, which have a PHS that consists of a two-step plateau extending down to zero, and consequently have the drawback of superimposing neutron events with the low-energy gamma-ray background naturally present in the same environments as neutrons.

If, however, the neutron conversion material were to be suspended in the gas, rather than deposited on the walls, and had very reduced dimensions, so that the secondary particles from the neutron capture reaction could escape to the gas with most of their initial energy, it would presumably be possible to collect the energy of both secondary particles from a single neutron capture, which allowed for a peak-like response of the detector. From this, the idea to replace the ^{3}He or ^{10}B atoms of a gas with suspended nanoparticles containing a neutron sensitive isotope was born, transforming a standard proportional gas mixture into a neutron sensitive aerosol.

The non-fixed nature of the fine powder dispersion in the gas excludes this detection concept from applications in which sub-millimetric spatial resolution is required. Nonetheless, RPMs and other large area detectors favour detection efficiency over spatial resolution, having typically only a very coarse two-dimensional resolution capability if several tubes are bundled in a matrix layout (or three-dimensional if resistive wires are used [128]). Therefore, the fine powder aerosol detector proposed can be considered a potential alternative to ^{3}He PCs if its performance meets the required standards.

4.1 Operation Principle

As already discussed, promising ^{3}He-free alternatives for neutron detection rely on the use of solid ^{10}B, which has a higher thermal neutron capture cross-section than ^{6}Li, and consequently the potential to achieve higher detection efficiency. These detectors typically use a solid coating of a boron-containing material, most commonly natural boron or boron carbide (B_4C), which can be enriched with the ^{10}B isotope, inside a gaseous detector. Since this material is not self-supporting, it is usually deposited either on the inner walls of the detector or in substrates inside it. This is a robust and well-known technology, which has been investigated since as early as the 1950s [129], but was recently revisited due to the ^{3}He shortage crisis.

The geometrical constrain that arises from energy and momentum conservation of the neutron capture reaction and results in the emission of the ^{7}Li ion and the α particle in opposite directions, dictates that only one of the reaction products can, at best, be emitted towards the gas in conventional boron-lined detectors (Fig. 4.1-left).

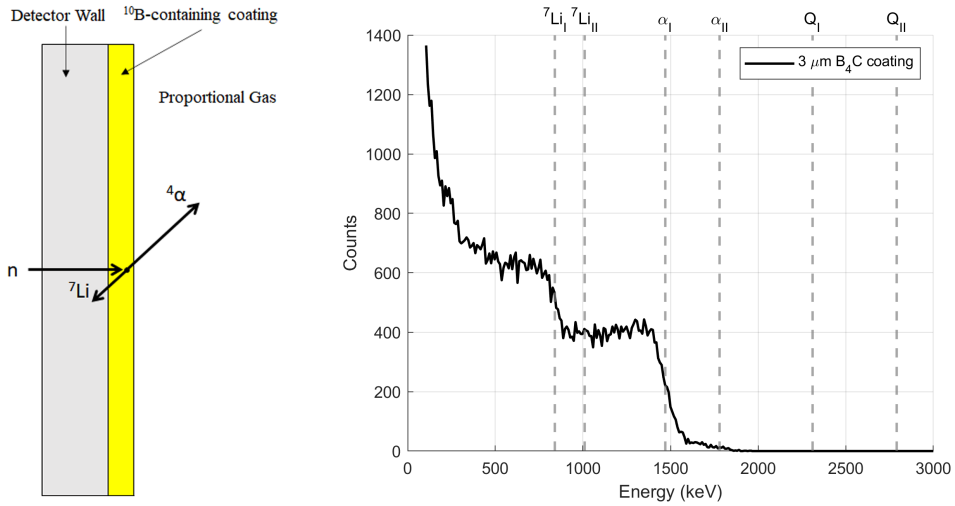

Figure 4.1: Left - Neutron capture reaction in a proportional counter coated with a ^{10}B-containing material. Right - Histogram of the deposited energies in a gaseous detector with a 3 μm thick B_4C wall coating, obtained by GEANT4 simulation. The dashed vertical grey lines mark the energies of the reaction products and Q-values of both branches of the ^{10}B neutron capture reaction 2.38: I – 94% branch; II – 6% branch.

It is therefore impossible to measure the total energy released in a nuclear capture reaction with such solutions, as can be done with ^{3}He proportional counters. Consequently, the response of these detectors does not feature a full energy peak, but rather an overlap of 2 continuous distributions corresponding to each secondary particle, which results in the typical 2-step pulse height distribution depicted in Fig. 4.1-right. This PHS shape is due to the fact that a fraction of the energy of the ^{10}B reaction products is lost while traversing the conversion material, before reaching the proportional gas where the detectable ionizations take place. This fraction depends on the distance travelled in the boron layer which varies in regard to the depth at which the neutron capture occurs, and the direction of the emitted particles. Therefore, the energy range of the ^{7}Li and α particles when reaching the gas goes from their maximum energy down to zero. The first case corresponds to neutron captures taking place near the surface of the conversion layer,

while the second to neutron captures that either occurred at a depth similar to or higher than the range of the secondary particles in that material, or in which the secondary particles were emitted in a near parallel angle in relation to the converter.

This shape of the pulse height distribution has an impact on the gamma-ray discrimination capability. The selection of neutron conversion material, whether solid or gaseous, has minimal impact on the energy deposited by electrons produced by the interaction of gamma-rays in the detector [53]. Consequently, the gamma-sensitivity, defined as the probability for a gamma-ray to generate a false count in a neutron measurement, is the same for boron-coated detectors and ^{3}He proportional counters [54]. However, for boron-coated detectors, the possible energy range for neutron detections overlaps with that arising from gamma-ray interactions, and this overlapping region must be rejected. This can cause a loss of neutron signal, particularly in environments with high gamma-ray interaction rates

The novel detection principle proposed to overcome this limitation consists of suspending boron-based nano/microparticles in a proportional counter by an appropriate gas flow which counter-acts the gravity force acting on the particles, thus forming an aerosol. The distinctive feature of this detection principle is the possibility of collecting nearly all the energy released in the ^{10}B neutron capture reaction, if the fine particles suspended in the aerosol have a diameter smaller than the range of the reaction products in the composing material, which is of a few microns for elemental boron or boron compounds. In an ideal scenario, the output pulses of this detector can be similar to ^{3}He or BF_3 gaseous detectors, showing a distinctive peak, with the added benefit of the PHS extending to higher energies, a valuable feature for the improvement of the gamma-ray discrimination, since it allows to set higher cut-off energy thresholds with minimal detection efficiency loss.

This detection concept was validated by GEANT4 simulations [85], considering a single sphere-like 1 μm diameter 99% ^{10}B-enriched boron carbide particle in the centre of an Ar:CO_2 (90%:10%) gas cylindrical volume at atmospheric pressure, shown in Fig. 4.2.

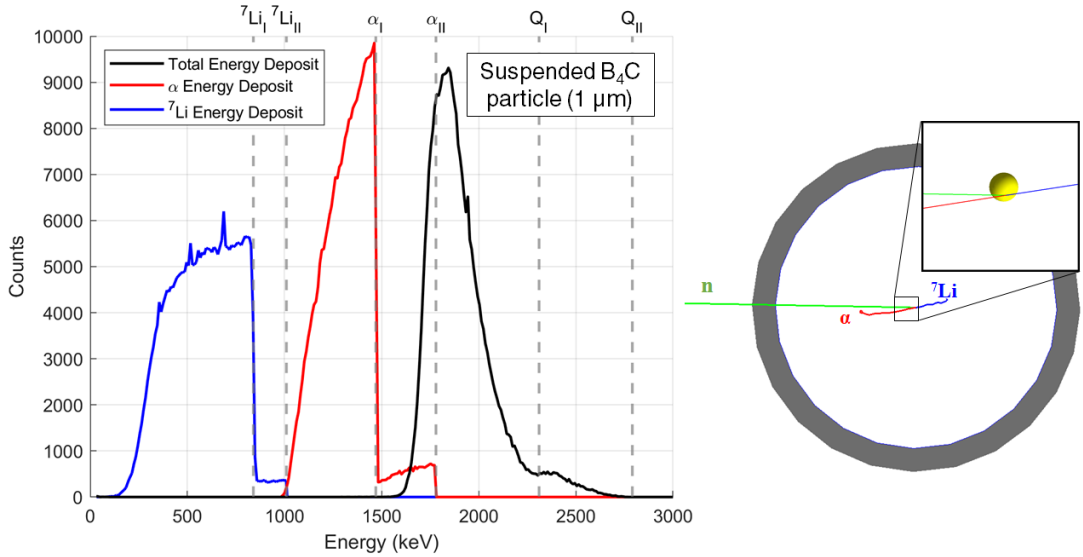

Figure 4.2: Left: GEANT4 simulation of the PHS of the energy deposited by the α (red) and ^{7}Li (blue) ions in the filling gas of the detector, along with their summed energy deposition (black) for each neutron capture. Right: Neutron capture reaction occurring in a suspended 1 μm diameter $^{10}B_4C$ microparticle.

A total of 10^7 incident thermal neutrons were defined, uniformly distributed over the particle cross-section. The incoming neutrons are converted inside the microparticle and both secondary particles of the nuclear reaction escape from it, depositing a large fraction of their initial energy in the proportional gas. This is somewhat analogous to a ^{3}He or BF_3 gaseous detector in which the ^{3}He/^{10}B atoms are replaced by $^{10}B_4C$ nanoparticles.

Because the diameter of the particle defined in the simulation is inferior to the range of the products of the neutron capture reaction, which in $^{10}B_4C$ is about 1.6 μm for ^{7}Li and 3.2 μm for the α particle [5], both manage to escape the microparticle. For this reason, the total energy deposited in the gas is always superior to the energy of the most energetic reaction product, the α particle, as evidenced by the black line in the plot of Fig. 4.2. However, it is virtually impossible for both reaction products to simultaneously escape the B_4C particle without at least one of them losing a fraction of their energy in ionizations and excitations inside it. Consequently, the peak response of the detector that corresponds to the 94% probability reaction branch is not centred at the Q-value (2.31 MeV), but at an inferior energy, about 1.85 MeV. This peak does not follow a Gaussian distribution, as is the case of the ^{3}He PC, but rather shows a right-tail, arising from neutron detections in which the secondary particles escape with successive higher energies, which depends on the precise location inside the nanoparticle where the neutron is captured and the emission direction of the secondary particles.

The energy fraction the ^{7}Li and α particles deposit in the gas decreases as the energy lost in interactions inside the B_4C nano/microparticle increases, and consequently depends on its size. Fig. 4.3 shows the simulation results obtained by varying the diameter of the suspended particle, which indicate that there is a particle diameter above which the peak response of the detector is no longer achieved.

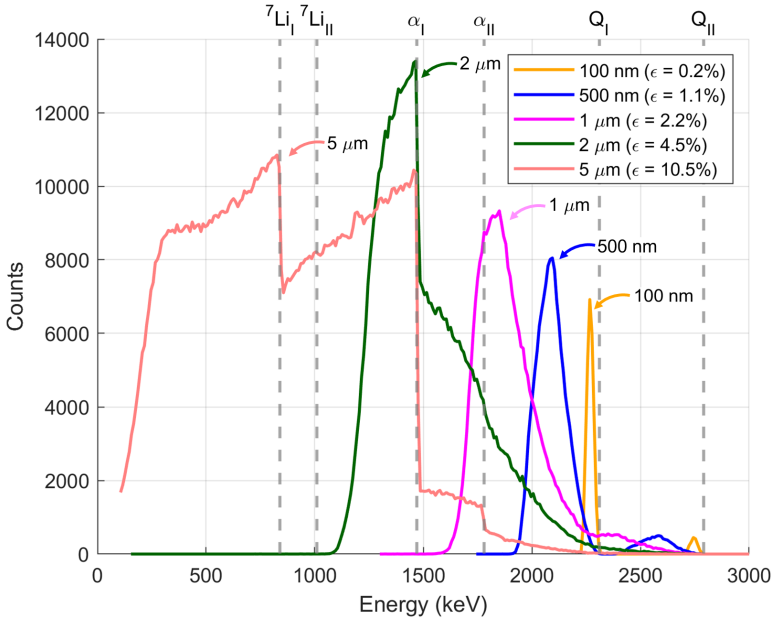

Figure 4.3: Effect of diameter variation of the suspended $^{10}B_4C$ particle in the simulated detector in the PHS and the correspondent detection efficiency (displayed in the legend for each diameter considered).

Particularly, for particle diameters of 1 μm and below, there is a high probability that a neutron capture results in both secondary particles simultaneously depositing a large part

of their initial energy in the gas, and as a result the detector output consists of a single peak. Among these, smaller particles allow for narrower peaks, and centred at higher energies. Indeed, for 100 nm nanoparticles, the peaks from the 94% ($Q_{\mathrm{I}} = 2.31$ MeV) and the 6% ($Q_{\mathrm{II}} = 2.79$ MeV) reaction branches are clearly distinguishable, and located very close to the full energy values of the corresponding reactions. The 2 μm particle starts to show a slightly different behaviour, where energy depositions that fall below the energy of the alpha particle occur. Also, the peak exhibits an accentuated edge in energy corresponding to the α particle from the first reaction branch ($\alpha_{\mathrm{I}} = 1.47$ MeV). This edge signals neutron detections in which the α particle reaches the gas maintaining its initial energy, while the ^{7}Li ion is absorbed inside the particle. This is an expected possibility, since the diameter of the B_4C particle is now greater than the range of the ^{7}Li ion. Hence, for neutron captures occurring near the edges of the microparticle in which the ^{7}Li ion is emitted towards its centre, this reaction product would have to transverse a distance greater than its range, and consequently loses all of its energy to interactions inside the microparticle before reaching the gas. This effect is aggravated for the 5 μm particle, for which only a residual amount of neutron captures result in both secondary particles simultaneously reaching the gas. The self-absorption inside the larger microparticle of, at least, one of the reaction products is now the most likely outcome, with the exception being the neutron detections that take place near the edges of the microparticle and in which the secondary particles are emitted roughly in parallel to the tangent of the surface limit, rather than in the direction of the centre of the particle.

Regarding the optimal B_4C particles diameter, there is evidently a compromise between the achievable energy deposition in the filling gas and detection efficiency (Fig. 4.3). The smaller a particle is, the larger the fraction of energy released in the neutron capture reaction can be deposited by the secondary products in the gas. At the same time, however, the less likely a neutron is to interact with one of the ^{10}B atoms in the particle. A linear relation between detection efficiency and particle diameter is found, up to a limit of ~ 5 μm. Beyond this, the relation is no longer liner, as presented in Fig. 4.4.

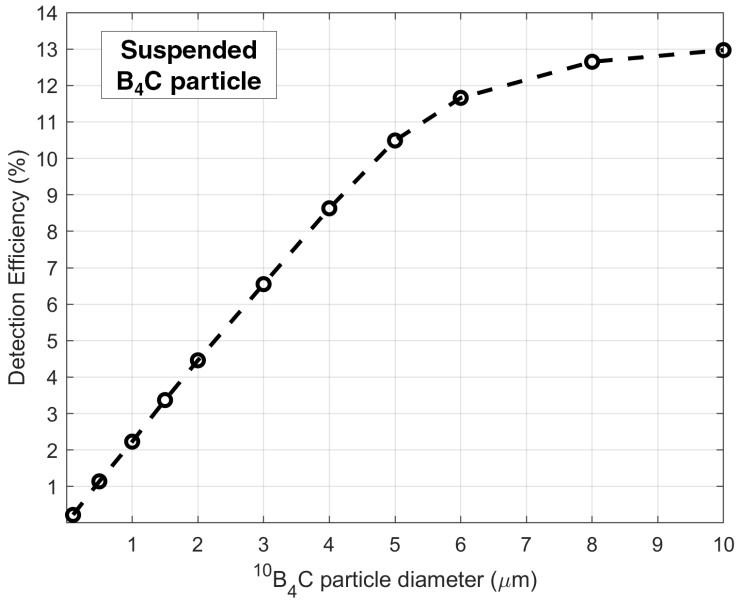

Figure 4.4: Detection efficiency as a function of diameter for a single suspended $^{10}B_4C$ particle.

From what was discussed, it can be assumed that a favourable average particle diameter for the neutron aerosol detector would be approximately 1 μm, which is about the size limit to allow for a distinct peak in the PHS output, while maximizing detection efficiency for this condition.

Besides the self-absorption of the neutron capture reaction products in the B_4C particles, it is also important to consider the impact of neutron captures occurring in particles very near or attached to the walls of the detector. This situation was simulated with GEANT4, also considering a 1 μm diameter $^{10}B_4C$ nanoparticle irradiated by 10^7 thermal neutrons uniformly distributed across its cross-section, but this time positioning the particle in contact with the inner walls of the detector. The results, presented in Fig. 4.5, show a remarkably different behaviour when comparing to the microparticle positioned in the centre of the detector. This is because only one of the secondary particles can now travel in the direction of the gas, while the other is emitted towards the wall. As a result, there is no possibility of achieving a full energy peak in the detector response. Instead, the total energy deposition PHS consists of an overlap between those of the ^{7}Li and α particles. The detector output in this case is similar to the wall-effect obtained with boron coated detectors, showing a two-step plateau that extends to the low energy region and reduces the ability to discriminate between neutron captures and gamma-rays induced events. Therefore, the natural attachment of B_4C particles to the walls as they are dispersed is an obstacle that must be addressed to optimize the response of the aerosol detector.

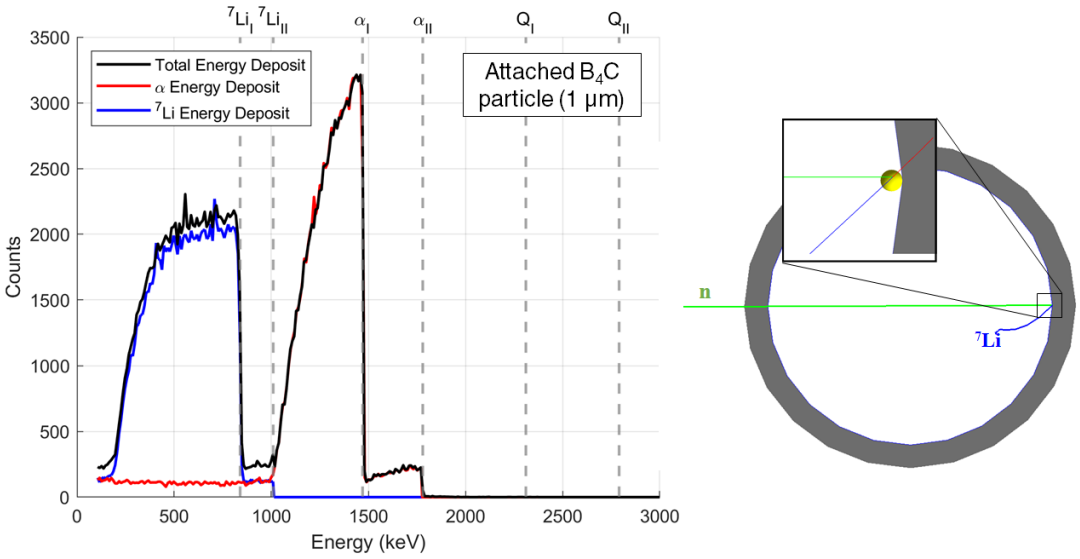

Figure 4.5: Left: GEANT4 simulation of the PHS of the energy deposited by the α (red) and ^{7}Li (blue) ions in the filling gas of the detector, along with their summed energy deposition (black) for each neutron capture. Right: Neutron capture reaction occurring in a 1 μm diameter $^{10}B_4C$ microparticle attached to the wall of the detector.

Prior to the work developed for the aim of this thesis, initial proof-of-concept tests were carried at the Swiss Spallation Neutron Source (SINQ) at Paul Scherrer Institute (PSI) [130]. The aerosol detector prototype was irradiated with a beam of cold neutrons (5 Å) with vertical and horizontal dimensions of 50 mm and 10 mm, respectively. The collimated beam irradiated the detector across its centre, at equal distances from the top and bottom flanges, with an intensity of 7×10^3 neutrons per second.

During the detector operation, gas circulated from the bottom to the top of the proportional counter, dragging along and suspending the B_4C microparticles. To minimize the contribution of neutron captures from nanoparticles attached to the walls, an electric field cage was installed, which consisted of a set of electrodes with a negative potential (electrostatic gate) around the central anode wire, forming a reversed electric field near the walls of the detector, preventing the primary electrons originated by neutron captures in nanoparticles attached to the walls from being accelerated towards the anode, and consequently, from being detected. Fig. 4.6 shows a scheme of the prototype detector, and the results of the irradiation measurements for several electrostatic gate polarizations.

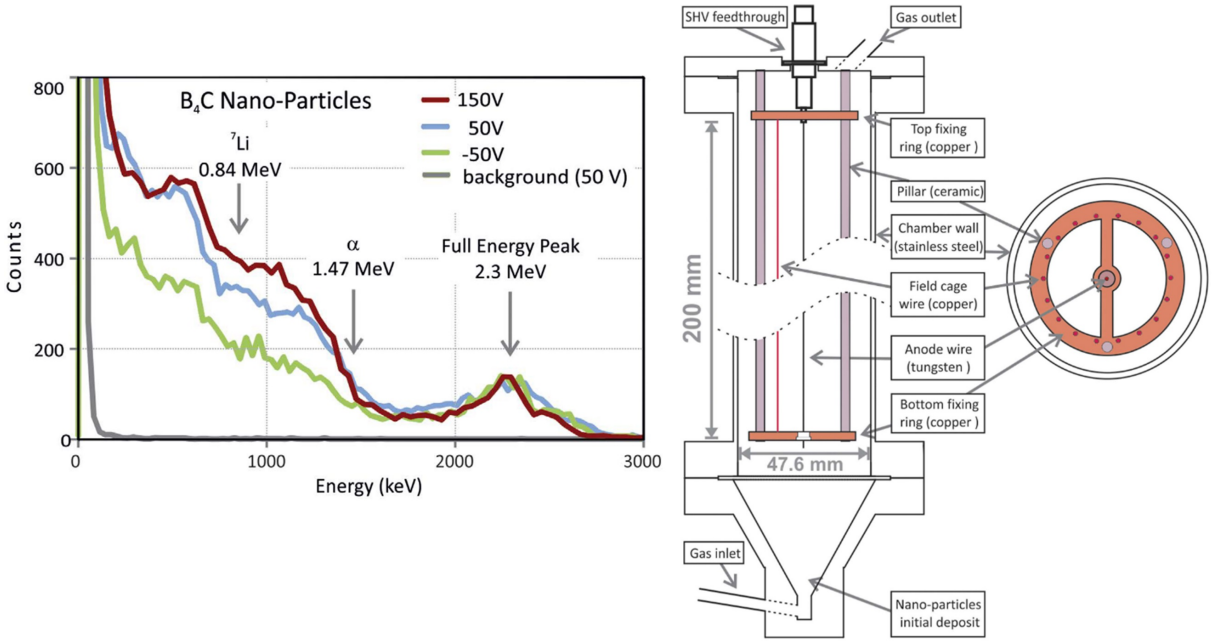

Figure 4.6: Left: Pulse-height distributions (normalized to the full energy peak) from cold neutron (5 Å) irradiation on the aerosol detector prototype with B_4C fine powder for several electrostatic gate polarizations, and acquisition time of 400 seconds. Right: Schematics of the proportional counter used in the preliminary irradiation tests. Only one of the 18 field cage wires is depicted on the front-view. The positions of the 18 field cage wires are depicted on the cross-section view, as well as the bottom fixing ring, where the anode wire is glued to. Image from [131].

Besides the two-step plateau characteristic from boron-coated detectors, a single peak is also visible in the detector response, indicating that some neutron detections occurred in microparticles dispersed in the proportional gas. A detection efficiency of 4% was achieved for an electrostatic gate polarization of −50 V.

4.2 Geometry and Materials

4.2.1 Fine Powder

The fine powder selected to form the neutron sensitive aerosol was B_4C Nanopowder provided by PlasmaChem GmbH (non ^{10}B enriched, with >97% purity). Non-enriched B_4C powder was more easily available, and therefore preferred for the prototyping stage.

However, the preparation of ^{10}B-enriched boron carbide nanopowder is viable, as reported in literature [132]. Although B_4C is not considered a hazardous substance, when in fine powder format it is considered irritant and therefore, when handling it, personal protection equipment should be used to prevent skin/eye contact and inhalation, namely gloves, safety goggles and dust masks [133].

Fig. 4.7 shows images of a B_4C fine powder sample, taken with the Tescan VEGA3 scanning electron microscope (SEM), under different magnifications. To determine the average particle diameter, a sample of the powder was characterized by the Beckman Coulter LS 13 320 granulometer, which analyses the light diffraction patterns of the nanoparticles dispersed in ethanol, exposed to a laser beam. This resulted in the particle size distribution plot presented in Fig. 4.8. The mean particle diameter value was determined to be d = 1.056 μm, with percentile values d_{50} = 1.029 μm, d_{10} = 0.553 μm and d_{90} = 1.602 μm. It should be noticed the fluid employed in the aerosol detector is different from the one used to suspend the particles for size characterization. Despite the use of rollers, magnetic stirrers and tube rotators to assure the suspension of sampled powders, it is impossible to guarantee that the agglomeration behaviour of the particles while suspended in liquid ethanol and in the filling gas of the detector is identical [134]. In addition, this behaviour also depends on environmental factors such as humidity. Thus, the approximate 1 μm mean diameter should be considered only as a reference value.

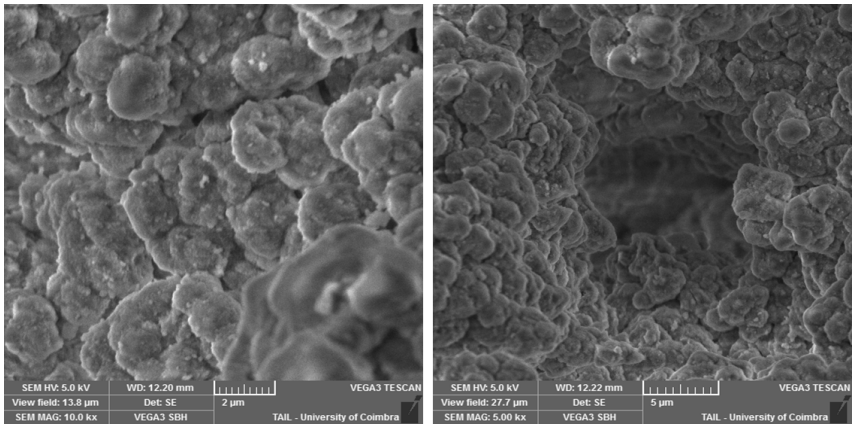

Figure 4.7: SEM images of a sample of B_4C fine powder selected for the aerosol detector, provided by PlasmaChem GmbH.

4.2.2 Detector Wall Material

When selecting the materials to build the aerosol detector chamber, different materials were investigated, searching for the most advantageous in terms of reducing the attachment of the fine powder to the detector components. Concerning the proportional counter walls, the requirement that it is made of a conductive material leads to consider as options stainless-steel and aluminium. Although aluminium is more transparent to neutrons, i.e., the probability of neutron scattering is lower, if this material happened to be more prone to nanoparticle attachment, stainless-steel would be preferable to reduce the wall-effect feature of the detector response. To determine this, two parallelepiped samples with square 20×20 mm^2 faces were machined, one made of aluminium and the other of stainless-steel. One side of each sample was carefully placed over a B_4C powder layer deposited on a Petri dish, one at a time. Subsequently, they were removed and

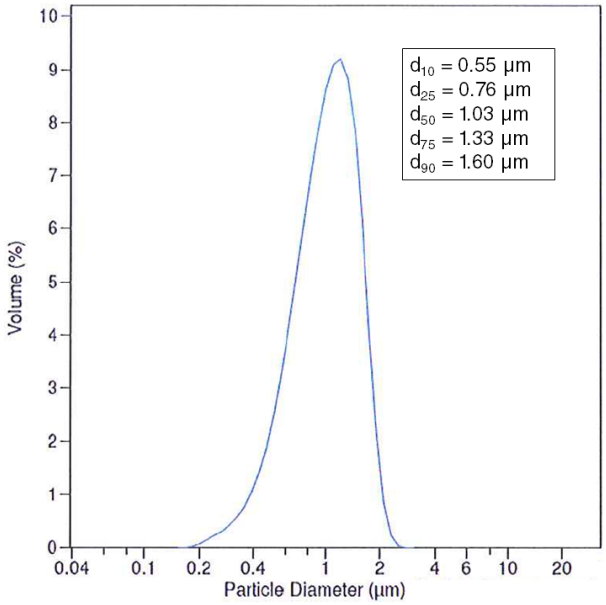

Figure 4.8: Particle size distribution of the B_4C fine powder.

placed over a paper with the side that was in contact with the powder facing down, and forced to slide a distance of 15 cm, to remove by friction the particles that were less strongly attached. Finally, a photograph was taken to visually compare if there were any significant differences in the attachment behaviour of the microparticles between the two materials. These are displayed in Fig. 4.9. At a first glance, no notorious differences are observed between the samples. However, when cleaning them with water and paper, it was verified that it was considerably harder to remove the nanoparticles attached to the aluminium sample than to the stainless-steel. For the latter, the nanoparticles appeared to be completely removed (as far as visually possible to access) with little effort.

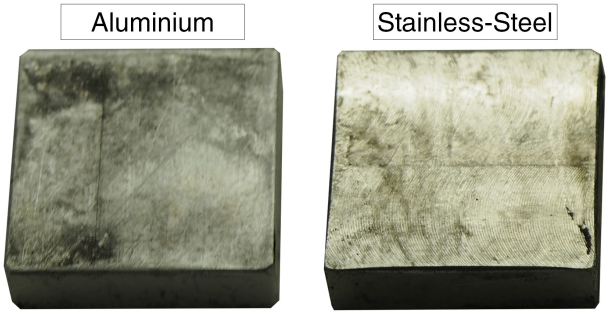

Figure 4.9: Aluminium (left) and stainless-steel (right) samples.

Because being able to effectively clean the detector after powder dispersion for different irradiation measurements is an important aspect, the selected material to build the aerosol detector prototype was stainless-steel. This test was a first-approach qualitative assessment of the attachment of the nanoparticles. But because reducing the attachment of the fine powder to the walls of the detector is a crucial parameter to optimize, this was subject to further investigation and will be discussed in depth in section 4.6.

4.2.3 Detector Geometry

The most common ^{3}He proportional counter diameter is 1 inch (25.4 mm) [92]. This relatively small diameter is compensated by the high pressure operation, significantly increasing the concentration of ^{3}He atoms and reducing the track length of the neutron capture reaction products in the gas. However, for the aerosol detection concept, a more detailed analysis of the ideal detector should be carried. Unlike conventional PCs, the ratio between the detector volume and its inner surface area is an important factor for the aerosol detector. Given the importance of maximizing the fraction of particles that are suspended in the gas, rather than attached to the walls, a high ratio between volume and inner surface area (V/A_{surf}) is desirable. Considering a collimated neutron beam with width inferior to the detector diameter, this ratio depends on the detector diameter and on the fraction of its volume that is traversed by neutrons. To demonstrate this, let us consider the geometric scheme of Fig. 4.10, illustrating the top view of a cylinder proportional counter of radius R traversed by a neutron beam of width x, aligned with its centre.

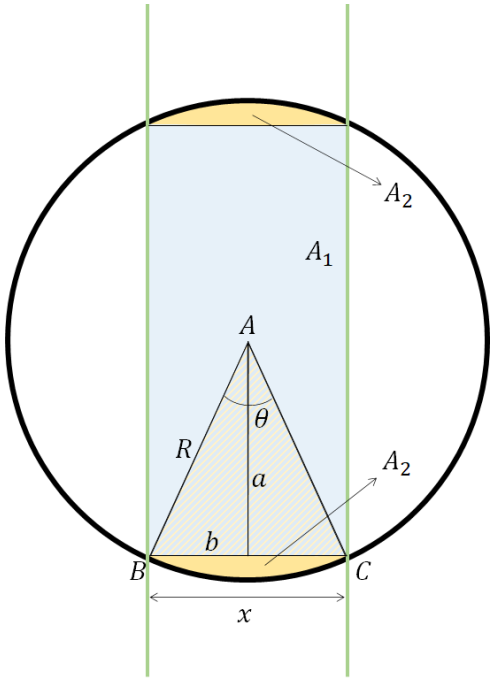

Figure 4.10: Top view geometric scheme of a neutron beam of width x traversing a cylinder of radius R, aligned with its centre.

In the depicted scenario, neutron captures can only occur with nanoparticles suspended in the detector volume given by the blue (A_1) and yellow (A_2) regions, which is of:

$$V = (A_1 + 2A_2)\ y_{\text{beam}} \tag{4.1}$$

where y_{beam} is the height of the neutron beam. From the trigonometric relation $\tan(\theta/2) = b/a$ and $b = x/2$, we can write A_1 as:

$$A_1 = 2\ a\ x = \frac{x^2}{\tan(\frac{\theta}{2})} \tag{4.2}$$

Note that θ is the angle defined by $B\hat{A}C$. A_2 can be calculated by subtracting the

triangle $\triangle ABC$ from the section of the circle defined by the angle θ, with area $R^2\theta/2$, thus obtaining:

$$A_2 = \frac{\theta R^2}{2} - \frac{ax}{2} \iff A_2 = \frac{\theta R^2}{2} - \frac{x^2}{4\tan(\frac{\theta}{2})} \tag{4.3}$$

Replacing the variables of equations (4.2) and (4.3) in equation (4.1), we get:

$$V = \left[\frac{x^2}{\tan(\frac{\theta}{2})} + \theta R^2 - \frac{x^2}{2\tan(\frac{\theta}{2})}\right] y_{\text{beam}} \iff V = \left[\frac{x^2}{2\tan(\frac{\theta}{2})} + \theta R^2\right] y_{\text{beam}} \tag{4.4}$$

The angle θ can be expressed in terms of the circumference radius and the beam width: $\frac{\theta}{2} = \arcsin(\frac{x}{2R})$. We thus obtain the detector volume traversed by the beam as a function of its diameter ($D = 2R$) and the beam width:

$$V(D,x) = \left[\frac{x^2}{2\tan(\arcsin(\frac{x}{D}))} + \frac{D^2}{2}\arcsin\left(\frac{x}{D}\right)\right] y_{\text{beam}} \tag{4.5}$$

Turning attention to the surface area of the fraction of the cylinder that is traversed by the neutron beam, we can write:

$$A_{\text{surf}}(D,x) = \left[2\ \widehat{BC}\ \right]\ y_{\text{beam}} = \left[2\ \theta\ \frac{D}{2}\ \right]\ y_{\text{beam}} = \left[2D\arcsin(\frac{x}{D})\right]\ y_{\text{beam}} \tag{4.6}$$

The ratio between the detector volume and its inner surface area as a function of its diameter and the width of the neutron beam is therefore given by:

$$\begin{aligned} \frac{V}{A_{\text{surf}}}(D,x) &= \frac{\left[\frac{x^2}{2\tan(\arcsin(\frac{x}{D}))} + \frac{D^2}{2}\arcsin\left(\frac{x}{D}\right)\right] y_{\text{beam}}}{\left[2D\arcsin(\frac{x}{D})\right]\ y_{\text{beam}}} \iff \\ \iff \frac{V}{A_{\text{surf}}}(D,x) &= \frac{x^2}{4\ D\arcsin(\frac{x}{D})\tan(\arcsin(\frac{x}{D}))} + \frac{D}{4} \end{aligned} \tag{4.7}$$

As expected, when the with of the beam equals the diameter of the cylinder, we obtain:

$$\lim_{x\to D} \frac{V}{A_{\text{surf}}}(D,x) = \frac{D^2}{4\ D\ \frac{\pi}{2}\tan(\frac{\pi}{2})} + \frac{D}{4} = \frac{D}{\infty} + \frac{D}{4} = \frac{D}{4} \tag{4.8}$$

which corresponds to the ratio between the volume and the surface area of a cylinder with length L:

$$\frac{\mathrm{V}}{A_{\text{surf}}}(x = D) = \frac{\pi\frac{D^2}{4}L}{\pi DL} = \frac{D}{4} \tag{4.9}$$

By plotting equation (4.7) as a function of the beam width for several detector diameters (Fig. 4.11), we come to the conclusion that the volume to surface area ratio increases for higher diameters and, for any set diameter, decreases for wider beams.

In light of these results, the selected diameter for the neutron aerosol detector was of 48 mm, roughly double of the typical 1 inch diameter of ^{3}He proportional counters. In irradiation experiments under a controlled environment, the width of the incident neutron

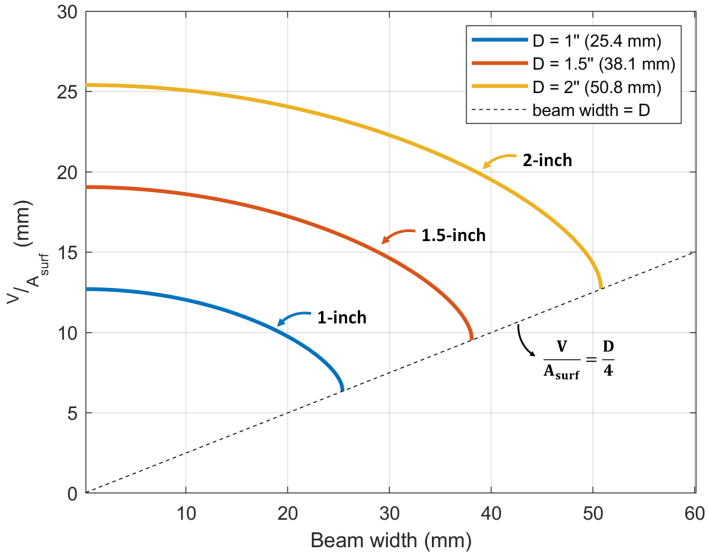

Figure 4.11: Volume to surface area ratio of the neutron aerosol detector for different diameters as a function of the incoming neutron beam width.

beam can be adjusted using a neutron absorbing mask, and can be a useful strategy to reduce the impact of the wall-effect in the detector response.

A technical drawing of the neutron aerosol detector prototype is shown in Fig. 4.12.

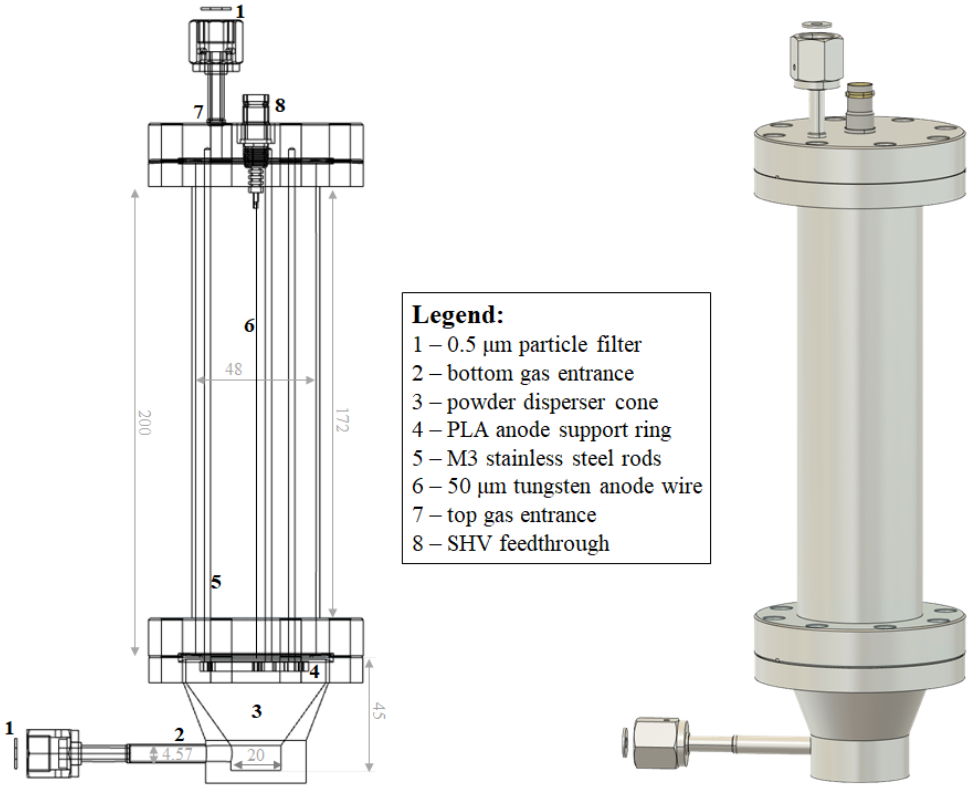

Figure 4.12: Technical drawing of the neutron aerosol detector prototype (dimensions in millimetres).

The main body of the detector consists of a stainless-steel cylinder soldered to ultra-high vacuum CF 50 (ConFlat) flanges [135] on each side. The top extremity is connected to an identical flange with an SHV feedthrough on its centre to polarize the anode wire, and a gas entrance with a 1/4 inch Swagelok fitting. Attached to the bottom of the detector is the particle disperser, which consists of a CF 50 flange soldered to a cone-shaped piece with a gas inlet also equipped with a 1/4 inch Swagelok fitting. The strategy used to insert the B_4C fine powder inside the detector consisted of priorly depositing it in the cone-shaped disperser, and subsequently attaching this component to the detector bottom. The dispersion of the powder is done by the gas flow itself, continuously flowing from the bottom inlet to the top outlet of the detector. Each pair of flanges is tightly sealed with a copper gasket. The top and bottom gas entrances are equipped with 0.5 μm Swagelok particle filters (SS-4-VCR-2-0.5M) to prevent the powder from escaping the detector. A 50 μm diameter gold-coated tungsten wire (detector anode) was soldered to the SHV connector on the top flange, stretched and glued to the centre of a 3D printed (PLA plastic) ring. This ring was supported by three 200 mm M3 stainless-steel rods evenly distributed across its diameter, fixed on one extremity to the PLA ring and on the other to the top flange. The use of 3D printed materials has shown the potential to offer a fast and cost-effective approach to detector prototyping, particularly in situations in which the outgassing of such materials is counterbalanced by the constant gas renewal of a detector operating in continuous gas flow [136, 137]. When a positive voltage is applied to the anode, an electric field is established inside the proportional counter which can reach values above the threshold for charge multiplication in a small region around the anode wire.

4.3 Operational Properties

The presence of nanoparticles in a gaseous proportional counter may impact its operational properties such as the avalanche gain, energy resolution or energy linearity. Therefore, it is essential to understand how these properties are affected by the presence of the fine powder, which was done by irradiating the detector with soft x-rays from a ^{55}Fe radioactive source, before and after inserting the B_4C microparticles.

The detector used in this work was similar to the one depicted in Fig. 4.12, with the addition of a 10 mm diameter window in its centre, made by a 50 μm thick aluminized Mylar film, glued to the detector with conductive epoxy. As the x-rays emitted by the ^{55}Fe source interact with the argon atoms of the gas by photoelectric effect, the primary electron clouds are accelerated towards the anode by the electric field applied, where in the close proximity of the wire the avalanche multiplication takes place. The resulting charge was collected with a charge sensitive preamplifier (Canberra 2006). The preamplifier signals were fed to a linear amplifier (Ortec 454), which output was connected to a multichannel analyser (MCA).

The proportional gas used was P10 (Ar:CH_4 in 90%:10% proportion), continuously flowing at a rate of 8 l/h. The gas outlet was connected, via a reservoir filled with low outgassing oil, to the atmosphere. The oil not only insulated the detector from the outer atmosphere, but also served as an additional security measure to prevent the microparticles from escaping to the atmosphere, in case they managed to pass through the filters, by sinking them to the bottom of the oil-filled container, since they are much denser than the oil (densities of 2.52 g/cm^3 and 0.88 g/cm^3, respectively).

The detector was irradiated with 5.9 keV x-rays from a ^{55}Fe source while the anode voltage was varied from 2000 V to 2400 V. Pulse height distributions were acquired for each anode voltage during 60 seconds, initially without the microparticles inside the detector and subsequently after depositing 3 grams of the B_4C fine powder in the hollow funnel-shaped part of the bottom flange. The method used for particle dispersion in the gas consisted in violently opening the gas flow for a few seconds and subsequently reducing it to 8 l/h, the rate used during data acquisition.

A comparison of the pulse height distributions recorded for an anode voltage of 2375 V without and with B_4C microparticles in the proportional counter is presented in Fig. 4.13. Along with the data points, a double peak Gaussian fit is shown for each pulse height distribution. The main peak corresponds to the full absorption of the 5.9 keV x-ray in the proportional gas, while the lower amplitude peak corresponds to the Kα-fluorescence escape peak of Ar.

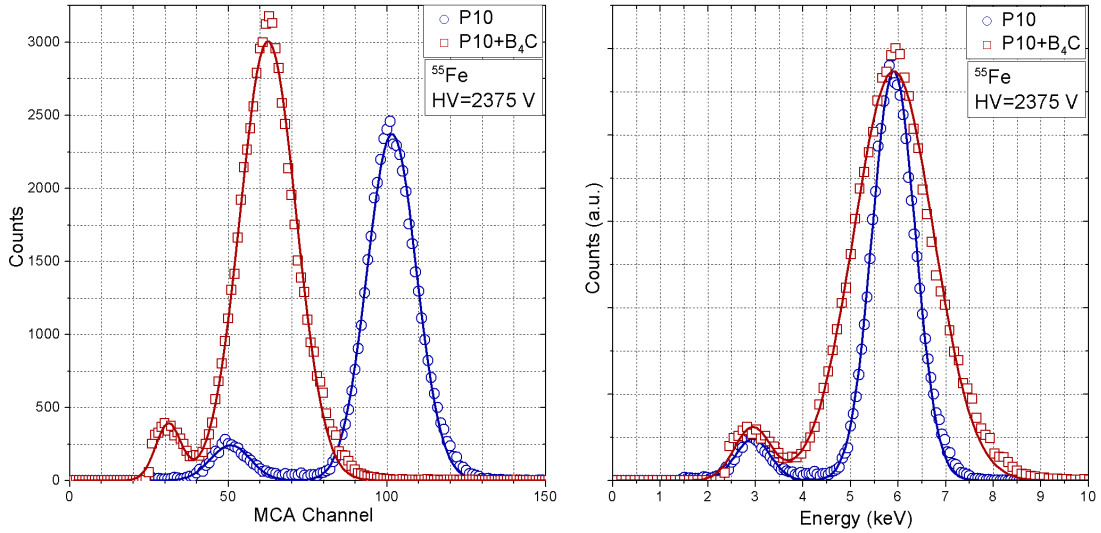

Figure 4.13: Pulse height distributions recorded by irradiation with x-rays from a ^{55}Fe source and an anode voltage of 2375 V without (blue circles) and with (red squares) B_4C fine powder dispersion. Acquisition time = 60 seconds. Left: Unnormalized data. Right: Normalization of P10+B_4C data, to match the counts and the centroid of the Gaussian fit obtained with P10.

The pulse height distribution recorded with the aerosol (P10+B_4C in Fig. 4.13) is shifted to lower energies when compared with the one recorded without B_4C particles. This was verified throughout all the anode voltage range.

In Fig. 4.13-right, the pulse height distribution taken with the B_4C microparticle aerosol was normalized so that its amplitude and centroid match the corresponding parameters extracted from the Gaussian fit applied to the PHS without microparticles. The MCA channel axis was also calibrated to the energy scale. A broadening of the 5.9 keV peak with the fine powder dispersion is clearly visible, which implies an energy resolution degradation. This effect also was observed for the whole range of applied anode voltages.

Fig. 4.14 illustrates the gain obtained with and without B_4C microparticles as a function of anode voltage. A gain drop by a factor of 36%, independent of the anode voltage, is observed in the presence of B_4C microparticles. Fig. 4.14 also shows that this microparticle induced gain drop can be compensated by increasing the anode voltage by

approximately 75 V.

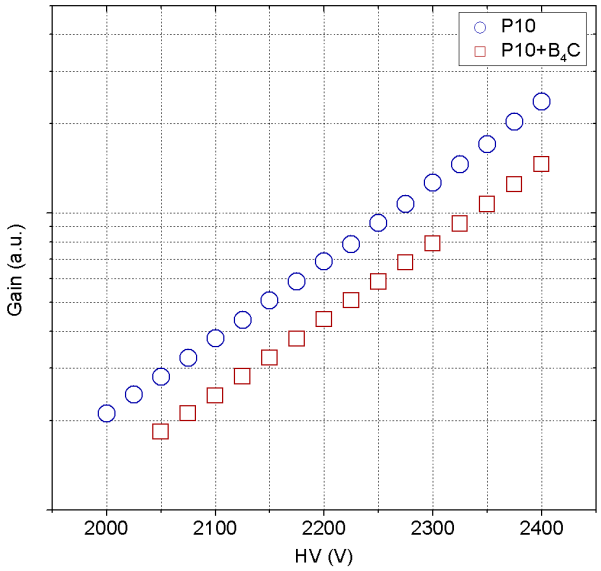

Figure 4.14: Logarithmic plot of the gas gain measured for each anode voltage without (blue circles) and with (red squares) B_4C fine powder dispersion. An average gain decrease by a factor of 36% was observed.

A similar analysis was performed for the energy resolution. The results, depicted in Fig. 4.15, show an average degradation of the energy resolution by 15% (absolute value) in the presence of B_4C microparticles, with little dependence on the applied anode voltage.

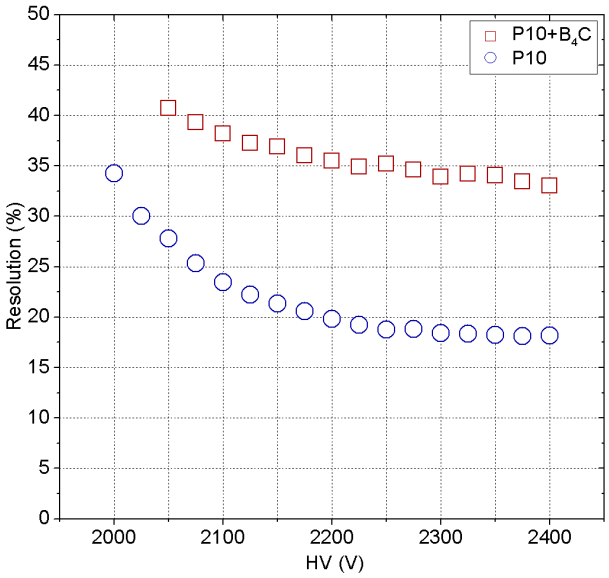

Figure 4.15: Energy resolution of the proportional counter versus applied anode voltage with (red squares) and without (blue circles) B_4C microparticles dispersion. An average energy resolution increase of 15% (absolute value) was observed when dispersing the B_4C.

The intrinsic energy resolution, a statistical limit associated with the minimum amount of fluctuation that will always be present on the detector signal, arising from the discrete

nature of the measured signal itself, was determined for each case. Overlooking electronic noise, which is typically a small contributing factor to the output signal of proportional counters, intrinsic energy resolution can be derived from [8]:

$$R = 2.355\sqrt{\frac{(F+b)}{n_0} + \frac{1}{n_0 M}} \tag{4.10}$$

where n_0 represents the number of primary ion-electron pairs created by the incident radiation, M the average gas gain, F the Fano factor and b the multiplication variance, associated to the relative variance of the number of electrons produced in an avalanche assuming a Polya distribution. The 2.355 factor arises from the ratio between the full width at half maximum (FMWH) of a Gaussian distribution and its standard deviation.

As discussed in section 2.3.3, the number of primary ion-electron pairs generated is proportional to the energy deposited by the incident radiation, E_i, and the proportionality constant between them is given by w, the mean energy required to form one ion-electron pair ($n_0 = E_i/w$).

The intrinsic energy resolution can be experimentally determined by considering the proportionality between the centroids of the 5.9 keV peaks in the pulse height distributions (A) and the detector gain (M):

$$A \propto n_0 M \implies A = n_0 M K_{el} \tag{4.11}$$

where K_{el} is a constant exclusively dependent on the electronics chain detector readout. After these replacements, we can rewrite equation (4.10) as:

$$R = 2.355 \times \sqrt{\frac{w(F+b)}{E_i} + \frac{K_e}{A}} \implies R^2 = 5.545 K_{el}\frac{1}{A} + 5.545\frac{w(F+b)}{E_i} \tag{4.12}$$

From equation (4.12), one can see that if, for the same incident energy (E_i), A is varied throughout a set of acquisitions (accomplished by varying the anode voltage), a linear relation between R^2 and $1/A$ is expected. Thus, a plot of R^2 versus $1/A$ is a reasonable approximation to extrapolate the intrinsic resolution of the detector, corresponding to the value of R^2 when $(1/A) \to 0$, i.e., the y-intercept of the function:

$$R_{\text{int}} = 2.355\sqrt{\frac{w(F+b)}{E_i}} \tag{4.13}$$

Since parameters w, F and b depend exclusively on the filling gas/aerosol, a variation of the $w(F+b)$ factor in the presence of the B_4C microparticles can be expected and therefore a variation of the intrinsic energy resolution as well.

Data in Figs. 4.14 and 4.15 was processed according to the described method and the results are presented in Fig. 4.16. The intrinsic energy resolution (R_{int}) obtained when the detector was filled with P10 gas was of 15%, increasing with the microparticles dispersion to 32%. Only the linear region of each R^2 versus $1/A$ curve, limited by the vertical dashed lines in Fig. 4.16, was considered for the fitting. This was because the effects that cause loss of linearity are not contemplated in equation (4.12), namely fluctuations in the number of primary electrons reaching the avalanche region for low voltages and fluctuations in the electric field due to the spatial positive charge accumulated for high

voltages. As expected, the linear portions of the curves are almost parallel, since the slope determined by K_{el} is similar for both cases.

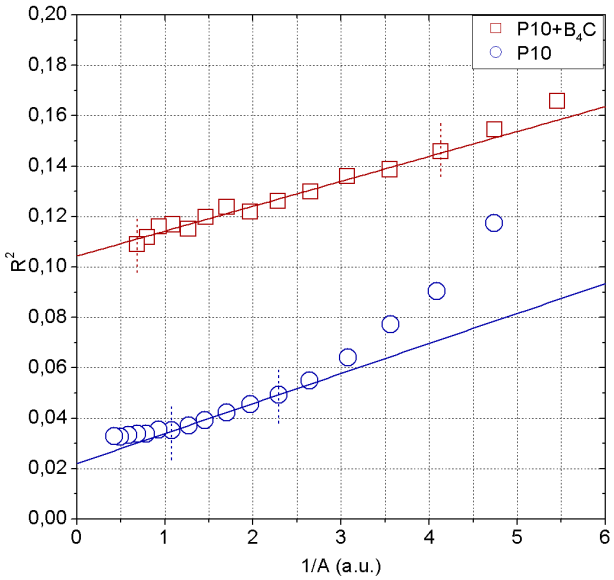

Figure 4.16: Square of the energy resolution versus 1/A without (blue circles) and with (red squares) B_4C fine powder dispersion. The extrapolated intrinsic energy resolution values are 15% and 32%, respectively.

One significant concern regarding this detection concept was that dispersing fine powder in a proportional counter could lead to the occurrence of electrical discharges, compromising its operation. However, the presence of the fine powder did not severely affect the proportional counter by causing discharges or other electrical instabilities during acquisition using soft x-rays.

The microparticles affected however the proportional counter performance, influencing the achievable charge gain and energy resolution. Despite the observed charge gain reduction, the 5.9 keV peak still exhibits a symmetric Gaussian shape 4.13. This indicates that the gain drop is not due to the absorption of primary or secondary electrons by the microparticles. If that were the case, a tail at lower energies would be present on the pulse height distribution as the number of captured electrons would depend on the distance travelled: the size of the electron cloud that reaches the multiplication region in the close proximity of the anode to be amplified would depend on the distance travelled in the aerosol. Interactions near the detector walls would result in smaller primary electron clouds reaching the multiplication region near the anode and give rise to pulses with lower amplitude. Consequently, a low-energy tail would be expected in the pulse height distribution. However, the presence of the microparticles did not cause this effect, but rather a symmetric broadening of the peak.

An analysis of the intrinsic resolution without and with microparticle dispersion provides an insight on the reasons behind the degradation of these parameters. From equation (4.13) we conclude the factor $w(F+b)$ has increased by a factor of 4.8 with the inclusion of the microparticles:

$$\frac{w_{\text{aerosol}}(F+b)_{\text{aerosol}}}{w_{\text{P10}}(F+b)_{\text{P10}}} \tag{4.14}$$

An increase in w due to the inclusion of microparticles is excluded by a pulse height distribution analysis: the discrete nature of the microparticles would cause any process induced by their presence to be also of non-continuous nature, affecting each event according to its degree of interaction with the microparticle. This would create changes in the pulse height distributions, most notably a tail for low energies on the 5.9 keV peak, which was not present in Fig. 4.13. Therefore, we conclude that the increase in the $w(F + b)$ factor is due to an increase in the avalanche gain fluctuations $(F + b)$, consequence of the electric field distortion in the regions near the microparticles.

4.4 Electric Field Simulations

To understand how the presence of B_4C microparticles in a P10 filled proportional counter affects its electrostatic field, computer simulations were developed using COMSOL, a multiphysics simulation software based on finite element method for the numerical modelling of physical systems [138]. For this simulation, the Electrostatics interface of the AC/DC module was used.

The magnitude of the electrical field (E) and electric potential (V) in a cylindrical proportional counter, as a function of the distance to centre of the detector (r) are respectively given by:

$$E(r) = \frac{\mathrm{HV}}{r \ln(\frac{c}{a})} \tag{4.15}$$

$$V(r) = \mathrm{HV}\left(1 - \frac{\ln(\frac{r}{a})}{\ln(\frac{c}{a})}\right) \tag{4.16}$$

where HV is the voltage applied to the anode (considering the cathode walls at ground potential), a the anode radius and c the cathode inner radius. According to the detector used in the soft x-ray irradiation measurements, $a = 25$ μm and $c = 24$ mm were specified. Although the anode voltage was varied throughout measurements with the ^{55}Fe source, the drop in charge gain and increase in energy resolution verified after the insertion of the fine powder was relatively independent of this parameter. For the simulation, the value HV = 2000 V was selected, but the conclusions can, in principle, be generalized for any voltage in the proportional region of operation.

Good energy resolution in a proportional counter is critically dependent on ensuring that each primary electron formed in an original ionization event is multiplied by the same factor in the gas multiplication process. The multiplication region in a proportional counter is limited to a small fraction of the detector volume, near the anode. It is in this region that the uniformity of the electric field plays a crucial role in the achievable energy resolution. When adding the B_4C microparticles inside the detector, the fraction of microparticles that have an expressive impact on the energy resolution of the detector are the ones situated in the multiplication region, including those that might be attached to the anode. For this reason, and to ease the computational requirements, in the simulations carried out, only the multiplication region of the detector was considered. This volume is dependent on the gas parameter K, which quantifies the minimum value of the electric field below which the avalanche multiplication of charges cannot occur and has a value of $K = 4.8 \times 10^6$ V/m for P10 at 1 atm [8].

From equation (4.15), we can deduce the distance from the centre of the detector in which the electric field is superior to K (Fig. 4.17-left). The multiplication region of the proportional counter with the considered parameters extends to 60 μm from the central axis of the detector (or 35 μm from the anode surface). At this distance, the electric potential can be obtained from equation (4.16), yielding 1745 V (Fig. 4.17-right).

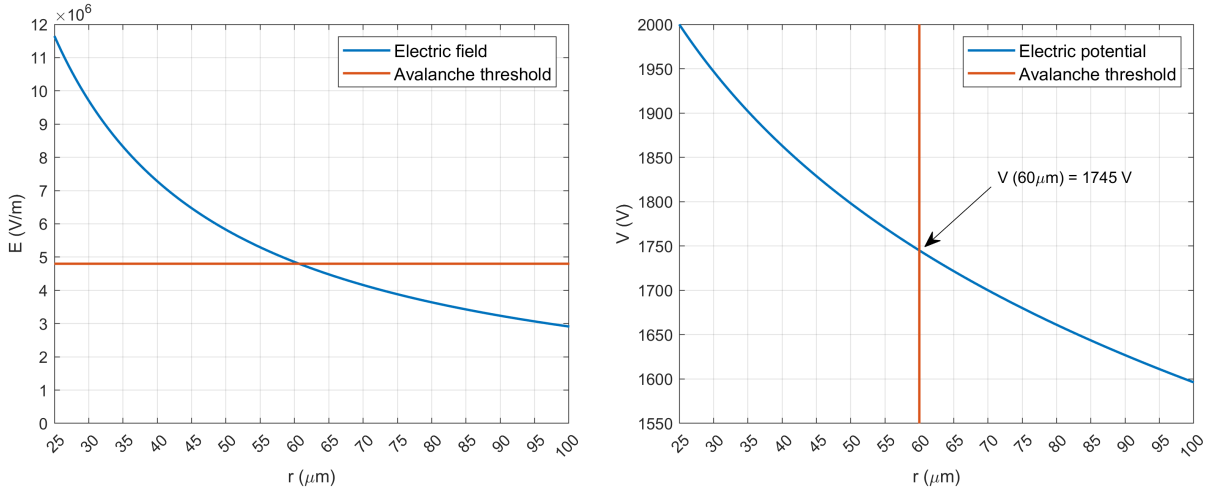

Figure 4.17: Left: Plot of the electrical field magnitude as a function of the distance to the anode (blue) and electric field value ($K = 4.8 \times 10^6$ V/m) below which charge multiplication cannot occur (red). Right: Plot of the electrical field magnitude as a function of the distance to the anode (blue) and distance that limits the avalanche multiplication region (red). The detector parameters considered were $a = 25$ μm, $c = 24$ mm, HV = 2000 V and $p = 1$ atm.

The geometry implemented in the computer simulations consists of a hollow cylinder with inner radius 25 μm with a voltage of 2000 V on its surface (anode limit), and an outer radius of 60 μm at 1745 V potential (multiplication region limit). Since due to the symmetry along the z-axis, and not considering the edges of the proportional counter, the detector height is irrelevant and was arbitrarily defined as 35 μm. On a plane parallel to the anode, 100 sphere-like B_4C particles (defined from the COMSOL material database) with 1 μm diameter were placed, uniformly distributed in a 10×10 array.

Fig. 4.18 shows the simulation result, plotting the electric field magnitude in a 2D colour plot for every point of the multiplication region. A fluctuation of the electric field magnitude is observed in the surroundings of the microparticles. In these regions, the electric field is higher in the axis perpendicular to the anode, and lower in the axis parallel to it. This effect becomes more evident for the microparticles closer to the anode, with the highest magnitudes of the electric field being achieved for the particles attached to it.

The results of the simulations indicate local electric field variations in the avalanche multiplication region due to the presence of B_4C microparticles. This leads to fluctuations in the avalanche charge multiplications which may explain the gain decrease and energy resolution increase verified after inserting the fine powder in the detector.

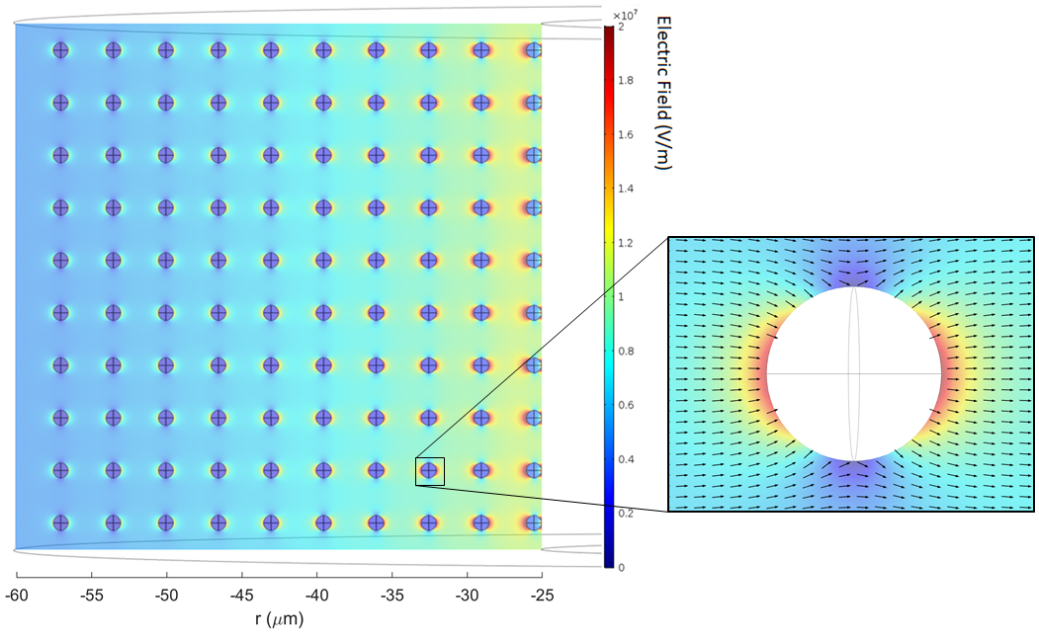

Figure 4.18: Left: B_4C particle distribution across the multiplication region of the detector defined in the simulation and 2D colour plot of the magnitude of the electric field. Right: Close-up look of the electric field fluctuation in the surroundings of a microparticle. The black arrows indicate the direction of the electric field at some points.

4.5 Particle Dispersion Optimization

One fundamental aspect for the feasibility of the aerosol detector is to ensure that the B_4C microparticles are homogeneously and continuously suspended in the gas volume during long operation periods. If the microparticles aggregate to each other, forming larger groups of particles, or if they attach to the inner walls, a contribution to the wall-effect in the pulse height distribution of the detector is expected, since the two secondary particles from the ^{10}B neutron capture reaction will no longer be able to simultaneously reach the proportional gas.

On a proportional counter operating in continuous flow, the gas is constantly flowing from one (or multiple) gas inlets to one (or multiple) gas outlets. This was the initially selected gas circulation mode with the aerosol detector, using the bottom entrance as the gas inlet and the top one as outlet. However, after some time with the gas continuously flowing, a large number of particles agglomerate on the top outlet. This clogging effect was experimentally observed, and is portrayed in Fig. 4.19, where a photograph of the gas outlet of a smaller size (36 mm internal diameter) prototype of the aerosol detector is presented.

One strategy to prevent this effect and increase the number of particles in the active detection volume for longer periods is to periodically invert the gas admittance and exhaust via the detector top and bottom gas connections, and thus alternating the direction of the gas flow inside the detector. This can be accomplished by using two solenoid valves, each one connected to one of the gas connections, as represented on the simplified detector scheme of Fig. 4.20. By using a pair of 3-port solenoid valves and connecting the appropriate ports of each one to the gas bottle, the bottom/top gas entrances and the exhaust to the atmosphere, the alternation between a gas flow from

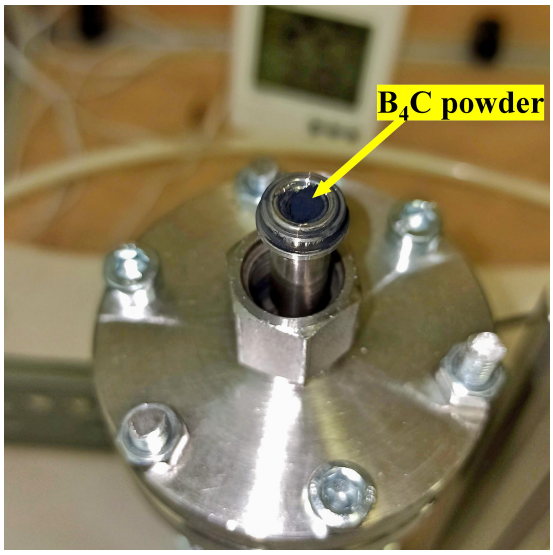

Figure 4.19: Effect of the agglomeration of B_4C microparticles on the top outlet that occurs when the gas is continuously flowing from the bottom inlet to the top inlet after a some time.

the bottom to the top (Fig. 4.20-left) and from the top to the bottom (Fig. 4.20-right) of the detector can be achieved as a function of a voltage signal supplied to each valve.

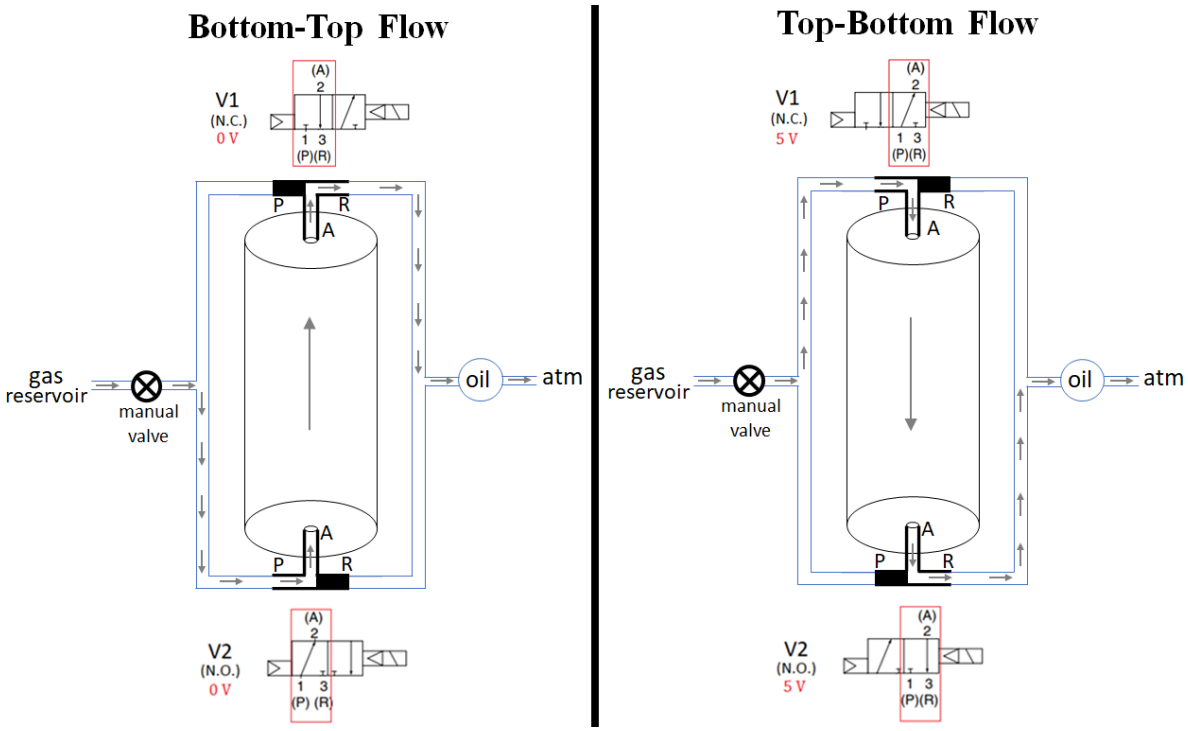

Figure 4.20: Gas circulation scheme and valve operation diagram of the solenoid valves system constituted by a pair of 3-port solenoid valves, with a normally closed valve on the top gas entrance (V1) and a normally open valve on the bottom (V2). The green arrows symbolize the direction of the gas flow.

This system was implemented using a normally closed valve (SMC SYJ314-SGE-M5) connected to the top gas entrance, designated Valve (V1), and a normally open valve

(SMC SYJ324-SGE-M5) connected to the bottom gas entrance, designated Valve 2 (V2). These have a recommended operating pressure range between 1.5 bar and 7 bar [139], although it was experimentally verified that providing a pressure of 1.2 bar was sufficient for proper functioning. They operate at a low voltage of 5 V, and can be fed and controlled by a microcontroller. For this purpose, an Arduino Uno board was used [140]. The port connections were arranged in such way that when no voltage was applied to the valves, a conventional gas circulation from the bottom to the top of the detector occurred. In contrast, when a 5 V voltage signal was sent to both valves, the direction of the gas flow is reversed, flowing from the top to the bottom of the detector. A photograph of the valves system is presented in Fig. 4.21.

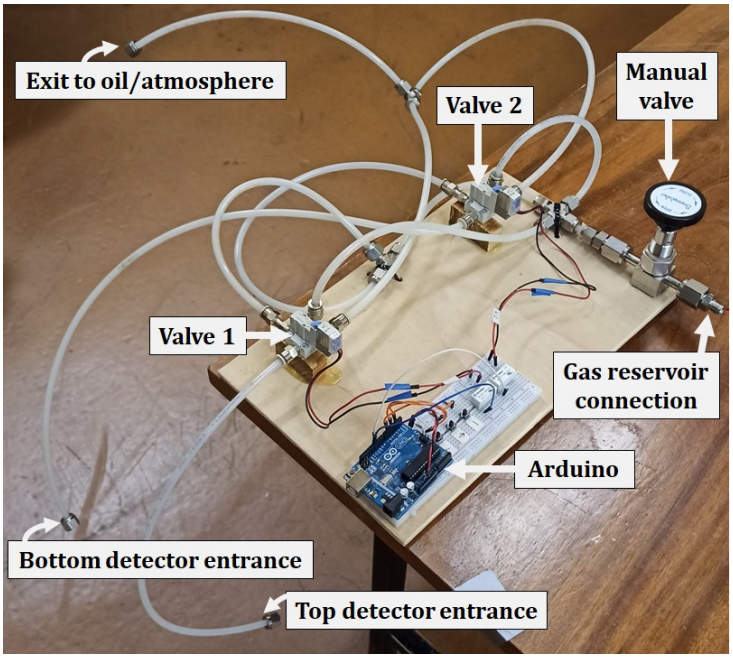

Figure 4.21: Photograph of the valves system used to alternate the flow direction of the aerosol detector, with the identification of each element.

The particle filters, which consist of porous 1/4 inch circular stainless-steel gaskets, are compressed between the Swagelok fittings of the detector entrances and the tubing that carries the gas from the bottle to the exhaust. It was verified that after a long period of a unidirectional gas circulation on the detector, the top particle filter agglomerates a vast amount of fine powder particles, eventually becoming saturated. This compromises not only the continuous and homogeneous dispersion of the particles, but also the ability for the gas itself to flow. Fig. 4.22-left, shows a photograph of a particle filter taken after detaching it from the top gas entrance, after 30 seconds of operation with the gas flowing from the bottom inlet to the top outlet. The use of solenoid valves to alternate the direction of the gas flow proved to be effective in the removal of the fine powder from the particle filters. After taking the photograph of Fig. 4.22-left, the filter was placed again in the top inlet with the same orientation (the side with particles facing down towards the detector). The direction of the gas flow was then reversed using the solenoid valves, and a new gas circulation took place, this time entering from the top inlet and exiting through the bottom outlet, for another 30 seconds. After this, the particle filter was again detached and a new photograph was taken, presented in Fig. 4.22-right, showing a visible improvement in the removal of the previously attached microparticles. Consequently, it

can be concluded that the use of solenoid valves is important to prevent the obstruction of the gas flow by the fine powder saturation of the particle filters.

Figure 4.22: Left: Photograph of the particle filter taken after detaching it from the top gas entrance, after 30 seconds of operation with the gas flowing from the bottom to the top entrances of the detector. Right: Photograph of the same particle filter after being placed in the same location and orientation, after an additional 30 seconds of gas circulation in the inverse direction.

COMSOL simulations of the gas flow inside the detector were developed to gain some insights on the behaviour of the microparticles as they are suspended by the gas, and to optimize the working parameters of the solenoid valves, namely the periodicity to reverse the direction of the flow. The central aspects to study were the average time it took for the particles to travel from the bottom inlet to the top outlet and which portion of them would get attached to the walls along this journey.

The simulation was implemented in two stages, first simulating the gas flow according to the defined geometry and parameters, and secondly simulating the motion of B_4C microparticles as they are dragged by the previously computed gas flow. For the first stage, the Fluid Flow interface from the Computational Fluid Dynamics module of COMSOL was used, while for the second stage the Particle Tracing module was used. A 3D geometry of a gaseous volume with the same dimensions as the aerosol detector shown in Fig. 4.12 was implemented, filled with argon at room temperature and atmospheric pressure, as defined by the properties inbuilt in the COMSOL material library.

Besides the gas properties, the flow rate at the inlet and the boundary conditions at the outlet must be specified. A rate of 8 l/h at the inlet was defined, in accordance with the study of the operational properties of the detector presented in section 4.3. The outlet condition consisted of fixing an atmospheric pressure at the outlet.

Beyond these parameters, the type of flow (laminate or turbulent) to simulate must also be selected by the user. To predict this, calculations of the Reynolds number (R_e) were performed. This is the variable used to determine the type of a fluid flow, distinguishing between laminar, transitional and turbulent flow depending on its value defined as [141]:

$$R_e = \frac{\rho v L}{\mu} \tag{4.17}$$

where L is the characteristic length of the flow, ρ and μ are respectively the fluid density and dynamic viscosity, and v its average speed. For circular pipes, in which the length of the pipe is much larger than its diameter, the characteristic length is taken as

its inner diameter. The speed of a fluid flowing through a circular pipe of diameter (D) can be related to its volumetric flow rate (Q) by:

$$v = \frac{4Q}{\pi D^2} \tag{4.18}$$

We can then rewrite equation (4.17) as:

$$R_e = \frac{4Q\rho}{\pi \mu D} \tag{4.19}$$

A fluid flow is defined as laminar when $R_e < 2100$, turbulent when $R_e > 4000$ and transitional when $2100 \leq R_e \leq 4000$ [141]. Considering a flow rate $Q = 8$ l/h, an inlet diameter of $D = 4.57$ mm and the properties of argon at room temperature ($\rho = 1.62$ Kg/m^3 and $\mu = 2.13 \times 10^{-5}$ Kg/m·s), the yielded value of the Reynolds number is $R_e = 47$, which is substantially low, belonging to the laminar flow region. Looking at equation (4.19) we can conclude that in the centre of the tube, where the diameter is superior to the inlet diameter, the Reynolds number would be even lower, and consequently the flow is granted to be laminar throughout the whole volume of the detector.

Attending to these calculations, a laminar flow was defined in the COMSOL simulation. The gas velocity profile calculated is presented in Fig. 4.23, considering the bottom gas entrance as the inlet and the top one as the outlet. This figure consists of a 2D colour plot of the magnitude of the velocity of the gas flow in the central section of the volume defined, represented in logarithmic scale to enhance the contrast. The gas velocity is greater in the inlet and outlet of the detector, due to the smaller diameter. Although there is some convection motion in the cone–shaped region of the detector near the bottom inlet, the gas velocity is uniform along the height of the detector cylinder, up until approaching the top region, where the velocity vector funnels in the direction of the outlet, as represented by the black arrows of Fig. 4.23. The gas velocity is slightly superior at the centre of the detector than near the walls.

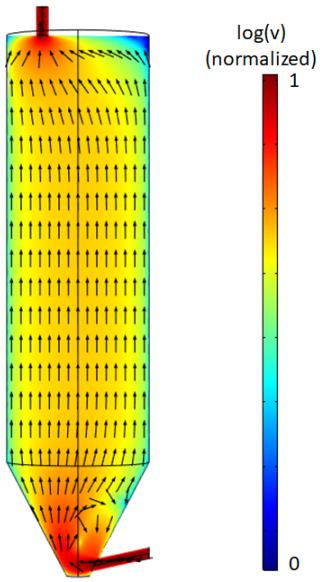

Figure 4.23: 2D colour plot (in logarithmic scale) of the magnitude of the velocity of the gas flow in the central section of the volume defined. The black arrows indicate the 2D projection of the direction of the velocity vector for some discrete points.

With the velocity profile of the gas flow calculated, the second stage of the simulation was implemented, focusing on tracing the motion of B_4C particles suspended by the gas flow. A total of 10^4 particles were defined, with a diameter of 1 μm and the density of boron carbide (2.52 g/cm^3). The number of particles selected was limited by the computational effort required by the simulation, and consequently the time it took for each simulation to run. However, the quantity defined is sufficient to provide enough statistics for an accurate insight of the particles dispersion behaviour. The forces considered to act on the particles were gravity and the drag force linked to the velocity profile of the gas. Because it was intended to analyse the preponderance of the particle attachment to the detector walls, it was established that for every particle coming in contact with the walls, they would get attached with a probability of 100%. Although this is an exaggerated scenario, it is the most useful for statistical purposes to find the percentage of particles that collide with the walls through time.

The simulation output showing the evolution of the motion of the B_4C particles as a function of time is presented in the time-lapse of Fig. 4.24-left, showing three instants corresponding to the initial moments of the dispersion, the moment when particles reach approximately half of the detector height, and the final instant of the simulation, in which some of the particles had already reached the outlet.

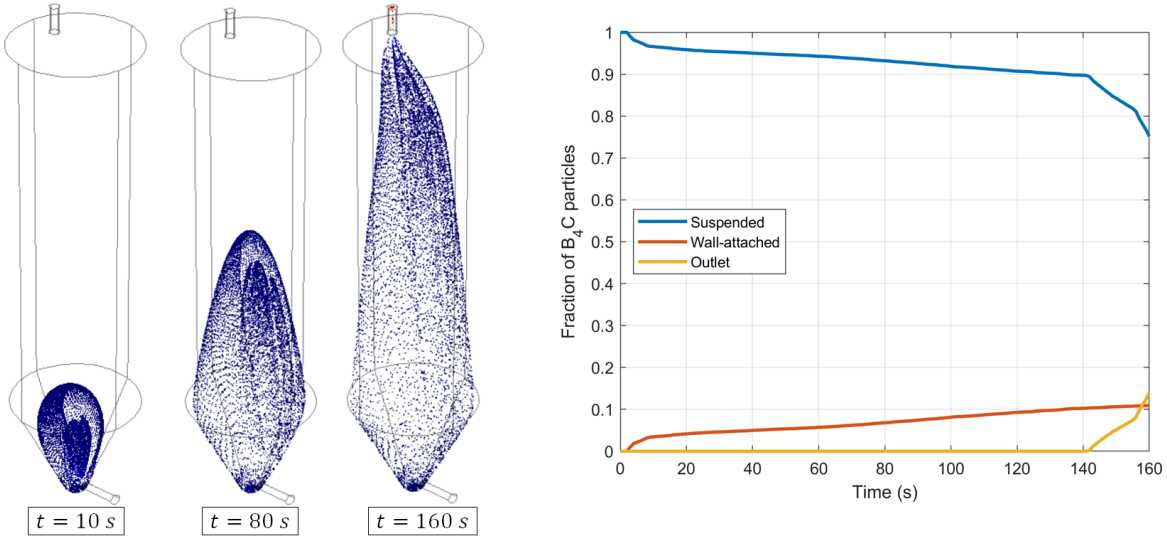

Figure 4.24: Left: Time-lapse of the motion of the B_4C particles suspended by the gas flow. Right: Plot of the fraction of particles that are suspended, attached to the walls and that have reached the outlet as a function of time.

In accordance with the fluid velocity profile of Fig. 4.23, it was verified that the velocity of the particles is higher in the first instants of the dispersion, while they are leaving the bottom cone-shaped disperser. As they travel through the cylindrical portion of the detector their velocity decreases, rising again when they reach the proximity of the top outlet. Because the gas velocity is superior in the centre of the detector cylinder than near the walls, the maximum height of the particle cloud is located in the central region. The concentration of particles is also superior in the central region than near the walls of the detector, although this effect is attenuated throughout time as the particles travel towards the outlet. Finally, it was verified that the fraction of particles attaching to the walls is higher on the bottom of the detector and progressively decreases along its vertical dimension.

Fig. 4.24-right shows the plot of the fraction of particles that are suspended, attached to the walls and that have reached the outlet as a function of time. From these results, it is expected that the wall attachment of the microparticles increases at a steady rate. By the time the first particles reach the outlet, approximately 10% of the initial amount are attached to the wall. However, the attachment probability upon a particle-wall interaction was defined as 100%, which is an exaggerated assumption. In a real scenario, particles would also be able to bounce off the walls, and consequently the realistic attachment fraction would be inferior. One aspect that stands out is the wide time-scale, with the simulation results indicating that it would take 140 seconds for the particles to reach the outlet, which might not meet the initial intuition. However, this can be explained by the low velocity of the gas flowing in the detector: from equation (4.18), the gas velocity in the cylindrical section of the detector for the considered flow rate of $Q = 8$ l/h is only of $v = 1.2$ mm/s. Naturally, this time interval is prone to a considerable uncertainty and should not be taken as a reliable prediction, but rather as a magnitude reference. The dispersion of a fine powder by a gas flow is a chaotic process, for which computer simulations have only a limited capability to realistically reproduce. In fact, just to be able to implement the COMSOL simulations for particle tracing, a set of crude simplifications had to be considered, such as a constant gas flow rate, a small number of B_4C particles with equal dimension and perfect spherical shape, their initial position in the simulation, and the fact that particle-particle interactions were not considered, neglecting the effects of particle agglomeration.

Recognizing the limitations of a simulation approach to study the behaviour of the B_4C particles inside the detector, an additional strategy was used, which consisted of building a simplified version of the aerosol detector with transparent acrylic walls, to see the dispersion of the particles and how it varies for different settings of gas pressure, flow rate and timings of the solenoid valves. This detector replica, depicted in Fig. 4.25, consisted of a 200 mm height and 36 mm internal diameter acrylic tube, attached to a top CF 43 flange with a gas entrance on its centre and to an identical CF 43 flange on the bottom, connected to a cone-shaped particle disperser.

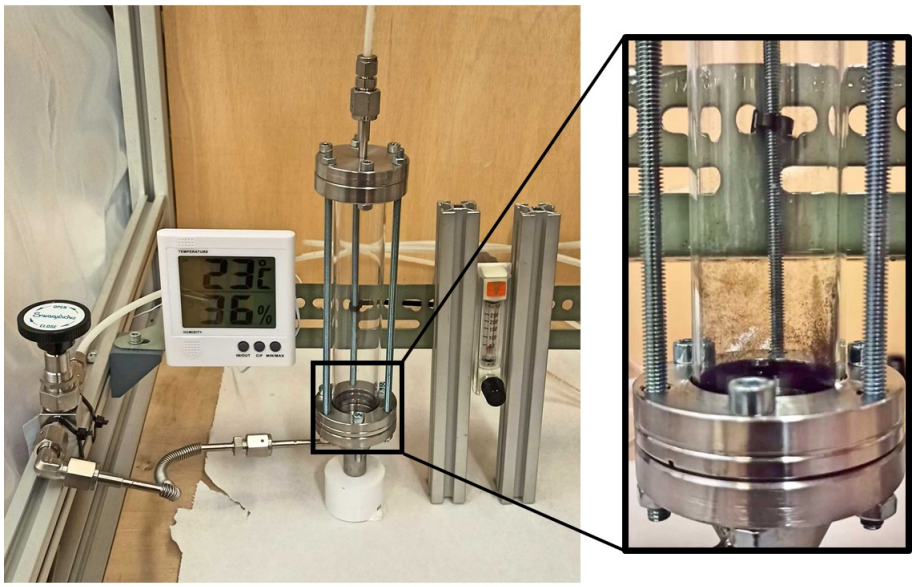

Figure 4.25: Experimental setup of the particle dispersion tests with the replica of the aerosol detector with transparent acrylic walls.

Three M3 rods connecting top and bottom flanges exerted pressure on the acrylic tube against two Viton o-rings (one at the bottom and the other at the top flange junctions) to seal the apparatus. Because the purpose of this test was simply to see the dispersion of the particles, and not having an operational detector, the electrical components of the detector (anode and feedthrough) were not installed.

The solenoid valves system previously described was connected to the bottom and top gas entrances, and to a P10 gas bottle. A flow meter was used to control and measure the flow rate of the gas. Several dispersion tests were carried, for flow rates between 3 l/h and 15 l/h, and for different operation times of the solenoid valves, ranging from 5 to 60 seconds, in search of the optimal conditions for continuous and homogeneous particle dispersion for long time periods.

Although higher flow rates (~ 15 l/h) led to a greater amount of particles in suspension, it was verified that the dispersion of the powder is generally very inefficient: only a small fraction of particles are actually suspended, while the vast majority remains deposited in the dispersion cone.

When the gas is flowing from the bottom to the top gas entrances, for the first dispersions, it is possible to see particles in suspension for at least the initial 30 seconds, approximately. However, after some additional time, this was no longer the case. Nonetheless, it is important to keep in mind that the human eye can only see the macroscopic particles, which are formed by the agglomeration of micrometric particles. Therefore, it is possible that smaller particles, with diameter around the previously measured mean value of 1 μm, can be in suspension for longer time periods. The motion of the visible particles during this time frame consisted of an upwards trajectory in a relatively straight line, and at approximately constant speed, which is in agreement with what was computed by the COMSOL simulations.

It was confirmed that inverting the direction of the gas flow using the solenoid valves was effective to remove the particles clogging and saturating the top gas entrance and particle filter: the moment that the gas flow direction was inverted, an abrupt ejection of particles from this region was observed.

Overall, after multiple particle dispersion tests under different settings, it was determined that the optimal valves system operation conditions to maximize the number of particles suspended over long time periods consisted of having a bottom-top gas flow for approximately 30 seconds, inverting then to a top-bottom flow for approximately 5 seconds. The duration of the latter flow orientation is significantly smaller because it is exclusively meant to remove the agglomerated particles constricting the top gas entrance and particle filter. After achieving this, there is no point in maintaining a top-bottom flow, since the suspension of the particles must be achieved by a drag force associated with a velocity profile pointing upwards, to counteract the gravity force acting on the particles. Naturally, these values arise from a qualitative observation with limited capabilities and therefore should be interpreted as suggestive values.

An important observation that was made is the fact that after several cycles of alternation of the gas flow direction, the quantity of suspended particles progressively decreases. Two factors contribute to this: the increase of the number of particles that attach to the wall, leaving less available to be suspended, and the fact that the gas tends to create a passage in the cone-shaped disperser by moving the deposited particles to the side, originating a path of least resistance which the gas will preferentially follow, dragging along a minimal amount of particles. This is a critical limitation for the operation of the aerosol detector for long time periods under stable and equal conditions, which can only

be resolved by introducing major changes in the strategy to disperse the fine powder.

Finally, it was observed that the attachment of the fine powder to the detector walls is considerably greater in the bottom portion of the acrylic tube, as depicted in Fig. 4.25-right, which is in agreement with the COMSOL simulation results.

4.6 Reducing Particle Attachment

The detector performance is compromised by the attachment of the B_4C fine particles to its inner stainless-steel walls. The contribution to the detector response from neutron captures occurring in particles in contact with the wall is analogous to that of boron lined detectors, consisting of a two-step plateau due to the wall-effect. Thus, to optimize the performance of the aerosol detector and extend the PHS to a higher energy range, it is fundamental to minimize the attachment of fine particles to its inner walls.

To achieve this, the effect of surface polishing in the attachment of B_4C microparticles to stainless-steel was investigated through image analysis of particles deposited on several samples, with different degrees of surface polishing, after dispersing the B_4C fine powder in controlled and identical conditions.

4.6.1 Surface Smoothness and Particle Attachment

The three main forces involved in the adhesion between particles and surfaces are the London-van der Waals force, the electrostatic force and the capillary force. The force of van der Waals is caused by the instantaneous dipoles induced in the neighbouring materials. The electrostatic force is the electric force between two charged bodies at rest. Particles carry some electric charge with them, and at low humidity they retain that charge, which is attracted by the charges of insulating and conductive surfaces. If enough moisture exists in the air, condensation can occur, and the capillary force becomes relevant, governed by the surface tension and the radius of the particle [142]. The London-van der Waals force is the dominant force in the particle-surface adhesion when the particle size is less than 50 μm, one order of magnitude higher than the electrostatic force. Contrarily, when the particle size is higher than 50 μm, it was verified that the electrostatic force has preponderance. On the other hand, the environmental humidity can lead to the condensation of the air between particles and the substrate, giving rise to very large capillary forces, increasing the total adhesion force. At relative humidity above 70% the capillary force is the dominant force [142, 143].

To experimentally measure the resulting particle-surface interaction forces, particle detachment studies have been performed, mainly based on the colloidal probe technique (using an atomic force microscope) [144–146], on centrifugal techniques [143, 147–149], and on airflow methods [150, 151]. Other techniques appeared, relying on inertial forces to measure the particle detachment from a surface using a Hopkinson bar system [152], or using vibrational methods [153].

To study the adhesion behaviour of the B_4C fine powder on the detector walls, and how it might be influenced by the surface roughness, the attachment of the powder to stainless-steel samples with different asperities was measured, using a gas flow to disperse the particles. Since the ratio between particle size and surface roughness plays an important role in the particle adhesion-removal balancing [154, 155], it is expectable to observe a change in the attachment of microparticles to stainless-steel surfaces by changing the

sharpness of the irregularities in the surface through polishing.

4.6.2 Polishing Effect on Static Friction Coefficient

To correlate the B_4C fine powder attachment to stainless-steel with the surface polishing, seven stainless-steel (316L) cylinders with 25 mm diameter and 7 mm height were machined. For each sample, one of its surfaces was manually polished with sandpaper of different grits: P120, P360, P500, P1200, P2000, P3000, and P6000, according to FEPA (Federation of European Producers of Abrasives) grit standard [156]. The polishing process was progressive: each sample was first polished with the most abrasive sandpaper and then with gradually less abrasive sandpapers, until the desired polishing was reached.

To quantify the surface smoothness achieved after polishing, the static friction coefficient relative to a reference material was determined of each sample . Friction force arises from the contact established between two surfaces. Although at a macroscopic scale it appears that when two smooth objects are touching this contact is distributed over their whole length, that is not the case from a microscopic perspective. In fact, contact is made only over an aggregate of tiny areas where the peaks of each body interlock, arising from the asperity that is inherent to every surface (Fig. 4.26). Because the microscopic peaks and valleys of a smoother surface are less accentuated than those of a rougher one, friction acting on it (relative to the same reference surface) is smaller.

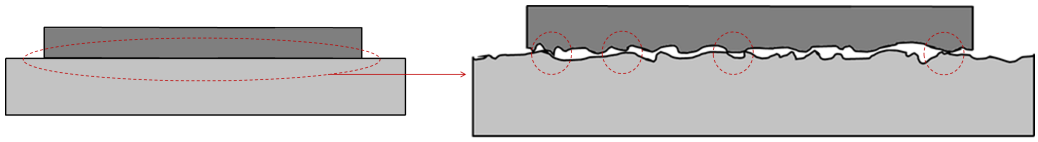

Figure 4.26: Left: Apparent (macroscopic) contact area between two surfaces. Right: Real (microscopic) contact area between two surfaces.

The motivation for this study is based on the assumption that the fine particles are prone to be captured by the microscopic peaks and valleys of a surface when coming in contact and get trapped. Hence, reducing the sharpness of these irregularities by surface polishing is expected to reduce the attachment of these particles.

Static friction force (F_s) between two objects is defined as:

$$F_s \leq \mu_s N \tag{4.20}$$

where N is the magnitude of the normal force exerted by one object on the other and μ_s a dimensionless constant defined as the coefficient of static friction. When the surfaces are on the verge of slipping (scenario depicted in Fig. 4.27), F_s reaches its maximum value and the equality of equation (1) is achieved:

$$F_s = \mu_s N \tag{4.21}$$

When solving the force diagram of Fig. 4.27 for the y and x-axis assuming a state of equilibrium, and consequently a null resultant force, we get:

$$\begin{cases} N = W_y = W\cos(\theta) \\ F_s = W_x = W\sin(\theta) \end{cases} \tag{4.22}$$

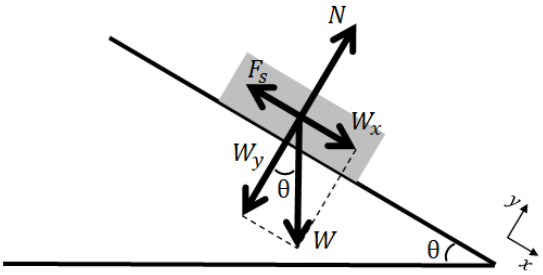

Figure 4.27: Force diagram of an object in an inclined plane. F_s is the static friction force, N the normal force acting on the top object, and W its weight, divided into its components W_x and W_y. For simplicity, F_s was represented with its origin in the centre of mass of the moving body, but in precision it acts on the touching surfaces of the two bodies.

Replacing the terms of equations (2) and (3) in equation (2) we finally obtain:

$$W\sin(\theta) = \mu_s W\cos(\theta) \iff \mu_s = \frac{\sin(\theta)}{\cos(\theta)} \iff \mu_s = \tan(\theta) \tag{4.23}$$

Thus, the static friction coefficient between two objects can be calculated by measuring the inclination angle θ when the forces that act upon the sliding object are balanced, which happens in the limit immediately before the top object starts sliding.

A setup was built to measure this angle, placing each polished stainless-steel sample on top of a Teflon surface and tilting it until the sliding motion was observed (Fig. 4.28).

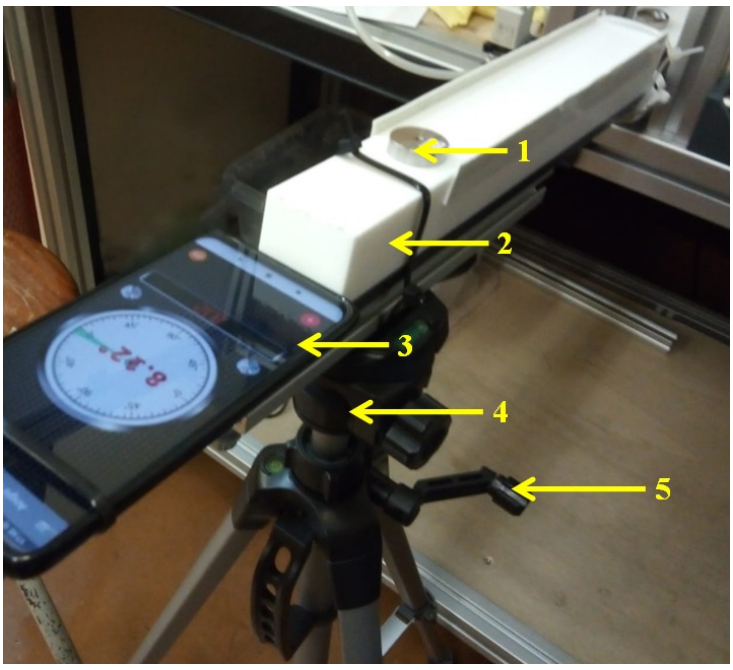

Figure 4.28: Apparatus used for the friction coefficient determination. Legend: 1 – Stainless-steel sample with the polished surface facing down; 2 – Teflon surface; 3 – Gyroscope sensor for angle measurement; 4 – Tripod; 5 – Handle to gradually increase inclination angle.

Teflon was selected as reference material because it has a very low static friction

coefficient ($\mu_s = 0.04$ for Teflon on Teflon [157]), minimizing the contribution of this surface to the variation of the sliding angle and consequently enhancing the dependence of this variable on the roughness of the stainless-steel samples. A tripod with adjustable height was attached to one edge of the Teflon surface, while the other was fixed. Starting from the horizontal position ($\theta = 0°$), the inclination angle was progressively increased and continuously monitored with a gyroscope sensor. The increase of the tripod height was performed manually at a very slow speed, to reduce the error in angle measurement. As soon as the sample started sliding, the respective angle was registered. For each sample, 16 measurements were carried out and averaged.

The static friction coefficients, taken from equation (4.23), are plotted against the sandpaper grit size of the respective sample in Fig. 4.29.

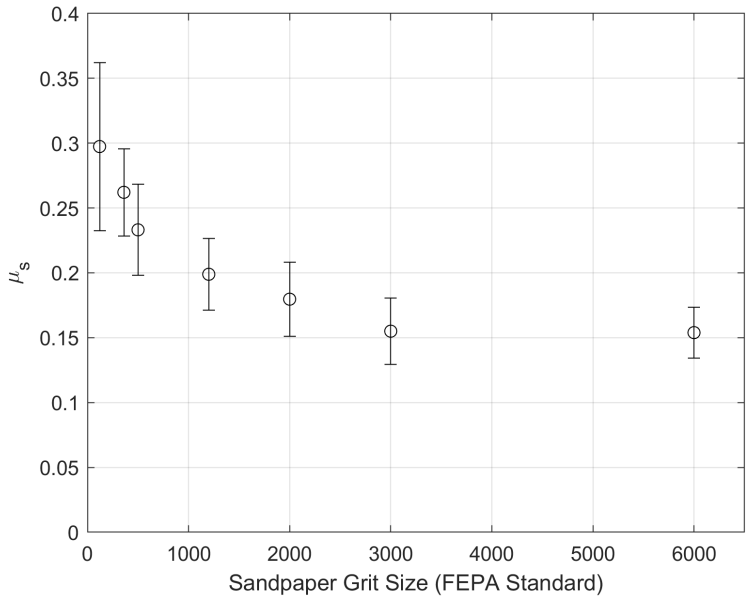

Figure 4.29: Plot of the static friction coefficients against the sandpaper grit size.

The error bars were calculated using the general uncertainty propagation formula:

$$\sigma_{\mu_s} = \sqrt{\left(\frac{\partial \mu_s}{\partial \theta}\right)^2 \sigma_\theta^2} = \frac{\sigma_\theta}{\cos^2 \theta} \tag{4.24}$$

The angle measurement uncertainty (σ_θ) for each sample was given by the standard deviation of the inclination angles average.

The results obtained confirm the expected decrease in static friction with increasing sandpaper grit sizes, a trend more noticeable for more abrasive sandpapers. The decrease in static friction is not linear, tending towards a limit beyond which static friction does not further decrease by surface polishing with higher grit sandpapers. This limit was experimentally determined to by around $\mu_s = 0.16$ for stainless-steel on Teflon.

4.6.3 Assessment of B_4C Microparticle Attachment

The apparatus developed to evaluate the attachment of B_4C fine particles to the stainless-steel samples was made of two main components: 1) a dispersion chamber (Fig. 4.30), that accommodates the sample and the fine powder for dispersion, equipped with

Swagelok SS-4-VCR-1 gas connections; 2) an image acquisition apparatus to register the difference on the sample surface before and after powder dispersion. This was achieved by taking a photograph of each sample before the dispersion (for background subtraction) and immediately after.

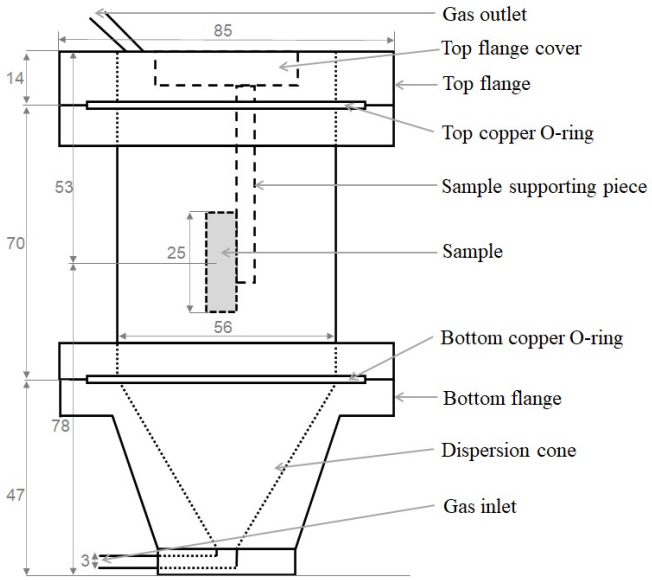

Figure 4.30: Cross view of the dispersion chamber used to disperse the fine particles and determine their attachment to the stainless-steel samples (dimensions in millimetres).

The experimental procedure for the particle attachment evaluation consisted of 6 sets of measurements. For each one, every sample was subject to the same dispersion conditions, in random order. At the end of each set of measurements, the samples were thoroughly cleaned and dried to eliminate traces of particles before commencing a new set. Room temperature and atmospheric humidity fluctuations can affect the attachment of the fine powder to the samples [142]. During the measurements here presented, these parameters were continuously measured and controlled, with values of (22 ± 1) °C and (55 ± 1) %, respectively.

To replicate the detector conditions, the samples were placed with its polished surface parallel to the gas flow inside of the dispersion chamber.

The dispersion chamber is composed by a top flange with a gas outlet and an orifice through which the samples were inserted and removed, a cylindrical tube where the sample was located during particle dispersion, and a bottom cone-shaped disperser in which ~ 0.5 grams of B_4C fine powder was deposited before the dispersions. The gas inlet and outlet were equipped with 2 micron filters (Swagelok SS-4-VCR-2-2M) to prevent the B_4C particles from escaping. Before being released into the atmosphere, the exhaust gas was forced to pass by a volume of a low outgassing oil, commonly used as a lubricant in vacuum pumps, which isolates the dispersion chamber from the atmosphere. The gas used for dispersion was CO_2. The gas selection can impact the particle dispersion, due to its density and viscosity. However, it should not affect the likelihood of a nano/microparticle getting attached to the sample surface when coming in contact with it, so the conclusions drawn while using CO_2 gas can be extrapolated to other commonly used proportional gases.

A scheme of the gas flow system is depicted in Fig. 4.31. The pressure at the entrance of the dispersion chamber was set and kept constant at 3 bar using a pressure

regulating valve connected to the CO_2 bottle. A 2-port normally closed solenoid valve (SMC VDW20KZ1D) programmed by an Arduino Uno microcontroller was used to ensure similar dispersion conditions for all samples. The solenoid valve was opened for a period of 1 second and closed for 2.5 seconds, a process repeated 20 times in a row for each dispersion. These parameters were found to be adequate to provide a reliable measurement of particle attachment with the imaging technique used.

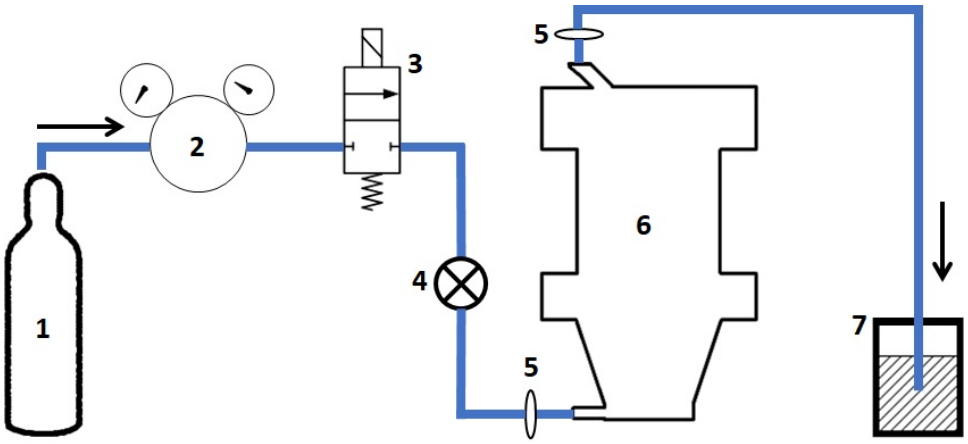

Figure 4.31: Gas flow layout scheme. The black arrow indicates the flow direction. Legend: 1 – High pressure (60 bar) CO_2 gas bottle; 2 – Pressure regulator; 3 – Low pressure solenoid valve; 4 – Manual valve; 5 – Particle filters; 6 – Dispersion chamber; 7 – Oil container.

To effectively compare the photographs taken before and after particle dispersion, it was fundamental to assure that the presence of the fine particles was the only changing parameter. To ensure this, both the camera and the samples were at fixed positions while taking the photographs. Ambient light, focus, lens aperture, exposure time, and other camera parameters were kept constant. For every sample, a background photograph was taken before inserting it into the dispersion chamber. To do this, the sample was placed in the sample holder (item 1 of Fig. 4.32), with the top flange cover and the sample supporting piece attached (Fig. 4.33-a).

After this process, the sample was placed inside the chamber for particle dispersion. When it was finished, a new photograph of the sample was taken, following the same procedure. This process was repeated for every sample, in each set of measurements. Fig. 4.32 shows a photograph of the complete experimental setup.

During the particle dispersion, the chamber was sealed with a Viton O-ring attached to the top cover (Fig. 4.33-a). Five screws exerted downward pressure on the top cover, squishing the O-ring and sealing the chamber (Fig. 4.33-b).

Because the B_4C fine particles have a distinctive black colour, which contrasts with the pale grey colour of the stainless-steel sample, the area fraction with microparticles attached can be determined by means of background image subtraction, using the photograph of the sample before dispersion as background. This was done with the assistance of computer software that subtracts the RGB values of the individual pixels located in the same position of both images [158]. Consequently, pixels of the same colour on the same positions of both pictures will return a value of 0, which translates into white coloured pixels. On the other hand, if the subtraction result goes above a user-controlled threshold, the corresponding pixel is highlighted in black. The result is a binary black and white image, from which the percentage of white pixels and black pixels are obtained.

The area fraction with B_4C fine particles attached is defined as the percentage of black pixels relative to the total number of pixels in the image, which was approximately 4×10^5. The described image subtraction process is illustrated in Fig. 4.34.

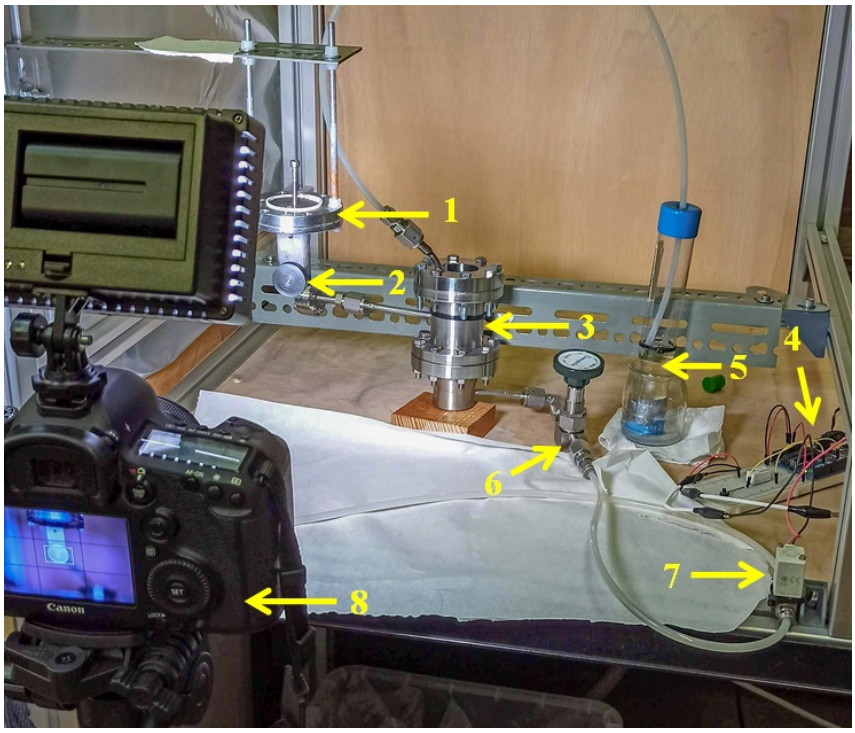

Figure 4.32: Experimental setup for the assessment of B_4C particle attachment to stainless-steel. Legend: 1 – Sample photography holder; 2 – Sample; 3 – Dispersion chamber; 4 – Valve microcontroller; 5 – Oil; 6 – Manual valve; 7 – Solenoid valve; 8 – Camera.

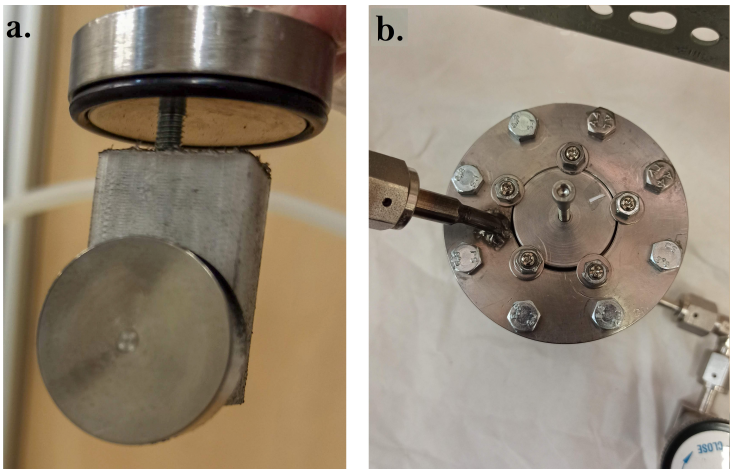

Figure 4.33: Sample assembly that is placed inside the dispersion chamber, consisting of the sample, a supporting piece, and the top flange cover with a Viton O-ring attached. b) Top view of the sealed dispersion chamber after the sample was placed inside it.

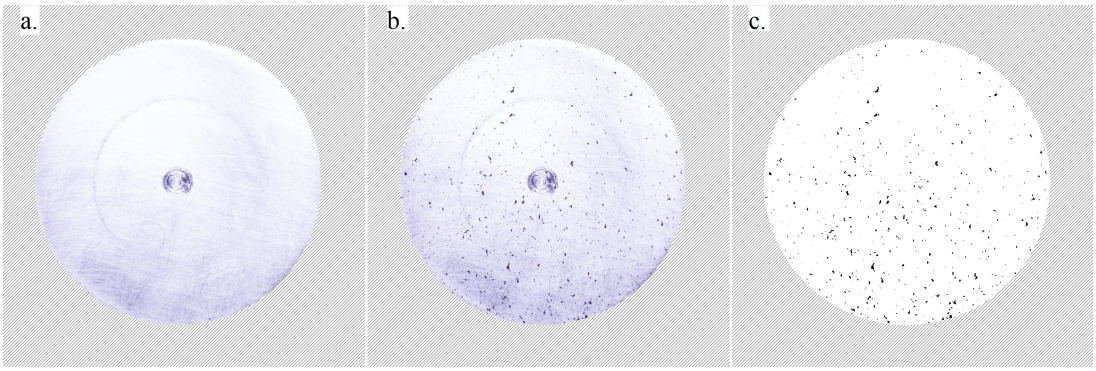

Figure 4.34: Image subtraction process carried to measure particle attachment. a) Photograph of a stainless-steel sample before particle dispersion. b) Photograph of the same sample after particle dispersion. c) Binarized result of the subtraction of the two previous images, with the black pixels showing the attached particles.

4.6.4 B_4C Attachment and Surface Smoothness

The area fraction with fine particle attachment is plotted against the sandpaper grit in Fig. 4.35. This plot suggests that, for polishing grades between P500 and P6000, increasing surface smoothness leads to a reduction of fine powder attachment. As was observed with the static friction coefficient, this decrease is not linear but rather appears to tend towards a stagnation limit. In fact, samples P3000 and P6000, which had very similar μ_s values, also show a very proximate attachment percentage. Considering that the attachment of fine particles is dependent on surface roughness, this validates that static friction coefficient is an adequate parameter to quantify roughness.

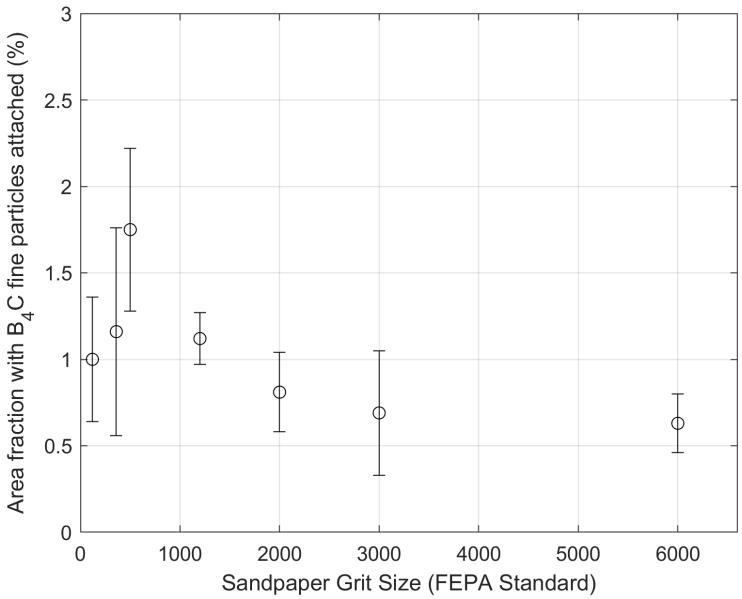

Figure 4.35: Plot of the area fraction with visible B_4C microparticles against the sandpaper grit size for the correspondent sample.

From Fig. 4.35, it is also observed that an increase in the attachment of fine particles with increasing polishing, up to samples polished with the P500 sandpaper grit. However,

for finer polishing sandpaper grit (above P1200) we observe a decrease with increasing polishing in the particle attachment. This suggests that the B_4C particle asperity may play an important factor in the particle attachment to stainless-steel. For significantly rough surfaces, different aspects may dominate the particle-surface adhesion phenomenon when comparing to smooth surfaces.

A reduction in particle attachment with the increase of surface smoothness for high polishing degrees is further evidenced by the plot of the attachment area fraction against the static friction coefficient, presented in Fig. 4.36. Insights for the explanation of this behaviour can be obtained by analysing the surface of the samples through SEM imaging, presented in Fig. 4.37.

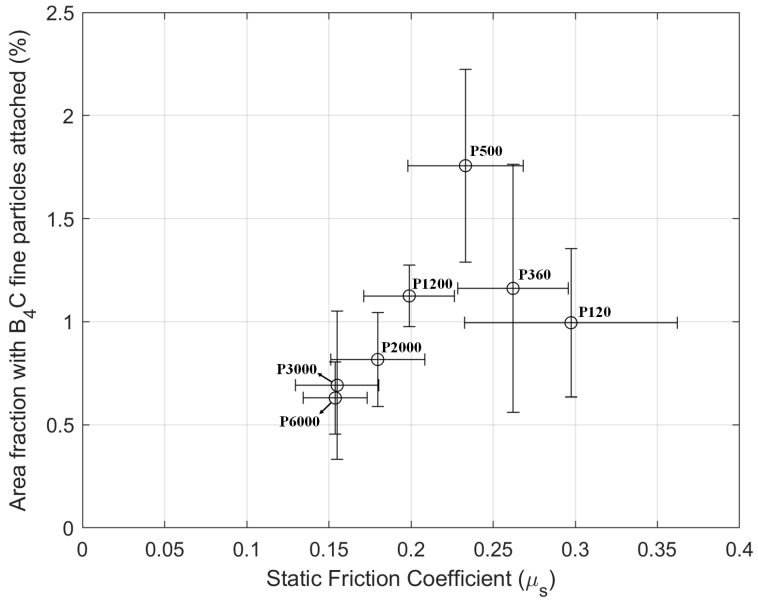

Figure 4.36: Plot of the area fraction with visible B_4C microparticles against the static friction coefficient.

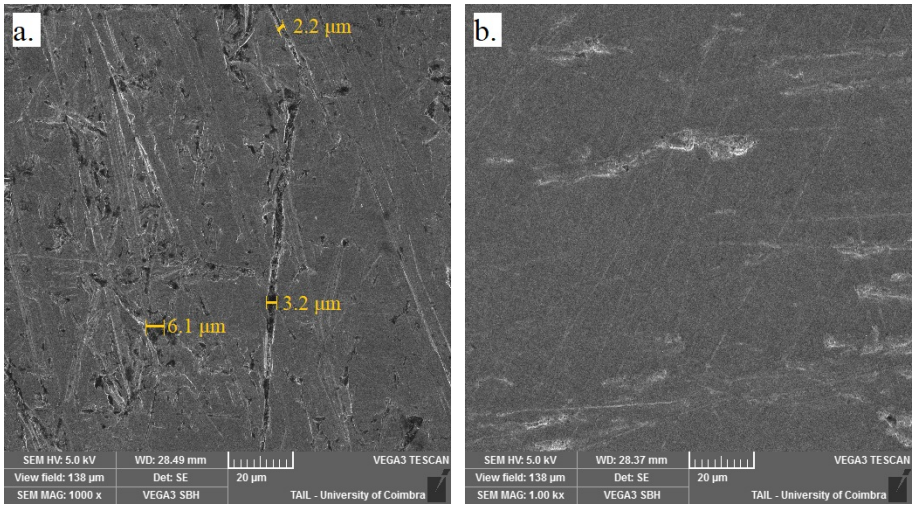

Figure 4.37: SEM images taken at a normal angle of: a) a rough surface sample (P500); b) a smooth surface sample (P6000).

Comparing the image of a sample with a rough surface (Fig. 4.37-a) with that of a sample with a smooth surface (Fig. 4.37-b), it is clear that in the first case there is a considerable amount of irregularities in the form of micrometric valleys, in which microparticles might get trapped. On the other hand, these irregularity features are virtually absent on a very smooth surface.

The results obtained indicate that a high level of surface polishing achieved through manual polishing with high grit sandpapers is an effective strategy to reduce B_4C fine powder attachment to stainless-steel surfaces.

As a consequence of the conclusions withdrawn from this study, the inner walls of the aerosol detector prototype were progressively polished up to P6000 grit sandpaper. This is expected to improve detection efficiency, by maximizing the number of suspended particles available for neutrons to interact with, and to reduce the wall-effect, by minimizing the probability of neutrons interacting with fine particles attached to the walls.

4.7 Front-end Electronics

To obtain intelligible bits of information from a nuclear reaction happening inside a detector, a chain of electronics components must be deployed, typically designated as the "front-end electronics", which amplify, shape, filter, and digitize the signal from the detector. Two modes of operation can be used to convert the charges collected at the detector electrodes into an electrical signal: current mode and pulse mode.

In current mode, a current measuring device is connected to the detector electrodes, which has a long response time when compared to the average time between individual current pulses from detection events, resulting in an average current measurement. This operation mode is mostly used in very high interaction rate environments, at which pulse mode operation becomes impracticable or impossible. Ionization chambers generally work in current mode, although their operation in pulse mode is also possible.

When operating in pulse mode, each detection event generates a distinguishable signal in the shape of an electrical pulse that carries the information of the charge deposited in that particular event. Therefore, the timing and energy of each interaction can be known. Proportional counters are almost always operated in pulse mode [8], and so is the aerosol neutron detector. A scheme of the electronics chain used in the irradiation experiments presented in the next sections of this chapter, is presented in Fig. 4.38.

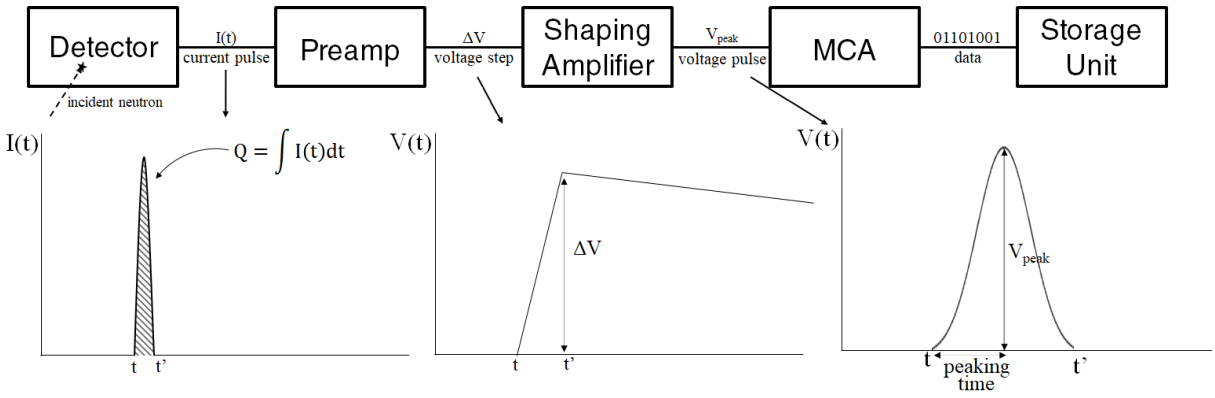

Figure 4.38: Diagram of the front-end electronics circuit at the detector output to convert, condition and digitize the detector signal.

A charge sensitive preamplifier is used to integrate the current pulse ($I(t)$) induced by the collection of charges at the anode from the avalanche electron multiplication. The current pulse is converted into a voltage step (ΔV) with amplitude proportional to the collected charge (Q), and consequently to the energy of the ionizing radiation deposited in the detector. After conversion, the voltage pulse has a rapid rise time, and a long decay time, which depend on the rise time and fall time constants of the preamplifier. To reduce the noise contribution to the detector response, the coaxial cable (with either BNC or SHV connectors) connecting the preamplifier to the anode feedthrough should be as short as practically possible. The HV applied to polarize the anode is also transmitted through the preamplifier, which besides the detector input, has an HV input to connect to a high voltage power supply. In the course of the experimental measurements of the aerosol detector, the HV power supply used was a CAEN N471A, with an output voltage range of ±8000 V, limited in current to 8 μA with 1 nA resolution [159]. Except when otherwise mentioned, the preamplifier used in irradiation measurements with the aerosol detector was a CANBERRA 2004 model, with a charge sensitivity of 0.2 V/pC, a 50 μs fall time constant and a rise time $<$ 33 ns [160].

When selecting this preamplifier, the charge sensitivity was made sure to fit the needs of the detector according to its expected response. While a high sensitivity is desired to produce large amplitude voltage steps and increase the SNR, it must not be too high as to go beyond the input range of the MCA (0-10 V), which would lead to signal saturation and loss of information. Thus, it is necessary to know the maximum possible charge collection at the anode, which depends on the detector gain and on the incoming radiation energy. The detector gain is quantified by its gas multiplication factor (M), which can be calculated from equation (2.44) as a function of the applied anode voltage (HV). This calculation is presented on the plot of Fig. 4.39 considering the geometry of the aerosol detector described in section 4.2.3, and the empirical parameters of P10 gas ($K = 4.8\times10^4$ V/(cm·atm) and $\delta V = 23.6$ V [8]), at atmospheric pressure.

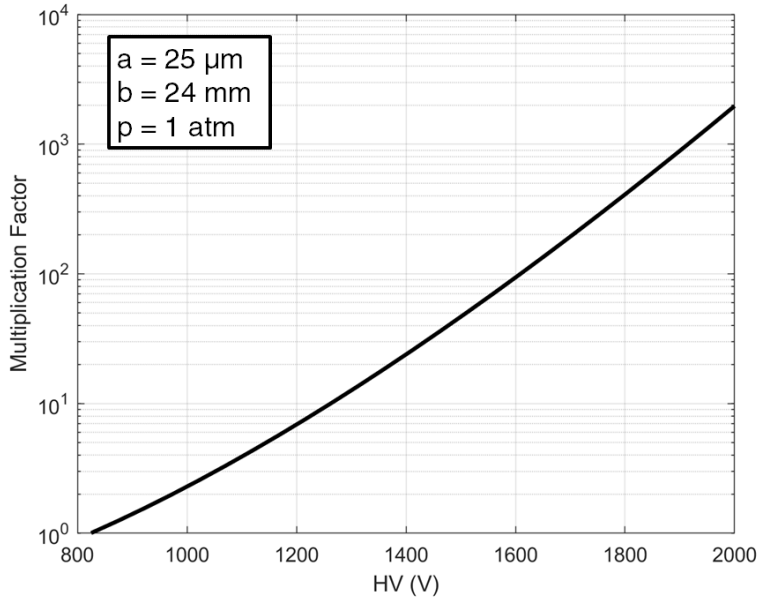

Figure 4.39: Theoretical gas multiplication factor of the aerosol detector, considering an anode radius $a = 25$ μm, a cathode inner wall radius $b = 24$ mm and atmospheric gas pressure.

The HV range considered in this plot is limited by the maximum recommended HV input of the CANBERRA 2004 preamplifier (2000 V), and the theoretical minimum anode voltage for electron avalanche multiplication to occur (HV_{min}). The latter can be derived from equation (2.44) by imposing a gas multiplication factor of 1, i.e., $\ln(M) = 0$. With this condition, equation (2.44) gives:

$$HV_{min} = K\ p\ a \ln(b/a) \tag{4.25}$$

Solving equation (4.25) with the variables of the detector geometry and gas parameters previously mentioned, we obtain $HV_{min} = 825$ V.

The maximum charge that can be collected by the anode also depends on the number of primary electron-ion pairs formed in the gas, which is given by the energy deposited in the counting gas (E_i) divided by w, the mean energy required to form one ion-electron pair (equation (2.40)). It should be noted that the deposited energy is not necessarily equal to the full energy of the incoming radiation. For instance, in the case of neutron detectors employing solid converters, the incoming radiation would correspond to the full energy of the secondary product that is emitted in the direction of the counting gas, while the deposited energy would take into account the energy lost in the solid converter as well as the energy carried by the particle when escaping the detector, in case it is not fully stopped by the gas. In the specific case of the aerosol detector, in the scenario of both secondary particles escaping with their full energy the microparticle where the neutron was converted, the maximum energy that can be deposited in the counting gas is of 2.79 MeV, corresponding to the full-energy of the 6% branch of the ^{10}B neutron capture (reaction (2.38)), as depicted in the GEANT4 simulation results of Fig. 4.2. Considering the $w = 26$ eV/ion-pair value for argon [6], this would give rise to the formation of $n_0 \sim 1 \times 10^5$ primary electron-ion pairs.

The charge (Q) collected by the preamplifier is related to the primary electron-ion pairs (n_0) and the detector multiplication factor (M) by [8]:

$$Q = n_0 e M \tag{4.26}$$

where e is the elementary charge ($e \approx 1.6 \times 10^{-7}$ pC). Having previously calculated M as a function of the supplied HV, and knowing the maximum theoretical value of n_0, we can plot the maximum charge that can be fed to the preamplifier as a function of HV, which is shown in Fig. 4.40-left. This charge is converted into a voltage signal according to the sensitivity constant of 0.2 V/pC, resulting in the maximum preamplifier voltage output plotted in Fig.4.40-right. We can therefore conclude that, even in case of collecting the full energy of the neutron capture reaction, the selected preamplifier will not produce an output signal with amplitude greater than the MCA input limit of 10 V.

The signal from the amplifier is fed to a linear amplifier, also designated as shaping amplifier. As the name suggests, the function of this component is to amplify the input signal, and shaping it into a quasi-Gaussian pulse, producing an output voltage signal with amplitude (V_{peak}) proportional to the deposited charge. While the signal pulse from the preamplifier has a long decay time, the output of the shaping amplifier should return rapidly zero to prevent pulses from overlapping, which would lead to the pileup of detection events. The shaping amplifier also filters high and low frequency noise to improve the SNR of the detector. The linearity of this component is also essential, meaning that the input and output voltages should be proportional.

The ideal peaking time (time interval between the beginning and the maximum

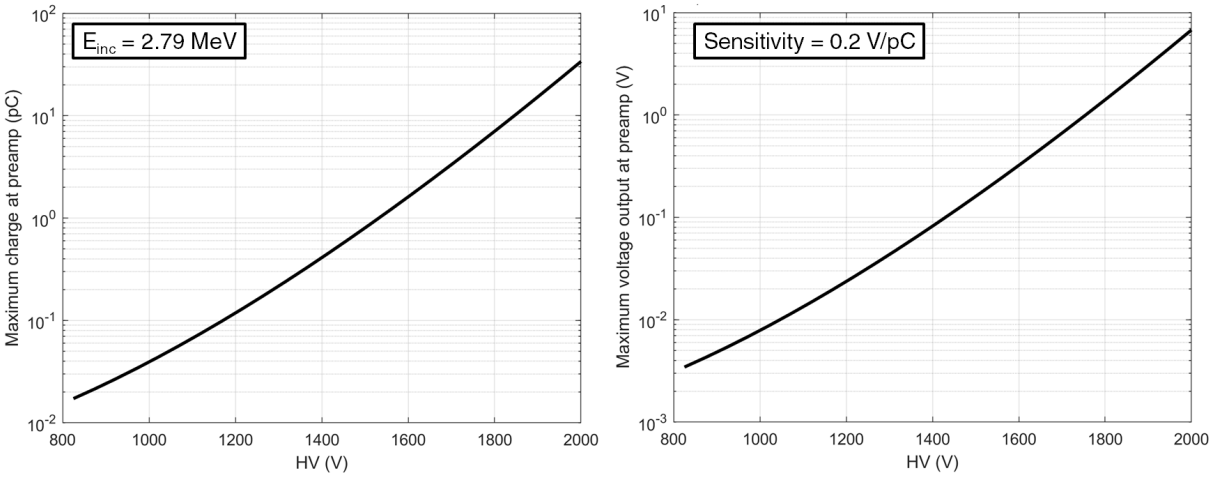

Figure 4.40: Left: Maximum collectable charge by the preamplifier as a function of applied voltage on the anode, considering a ionizing radiation of 2.79 MeV (corresponding to 1.073×10^5 primary electron-ion pairs in argon). Right: Maximum voltage output at the preamplifier considering a charge sensitivity of 0.2 V/pC.

amplitude of the pulse) depends on the detector properties and on the source activity. Therefore, this parameter of the shaping amplifier is empirically selected depending on the irradiation conditions of the experimental measurements. The same occurs for the amplifier gain, which is adjusted for each acquisition so that the spectrum is distributed over the entire range of the MCA channels.

At the end of the front-end electronics is the data acquisition system (DAQ), composed by the MCA and a data storage unit, which most frequently is a computer. The MCA digitizes the analog output of the shaping amplifier, measuring the amplitude of each pulse. The histogram of the several pulse amplitudes registered over a period of time forms the pulse height distribution, which is a useful tool to visualize the energy distribution of the interactions registered by the detector. The multichannel analyser used in the experimental activities of the aerosol detector was an Amptek MCA 8000D. This is a compact high-speed ADC (100 MHz, 16 bit) with a conversion time of 10 ns and a 0-10 V input range, accepting pulses with a minimum peaking time of 500 ns [161]. The digitized signal is finally transferred to a computer with a DAQ software compatible with the MCA (also provided by Amptek), for data rendering and storage.

4.8 Irradiation Measurements

4.8.1 Neutron Irradiation at ILL

The first neutron irradiation measurements after the detector developments described over the course of this chapter were performed at Institute Laue-Langevin (ILL), an international research facility located in Grenoble, France, which main facility is a nuclear reactor, producing neutrons by the fission of ^{235}U. The neutrons are then guided to a suite of around 40 high-performance instruments for users to conduct irradiation experiments, in a variety of scientific fields [70].

After being thoroughly cleaned, the detector was shipped to ILL without the fine powder inside, to prevent it from being dispersed and attaching the walls and the internal

structures of the detector due to the turbulence experienced during transportation. Thus, the powder was transported separately, inside tightly sealed plastic bags, with a priorly weighted amount.

The powder was inserted inside the detector at the chemistry laboratories of ILL, in a fume hood specifically dedicated to the handling of nanoparticles. For this, the cone-shaped disperser was detached, $\sim$ 1 gram of B_4C microparticles from the previously weighted powder bags was deposited, and the detector was then sealed again.

A difference between the scheme of Fig. 4.12 and the detector used in these measurements was the use of a Macor column with 5 mm diameter and 47 mm length instead of the 3D printed PLA ring to attach the anode to. This piece was supported with epoxy glue on both edges to the bottom of the cylindrical portion of the detector, across its diameter. A 1 mm hole was drilled at half length of the pillar through which a stainless-steel needle was inserted and fixed. The anode wire was first soldered to the feedthrough on the top flange, made to go through the needle and then attached to a suspended weight to keep the tension of the wire while an epoxy glue was applied in order to attach the anode wire to the needle. This strategy was meant to reduce the amount of material in the detection volume to which the fine powder could attach to, specifically the three M3 rods that had to be used to secure the bottom anode fixing ring, which extended from this piece up to the top flange. This was the same reason behind the choice of discarding the electric field cage described in section 4.1, with 18 wires that also extended across the length of the anode, which amounted to a considerable extent of surface area to which the particle could get attached.

A photograph of the experimental setup at ILL is shown in Fig. 4.41.

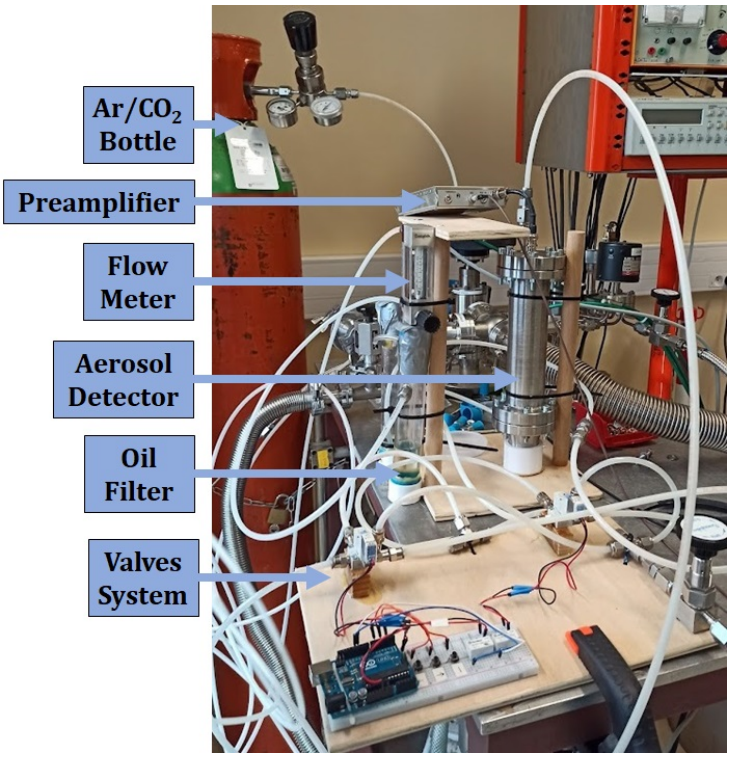

Figure 4.41: Photograph of the experimental setup installed at ILL for detector irradiation with thermal neutrons from an ^{241}AmBe isotopic source.

Out of range in this image is the DAQ system, composed by the MCA described in section 4.7 connected to the preamplifier and a computer to which data was transferred.

A preamplifier provided and developed by ILL was used, which was also a signal shaping circuit embedded and therefore was directly connected to the MCA. Its sensitivity was 2 V/pC, with a peaking time of 4 μs.

An ^{241}AmBe source was used for neutron irradiation, surrounded by a thick layer of a polyethylene moderator to thermalize neutrons that were emitted isotropically in all directions. The source had a cylindrical shape of relatively large dimensions, with approximately 15 cm diameter and almost covering the full height of the detector cylinder after being placed in a support next to it.

Ar:CO_2 gas in 90%:10% proportion was used throughout these measurements. It was first opened at a very low flow rate from the bottom inlet to the top outlet for approximately one hour to purify the gas inside the detector without immediately dispersing a large number of nanoparticles. During this time, the HV fed to the anode was raised to 1700 V.

After this, the gas flow was increased to 8 l/h with the purpose of dispersing the microparticles. However, it was verified that this increase in flow led to a significant rise of the detector leakage current and occasional electrical discharges, which severely conditioned the operation of the detector under the intentioned conditions. For the same reason, it was not possible to test the detector operation with the solenoid valves system periodically reversing the gas flow because, as mentioned in section 4.5, that required to increase pressure in the pressure regulator connected to the gas bottle, which in term led to an increase of the gas flow that was verified to be sufficient to cause the mentioned electrical instabilities in the detector.

To overcome this, while trying to have microparticles suspended during acquisitions, the strategy adopted consisted of lowering the anode polarizing voltage when the gas flow was increased to disperse the particles, and after some time closing the gas flow and rising back the polarizing voltage.

An example of a PHS acquired in these conditions, for a 300 seconds acquisition time and an anode voltage of 1700 V is presented in Fig. 4.42-left (blue plot).

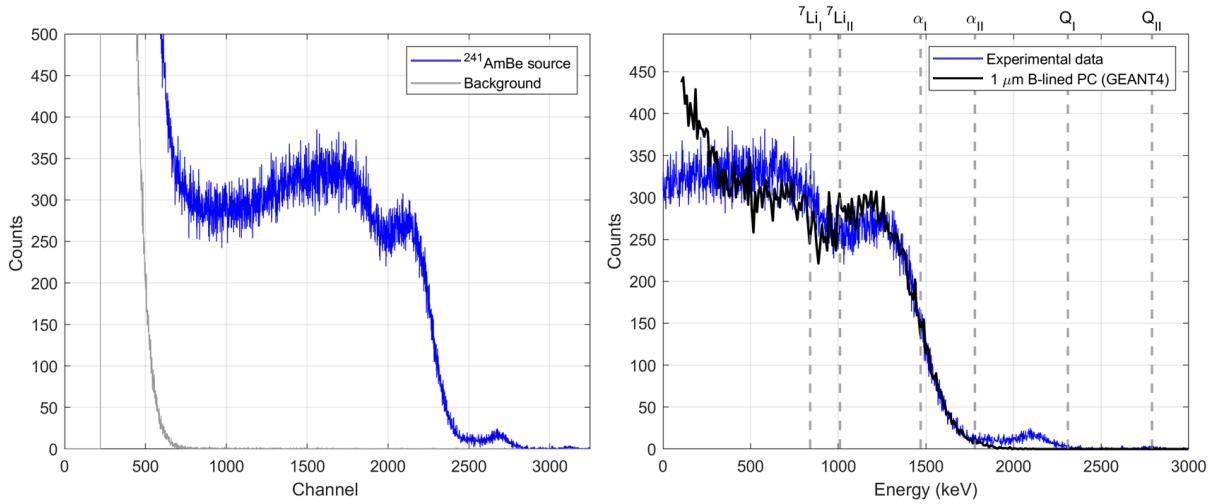

Figure 4.42: Left: PHS of the aerosol detector irradiated by thermal neutrons (blue plot) acquired immediately after closing the gas flow, after being opened at a flow rate of 8 l/h for approximately 30 seconds (HV = 1700 V and acquisition time = 300 seconds). Right: Energy calibration of the acquired spectrum (blue plot) and comparison with GEANT4 simulations of a B-lined detector with 1 μm coating thickness (black plot).

A background spectrum (grey plot) under the same conditions was acquired immediately after, by removing the neutron source from the proximity of the detector. A detector response similar to that of conventional boron coated detectors was obtained, caused by neutron captures in microparticles attached to the walls. This shows that, although the study described in section 4.6 suggested that polishing the detector inner walls lead to a decrease of particle attachment, this effect is not sufficient to eliminate the attachment of the fine powder, and its presence in the walls is still high enough to dominate the detector response. Energy calibration was performed (Fig. 4.42-right) using as reference the middle points of the ^{7}Li and alpha ions detection edges, with known energies of 0.84 MeV and 1.47 MeV, respectively. When compared to what would be expected from a B-lined proportional counter with similar geometry and a 1 μm thick B_4C coating, based on a GEANT4 simulation normalized in amplitude and energy resolution (25%) to fit the experimental data (black plot), a good match is observed.

However, a smaller peak at higher energies is also visible, with centroid around the MCA channel 2700 which, according to the energy calibration calculations, corresponds to an energy of approximately 2.1 MeV. This peak is not a characteristic expected of a B-lined PC (refer back to Fig. 3.7). For one, it does not have a plateau shape, which should be the case if it was attributed to the 6% alpha particle reaction branch (1.78 MeV), but rather a distinctive peak shape, centred at a higher energy. Additionally, the limited energy resolution measured and described in section 4.3 does not make it plausible to be able to distinguish so clearly the alpha particle from the 6% reaction branch from the end of the edge of the alpha particle from the 94% reaction branch. This is also proven by the comparison between the experimental data and the GEANT4 simulation, which was normalized in amplitude and energy resolution to fit the experimental data, and yet the mentioned peak is clearly an extra feature to the simulation.

Consequently, the presence of this small peak suggests that a fraction of neutron captures occurred in suspended particles, in which both secondary reaction products deposited a fraction of their energy in the counting gas, as had been previously observed in the preliminary proof-of-concept tests at PSI (Fig. 4.6). The fact that this energy does not match the full energy released in the ^{10}B neutron capture reaction (Q = 2.31 MeV for the 94% probability branch) is expected, since both reaction products cannot escape the B_4C without losing a fraction of their energy in collisions inside the particle, as was verified by the simulations previously presented in Fig. 4.2.

After these results, a new set of measurements was carried, this time programming the MCA to make consecutive short acquisitions (5 seconds each) while varying the gas flow and adjusting the HV supply to ensure the electrical stability of the detector, with the intention of tracking how its response was influenced by variations of the gas flow and the associated particle dispersion behaviour. From these measurements, a series of acquisitions are particularly relevant, presented in Fig. 4.43, taken immediately after closing the gas flow when it had been previously opened at a very high flow rate, saturating the flow meter ($>$ 15 l/h) for about a minute, at an anode voltage of 1800 V.

The signal from neutron detections progressively rises to higher energies after closing the gas flow. As this happens, a single peak is formed, with a distinctively high counting rate, compatible with what can be expected from the aerosol detector when most neutron captures occur in suspended B_4C microparticles. Fig. 4.44 shows the sum in counts of the spectra labelled 4, 5 and 6 of Fig. 4.43, in which the peak remained centred at an approximately constant position.

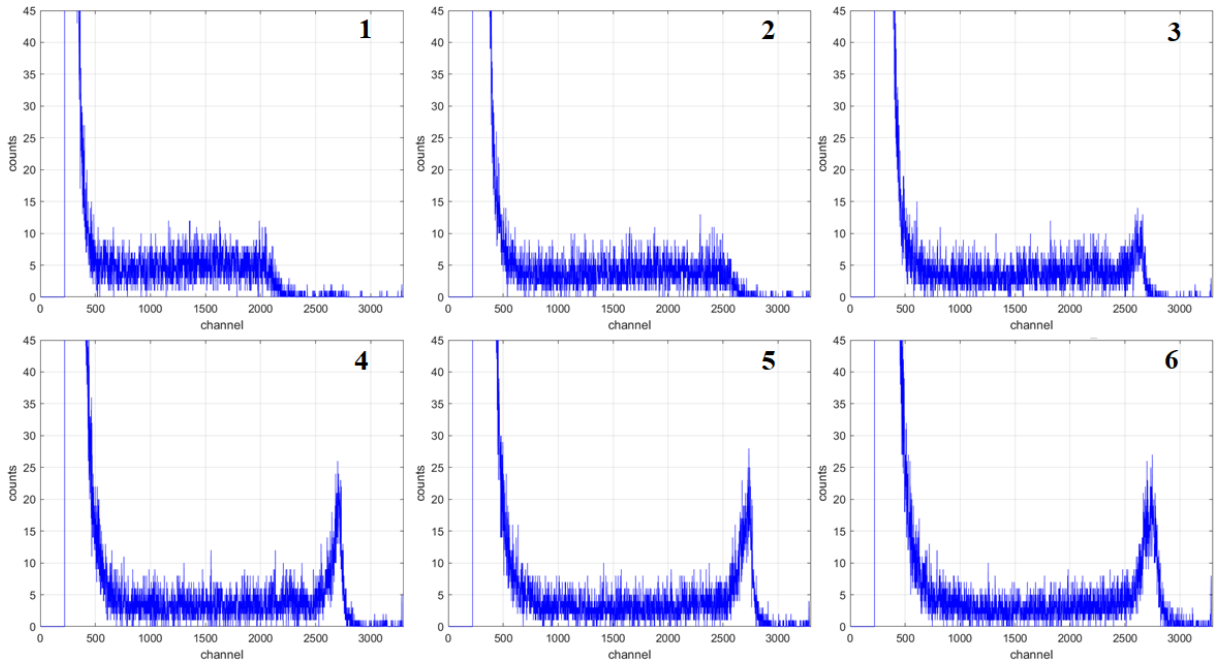

Figure 4.43: Time-lapse (order given by the numbers on the top right) of the signal from neutron detections progressively rising to higher energies, after closing the gas injection. Each spectrum corresponds to a 5 second acquisition, with HV = 1800 V.

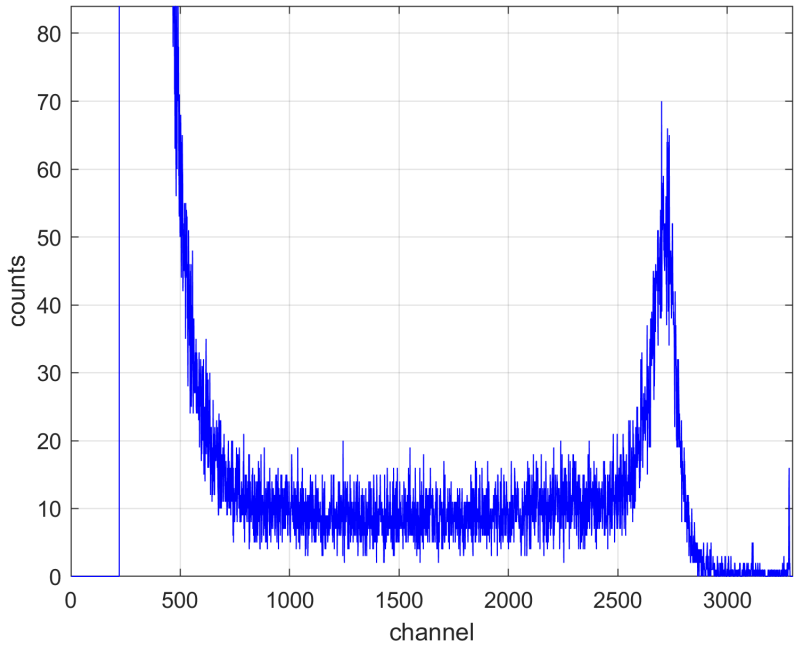

Figure 4.44: PHS obtained by summing the acquisitions labelled 4, 5 and 6 in Fig. 4.43, for which the position of the peak was stabilized.

Because the gas had been flowing from the bottom inlet to the top outlet immediately before closing the gas injection for the sequential acquisitions shown in Fig. 4.43, it is expected that a significant amount of B_4C particles is still in suspension, which can explain the observed peak, arising from neutron captures occurring in suspended particles, at a much higher interaction rate compared to those occurring in the particles attached to the wall. Due to the short time of each acquisition, not enough statistics was acquired

to identify the alpha and ^{7}Li signatures of the two-step plateau from the wall-effect, and consequently, energy calibration is not possible. This peak was only present in the detector response for a brief period: after the last acquisition depicted in Fig. 4.43 the HV supply was dropped down to 1700 V and by doing so, the peak shifted to the left and its amplitude decreased until it was no longer distinguishable from the electronic noise.

The results obtained indicate the detection of neutron captures in suspended B_4C particles. However, the measurements were very conditioned by the little margin to control the gas flow and the HV supply without causing electrical instabilities.

After further investigation back in the LIBPhys laboratory, the high leakage current and occasional electric discharges were attributed to the fact that the suspension of the B_4C powder was creating an electrically conductive path between the top of the anode wire, soldered to the SHV feedthrough and the surface of the cathode flange. The evidence for this was the fact that the leakage currents was only critically high when the gas was flowing in the bottom-top direction, and proportional to the intensity of the gas flow. In contrast, when the gas was injected from the top entrance, the leakage current was only residual (< 1 nA), even for very high flow rates. This is compatible with the possibility that having a greater concentration of particles in the top volume of the detector, near the feedthrough, led to the substantial increase of the leakage current and occasional discharges.

This issue was addressed by redesigning the top flange, increasing the distance between its inner surface and the conductive end of the feedthrough as illustrated in Fig. 4.45. This was achieved by drilling an 8 mm deep hole on the top surface of the flange in such way that the SHV connector was partially bellow this surface, leaving the attachment point for the anode wire at a larger distance from the top flange.

Figure 4.45: CAD design of the top flange used at the irradiation measurements at ILL (left), and upgraded design increasing the spacing between the conductive end of the feedthrough and the flange surface by 8 mm (right).

One additional alteration to the detector was the replacement of the Macor pillar used to fix the anode by the 3D printed PLA ring already described in section 4.2.3. This was motivated by the fact that when using the former, detaching the top flange to open the detector resulted in breaking the anode wire, since it was fixed on one end to the feedthrough of the top flange and on the other end to the Macor pillar, that was glued to the detector walls. This made the processes of removing the B_4C fine powder, cleaning the detector and eventual future modifications that required opening the detector inconvenient and time-consuming. Additionally, when the detector was opened after the irradiation measurements at ILL, it was verified that the surface of the pillar had some particles attached to it, predominantly on the surface facing up towards the top flange, due to the

settling of the suspended particles by action of gravity. This could ultimately create a conductive path between the anode and the cathode walls which would compromise the detector operation.

4.8.2 Alpha Particles Irradiation

Before new neutron irradiation measurements (described in section 4.8.3), the upgrades on the detector were tested at LIBPhys, using an ^{241}Am isotopic source. As exposed in section 2.2.1, the natural decay of this radionuclide to ^{237}Np results in the emission of alpha particles with an energy of 5.5 MeV [162]. However, a shielding layer is attached to the source, which attenuates the alpha particles and causes a reduction of the average energy with which they leave the collimator. In a previous work, this energy was experimentally determined for the same source, and the value 4.95 MeV was measured [163].

Because the alpha particles have high stopping power, they are severely attenuated by just a few microns of solid material, and are therefore unable to traverse the detector wall. Consequently, the source was placed inside the detector, which was technically simpler than equipping it with a very thin window. This was achieved by linking with tape two of the M3 rods that connected the anode fixing to the top flange, and securing the source to the tape, at approximately half length of the anode and with the collimated side pointing towards it.

Because it was intended to operate the detector with the B_4C fine powder inside it, the source was covered with a thin layer of plastic wrap, to prevent it from being contaminated with microparticles. This further attenuates the average energy of the alpha particles when entering the gaseous volume of the detector. To estimate this energy, before inserting the powder in the detector, measurements were done with the source inside the detector before and after coating it with the plastic wrap. The results are presented in Fig. 4.46, using P10 gas in continuous flow at atmospheric pressure.

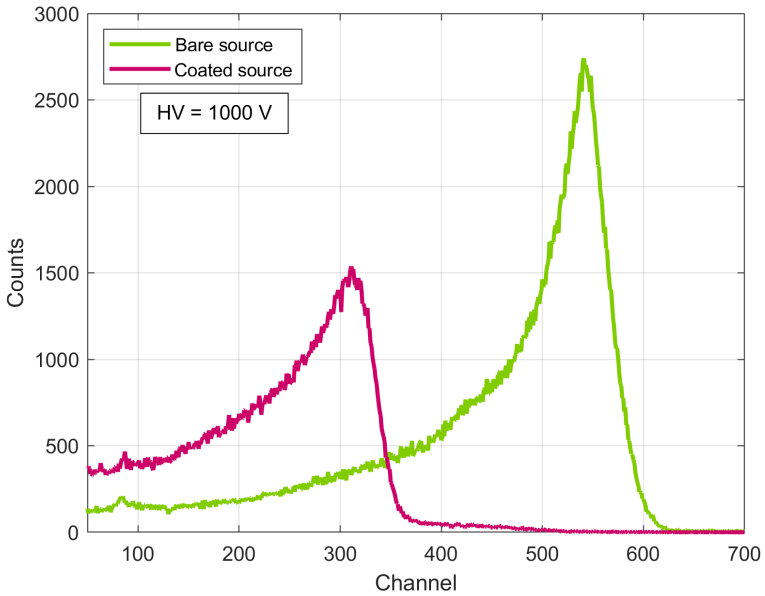

Figure 4.46: Detector irradiation by alpha particles from an ^{241}Am source placed inside the detector before (green plot) and after (magenta plot) coating it with plastic wrap. HV = 100 V. Acquisition time = 120 seconds.

The left-tail, visible on both plots, is a characteristic of alpha particle sources, due to the fact that only alpha particles that are perfectly collimated deposit the full energy carried after crossing the shielding layer, while those that partially traverse the lead collimator will escape the source with progressively less kinetic energy.

As expected, a drop in the average energy of the detected alpha particles is observed, evidenced by the left-shift of the PHS after covering the source with plastic wrap. The energy peak is now centred at 57% of the value obtained with the bare source, which translates into a reduction of the average alpha particle from 4.95 MeV to 2.82 MeV. Conveniently, this energy is close to the maximum energy released in the ^{10}B neutron capture reaction (2.79 MeV), and therefore an appropriate value to test the detector in similar conditions to those expected under thermal neutron irradiation.

After this, 1 gram of B_4C powder was placed in the disperser cone which was then reattached to the detector. A set of acquisitions (120 seconds each) were first carried varying the anode voltage, with the detector in a continuous unidirectional gas flow from the bottom inlet to the top outlet, at a rate of 12 l/h (blue triangles in Fig. 4.47). Afterwards, for some of the previous voltages applied corresponding to the proportional region of operation, the solenoid valves system was used to periodically reverse the direction of the gas flow, in intervals of 30 seconds of a bottom-top flow followed by 5 seconds of a top-bottom flow (red circles in Fig. 4.47). In both sets of acquisitions, the pressure reducing valve was fixed at 1.5 bar.

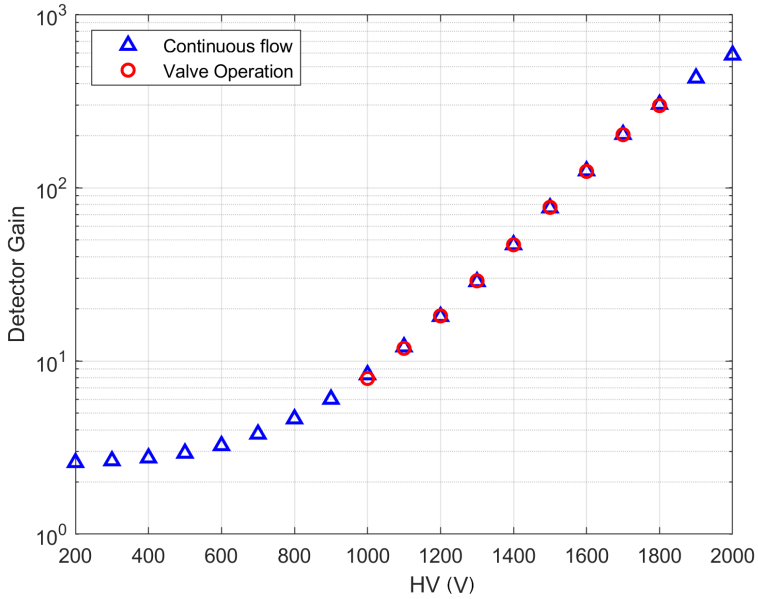

Figure 4.47: Detector gain as a function of the anode voltage measured with alpha particle irradiation with B_4C fine powder being dispersed by an unidirectional gas flow (blue triangles) and using the solenoid valves system (red circles).

It is worth noticing that the gain curve obtained agrees with the theoretical calculations for the minimal threshold for avalanche multiplication of 825 V presented in section 4.7, since it is verified that this is the value around which the detector gain and the supplied polarizing voltage are directly proportional. It is also observed that the solenoid valves system did not induce any significant gain fluctuations, since the measurements performed with and without it are very similar.

Most importantly, the leakage currents were only residual during the whole detector operation time in both sets of acquisitions, and no electrical discharges occurred. The leakage currents had values < 1 nA throughout most of the applied voltage range, rising to $\sim$3 nA at HV = 1800, and from there on increasing proportionally with the anode voltage, reaching a maximum value of 12 nA for HV = 2000 V.

Based on these results, it was inferred that the detector upgrades, specifically the new top flange design, were effective in resolving the electrical instabilities experienced at ILL.

4.8.3 Neutron Irradiation at ICNAS

After verifying that the detector was operating under stable conditions through the alpha particle irradiation experiments, it was taken to ICNAS (Institute for Nuclear Sciences Applied to Health), a research facility of the University of Coimbra that congregates in the same building the main modalities of medical imaging, and which is equipped with two cyclotrons for the production and investigation of radioactive tracers [164]. One of them is the KIUBE cyclotron from IBA (Ion Beam Applications), used to produce several radioisotopes [165].

When the cyclotron is used to produce the ^{18}F isotope via the ^{18}O(p,n)^{18}F reaction by accelerating protons (until reaching 18 MeV energy) into a liquid target of ^{18}O enriched water, fast neutrons are emitted. These have an energy range that extends up to $\sim$ 15 MeV, with a peak centred around 1 MeV, as plotted in Fig. 4.48.

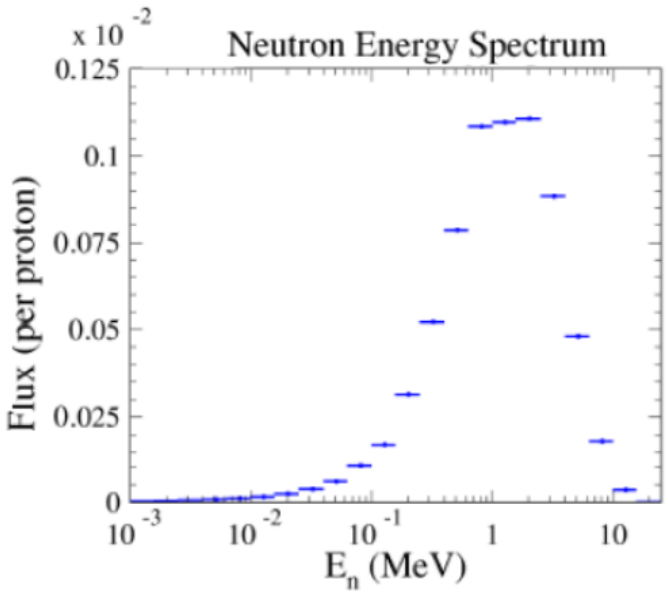

Figure 4.48: Neutron emission energy distribution from the ^{18}O(p,n)^{18}F reaction by 18 MeV protons. Image from [166].

The ^{10}B neutron capture cross-section is very low for such high energies, with a value of just $\sim \sigma = 0.2$ barn for 1 MeV neutrons, when compared to $\sigma = 3840$ barn at thermal energy (refer back to Fig. 2.12). Consequently, neutron moderation is required to increase neutron capture probability and detection efficiency. This was achieved by placing two water containers, with a diameter of 22 cm, aligned between the detector and the cyclotron. Because neutrons are isotropically emitted in a 4π angle, the detector was positioned as close as possible to the liquid target in the cyclotron, to maximize the neutron flux traversing it.

The counting gas used was Ar:CO2 (80:20). To prevent neutron activation, the bottle was placed outside the cyclotron bunker. The same was done with the remaining components of the front-end electronics (HV supply, shaping amplifier, MCA and computer), to prevent damage by irradiation. This radiation damage concern came from the high intensity of gamma-rays present in the bunker due to the cyclotron operation, emitting gamma-rays isotropically in the process of producing the ^{18}F radioisotope, with wide energy range, extending up to $\sim$ 10 MeV. These gamma-rays originate mostly in secondary neutron captures in surrounding target materials [166]. The coaxial electrical cables and the gas tubes passed under the floor to a radiation safe zone outside the bunker.

Only the components that were required to be near the detector were installed inside the bunker, namely the preamplifier, since a long SHV cable connecting it to the anode would severely worsen the SNR of the detector, and the solenoid valves system, to which the connecting tubes were adjusted to allow it to be placed behind a concrete wall to reduce radiation incidence. A photograph of the setup installed inside the bunker near the cyclotron is shown in Fig. 4.49.

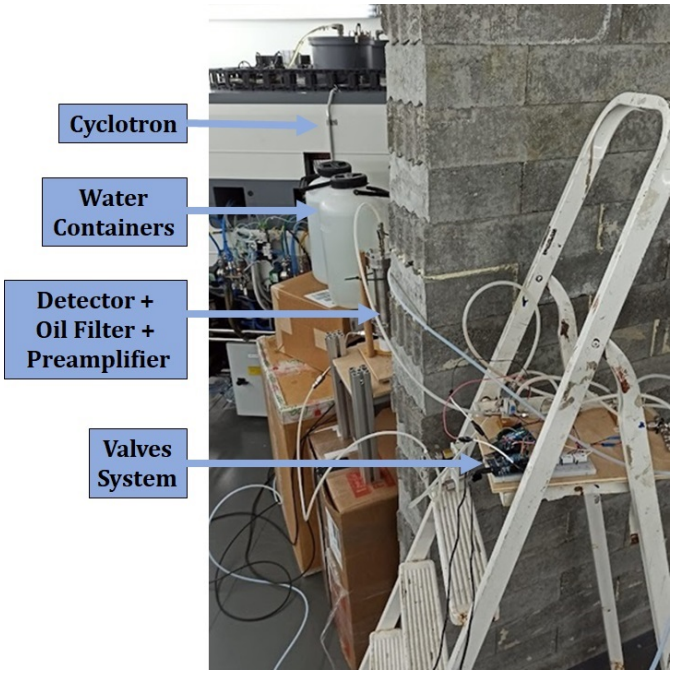

Figure 4.49: Experimental setup installed at ICNAS for irradiation neutrons produced by the KIUBE cyclotron, thermalized by two water containers placed between the cyclotron and the detector.

After installing the detector, the gas flow was opened firstly flowing unidirectionally from the bottom inlet to the top outlet at a very low rate to purify the gas before starting particle dispersion. After some time, the flow rate was violently increased, saturating the flow meter ($>$ 15 l/h), to disperse the particles. Subsequently, the proton beam of the cyclotron was switched on to produce fast neutrons and several short-time acquisitions were made to adjust the anode polarizing voltage, the linear amplifier gain and the peaking time. After this iterative process, a PHS was acquired for an anode voltage of 2100 V and a peaking time of 2 μs, shown in Fig. 4.50-left.

A similar procedure was taken using the solenoid valves system to alternate the direction of the gas flow, defined for 10 seconds in bottom-top direction, followed by 2 seconds of top-bottom direction. The short valve alternating timings in relation to

the comments of section 4.5 was motivated by the intention of increasing the number of complete cycles in face of a relatively short acquisition time. The resulting PHS is shown in Fig. 4.50-right, for an anode voltage of 2300 V and the same peaking time.

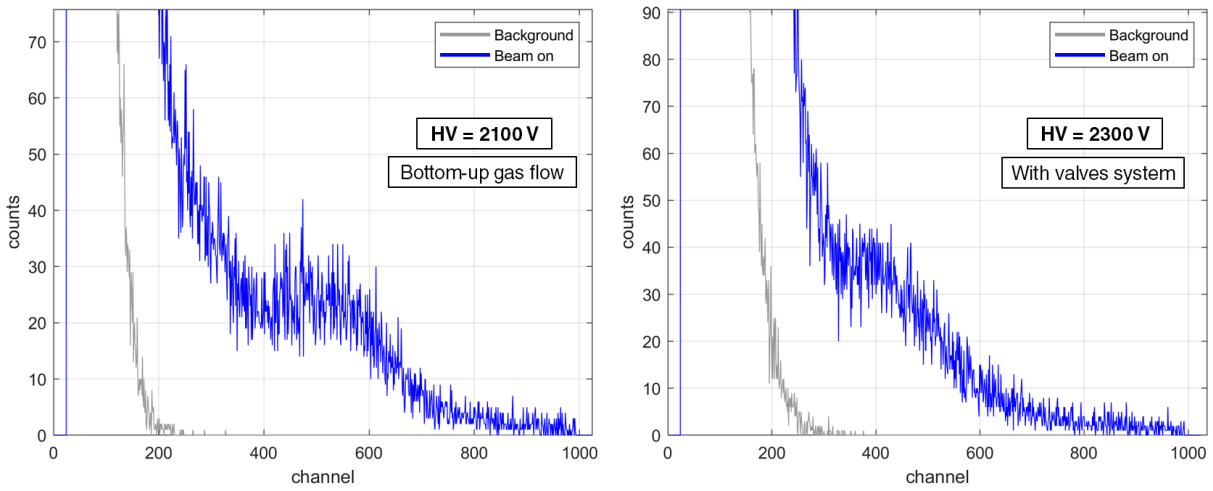

Figure 4.50: Left: PHS acquired with neutrons from the KIUBE cyclotron using a unidirectional gas flow (blue curve), and the corresponding background signal (grey curve) acquired before switching on the proton beam (HV = 2100 V and acquisition time = 50 seconds for both plots). Right: PHS acquired using the solenoid valves system, defining 10 seconds of bottom-top dispersion and 2 seconds of top-bottom dispersion, along with the corresponding background PHS (grey curve), acquired before switching on the proton beam (HV = 2300 V and acquisition time = 100 seconds for both plots).

A background PHS was also acquired in the same operating conditions for each case (with and without the solenoid vales system), before switching on the proton beam. The signal from this background is generated not only due to electronic noise, but also due to low energy depositions of gamma-rays traversing the detector volume, arising from a second cyclotron that shared the same bunker and that was in continuous operation during the whole experimental campaign.

When using the solenoid valves, the gas pressure at the pressure regulating valve attached to the gas bottle had to be increased slightly above atmospheric pressure due to the valve requirements exposed in section 4.5. This resulted in a decrease in the detector gas gain, which was compensated by increasing the anode voltage.

Although a stable operation of the detector was achieved, without electrical discharges or problematic leakage currents, both with and without using the solenoid valves system, a high energy peak from the simultaneous detection of both secondary products of a single neutron capture reaction was not observed in any case. The lump feature visible on the left and right plots of Fig. 4.50 appears to correspond to the plateau of the alpha particle, while that of the ^{7}Li is not distinguishable in the gamma background region. Due to the bunker environment where the detector was placed, with two operating cyclotrons emitting gamma-rays in high intensity, the gamma interaction rate in the detector was extremely high, which led to pile-up and a consequent extension of the gamma background signal to high energies, superimposing with the signal from neutron detections.

Because of the high levels of radiation produced by the cyclotron, irradiation times had to be kept to a maximum of a few minutes. For safety measures, higher irradiation times would forbid entering the bunker for several hours, which was not practically feasible due

to the requirement of disassembling the detector setup by the end of the measurements. This inhibited the use of the acquisition technique employed at ILL, programming the MCA to perform many consecutive short time acquisitions (summing up to a considerable amount of time) to have a glimpse of the detector response on shorter time scales.

4.9 X-Ray Detection Capability

Although gaseous detectors are a widely spread technology in some scientific applications, they are inefficient when used in the detection of hard x-rays or gamma-rays. Due to the low density of gases, the absorption probability of x-rays in a gaseous volume drops abruptly with increasing photon energies, as portrayed in the simulation results of Fig. 4.51. As so, in what concerns detection efficiency, and for higher photon energies, gaseous detectors are generally outperformed by solid-state detectors such as scintillators or semiconductors sensors, which are roughly 10^3 times denser, and consequently have associated a much higher probability of interaction with the incoming photons.

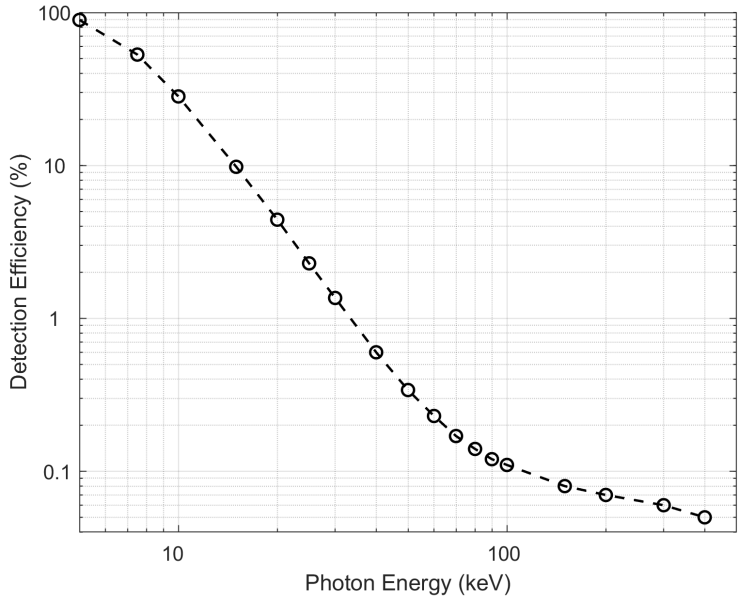

Figure 4.51: Detection efficiency calculated by GEANT4 simulation of incoming photons with different energies entering a 36 mm diameter cylindrical P5 gas volume (Ar:CH_4 in 95%:5% proportion) at atmospheric pressure.

Inspired by the neutron aerosol detector, a new type of hard x-ray gaseous detector is here presented, which uses high-Z nanoparticles dispersed in a gaseous atmosphere to increase the photoelectric effect probability, converting high energy photons into photoelectrons, lower energy characteristic x-rays and Auger electrons. These have considerably higher stopping power in the counting gas, and therefore an increase in detection efficiency can be expected.

4.9.1 Detection Principle

The operation principle of this detector is analogous to that of the aerosol neutron detector, with a two material mechanism for the detection of high energy photons: using a solid to increase the interaction probability by photoelectric effect, converting the high energy photons into secondary radiation (photoelectrons, lower energy photons and Auger electrons), and a gas in which, similarly to a standard proportional counter, the secondary radiation will produce gas ionizations, resulting in the production of ion-electron pairs.

The probability of photoelectric absorption by an atom is enhanced for materials with high atomic number (Z), being roughly proportional to $\frac{Z^n}{E^{3.5}}$, where E is the energy of the incoming photon and n varies between 4 and 5 over the photon region of interest [8]. This makes high-Z materials ideal to promote the photoelectric effect. The heaviest stable element in the periodic table is bismuth (more accurately, it is vestigially radioactive with a half-life of 1.9×10^{19} years, which is, in practice, negligible [167]), and it is available in nanoparticles format both in its elemental form and as a molecular compound such as Bi_2O_3. This makes bismuth nanoparticles an ideal candidate to compose the hard x-ray sensitive aerosol.

The detection concept feasibility was first examined through GEANT4 simulations. A simplified detector geometry was implemented based on a new detector prototype, consisting of a 36 mm diameter and 200 mm height cylindrical P5 gas volume (Ar:CH_4, 95%:5%) at atmospheric pressure, surrounded by a 2 mm thick stainless-steel wall. A variable number of 150 nm diameter spheric Bismuth(III) Oxide (Bi_2O_3) nanoparticles were placed inside the gas volume. A primary particle beam of 59.5 keV monoenergetic photons was pointed perpendicularly to the detector axis. The photon initial positions were uniformly distributed over the nanoparticles cross-section. The energy of the primary photons corresponds to the most intense gamma-ray emission of an ^{241}Am source, used in the experimental work of this study (section 4.9.2). For each incoming photon, the simulation recorded solely the energy deposited in the gas, excluding the fraction lost inside the nanoparticles. The simulation output (Fig. 4.52-left) for 10 Bi_2O3 nanoparticles with 150 nm diameter shows that the detection of the incident radiation is mostly achieved by the occurrence of the photoelectric effect in three materials: the stainless-steel walls of the detector, the Bi_2O_3 nanoparticles and the P5 gas itself. The response of a real detector is restrained by several operational characteristics, one of them being energy resolution. To resemble the expected pulse height spectrum (PHS) of a real detector, a random fluctuation component was added to the energy values of Fig. 4.52-left, adjusted to obtain an energy resolution of 15% FWHM, which is in range of the expected resolution for 60 keV (Fig. 4.52-right).

The detector walls are made of the stainless-steel, defined in the GEANT4 material database with the composition of Fe (74%), Cr (18%) and Ni (8%). The occurrence of the photoelectric effect in the detector walls, before or after the primary photons transverse the gas, is mostly evidenced by the three low-energy peaks labelled in Fig. 4.52-left, corresponding to the characteristic x-rays Kα (6.4 keV) and Kβ (7.1 keV) of Fe, and Kα (5.4 keV) of Cr. Because these have significantly lower energy than the primary photons, they are effectively stopped and detected when emitted towards the gas. The characteristic x-ray emissions of Ni are negligible in the PHS of the simulated detector due to its relatively low percentage in the stainless-steel composition.

A superimposing contribution to the detector response in this energy range comes from the Compton interaction (inelastic scattering) of the incoming radiation with the

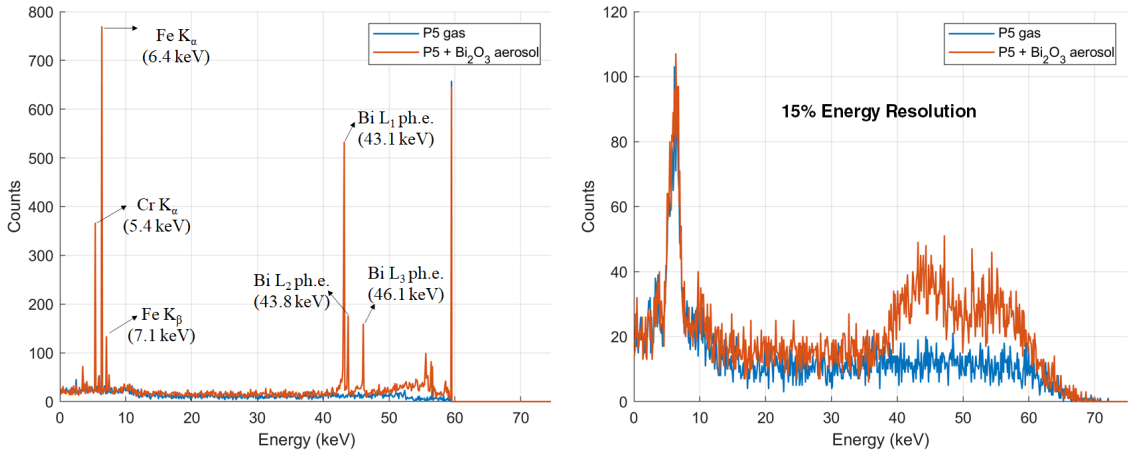

Figure 4.52: Left: GEANT4 simulation outputs of the energy deposited by 59.5 keV photons in a proportional counter filled with a standard P5 mixture (blue) and an aerosol detector with 10 aligned 150 nm diameter Bi_2O_3 nanoparticles (red). Right: Addition of a 15% FWHM energy resolution fluctuation to the simulation output.

gas, consisting of a partial energy transfer from the incident photon to an electron of an Ar atom, which results in its ejection (recoil electron). This creates an electron-ion pair that can subsequently ionize the surrounding gas atoms, producing a detectable signal. For the energy ranges concerned, the occurrence probability of the Compton interaction competes with the photoelectric effect, and increases for higher incoming photon energies while decreasing for higher-Z materials (Fig. 4.53-left). For 59.5 keV, the expected ratio of Photoelectric/Compton interactions with Ar atoms is roughly 0.6/0.4 [9], which is sufficient to be noticeable in the detector response. Due to the low occurrence probability in Bi, and the fact that the volume fraction of this material is residual when compared to Ar, the Compton effect in the nanoparticles is insignificant.

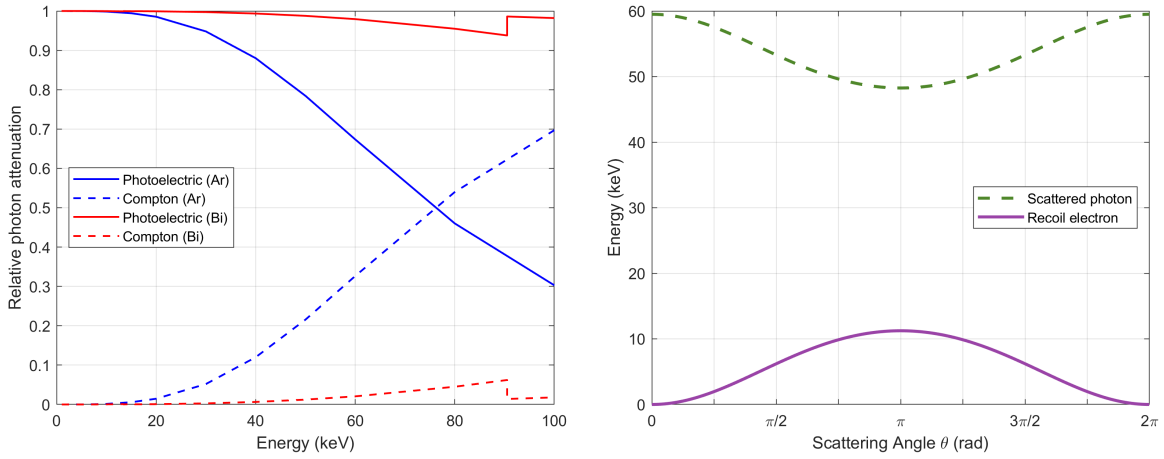

Figure 4.53: Left: Relative photon attenuation by photoelectric and Compton interactions in argon and bismuth (data from [9]). Right: Energy transferred across the scattering angles θ to the scattered photon and recoil electron in the Compton interaction of a 59.5 keV photon.

The energy transferred to the recoil electron depends on the incoming photon energy

and the scattering angle, as postulated by equation (2.15) presented in section 2.1.3. Fig. 4.53-right shows the possible energy range of the recoil electron and scattered photon for incident 59.5 keV photons, as a function of the scattering angle. The maximum electron recoil energy is 11.2 keV, which is why a small step in the number of counts around this value is visible on the simulated detector response of Fig. 4.52-left.

The effect of the Bi_2O_3 nanoparticles in the detector is most evidently manifested by the peaks corresponding to the photoelectrons ejected from the L_1, L_2 and L_3 atomic shells of bismuth, with energies listed in Table 4.1, which arise from the photoelectric absorption of the incident photons by the Bi atoms of the nanoparticles. The kinetic energy of the ejected photoelectron is given by the difference between the energy of the incoming photon and the shell binding energy from which the photoelectron is ejected. Because the K shell binding energy (90.5 keV) is greater than that of the incoming photons, the photoelectric process is impossible to take place in this shell, and the L shell becomes the most likely for this interaction to occur.

Photoelectron shell (binding energy)	Photoelectron kinetic energy	Transition shell (binding energy)	Characteristic x-ray (energy)
L_3 (13.42 keV)	46.1 keV	M_5 (2.58 keV)	$L\alpha_1$ (10.84 keV)
		M_4 (2.69 keV)	$L\alpha_2$ (10.73 keV)
		N_5 (0.44 keV)	$L\beta_2$ (12.98 keV)
L_2 (15.71 keV)	43.8 keV	M_4 (2.69 keV)	$L\beta_1$ (13.02 keV)
L_1 (16.38 keV)	43.1 keV	-	-

Table 4.1: Dominant electron transitions between the shells of a bismuth atom when interacting by photoelectric effect with a 59.5 keV photon.

The high kinetic energy of the photoelectrons assures there is a great probability that they will escape the nanoparticles, losing only a very small fraction of their initial kinetic energy [3], which leads to the very well defined peaks in the simulated detector response. It is also possible for these high energy electrons to transverse the gas volume and reach the detector wall before completely losing their energy in ionization processes in the gas, which contributes to the plateau of uniformly distributed events extending from the maximum photoelectron energy down to zero in the PHS of Fig. 4.52.

The ejection of a photoelectron is accompanied by the emission of characteristic x-rays and/or Auger electrons. The relative probabilities of these effects depend on the material Z number and on the shell in which the photoelectric process takes place. Attending to Fig. 4.54, and taking into account that for Bi ($Z = 83$) the photoelectric effect cannot occur in the K shell for the considered incoming photon energy, the emission of Auger electrons is the dominant electron recombination process for both the L and M shells.

The ejected Auger electrons are mostly distributed across an energy range from 12 keV down to just a few eV (this was verified by the GEANT4 simulation). The projected range of a 12 keV electron in Bi_2O_3 is approximately 400 nm, being reduced to 150 nm for energies around 7 keV [3]. This implies that a significant number of Auger electrons do not have enough energy to escape the nanoparticles, and in such cases only the energy of the photoelectron is deposited in the gaseous volume. When the electron recombination of the Bi atom is achieved via characteristic x-ray emission, the energies of the most intense spectral lines (Table 4.1) are high enough for it to escape the nanoparticle, with a probability higher than 98% [3]. However, they are still inefficiently stopped by the gas (Fig. 4.51), again resulting in the photoelectrons being the sole contributor to the detector

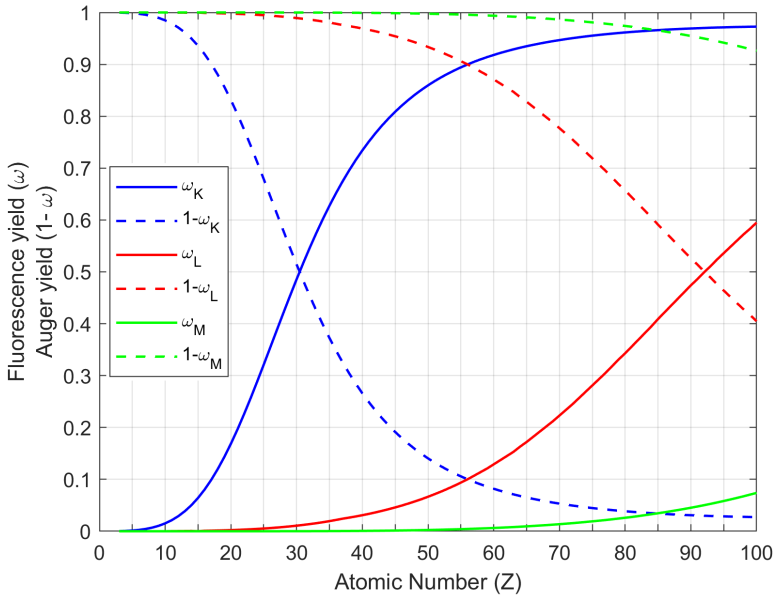

Figure 4.54: Fluorescence (ω) and Auger ($1-\omega$) relative yields for the K, L and M shells across Z. Data from [168].

response. The exceptions of the mentioned behaviours are manifested by the counts in the 46.1-59.5 keV region, attributed to the occasions in which both an L shell photoelectron and the respective characteristic x-rays and/or Auger electrons deposit their energy in the gas. Another relevant, although smaller, contribution to the detector response in this energy range are the photoelectrons emitted from the M shell of Bi, with energies between 55.5 keV and 57 keV.

Finally, the full-energy 59.5 keV peak originates from the photoelectric effect in the Ar atoms of the gas, in which the energy of the photoelectron and the significantly less energetic characteristic x-rays (around 3 keV) and/or Auger electrons is entirely deposited in the gas.

4.9.2 Materials and Methods

A pre-assembled prototype of the aerosol detector, previously used for neutron detection, was used to test this hard x-ray detection concept. The geometry of this detector is similar to the one described in section 4.2.3, with the exception of using a tube with smaller diameter (36 mm) and superior length (250 mm), with CF 43 flanges soldered on its extremities. However, the anode length was approximately the same (200 mm), as was its material and diameter (50 μm gold-coated tungsten wire). Additional differences between this detector and the one used for neutron detection were the fact that its inner walls were not polished, and the addition of a 10 mm diameter window in its centre, made of a 50 μm thick aluminized Mylar film, glued to the detector with a conductive epoxy. A 3D printed anode supporting ring was also used to fix the anode, with three M3 rods that connected it to the top flange, this time made of polyoxymethylene (POM), a high hardness machinable plastic. To prevent nanoparticle leakage to the atmosphere, the detector was also equipped with 0.5 μm particle filters (SS-4-VCR-2-0.5M) on the gas inlet and outlet, and an oil reservoir connected to the detector outlet was used to isolate the detector from the outer atmosphere. A scheme of the detector used in this work is

presented in Fig. 4.55.

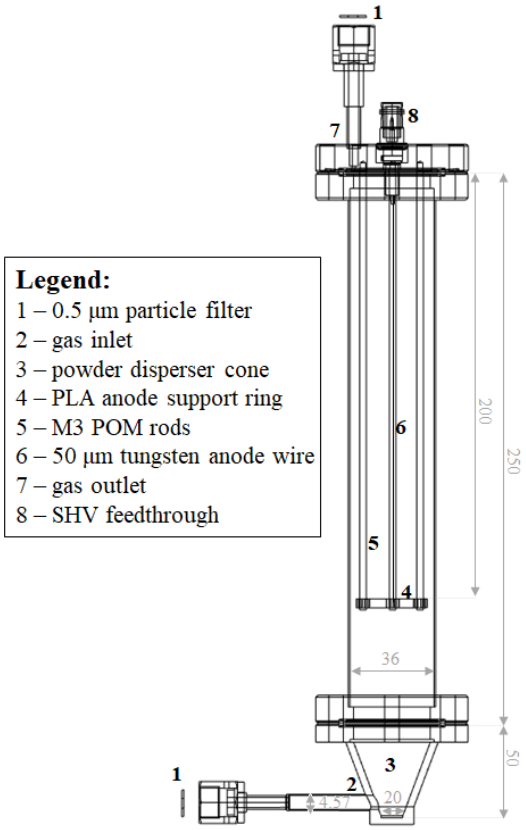

Figure 4.55: Technical drawing of the high-Z nanoparticle aerosol hard x-rays detector prototype.

Bismuth(III) Oxide (Bi_2O_3) nanoparticles from Sigma Aldrich were used (particle size 90-210 nm) to form the aerosol. This substance is not considered to be either persistent, bioaccumulative or toxic [169], and the recommended safety procedures for handling this fine powder are the same as described for the B_4C powder. The counting gas used was P5 (Ar:CH_4 gas in 95%:5% proportion) at atmospheric pressure. The electronics chain in the front-end of the detector was the same as described in section 4.7.

The detector was irradiated, before and after inserting the nanoparticles, with two collimated radioactive sources, in separate moments. A ^{55}Fe soft x-ray (5.9 keV) source was used to study the impact of adding the nanoparticles in the detector gain curve, by making successive acquisitions varying the anode bias voltage between 1700 V and 2050 V in 50 V steps, before and after inserting the Bi_2O_3 nanoparticles. An ^{241}Am gamma-ray (59.5 keV) source was used to compare the detection efficiency obtained before and after forming the aerosol, also by acquiring spectra for several anode polarizing voltages before and after the addition of the fine powder. Both sources were placed immediately in front of the detector window, in a fixed support with marks to ensure, as much as possible, that the sources were kept in the same position and orientation throughout every measurement.

After the acquisitions without the Bi_2O_3 nanoparticles, a few grams of this material were placed in the dispenser cone, immediately in front of the detector inlet. Before the new set of measurements, the gas was allowed to flow through the detector at a rate of 15 l/h, to disperse the nanoparticles and form the aerosol. Afterwards, the flow rate was adjusted to 8 l/h, a value kept constant throughout measurements.

4.9.3 Results and Discussion

An example of a PHS acquired with the ^{55}Fe source to calculate the gas gain curve is presented in Fig. 4.56, already with the Bi_2O_3 powder inside the detector. The energy resolution measured for the 5.9 keV peak was 17.6%. This peak corresponds to the Kα line of ^{55}Mn, to which ^{55}Fe naturally decays by electron capture. The smaller amplitude peak in the curve fitting (grey dashed lines) centred at 6.5 keV corresponds to the Kβ emission, and was not accounted for in FWHM calculation of the 5.9 keV peak.

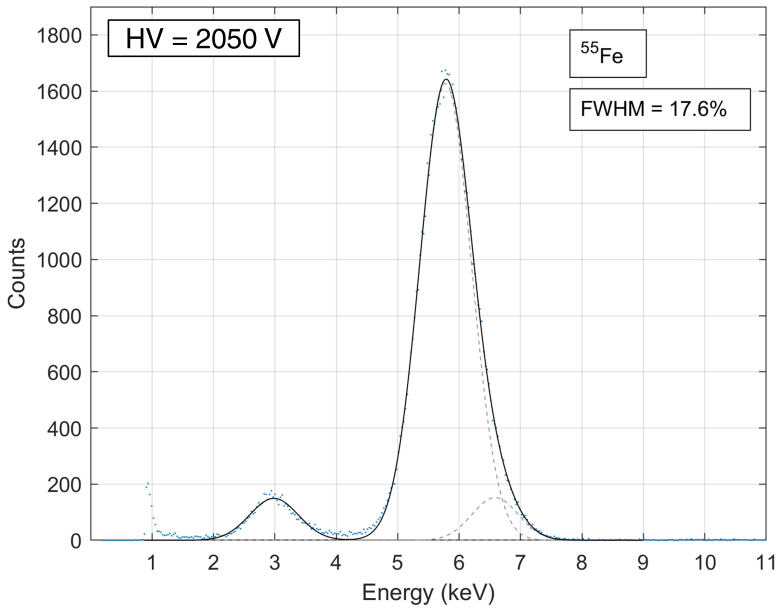

Figure 4.56: PHS of the Bi_2O_3 aerosol detector irradiated by a ^{55}Fe source. The energy resolution (FWHM) for the 5.9 keV peak was of 17.6%. The dashed grey lines correspond to two Gaussian curves centred at 5.9 keV and 6.5 keV, corresponding respectively to the Kα and Kβ transitions of ^{55}Mn. Acquisition time = 300 seconds.

A decrease in the detector gain with the presence of the Bi_2O_3 nanoparticles was observed, as evidenced by the gas gain curve in Fig. 4.57. This had also been observed with the B_4C particles in the neutron aerosol, as explained in section 4.3. Similarly, this can be easily compensated by increasing the anode voltage.

The main purpose of this study was to experimentally verify if the addition of high-Z nanoparticles to a gas filled proportional counter would improve the detector efficiency for hard x-rays and gamma-rays. In that regard, the PHS acquired with irradiation of 59.5 keV gamma-rays from an ^{241}Am source shows an increment of about 3.6 times in the number of counts (area under the peak curve) for this energy after inserting the Bi_2O_3 nanoparticles, as depicted in Fig. 4.58.

The spectra with and without nanoparticles correspond to acquisitions made with an anode bias voltage of 2050 V and 2000 V, respectively. These were the selected voltages to compare the detector responses because its gain is similar in both cases, evidenced by Fig. 4.57.

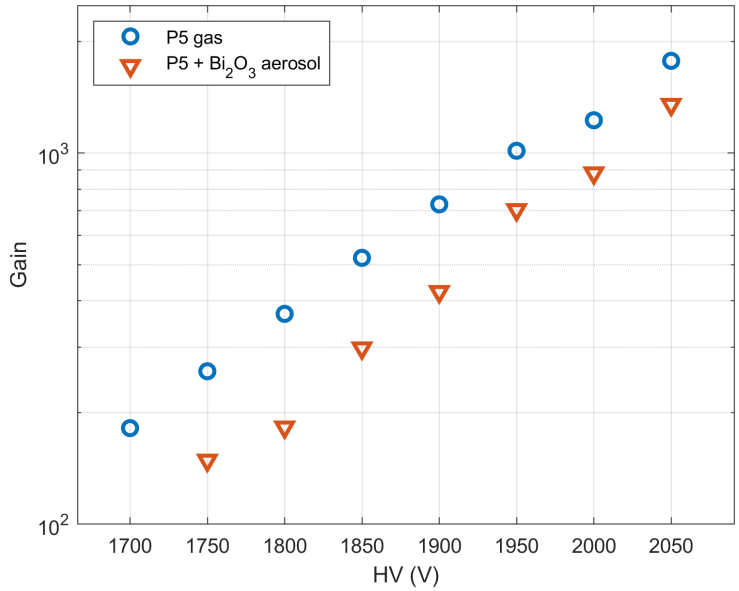

Figure 4.57: Logarithmic plot of the gas gain measured for each anode voltage without (blue circles) and with (red triangles) Bi_2O_3 nanoparticles dispersion.

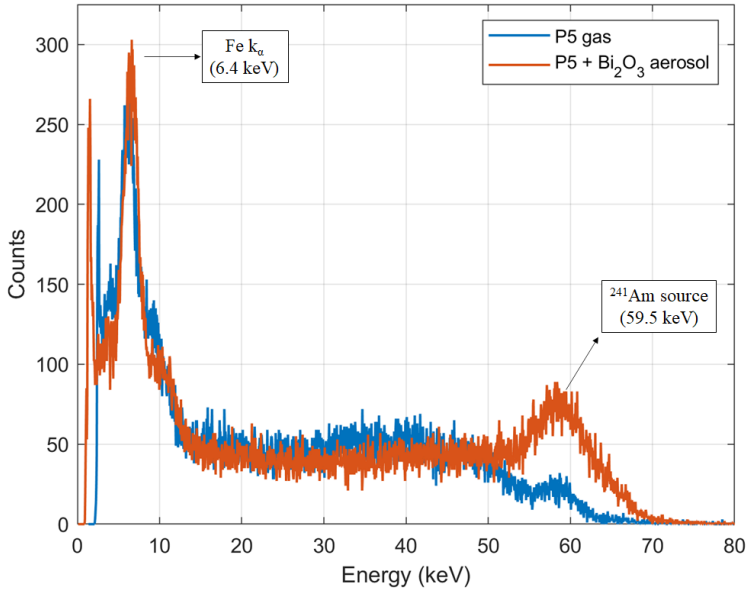

Figure 4.58: Energy calibrated PHS registered with (red plot, HV = 2050 V) and without (blue plot, HV = 2000) Bi_2O_3 nanoparticles in the detector, irradiated by gamma-rays from a ^{241}Am source. The relative positions of the source and the detector were the same for both acquisitions, as was the acquisition time (300 seconds).

The ^{55}Fe source was also used for energy calibration of the spectra acquired with the ^{241}Am source, since its 5.9 keV line and the argon escape peak at 2.9 keV can be clearly resolved, as was seen in Fig. 4.56. To do this, the ^{241}Am source was replaced by the ^{55}Fe source as soon as the acquisition was through, while keeping every detector operation parameter unchanged, and a new acquisition was made.

A decent agreement was achieved between simulation and experimental results, despite the limitations of developing a realistic simulation of an aerosol detector. In fact, several simplifications had to be made in the simulations, such as the number of suspended particles, their diameter and distribution and the fact that they were static. These simplifications can help to explain the differences between the simulation and experimental results, namely the inferior number of counts in the 40 keV - 50 keV region. For instance, the case might be that in the real detector, the average particle diameter of the suspended particles was inferior to that considered in the simulations (150 nm). This would translate into a higher probability of the Auger electrons, emitted along with the photoelectron in the photoelectric effect, escaping the Bi_2O_3 nanoparticles, and consequently a smaller intensity of the escape peaks in the mentioned energy range.

Finally, it is important to regard that, similarly to the neutron aerosol detector, it is expected that a fraction of the photon interactions occur in nanoparticles that get attached to the detector walls. Unlike the neutron nuclear capture reaction, the particles released in the photoelectric effect (photoelectron, characteristic x-ray and Auger electrons) are not necessarily emitted in opposite directions, and consequently there is no wall-effect. Therefore, even photon interactions occurring in particles attached to the wall can contribute to the full peak visualized in Fig. 4.58. After finishing the experimental work, it was verified that the particle filter in the top inlet had a significant amount of nanoparticles lodged, similarly to what had previously been observed in Fig 4.22-left for the B_4C powder, which indicates that the nanoparticles were indeed in suspension during measurements. Therefore, it is reasonable to assume that the increase in detection efficiency for the 59.5 keV peak can be attributed to interactions occurring both in suspended and attached nanoparticles. Additionally, an interaction occurring in an attached particle would not contribute as much to the full energy peak, when compared to a suspended particle. This is because, for the former, there is a probability of $\sim$50% that one or several of the particles generated in the photoelectric effect are emitted towards the wall, and consequently of not depositing its energy on the counting gas. This would lead to an increase of the escape peaks amplitude, which was not observed in the acquired spectra.

In conclusion, it was demonstrated that it is possible to increase the detection efficiency of a proportional counter for high energy photons by forming an aerosol composed by high-Z nanoparticles. In this experimental work, an increase in counts by a factor of 3.6 was observed for the 59.5 keV peak from an ^{241}Am gamma-ray source, using Bi_2O_3 nanoparticles dispersed in P5 gas. These preliminary results can be relevant in the development of this technique for the detection of hard x-rays or gamma-rays in applications where gaseous detectors are convenient, for instance due to their inexpensive cost and when large dimension detectors are required.

5 Thin Film Coincidence Detector

Modern large-scale neutron research facilities around the world, which combined count every year with thousands of experiments that involve neutron irradiation over a wide range of scientific fields, are complex infrastructures which harmoniously integrate advanced technologies for the production, moderation, guiding and detection of neutrons. On the end of this chain, these facilities rely on high performance position sensitive neutron detectors (PSND), in aspects such as detection efficiency, counting rate capability and spatial resolution [170].

Specifically, when construction of ESS is finished (user programme is expected to begin in 2023 [19]), it will provide the highest neutron beam brightness ever achieved. To take full advantage of this power, detector features must be improved to a point beyond the performance capability limits of ^{3}He detectors (namely in what regards position resolution and counting rate [83]), which allied to the severe shortage of this material, exposed in section 3.2, makes it imperative to develop suitable ^{3}He-free neutron detectors.

On the previous chapter, a boron aerosol detection alternative was presented. However, the non-fixed nature of the micro/nanoparticles as they are suspended by the gas flow makes it ineligible for use in imaging applications or in instruments that require millimetric ou submillimetric position resolution, since it is impossible to predict or identify the precise location of the fine powder boron particle in which the neutron capture occurred.

In this chapter, the idea of using submicrometric materials for neutron conversion will be elaborated, this time focusing on improving the spatial resolution of gaseous PSND. The idea revolves around tackling one specific position resolution limiting factor on such detectors: the fact that the range of the secondary products from the neutron capture reaction extends for several millimetres in gases at atmospheric pressure, which, at least for some neutron detectors [126], is claimed to be the biggest source of uncertainty for the determination of the neutron capture interaction site.

Here will be presented the operation principle, simulation results and first development stages of a novel neutron detection concept which consists of deploying micrometric/submicrometric neutron detection layers to allow for both secondary particles from the neutron capture reaction to escape it, and take advantage of the fact that these are emitted on opposite directions along the same line to pinpoint the spatial coordinates in which the neutron was captured. Because each secondary particle is detected independently and they are identified to have originated from the same neutron capture reaction through temporal coincidence, we designate this concept as the "coincidence detector".

5.1 Limitations of Gaseous Boron PSND

Since the secondary particles from the ^{10}B reaction have a range of only a few micron in solids, increasing the thickness of the conversion layer only leads to an increase in neutron detection efficiency up to a certain limit, as previously discussed in section 3.4.1. After that, the reaction products can no longer reach the gas and are absorbed in the solid layer, resulting in undetected neutron captures. When looking at the effect of converter thickness in the efficiency of boron coated detectors, it is important to distinguish between two possible scenarios depending on the neutron incidence direction: back scattering mode and transmission mode (Fig. 5.1-left).

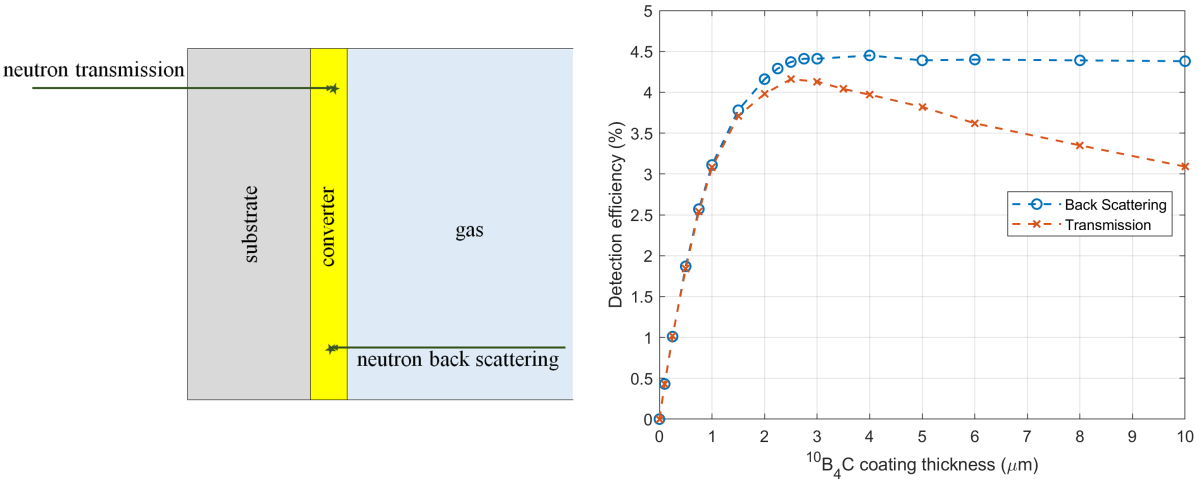

Figure 5.1: Left: Comparison of the geometrical layout of a neutron interaction in transmission mode and back scattering mode. Right: Detection efficiency yield of GEANT4 simulations of a gaseous detector with a single ^{10}B-enriched B_4C layer of variable thickness, for neutron incidence in transmission mode and backscattering mode.

In back scattering detections, the neutron beam is incident from the gas side, meaning that the neutrons that are captured never traverse the substrate. In this case, detection efficiency increases with coating thickness, as more ^{10}B atoms lead to more neutron captures. However, this increase tends to stabilize, reaching a maximum value, after which it plateaus. This saturation arises from the limited range of the secondary particles of the ^{10}B reaction in solids, which is of just a few microns. When a neutron capture occurs at a depth greater than the secondary particles range, these are unable to reach the gas, and such interactions are consequently undetectable. For a perpendicularly incident beam of thermal neutrons, the maximum detection efficiency achievable by a ^{10}B-enriched B_4C coating is approximately 4.5% (considering a gamma discrimination threshold of 100 keV), reached at a thickness of 3 μm (Fig. 5.1-right). While higher efficiencies are achieved with colder neutrons, for which ^{10}B presents higher neutron capture cross-section, the 3 μm thickness saturation is independent of the neutron energy, as the secondary particles are emitted with the same energy and therefore have the same range in the converter.

When neutrons interact in transmission mode, the substrate or wall on which the boron layer is deposited is the first region to be traversed. A similar trend to back scattering mode is initially observed, with efficiency increasing up to a thickness limit, which in transmission mode is approximately 2.5 μm. However, this now corresponds to

a maximum value after which detection efficiency begins to drop, as increasingly more neutrons are absorbed before reaching the converter region where the secondary particles could potentially reach the gas (Fig. 5.1-right). For B_4C thicknesses beyond $\sim 100\mu$m, neutrons are no longer transmitted, being fully absorbed by the converter.

In boron-lined proportional counters, the coating is performed in the inner walls, and as so both transmission and back scattering occur. Due to their cylindrical geometry, neutrons enter the detector in transmission mode, traverse the gas (in case they are not captured), and can back scatter in the diametrically opposite coating side. As a result, the efficiency of a single boron-lined proportional counter consists of the sum of the individual efficiencies in transmission and back scattering mode. Indeed, the GEANT4 simulation of a 50 mm diameter boron-lined cylinder (Fig. 5.2) yields a detection efficiency similar to the sum of the two plots of Fig. 5.1-right.

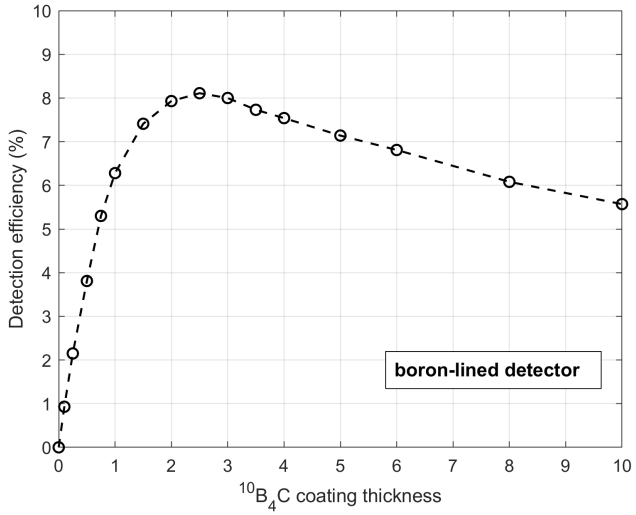

Figure 5.2: Detection efficiency yield of GEANT4 simulations of a 50 mm diameter boron-lined proportional counter with variable $^{10}B_4C$ coating thickness.

As seen, increasing the thickness of the neutron conversion material is only effective up to a certain point. Higher efficiencies can nevertheless be achieved using two independent strategies. The first consists of stacking several consecutive detection layers [97, 105, 109, 171], in such way that neutrons transverse more boron content without increasing the thickness of any individual layer in which the neutron may be captured, and consequently not decreasing the probability of the secondary particles escaping the conversion layer. In order to optimize detection efficiency, the ideal coating thickness of each individual layer reduces as the number of stacked layers increases.

The second alternative comprises tilting the detection layer [111, 114] in such way that neutrons are incident at a grazing angle, typically in the range 5°-10°, in which detection efficiency rapidly increases as the incidence angle decreases (Fig. 5.3-right). As a result, neutrons traverse more conversion material, proportionally to $t/\sin\theta$, t being the coating thickness and θ the incidence angle (Fig. 5.3-left), while the secondary particles have the same probability of escaping the layer because the actual thickness of the converter is not increased. This strategy results in a 5.8 factor path increase for a 10° angle, and a 11.5 factor for 5°. Decreasing the incidence angle below 5°may not be advantageous, not only due to technical difficulties, but also because neutron reflectivity begins to play a significant role, especially for colder neutrons, which not only reduces the maximum

achievable detection efficiency but can also generate a source of background in the detector due to unwanted deflections of neutrons [172].

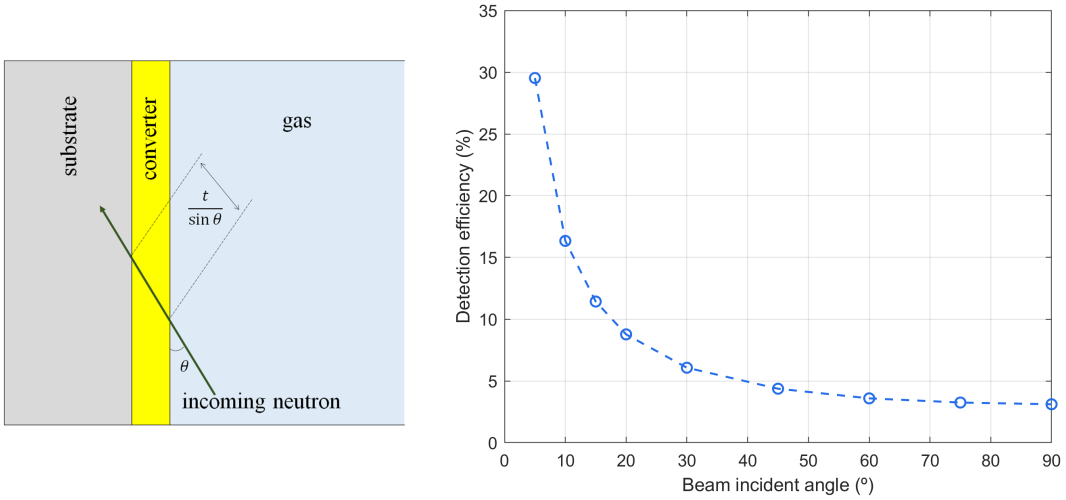

Figure 5.3: GEANT4 simulation of the detection efficiency of a gaseous detector with a 1 μm thick $^{10}B_4C$ layer, for multiple neutron incidence angles in back scattering mode.

Upon a neutron capture in which the ^{7}Li or α particles escape the conversion material, and assuming that they are fully stopped by the gas, the ionization of the gas generates a number of electron-ion pairs proportional to the energy with which the particles escaped the conversion layer. These are created along the tracks of the particles in the gas, which can extend up to several millilitres for gases at atmospheric pressure. Figure 5.4 shows the simulation results of the range distribution of the boron neutron conversion reaction products originated in a 3 μm thick ^{10}B-enriched B_4C layer as they penetrate Ar:CO2 (90%:10%), a commonly used gas in boron-coated gaseous detectors, at atmospheric pressure. An energy cut of 100 keV was applied, which results in a near absence of histogram counts for ranges under 1 mm.

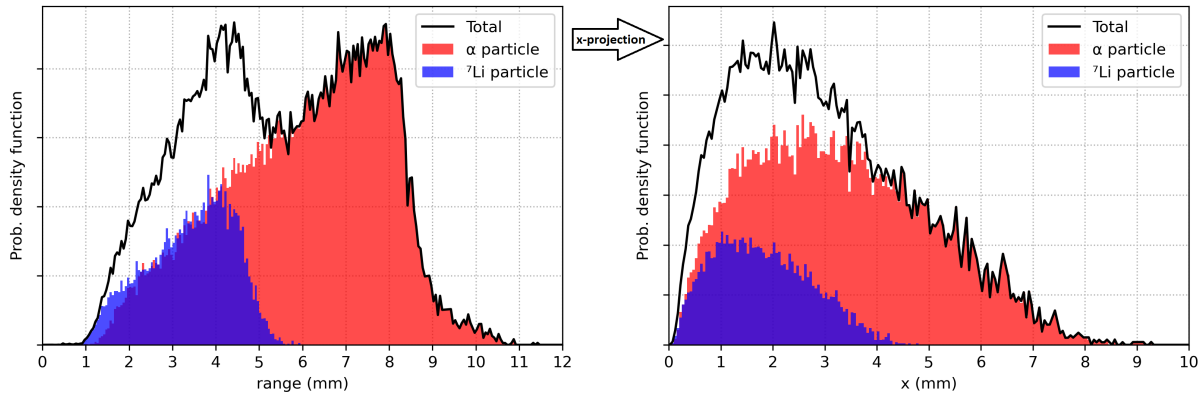

Figure 5.4: Distribution of ^{7}Li and α particle ranges emerging from a 3 μm ^{10}B-enriched B_4C layer into Ar:CO2 (90%:10%) gas at atmospheric pressure, with incident thermal neutrons from the gas side (back scattering mode). An energy cut of 100 keV was applied, which results in a near absence of histogram counts for ranges under 1 mm.

The simulation indicates that the total range of the ^{7}Li and α particles can extend from zero to about 11 mm, depending on the depth at which the nuclear capture occurs and the

direction in which the particles are emitted. If we consider the projection of the track on a single dimension, e. g. the x coordinate, the maximum projected range is approximately 8 mm. Consequently, the trail of electron-ion pairs generated along the tracks of the particles can also extend for a similar range. These are accelerated by a uniform electric field and collected by a readout electrode, which gives the unidimensional or bidimensional information of the particle track. Typical readouts consist of multi-wire proportional counters (MWPCs) [109], strip planes [100] or padded anodes [37, 121, 173]. MWPCs can simultaneously induce the Townsend avalanche multiplication of the primary electrons, and are capable of 2D position by applying the charge division method using resistive wires [107, 128, 174]. Strip planes and padded anodes require the use of a separate mechanism for charge multiplication, such as gas electron multipliers (GEMs) [117]. While anode pads are intrinsically capable of 2D resolution, as they generally are two dimensional structures, to obtain 2D information on the particle trajectory using exclusively strips planes, 2 perpendicular sets can be used, each resolving one dimension [175]. Other common strategy is to perpendicularly combine anode wires with cathode strips, to respectively pick up the electrons and ions from the Townsend avalanche multiplication [114].

To optimize spatial resolution, it is desirable to have a minimal distance between each individual wire, strip or pad cell (pitch). However, it is technically challenging to reach sub-millimetre pitches, and typical values are of a few millimetres [86]. Often, several individual readout units are triggered by the ^{7}Li and α particles tracks in the gas, which causes an indetermination of the position of the neutron interaction. Also, the energy lost by the particles along the tracks is not constant, nor necessarily greater at the beginning than at the end of it. In fact, for α particles that escape the conversion layer preserving a big fraction of their initial energy, the number of generated primary electrons and consequently the readout signal increases at the end of the track (Fig. 5.5), which adds complexity to the estimation of the neutron interaction site.

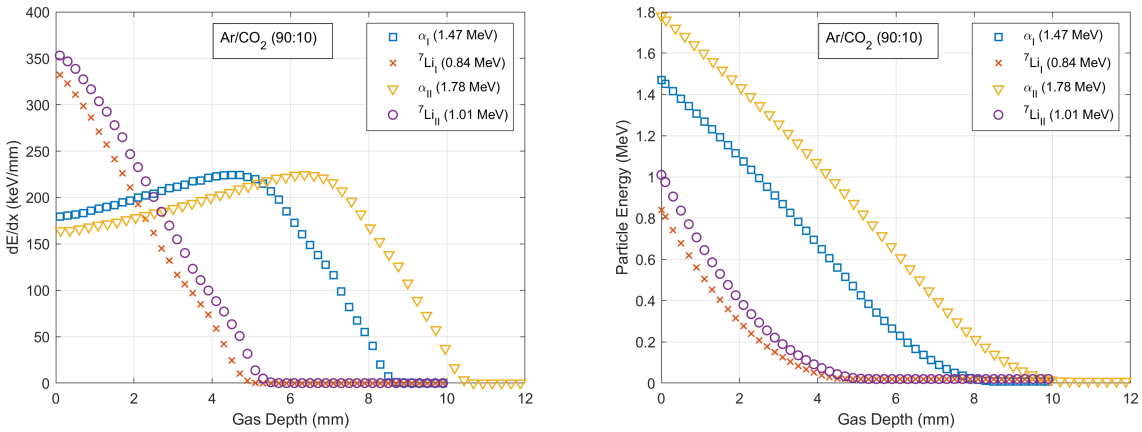

Figure 5.5: Stopping power (left) and remaining energy (right) of the ^{10}B neutron capture reaction products along their path in Ar:CO2 (90%:10%) at atmospheric pressure, for ^{7}Li and α particles entering the gas layer perpendicularly. Values derived from SRIM simulations [5].

As consequence, the long particle tracks in the gas intrinsically limit spatial resolution of PSND, being in some cases reported as the larger contributor to the uncertainty associated to position resolution [126]. To compensate for this, the centre of gravity

method can be used in which a large number of neutron events, isotropically distributed around the coordinates of the neutron interaction site are necessary for its identification [176].

Increasing gas pressure would reduce the range of the ^{10}B reaction secondary particles and consequently reduce uncertainty in the neutron position reconstruction. However, it brings problems of its own, such as requiring the detector to operate at higher voltages to maintain charge gain. It also poses a mechanical challenge for two dimensional wire chambers of reasonable size [127]. Additionally, withstanding a substantial pressure differential would require the use of thicker entrance windows, which in turn increases the probability of neutrons being scattered or absorbed before reaching the sensitive region of the detector, especially at higher neutron wavelengths [177]. The probability of neutron interactions with the gas also increases, which may cause neutron scattering before reaching the conversion layer, deflecting their trajectory, and being captured and detected in a position which does correspond to their original flight path, resulting in an additional background source for PSND. The possibility of having thin entrance windows and low gas pressures also reduces the sensitivity to gamma-ray, which is, as previously discussed, other undesired background source.

In light of the described limitations of conventional boron-coated detectors, a novel strategy to improve the spatial resolution of PSND is proposed: using a thin (submicrometric) layer of a ^{10}B-containing material deposited on an thin substrate, in such way that both fission fragments escape the solid layer. Independent readout structures on opposing sides of the detection layer simultaneously detect the track of each particle. Because the particles are emitted along the same line, by combining the time coincident information of each readout we obtain a more complete profile of the ^{10}B neutron capture reaction, and can pinpoint the neutron interaction site even for a single neutron capture. Attending to its operation principle, we designate it as the "coincidence detector".

5.2 Operation Principle

Although the range of the ^{7}Li and α fission fragments emitted in the ^{10}B neutron capture reaction in most solids is only of a few microns, conventional boron-coated gaseous neutron detectors use conversion layers with a combined (converter plus substrate) thickness of at least hundreds of microns, frequently extending to millimetres. Therefore, the extraction of the neutron interaction site information for each neutron detection takes into account only one of the fission fragments, which is isotropically emitted and consequently will leave a track of electron-ion pairs along a random direction in the gas. The precise location of the neutron capture site is therefore impossible to determine from a single neutron capture, since the primary ionizations track will extend over several millimetres, which in turn results in a readout charge collection across several millimetres as well. That could, however, be achievable if the track of the other fission fragment, simultaneously produced and emitted along the same line, was to be known. This would require the independent detection of each particle and a subsequent reconstruction of the common origin of both tracks. Such method has the advantage of requiring less statistics for neutron position determination, meaning less beam time or the efficient use of less intense sources. Another consequence is that the detector could afford to be less efficient, because identical precision in the interaction site reconstruction could be derived from less neutron captures, which in term reduces the counting rate.

Let us consider the two-dimensional projection (z,x) of the reaction products of a neutron capture occurring at the centre of what will be designated as the coincidence detector, depicted in Fig. 5.6, obtained through GEANT4 simulation.

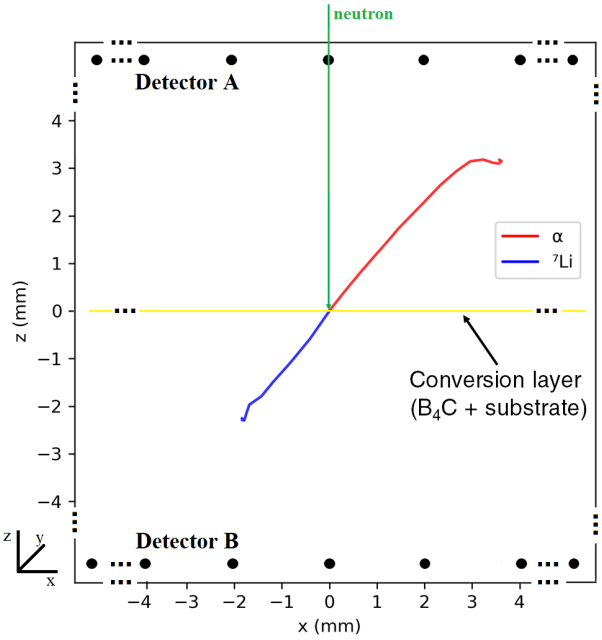

Figure 5.6: Scheme of the neutron coincidence detector operation principle, in which both reaction products from the ^{10}B reaction are independently detected at coincident times. Two separate readout systems (detector A and detector B) are used to detect each particle, emitted from a conversion layer made of 1 μm $^{10}B_4C$ symmetrically deposited on a 0.5 μm Mylar substrate.

Detectors A and B represent two independent readout structures, which can, for instance, be two MWPCs. For simplicity, we focus on determining the neutron interaction site along a single coordinate (in this case, x) but the same conclusions could be withdrawn for two dimensions (x,y), simply by considering that each of the detectors A and B are composed of two perpendicular sets of wires or a combination of wires and strips. If the solid layer composed by the boron material plus the substrate is thin enough, and a neutron capture reaction occurs, it is possible for both fission fragments to escape it, and ionize opposite regions of the surrounding gas. If a positive high voltage is applied to the electrodes of detectors A and B, while keeping the solid conversion layer at ground potential, an electric field is established that will accelerate the primary electrons generated along the ionizing tracks of each particle to its respective detector. For the specific neutron capture depicted in Fig 5.6, neglecting the diffusion of electrons in gas as they are accelerated towards the anode wires, the x-projection of the α particle track seen by detector A would extend for approximately 4 mm, while the x-projection of the ^{7}Li ion seen by detector B would extend for approximately 2 mm. Because each detector is composed of discrete wires, this means that several of them would be triggered. The neutron interaction position estimation would depend on the charge collected by each wire, which in terms depends on the way that the fission fragments lose energy along their tracks, which varies depending on the energy with which the particles escape the solid layer. As an example, the estimation of the neutron capture position for the specific track represented in Fig 5.6 would lay between 0 mm and 4 mm for the α particle (detected

by detector A) and between -2 mm and 0 mm for the ^{7}Li ion (detected by detector B). However, correlating the information of both detectors, by averaging the neutron capture site estimated by detector A and B would yield a value closer to 0 mm, i.e., the actual site of the neutron interaction. As will be seen ahead, this average is not necessarily the geometric average. The energy deposited by each particle on the gas is proportional to the collected charge, and this information can be effectively used to improve the neutron interaction site reconstruction.

5.3 Materials

The materials to consider in the development of the coincidence detector are mainly divided into 3 categories: neutron converter, substrate and filling gas.

Regarding the gas, any typical affordable proportional gas based on a mixture of a noble gas and a molecular gas for quenching is suitable. P10, a mixture of 90% Ar with 10% CH_4 is often regarded as the most preferred gas in proportional counters. However, among gases, hydrogen has by far the highest neutron scattering cross-section [178]. In case of interaction, this causes neutrons to deflect their trajectory towards the conversion layer, and end up either not traversing it, which results in efficiency loss, or being converted and detected in a position that does not reflect the original neutron direction, contributing to an additional neutron position determination uncertainty. For this reason, H-containing gases are generally avoided and the quenching gas choice often falls on CO_2.

The choice of the neutron conversion material is mostly restricted by the neutron capture absorption cross-section. As overviewed in section 2.2.4, other than ^{3}He, only a few stable isotopes have an appreciable thermal neutron capture cross-section, namely ^{6}Li, ^{10}B, ^{113}Cd, ^{155}Gd and ^{157}Gd. Despite having the largest neutron capture cross-section, gadolinium and cadmium are not the most convenient to use in detectors due to the nature of their neutron capture reaction, which results in the emission of high energy gamma-rays, which are virtually undetectable by gaseous detectors, and conversion electrons with inferior energy and stopping power than the fission fragments of the ^{6}Li and ^{10}B reactions.

The remaining solutions are then ^{6}Li and ^{10}B, which dominate the ^{3}He-free detector alternatives. Both can be used in their elemental forms or in compounds, such as B_4C (boron carbide), BN (boron nitride) and LiF (lithium fluoride). Because compounds are formed by elements with different neutron capture cross-sections, it is typically the neutron absorption length (λ) that is considered to quantify neutron capture probability, which is the inverse of the absorption coefficient (α), given by:

$$\alpha = \frac{1}{\lambda} = N\sigma = \frac{\rho N_A}{M}\sigma \tag{5.1}$$

where σ is the neutron capture cross-section and N the atomic number density (number of nuclei per unit volume), which is related to the density of the material (ρ), the molar mass (M) and the Avogadro constant (N_A).

The attenuation of neutrons traversing a given material is given by:

$$\frac{I(x)}{I_0} = e^{-\frac{x}{\lambda}} \tag{5.2}$$

where $I(x)/I_0$ corresponds to the fraction of neutrons transmitted after a travelled distance x. Thus, for materials that have a neutron capture cross-section much higher than

the neutron scattering cross-section, the probability of a neutron not being transmitted, i.e., being captured over a distance x in a given material is:

$$p(x) = 1 - e^{-\frac{x}{\lambda}} \tag{5.3}$$

and consequently a function of the thermal neutron absorption length. Analysing equation (5.3), it is evident that a good neutron converter should have a small λ, which maximizes $p(x)$. The values of λ for each potential neutron converter here considered are presented in Table 5.1.

Material	λ (μm)
^{10}B	20.0
$^{10}B_4C$	23.0
^{10}BN	47.3
^{6}LiF	173.9
^{6}Li	229.6

Table 5.1: Absorption length of thermal neutrons in ^{10}B, $^{10}B_4C$, ^{10}BN, ^{6}Li and ^{6}LiF, enriched by their neutron sensitive isotope.

The plot of equation (5.3) (Fig. 5.7), shows that for any of the considered converters, the thickness range of a few micron typically used in neutron detectors is far from their full potential for neutron absorption.

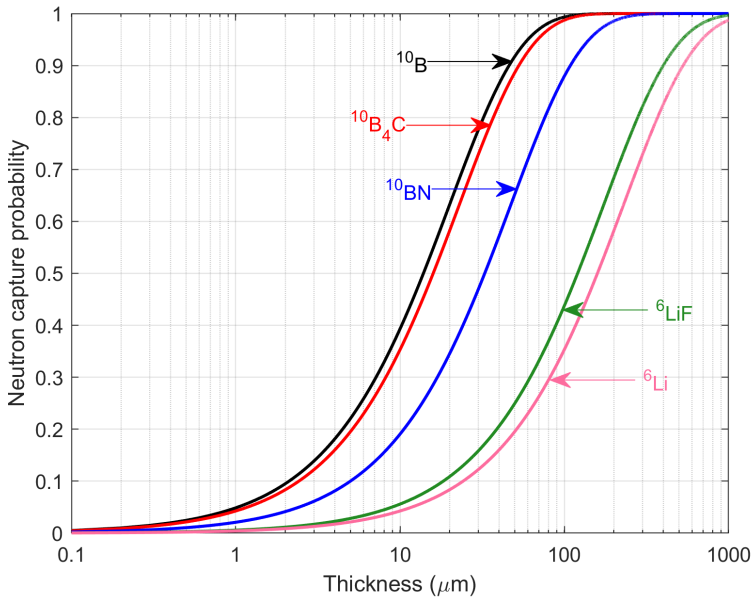

Figure 5.7: Neutron capture probability for thermal neutrons, calculated from the neutron absorption length for ^{10}B, $^{10}B_4C$, ^{10}BN, ^{6}Li and ^{6}LiF (enriched in their neutron sensitive isotope).

The choice for such relatively low thicknesses derives from the limited ranges of the neutron capture reaction products in solids. Hence, the selection of the converter thickness is based on optimizing the compromise between the number of neutrons that are captured, and the number of neutrons whose capture reaction occurs near enough the surface so

that the secondary products manage to reach the gas to be detected. It is then important to have a precise notion of the range of the secondary particles from the neutron capture reaction in the relevant materials, which was calculated with the SRIM software [5]. Table 5.2 shows the Continuous Slowing Down Approximation (CSDA) range (defined as the mean free path of a charged particle in an absorber) of the ^{10}B and ^{6}Li neutron capture reaction reaction products in the regarded conversion and substrate materials, as well as in Ar:CO_2 (90%:10%) gas at atmospheric pressure.

	^{10}B Reaction (94% branch)		^{10}B Reaction (6% branch)		^{6}Li Reaction	
	^{7}Li* (0.84 MeV)	α (1.47 MeV)	^{7}Li (1.01 MeV)	α (1.78 MeV)	α (2.05 MeV)	^{3}H (2.73 MeV)
^{10}B	1.8 μm	3.5 μm	2.1 μm	4.4 μm	-	-
$^{10}B_4C$	1.6 μm	3.2 μm	1.8 μm	4.0 μm	-	-
^{6}Li	-	-	-	-	23.2 μm	133.0 μm
^{6}LiF	-	-	-	-	6.1 μm	31.0 μm
Mylar	3.3 μm	6.1 μm	3.6 μm	7.4 μm	8.7 μm	51.8 μm
Kapton	3.3 μm	6.0 μm	3.6 μm	7.3 μm	8.6 μm	51.2 μm
Al	2.3 μm	4.7 μm	2.6 μm	5.7 μm	6.7 μm	38.0 μm
Ar/CO_2	4.3 mm	8.1 mm	4.8 mm	9.9 mm	11.6 mm	66.5 mm

Table 5.2: CSDA range of the ^{10}B and ^{6}Li neutron capture reaction in the relevant neutron converters, substrate materials, and in Ar:CO_2 (90%:10%) gas at atmospheric pressure.

Besides the physical characteristics of the converter materials discussed, it is also important to take into account their chemical characteristics, which end up being a decisive factor. On this matter, ^{6}Li, the lightest and most electropositive metal, is extremely reactive, corrosive and flammable, which makes for complicated handling procedures and inconvenient to use in detectors, since it reacts even with the argon present in proportional gases [179–181]. Therefore, the stable compound ^{6}LiF is preferred. However, like most inorganic fluorides, this compound is GHS (Globally Harmonized System) classified as "acutely toxic" and "irritant" [182], requiring special safety precautions for its manipulation, which adds a complexity layer in substrate deposition and assembling in a detector.

Due to these limitations, along with the fact that the ^{6}Li isotope has an inferior thermal neutron capture cross-section, which intrinsically reduces detection efficiency by $\sim 75\%$ compared to ^{10}B, boron alternatives are more vastly deployed. Among these, elemental boron is prone to oxidation and has poor electrical conductivity (ρ(B) $\sim 10^{6}$ Ω·m), which is a drawback both for its deposition on a substrate, and application in detectors where it serves as a cathode. Thus, the most stable compound of boron, B_4C, is generally preferred: it is not only more affordable, but also has excellent thermal stability, chemical resistance, mechanical properties (high hardness) and better conductivity ($\rho(B_4C) \sim 10^{-3}$ Ω·m) [183, 184]. Studies have also shown that $^{10}B_4C$ films are not damaged by radiation during many years in a neutron detector, which discards critical ageing effects [185]. BN is a common choice among semiconductor neutron detectors due to its wider bandgap (5.5-6.5 eV), compared to B_4C (1.9-2.4 eV), which allows for operation at higher voltage with reduced leakage currents [186–188]. However, it is not a common choice in gaseous

detectors since it does not have any other particular characteristic superior to B_4C and has lower neutron capture probability. And so, assessing all potential conversion materials, B_4C can be regarded as the most advantageous.

Focusing now on the substrate, three potential materials were considered: aluminium, Mylar and kapton. The most decisive parameters to attend to are the mechanical capability to endure the converter film deposition process, density, neutron transparency, and availability in thin enough films.

Aluminium, Mylar and Kapton are among the popular substrate materials suitable for film deposition techniques such as magnetic sputtering and chemical vapour deposition (CVD), with aluminium being the most frequently used for B_4C deposition in neutron detectors. However, unlike the detector here proposed, conventional neutron detectors do not have to consider the energy lost by the secondary particles in the substrate, which depends on the material density, since the active detection region is only on the converter side. Both Mylar, the commercial name for BoPET (biaxially-oriented polyethylene terephthalate) and kapton, have inferior density (1.40 g/cm^3 and 1.42 g/cm^3, respectively) than Al (2.7 g/cm^3), which results in a larger range of the neutron capture reaction products in these materials (Table 5.2), and can positively impact the coincidence detector.

On the other hand, because both Mylar ($C_{10}H_8O_4$) and kapton ($C_{22}H_{10}N_2O_5$) are hydrogen rich compounds, they are expected to be less transparent to neutrons than Al, i.e., more prone to scattering. This was examined through GEANT4 simulations, making a punctual thermal neutron beam transverse a wall of variable thickness for each substrate material considered, and a sensitive detector of residual size aligned with the beam on the opposite side of the wall, in such way that only neutrons that were not scattered would reach the sensitive volume (Fig. 5.8).

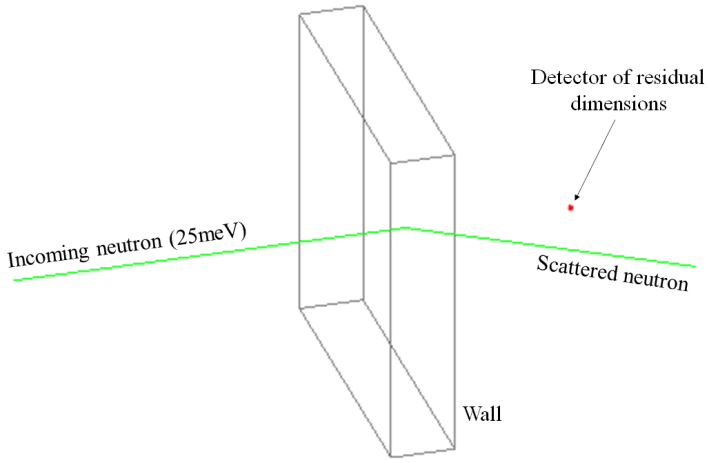

Figure 5.8: GEANT4 simulation of a punctual thermal neutron beam traversing a wall of variable thickness to determine the impact of neutron scattering in aluminium, kapton and Mylar.

Vacuum was defined as the surrounding material to ensure that scattering occurred only on the wall. The simulation output (Fig. 5.9) showed, as expected, that aluminium is significantly less prone to neutron scattering than the hydrogenated materials. Among kapton and Mylar, the first one is also superior in terms of neutron transmission. This concern becomes more relevant in a scenario where consecutive detection layers are

stacked to improve detection efficiency. But even in that case, considering 10 stacked 1 μm layers, which add up to an overall substrate thickness of 10 μm, the calculated neutron transmission was of 99.99% for aluminium, 99.90% for kapton, and 99.86% for Mylar, which indicates that neutron transparency is not a decisive factor in the substrate selection, and should have an overall relative small impact in the performance of the detector.

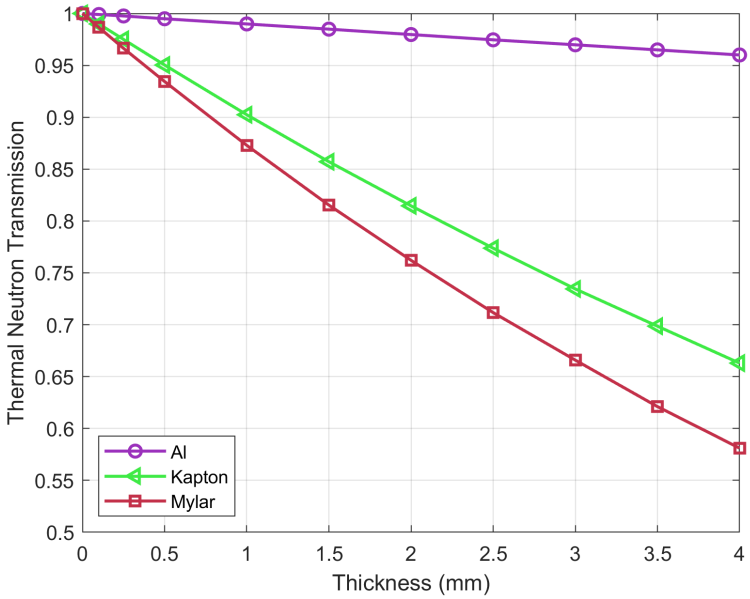

Figure 5.9: Fraction of transmitted thermal neutrons as a function of distance travelled in aluminium, kapton and Mylar.

The availability of thin films turns out to be the most determining factor for the substrate material decision. While the search for kapton in thicknesses below 1 μm was not successful, the remaining options are commercially available in thicknesses of (0.4 μm $\pm$ 25%) and (0.8 μm $\pm$ 25%) for aluminium and (0.5 μm $\pm$ 20%), (0.7 μm $\pm$ 20%) and (0.9 μm $\pm$ 20%) for Mylar [189, 190].

Square 0.4 μm thick aluminium foils (160$\times$160 mm^2) were acquired, along with 0.5 μm and 0.9 μm thick Mylar rolls, with 315 mm width and a few meters long. The aluminium foils were very fragile and difficult to manipulate. The simple action of trying to manually suspend a foil by holding its edges was prone to damage by wrinkling or tearing it (as can be seen by the bottom left corner of Fig. 5.10). This makes stretching it evenly on a frame a complicated task, which is an fundamental aspect to ensure a homogeneous deposition of the neutron conversion material in the coating process.

The attempt to stretch Mylar proved to be far less challenging, as this material exhibits superior elasticity and robustness for both experimented thicknesses (0.5 μm and 0.9 μm). By adopting a 2 stage stretching process, it was possible to achieve an even Mylar surface with an effective area of 100$\times$100 mm^2 and adequate surface tension. The first stage consisted of using double side adhesive tape double on a larger acrylic frame, and placing the Mylar foil on it, while keeping it as stretched as possible by holding its edges (Fig. 5.11-left). This results in a somewhat decent surface tension, but still with room for improvement. The double side adhesive tape also is not a proper ultimate fixer: it was observed that the Mylar adhesion to the tape is not strong enough and will tend to slip-off

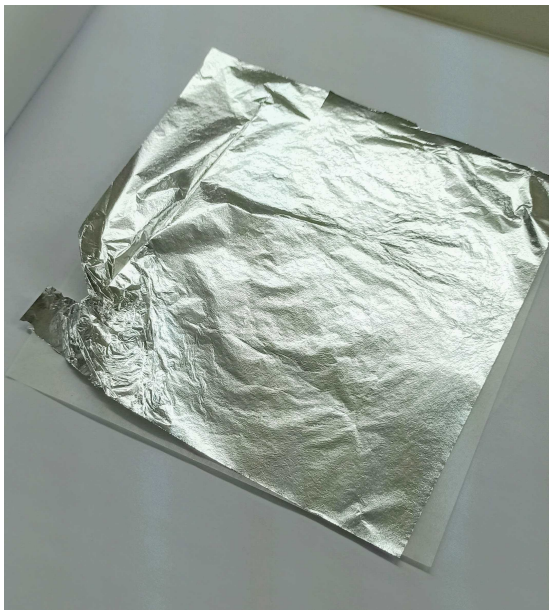

Figure 5.10: Aluminium foil 0.4 μm thick and with 160×160 mm^2 dimensions.

after a few days. The second stage involved the use of an aluminium frame with a 100×100 mm^2 opening and a shallow grove surrounding it to deposit on it a layer of epoxy glue (Fig. 5.11-right). This frame was placed on a support of enough height to guarantee that the acrylic frame would be suspended when contact was made between the frame and the acrylic surface, with the side in which the Mylar was initially stretched facing down. In this manner, the gravity of the acrylic frame maintained the Mylar surface tension on the frame opening while the glue cured. After the glue curing time was over, the Mylar was properly fixed by the epoxy glue, and the acrylic and aluminium frame could easily be separated by cutting the excess material around the glue grove. This process was successful for both 0.5 μm and 0.9 μm thick Mylar foils, producing excellent quality, perfectly stretched foils with active area of 100×100 mm^2.

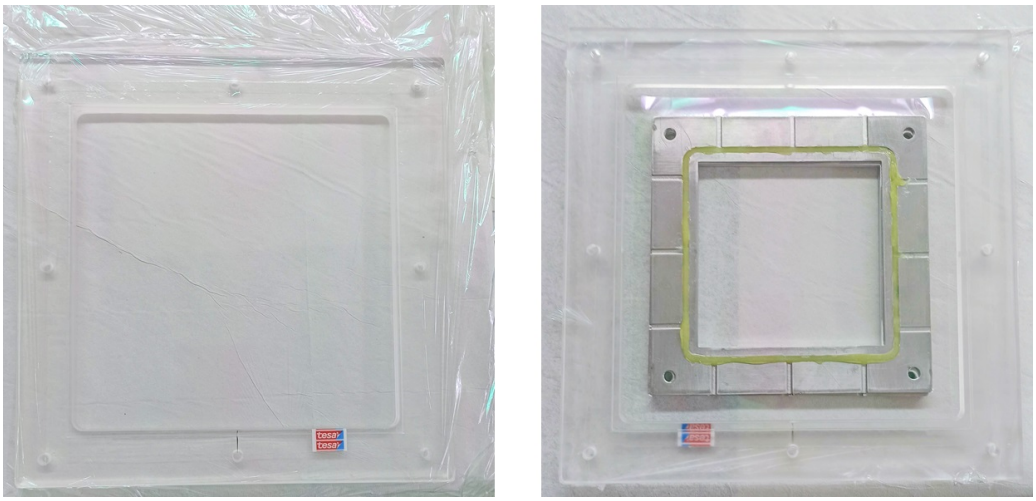

Figure 5.11: Mylar stretching process, by which the Mylar foil is firstly stretched and held with adhesive tape on a larger acrylic frame (left), which is then suspended on top of an aluminium frame with a 100×100 mm^2 opening and epoxy glue surrounding it (right).

5.4 Geometry Considerations

Beyond the material selection, there are also different possibilities in the geometry of the detection layer, comprised by the neutron converter and the substrate, concretely their relative disposition and thicknesses.

Two alternatives are viable for the coating deposition process: either depositing the full desired thickness of the neutron converter material on one side of the substrate, or dividing it by the opposite sides of the substrate, resulting in a symmetric layout of the detection layer. These two options are depicted in Fig. 5.12.

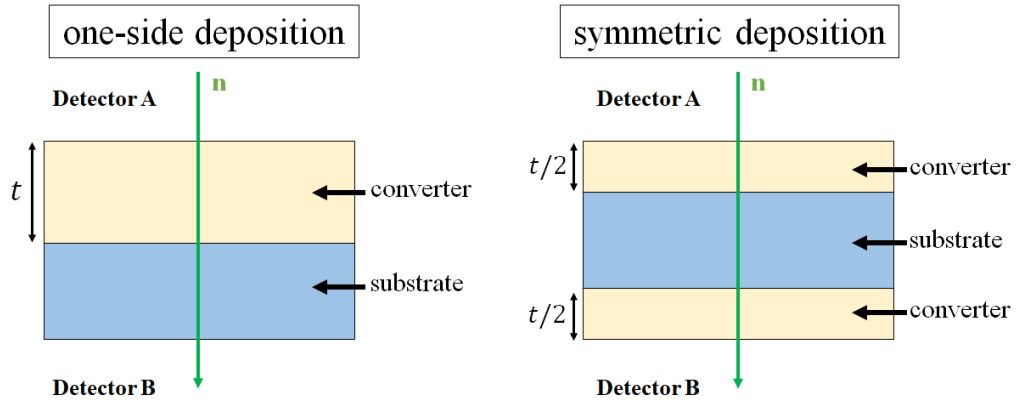

Figure 5.12: Possible converter coating layouts: one-side deposition (left) and symmetric deposition (right).

To optimize the coincidence detector, the ideal thickness (t) of the conversion layer must be assessed for each deposition alternative as well as for the different substrates. Although the substrate material is imperative for the B_4C coating, its overall impact on the detector is essentially a negative one, causing the absorption of the secondary particles from the neutron capture reaction and consequently efficiency loss. Also, the choice of the substrate material is mostly restricted by its availability in films of submicrometric thickness.

In this section, the study of the coating possibilities is presented, for each of the previously described suitable substrate materials, based on GEANT4 simulations, considering the multitude of possible converter and substrate materials layout. The conversion material considered was B_4C boron-enriched with 99% ^{10}B, as reported achievable in literature [183], irradiated by thermal neutrons at a perpendicular angle. Each data point and PHS was obtained by simulating 10^6 neutrons irradiating a single detection layer, which represented a compromise between computation time and collection of adequate statistics. It was verified that increasing the number of incident thermal neutrons in the simulations beyond this value did not lead to significant fluctuations on the results and therefore resulted in an unnecessarily excessive computation time. An energy threshold of 100 keV was applied, the typical value considered in boron coated gaseous neutron detectors to discriminate against gamma rays and electronic noise [109], which influences the calculated efficiency and the shapes of the PHS.

5.4.1 0.4 µm Al substrate

Although stretching the aluminium foils is technically more difficult than Mylar, it is not deemed as an impossible endeavour, if efforts in finding an effective strategy are made. Therefore, it is worthy of analysis as a potential substrate material. The results of the influence of the B_4C layer thickness on detection efficiency are presented in Fig. 5.13, for the two considered coating layouts: one-side and symmetric.

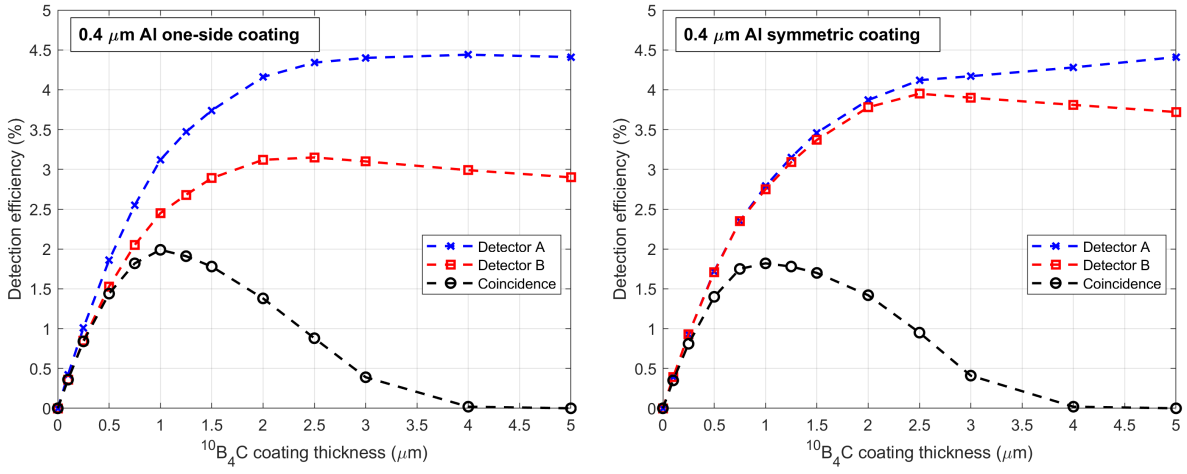

Figure 5.13: Detection efficiency as a function of the total $^{10}B_4C$ thickness deposited on a 0.4 μm Al substrate for one-side coating (left) and symmetric coating (right).

Detector A reflects the neutron detections on the top gas region, which was also the neutron origin, and hence detections that occur in back scattering mode. In contrast, detector B accounts for events detected on the bottom gas region, i.e., in transmission mode. This is true for both one-side and symmetric depositions. The coincidence detections consist only of neutron captures that simultaneously deposit energy (superior to the 100 keV threshold) on both gas regions. Therefore, the efficiency of the coincidence detector is naturally not equivalent to the sum of the efficiencies of detector A and B, because a number of neutron captures will result in only one of the secondary particles escaping to one of the gas regions, and consequently contribute to the detection efficiency of only that particular detector (A or B) without contributing to the coincidence detector efficiency. From this standpoint, it is evident that the coincidence detector efficiency will be inferior to the individual efficiencies of detector A or detector B, regardless of the coating thickness.

The efficiency curves of detector A and B in the one-side deposition layout follow the typical behaviour of boron coated detectors in back scattering and in transmission mode, respectively, as previously described and portrayed in Fig. 5.1. Hence, the efficiency of detector A increases until a B_4C thickness of 3 μm is reached, and saturates for superior values, while detector B has its maximum value around 2.5 μm and begins to drop thereafter.

On the other hand, when regarding the symmetric coating alternative, detectors A and B show a different behaviour, in which the efficiency of detector A continuously increases up to 5 μm, while detector B also has a maximum value around 2.5 μm and a subsequent drop, but reaches higher efficiency values when compared to the one-side deposition. Regarding detector A, this difference is explained by the fact that by using

a symmetric coating, a fraction of the neutron detections of detector A arise from back scattering neutron captures from the bottom layer, with secondary particles traversing the substrate, a scenario that does not occur for detector A using a one-side coating. This leads to an additional energy lost and a correspondent probability decrease for the secondary particles to reach this detector, which results in efficiency reduction. However, as the coating thickness increases, secondary particles from neutron conversions on the bottom layer which reach the top gas region are less likely, and eventually impossible beyond a certain limit. Therefore, for higher thickness, the efficiency of detector A depends solely on neutron captures occurring on the top coating layer, and equals that of the one-side deposition, which is evidenced by the fact that the total deposition of 5 μm in a symmetric layout (corresponding to 2.5 μm on the top side) results in approximately the same efficiency for detector A achieved in a 2.5 μm one-side coating.

A more notorious change in the efficiency curve is obtained for detector B. While the secondary particles that reach detector B with a single coating layer always have to traverse the substrate to be detected, that is no longer necessarily the case in the symmetric deposition. Indeed, with this layout, the secondary particles emitted in neutron conversions in the bottom layer only traverse less than half of the total coating thickness, which leads to a significant increase in the efficiency of detector B.

Focusing on the efficiency of the coincidence detector, it is verified that for both deposition layouts, the optimal B_4C thickness is 1 μm, meaning that this is the value for which the neutron captures produce the most secondary particles simultaneously capable of escaping the conversion layer. The efficiency obtained for this thickness was 1.99% for the one-side coating and 1.82% for the symmetric. Despite the slight decrease for the latter, the fact that the symmetric deposition has a broader efficiency peak around 1 μm can be beneficial to account for uniformity fluctuations across the surface that are inherent to coating techniques.

Comparing now the PHS of each detector for the 1 μm B_4C coating thickness which optimizes the coincidence detector efficiency, presented in Fig. 5.14, significant differences are observed for the two deposition layouts.

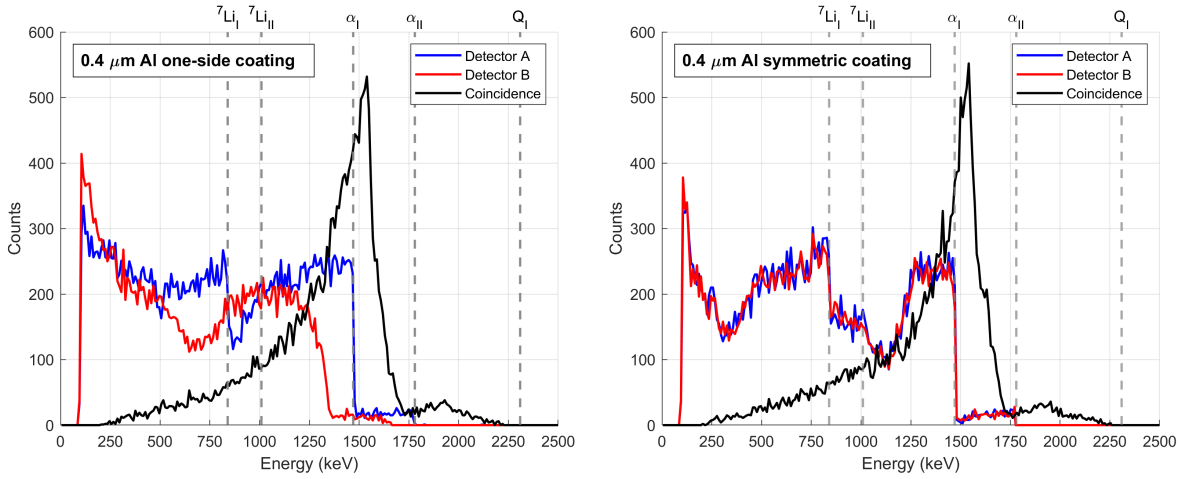

Figure 5.14: Simulated PHS of detector A, detector B and the coincidence detector considering a one-side (left) and a symmetric (right) coating of 1 μm thick enriched $^{10}B_4C$ on a 0.4 μm Al substrate. A threshold energy of 100 keV was considered, for each detector individually.

For both one-side and symmetric coatings, the PHS of detector A are identical, and

similar to that of conventional boron coated detectors, as previously seen in Fig. 4.1. This is also the case for the PHS of detector B with a symmetric coating. However, for detector B, a different shape is obtained in the one-side coating layout. In this case, the ^{7}Li and α particles have a good chance of entering the gas region of detector A virtually with their whole initial energy, if the neutron capture occurs near the surface of the converter. Thus, we observe a steep drop for the energies of the 94% reaction branch (E(^{7}Li) = 840 keV and E(α) = 1470 keV) for detector A, as marked by the dashed vertical grey lines in Fig. 5.14. In opposition, the secondary particles must always traverse the substrate to be detected in the gas region of detector B, so it is inevitable that an appreciable fraction of their initial energy is lost by ionizations and excitations in that medium. Consequently, the ^{7}Li and α edges occur at inferior energies. In the symmetric option, neutron captures can occur at the converter surface bounded by either the gas region of detector A or of detector B, and consequently their PHS are identical.

The PSH of the coincidence detector is obtained by summing the energies of detectors A and B for coincident events, meaning that an energy above the 100 keV threshold was simultaneously detected in both detectors, for the same neutron capture. This is naturally different than the simple sum in counts of the PHS distributions of detectors A and B, and thus the PHS of the coincidence detector has a different shape, with some similarities to that of ^{3}He and BF_3 gaseous detectors (Figs. 3.5 and 3.6). Specifically, the peak observed for the coincidence detector is analogous to the full neutron capture reaction energy peak in the mentioned gaseous detectors. However, for the coincidence detector, this peak is not centred at the full capture reaction energy (Q_I = 2310 keV), since it is impossible for both secondary particles to reach the gas without losing some of their energy in the solid detection layer. As a result, the peak is shifted to lower energies, with its centroid around 1540 keV for both one-side and symmetric coatings. The peak is also broader for both situations, due to the high variation of the energy lost by the secondary particles in the solid layer, and does not have a Gaussian shape, but rather a long tail down to lower energies, due to the contributions of neutron captures in which the secondary particles lose a more significant fraction of energy before reaching the gas. The symmetric coating option exhibits a slightly narrower peak, which indicates less fluctuation on the overall energy with which the secondary particles reach the gas for coincident neutron detections. A smaller peak is also visible around 1950 keV, attributed to the ^{10}B neutron captures from the 6% probability branch (Q_{II} = 2790 keV).

The differences between the two coating options can be evaluated by means of the energy distribution between detectors A and B for the coincident events in both detectors. This can be visualized as a 2D histogram where each data point is obtained by considering, for a given neutron capture, the energy deposited in detector A as the x-coordinate, and the energy deposited in detector B as the y-coordinate (Fig. 5.15)

Looking at Fig. 5.15, it is clear that a fraction of neutron captures that contribute to the coincidence detector response may deposit a lot of energy on detector A, while depositing on detector B an energy only slightly above the 100 keV discrimination threshold, or vice-versa. Let us consider a specific example: when comparing a neutron capture reaction that results in an energy detection of 900 keV on detector A and 100 keV on detector B, with one that results in an energy deposition of 500 keV on the two detectors, both neutron captures equally contribute to the coincidence detector efficiency, as the energies at stake are not inferior to the 100 keV threshold, and both also equally contribute to the PHS of the coincidence detector, as both deposit a total amount of 1 MeV. However, the first scenario is not the ideal one, since in a real detector, the

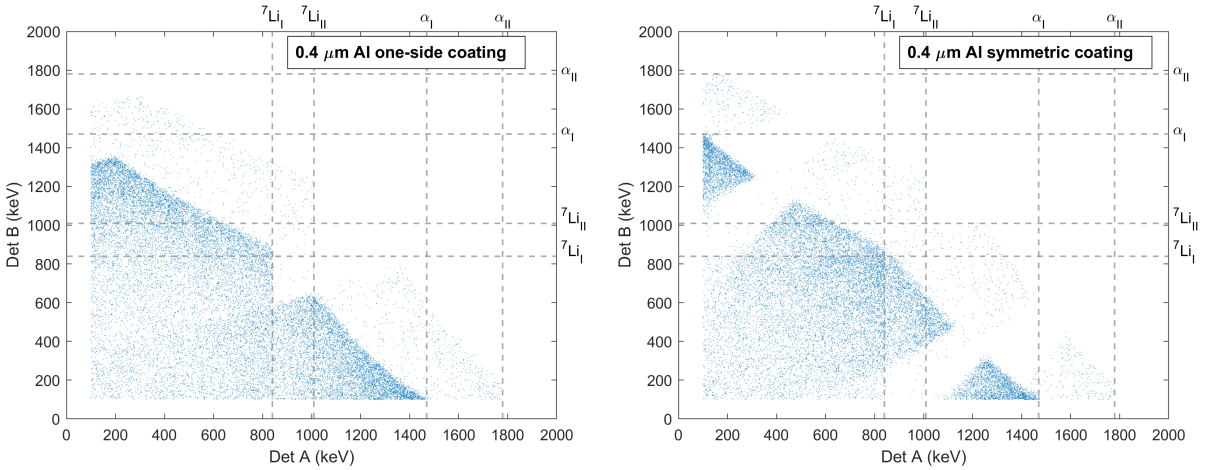

Figure 5.15: 2D histogram of the energy distribution across detector A and B for the coincident detector with a 1 μm coating of enriched $^{10}B_4C$ on a 0.4 μm Al substrate. A threshold energy of 100 keV was considered for each detector individually.

probability of low energy secondary particles reaching the gas and not being detected is higher than in simulations, since GEANT4 does not account for the electron drift, and consequently the potential loss in the number of primary electrons, as they are accelerated towards the multiplication region, due to interactions with gas molecules, namely electron attachment and recombination. This reduction on the number of primary electrons would lead to less electron avalanches and consequently to a decrease in the energy collection, that for low energy events could determine if they fall above or below the discrimination threshold.

Therefore, the coincidence detector should be optimized to maximize the energy balance between detector A and B. An additional reason for favouring this balanced energy deposition is the fact that having similar secondary particle ranges across the gas regions on both sides of the detection layer yields better neutron interaction site estimations when compared to neutron captures that result in a large particle track on one side of the detector and a small one on the other, as will be further discussed in the next section.

As evidenced by Fig. 5.15, the selection between one-side or symmetric coating results in different energy depositions across detectors A and B. Coincident neutron captures in which the energy is evenly distributed among both detectors will appear on the central region of the histograms, while events with a significant energy discrepancy between detector A and B will appear near the left y-axis, in case the energy deposited in detector B is superior, or close to the bottom x-axis, in the other case. Although visually it might not be immediately perceptible which of the coating layouts results in a greater density of events in the central region of the histogram, this can be calculated by setting successive energy thresholds to account only for the events in which both detectors registered an energy superior to a given energy limit. For instance, let us compare for both coating layouts the fraction of coincident neutron captures in which both the energy deposited in detector A and in detector B is superior to 500 keV, represented by the red regions of Fig. 5.16.

The fraction of data points that fall above the described region for the one-side coating geometry is 23%, inferior to that found for the symmetric coating, of 38%. This superiority of the symmetric coating is not only observed for the 500 keV example, but for any energy

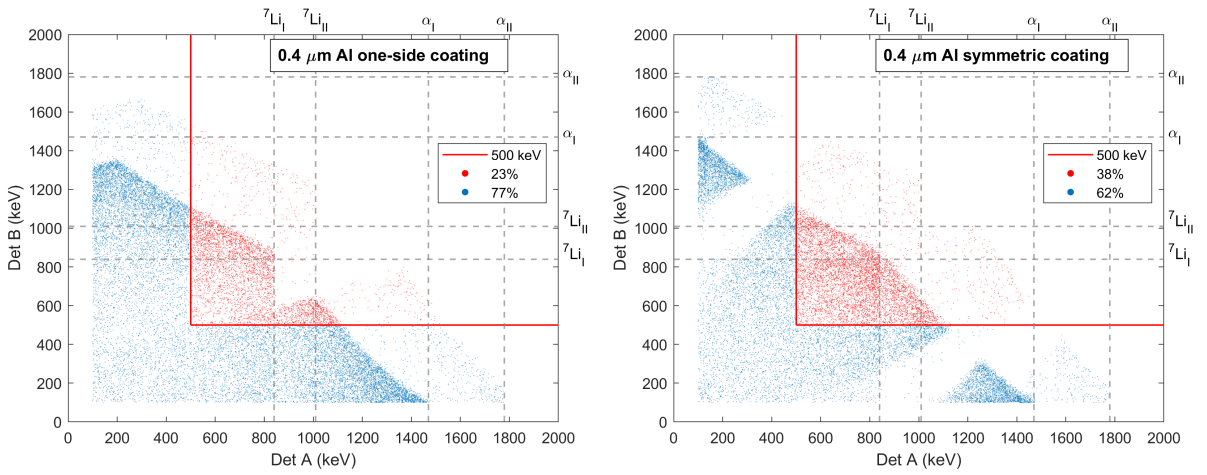

Figure 5.16: Representation (in red) of the fraction of coincident neutron captures that result in an energy deposition above 500 keV, for both detectors A and B, considering a one-side (left) and a symmetric (right) coating of 1 μm thick enriched $^{10}B_4C$ on a 0.4 μm thick Al substrate.

threshold that might be considered, as depicted in Fig. 5.17, which plots the fraction of coincidence detections that simultaneously deposit in detector A and in detector B an energy superior to the thresholds contemplated in the x-axis.

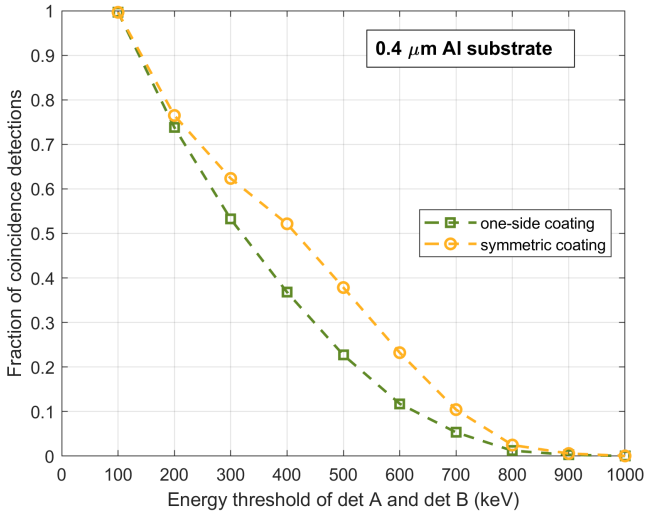

Figure 5.17: Fraction of coincident neutron captures that simultaneously result, for both detectors A and B, in an energy deposition above the energy thresholds considered in the x-axis, deploying a one-side (green squares) and a symmetric (yellow circles) coating of 1 μm enriched $^{10}B_4C$ on a 0.4 μm thick Al substrate.

Attending to these results, the symmetric coating results in a more balanced energy distribution across detectors A and B. Additionally, this distribution is essentially symmetric. If we imagine in Fig. 5.15 or 5.16 the line Det A = Det B, i.e., linking the points (0,0) and (2000,2000), we find that the 2D histogram is mirrored in relation to this line. This makes the detector symmetric and its response independent of the neutron incidence side.

5.4.2 0.5 µm Mylar substrate

As previously discussed, Mylar is also an adequate substrate material to be considered, and 100×100 mm^2 effective area foils were successful prepared for $^{10}B_4C$ deposition. A fundamental difference between aluminium and Mylar is the fact that the latter is an insulator. Because the neutron conversion layer acts as a cathode, it should be able to conduct the positive charges resulting from primary ionizations and the avalanche multiplication of electrons in the gas as quickly as possible, to avoid charge accumulation and consequent distortion of the electric field. Since boron carbide is a relatively good conductor, when a symmetric coating is considered, both surfaces of the substrate are able to effectively evacuate charges. However, if the coating is deposited only on one side, the opposing substrate side would have the insulator Mylar exposed, leading to the accumulation of charges in this region and consequent space charge buildup that may distort the electric field. This was not a problem with the aluminium substrate, since the one-side coating would leave the aluminium surface exposed, which is an even better conductor than boron carbide ($\rho(Al) \sim 10^{-8}$ Ω·m).

To compensate for this, a one-side deposition requires to perform an additional coating of a thin layer of a conducting material, such as aluminium, on the side of the exposed Mylar. Although the deposition by evaporation of an aluminium layer as thin as 15 nm is a relatively simple procedure [131], it comes with the drawback of adding more material to the path of the secondary particles, which implies additional energy losses and a slight decrease of the detection efficiency of coincident events.

The simulation results here presented for the one-side coating take into consideration a 15 nm Al layer on the opposite side of the boron carbide coating. Fig 5.18 shows the efficiency of detectors A, B and the coincidence detector as a function of the $^{10}B_4C$ coating thickness for the one-side and symmetric depositions.

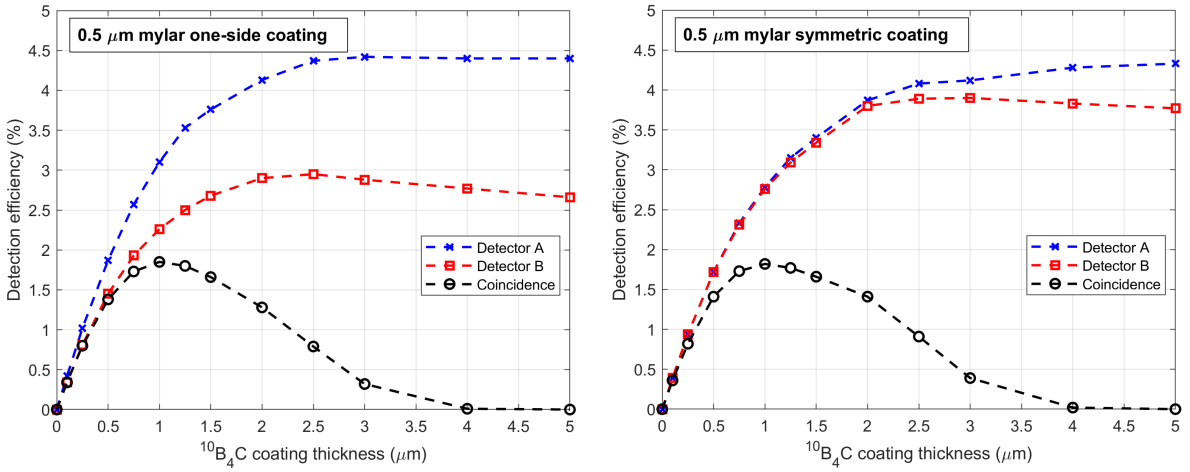

Figure 5.18: Detection efficiency as a function of the total $^{10}B_4C$ thickness deposited on a 0.5 μm Mylar substrate for one-side coating (left) and symmetric coating (right).

The same analysis for the behaviour of the efficiency curves seen for detectors A, B and the coincidence detector in the previously discussed 0.4 μm Al substrate is applicable. Also similarly, the highest detection efficiency is achieved at a coating thickness of 1 μm for both deposition layouts and the larger plateau in the efficiency peak for the symmetric coating is also observed. The efficiency of the coincidence detector for 1 μm was 1.85%

for the one-side coating and 1.82% for the symmetric coating. As it was verified with the aluminium substrate, the one-side deposition yields a slightly higher efficiency, although this difference is now less expressive, which can be explained by the extra 115 nm of solid material (100 nm from the Mylar substrate, and 15 nm from the additional aluminium layer), causing less secondary particles to reach detector B and consequently a decrease in the coincidence detector efficiency. Comparing to the aluminium substrate, there is an efficiency reduction in both deposition layouts. This indicates that, although aluminium is more dense than Mylar, which makes for inferior ranges of the secondary particles, the increased thickness of the substrate overshadows that effect.

The comparison of the pulse height spectra for a 1 μm coating thickness is presented in Fig. 5.19.

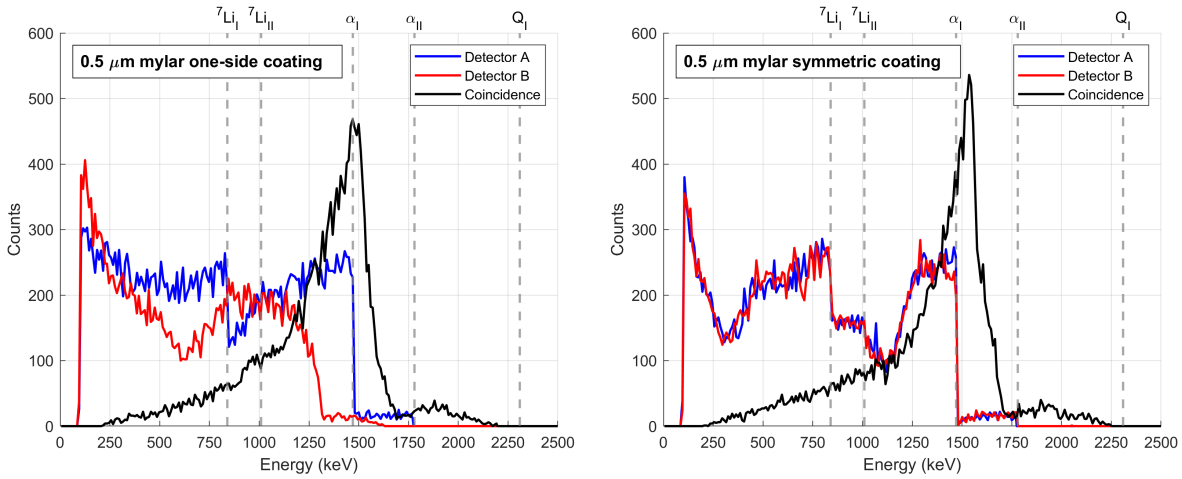

Figure 5.19: Simulated PHS of detector A, detector B and the coincidence detector considering a one-side (left) and a symmetric (right) coating of 1 μm thick enriched $^{10}B_4C$ on a 0.5 μm Mylar substrate. A threshold energy of 100 keV was considered.

For the symmetric deposition, they are similar to those obtained for the aluminium substrate (Fig. 5.14). However, looking at the one-side coating, detector B shows now a subtle shift to lower energies relatively to what was observed for the aluminium substrate. This confirms that indeed the secondary particles lose, on average, more energy when traversing a 0.5 μm Mylar layer than a 0.4 μm aluminium one. As a consequence, due to the inferior energy contributions from detector B, a shift to the left in the coincidence detector peak is also observed, which now is approximately coincident with the energy of the alpha particle of the 94% reaction branch. Comparing the coincidence detector response for the one-side and symmetric coatings, the peak is now centred at a slightly higher energy for latter.

A 2D histogram analysis of the energy distributions across detector A and B for coincidence detector events was also conducted, presented in Fig. 5.20. The histograms are very similar to those observed for the aluminium substrate.

Again, the symmetric coating provides a mirrored detector response, as well as a higher concentration of events landing in the central region of the histogram, making for a smaller energy discrepancy between detectors A and B, as evidenced by Fig. 5.21.

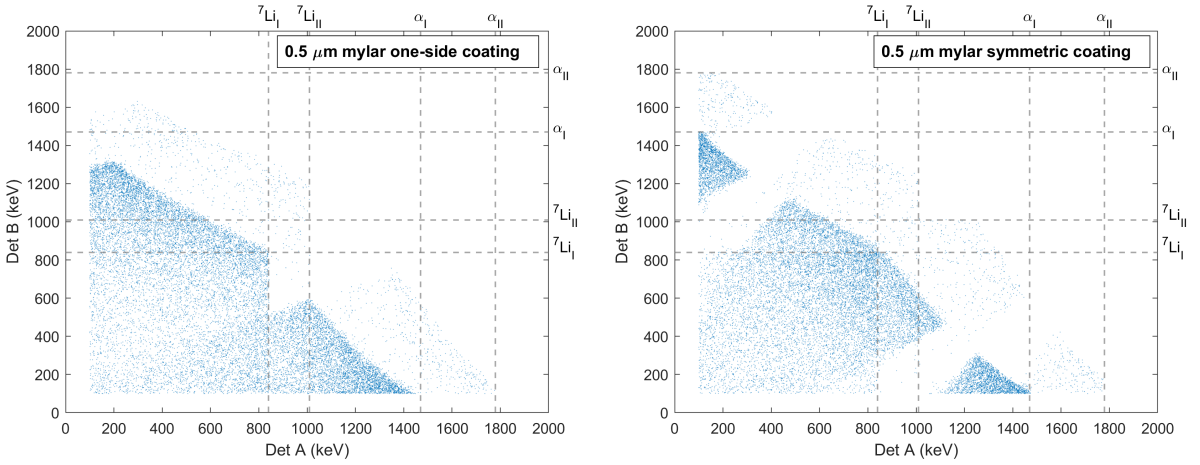

Figure 5.20: 2D histogram of the energy distribution across detector A and B for the coincident detector with a 1 μm coating of enriched $^{10}B_4C$ on a 0.5 μm Mylar substrate. A threshold energy of 100 keV was considered.

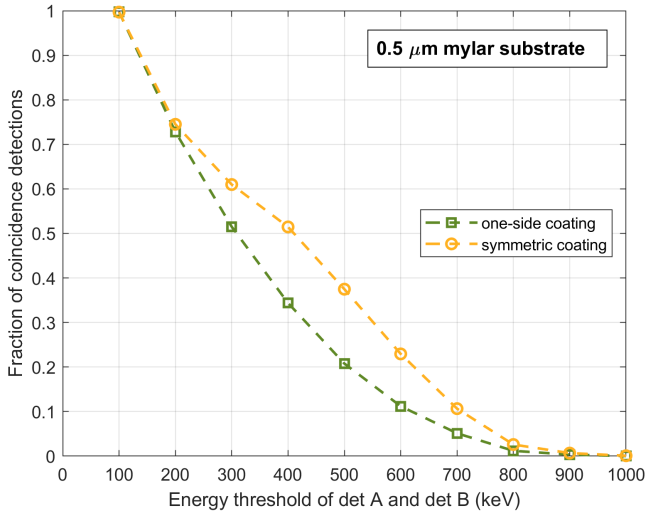

Figure 5.21: Fraction of coincident neutron captures that simultaneously result, for both detectors A and B, in an energy deposition above the energy thresholds considered in the x-axis, deploying a one-side (green squares) and a symmetric (yellow circles) coating of 1 μm enriched $^{10}B_4C$ on a 0.5 μm thick Mylar substrate.

5.4.3 0.9 µm Mylar substrate

As with the 0.5 μm thickness, stretching the 0.9 μm Mylar film on a 100×100 mm^2 frame for $^{10}B_4C$ deposition was successfully achieved, producing a result visually indistinguishable from the 0.5 μm frame. As previously discussed, the substrate should ideally be as thin as possible, but because the capability to resist the coating deposition process was initially uncertain, a conservative decision was made to test the boron carbide coating with the 0.9 μm film first, as its higher thickness should make it more robust. However, this would only be a viable alternative if this substrate is not too thick to compromise the viability of the coincidence detector. With this in mind, GEANT4 simulations for a 0.9 μm thick Mylar substrate were also performed, for the two coating layouts possibilities. As it was the case with the 0.5 μm Mylar film, to coat this substrate only on one side would require the deposition of a thin aluminium layer on the opposite side, which was taken into consideration in the simulated detector geometry, with a 15 nm thickness. The efficiency comparison for one-side and symmetric depositions is presented in Fig. 5.22.

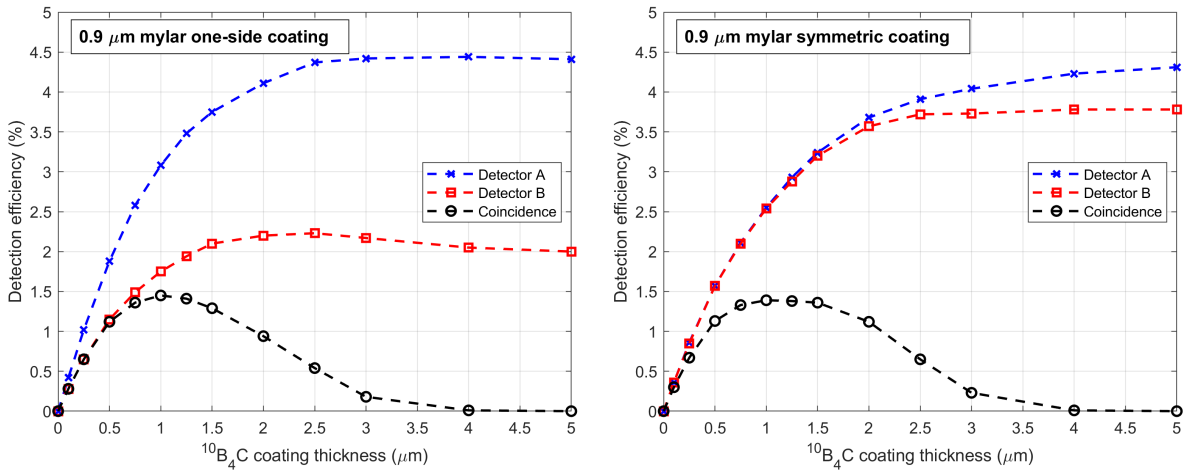

Figure 5.22: Detection efficiency as a function of the total $^{10}B_4C$ thickness deposited on a 0.9 μm Mylar substrate for one-side coating (left) and symmetric coating (right).

For the one-side coating, the only relevant difference between the use of 0.5 μm and 0.9 μm Mylar substrates is the efficiency decrease of detector B for the latter, as expected, which in also results in an efficiency decrease of the coincidence detector (1.45% for a $^{10}B_4C$ thickness of 1 μm). Comparing now the symmetric coatings, the efficiency decreased by about 0.22% for detectors A and B in regard to the 0.5 μm substrate, which resulted in a decrease by 0.43% for the coincidence detector, obtaining now a maximum value of 1.39%. So, considering the symmetric coating, the coincidence detector has an expected efficiency 1.3 times higher deploying a 0.5 μm Mylar substrate, which can account for a significant advantage, especially when considering the low efficiencies in question.

The PHS for the 1 μm $^{10}B_4C$ coating for both deposition layouts is presented in Fig. 5.23. For both layout configurations, an overall amplitude decrease of detector A, B and the coincidence detector is observed when comparing to the 0.5 μm substrate. For the one-side coating, a shift to lower energies of the PHS of detector B is also observed, confirming the excepted increase of the average energy lost by the secondary particles in the substrate. As a consequence, the coincidence detector peak is also significantly shifted

to the left, in such way that the energy difference of this peak between the one-side and symmetric depositions is now more evident than for the 0.5 μm Mylar substrate, despite the peak of the symmetric coating having also slightly shifted to lower energies.

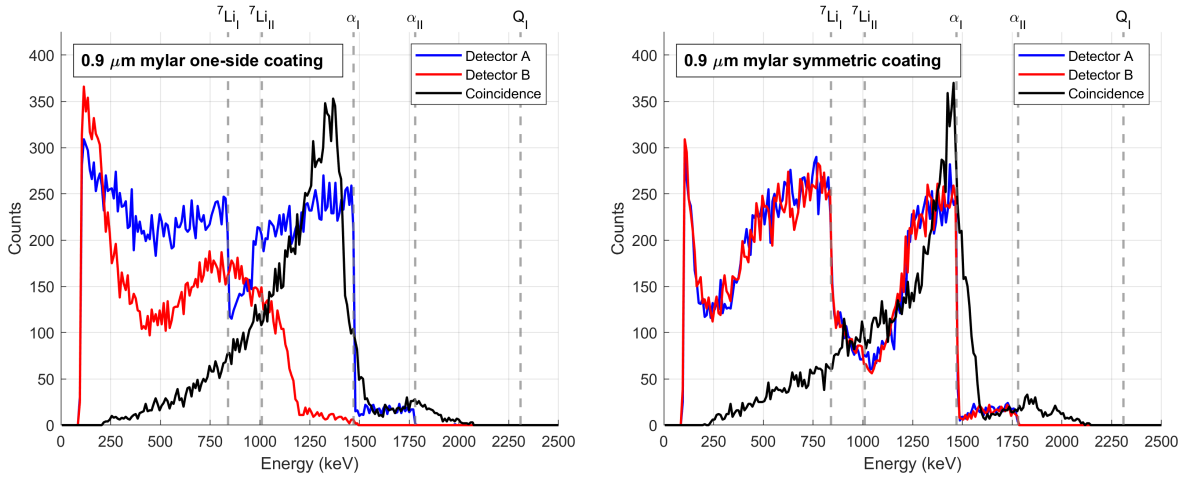

Figure 5.23: Simulated PHS of detector A, detector B and the coincidence detector considering a one-side (left) and a symmetric (right) coating of 1 μm thick enriched $^{10}B_4C$ on a 0.9 μm Mylar substrate. A threshold energy of 100 keV was considered.

Focusing on the energy distribution of the coincidence detector among detectors A and B, the 2D histogram comparison is presented in Fig. 5.24.

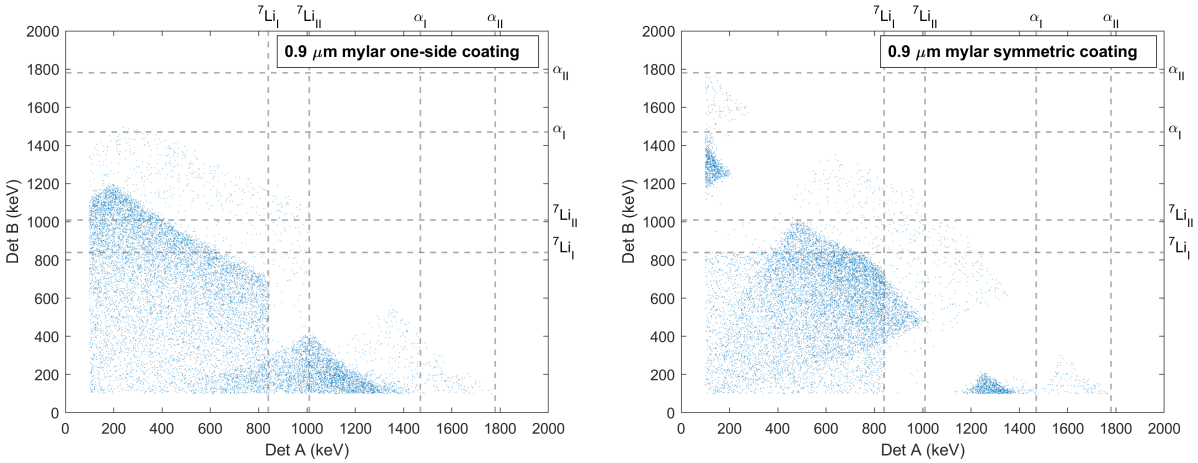

Figure 5.24: 2D histogram of the energy distribution across detector A and B for the coincident detector with a 1 μm coating of enriched $^{10}B_4C$ on a 0.9 μm Mylar substrate. A threshold energy of 100 keV was considered.

Comparing to the 0.5 μm Mylar substrate, there is an overall reduction on the number of data points, as expected by the decrease of the coincidence detector efficiency. While for the symmetric deposition, this reduction occurs evenly for both axes, for the one-side coating it affects mostly the y-axis, reflecting the inferior energy collected by detector B. Similarly to the previously analysed substrate options, the symmetric coating histogram is mirrored, while the one-side coating is not. The first also shows more events in the central region (Fig. 5.25), leading to a more balanced energy distribution between detectors A and B.

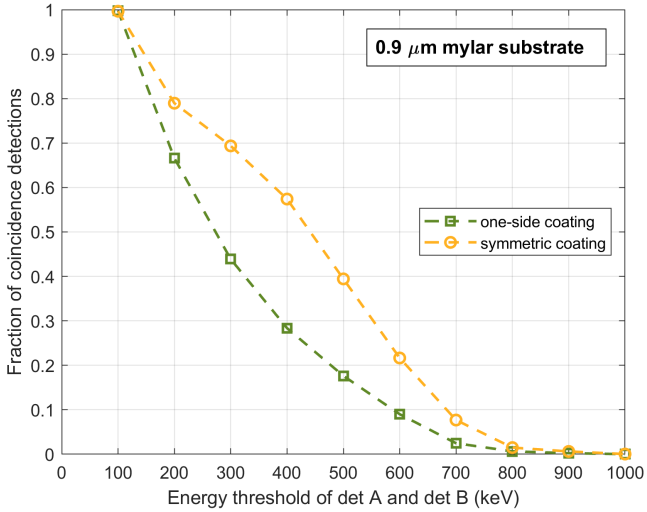

Figure 5.25: Fraction of coincident neutron captures that simultaneously result, for both detectors A and B, in an energy deposition above the energy thresholds considered in the x-axis, deploying a one-side (green squares) and a symmetric (yellow circles) coating of 1 μm enriched $^{10}B_4C$ on a 0.9 μm thick Mylar substrate.

5.4.4 Overall Comparison

Having now analysed the three substrate options considered, Table 5.3 summarizes the relevant efficiencies obtained through simulations.

	0.4 μm Al		0.5 μm Mylar		0.9 μm Mylar	
	One-Side	Symmetric	One-Side	Symmetric	One-Side	Symmetric
Det A	3.12%	2.79%	3.10%	2.78%	3.08%	2.55%
Det B	2.45%	2.75%	2.26%	2.76%	1.75%	2.54%
Coincidence	1.99%	1.82%	1.85%	1.82%	1.45%	1.39%

Table 5.3: Detection efficiencies derived from GEANT4 simulations for each considered substrate material and coating deposition layout, for the ideal thickness in terms of detection efficiency of 1 μm $^{10}B_4C$.

The ideal thickness (in terms of detection efficiency) of the boron carbide coating, 1 μm, is independent of the substrate thickness and the deposition layout. As expected, the efficiency of detector A for the one-side coating geometry does not show significant fluctuations over the thickness and material of the substrate, since the neutrons captures that contribute to this efficiency never traverse it. However, detector B is severely influenced by it, decreasing in efficiency as thicker substrates are considered. It is also clear that the one-side coating geometry provides slightly superior efficiencies for the coincidence detector, although this difference can only be considered expressive for the 0.4 μm Al substrate. On the other hand, the fact that the efficiency of detector A and detector B is very similar for the symmetric coating may be a greater benefit, as is makes for a balanced counting rate and a similar response of both detectors, while using the same bias voltages and energy thresholds, which should facilitate the analysis of the acquired data. Additionally, the symmetric deposition avoids the additional thin aluminium coating of the mylar substrates and results in a flatter efficiency peak, which is

an attractive benefit to compensate for thickness uniformity fluctuations across the coated surface. Finally, the fact that this deposition layout results in a symmetric distribution of energies across detector A and B, makes the coincidence detector essentially symmetric, producing the same results regardless of the incident neutron direction.

Based on these results and observations, a coating test with enriched $^{10}B_4C$ on a 0.9 μm Mylar foil was carried out at Paul Scherrer Institute (PSI), by DC-magnetron sputtering. The reason to select this thickness over the 0.5 μm film, was to have a conservative approach when testing the adequacy of this thin material as a substrate for the mentioned coating technique. A symmetric ^{10}B enriched boron carbide deposition with 0.5 μm thickness on each side of the substrate was chosen. The fact that 1 μm was the maximum limit of the coating thickness capacity was an additional motivation to prefer the symmetric coating [191], avoiding the operation of the sputtering machine in limit conditions, which could induce greater thickness non-uniformities.

Although boron carbide adhered properly to the substrate, the Mylar foil lost some of its initial surface tension, presumably due to thermal expansion derived from the sputtering process. This should, however, be easily compensated by sacrificing part of the initially coated area, using a smaller frame to repeat the procedure previously described with the acrylic and aluminium frames in section 5.3. By suspending the coated 100×100 mm^2 area over a smaller frame, for instance, with 50×50 mm^2 effective area, with epoxy glue around the opening, the stretching process should be analogous to the initial preparation of the Mylar frames, and therefore expected to be successful. This strategy is schemed on Fig. 5.26. On future tests, a frame with 100×100 mm^2 effective area coating can, in principle, be achieved by compensating for the surface tension loss using an initial frame with larger coating area, and deploying the same strategy.

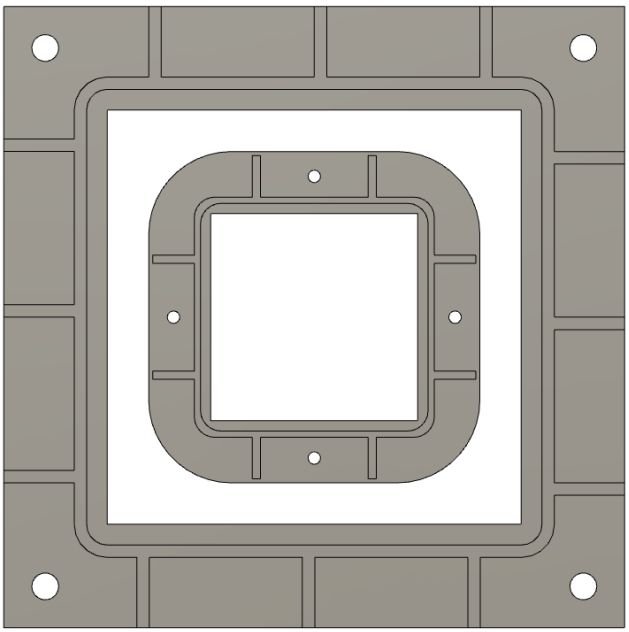

Figure 5.26: Procedure to recover the initial surface tension of the Mylar foil, by suspending it over a smaller frame with epoxy glue surrounding the opening, analogously to the procedure for the initial preparation of the Mylar frames.

5.5 Neutron Capture Position Reconstruction

The coincidence detector is being developed as a PSND. Therefore, a fundamental aspect of its characterization is the spatial resolution. Three major effects influence the spatial resolution of neutron gaseous detectors with solid converters. One is the resolution limit of the readout system, which for discrete wires or strips with pitch d is given by the standard deviation of a continuous uniform distribution, and therefore $\sigma = \frac{d}{\sqrt{12}}$. Other contribution to the spatial resolution limitation is the scattering of neutrons by the gas, walls or solid structures inside the detector, especially those containing hydrogenated materials, which cause the deflection of neutrons and induce a detection signal that does not correspond to their original trajectories. Finally, there is the ionization track length of the neutron capture reaction secondary particles, which for some detectors makes up the largest part of the spatial resolution [126]. Therefore, it can by expected that by addressing the limitation caused by the long ionization tracks in the gas, a significant improvement of spatial resolution will follow.

The estimation of the spatial coordinates in which the neutron capture occurs is achieved by processing and analysing the readout signals, and different techniques and algorithms may be used to optimize it [176], according to the readout mechanism deployed by the detector (MWPCs, strips, GEMs or pads). The readout signal is dependent on the electron/ion captures by the electrodes, which in term depends on the formation of the primary charges by the neutron capture reaction secondary particles. Therefore, by knowing the trajectory coordinates of the secondary particles and the energy deposited on the gas along their tracks, it is possible to have some insight on what would the estimated neutron capture site be, even if not taking into consideration the limitations of the readout system itself. Through GEANT4 simulations, it is possible to access this information, and therefore compare the estimation of the neutron capture interaction site for different detectors. Additionally, the actual neutron capture coordinates are also known, so their accuracy can be measured.

In our case, we are interested in comparing the estimated neutron capture site of the coincidence detector and a conventional boron coated detector. For the first case, we can use the track information of the two secondary particles that are emitted in opposite directions upon a neutron capture, and consequently deposit their energy on opposing sides of the filling gas. This is true for any of the above considered possible implementations of the coincidence detector, namely in what concerns substrate material and thickness, boron carbide coating thickness or deposition layout. As for the conventional boron coated detector, which we will henceforth designate as "thick detector" (because the thickness of the converter plus the substrate is too large to allow both secondary particles to escape it), only one of the secondary particles (at most) escapes to the gaseous region. If we consider its operation in back scattering mode, it would be the analogous situation of regarding only the events that are detected by detector A in the coincidence detector.

The GEANT4 simulations presented in section 5.3 for the investigation of different materials and their thickness in the detector response only took in consideration the energy deposited in the gas. However, to estimate the neutron capture interaction site it is also necessary to have the information of the particle trajectory coordinates and how energy is transferred to the gas along the tracks. Therefore, a new simulation was implemented. To describe it, let us consider the secondary particles tracks arising from a neutron capture

reaction in the coincidence detector, obtained through GEANT4 simulations, depicted in Fig. 5.27-left. As illustrated, the neutron is incident from the top region (gaseous volume of detector A) and reaches the $^{10}B_4C$ layer perpendicularly, being captured at the (x,y) coordinates (0,0). The yellow dots along the ^{7}Li and α particle tracks represent discrete simulation points. Every two consecutive points of a given track constitute a step, and the information of the energy lost by a particle on each step (dE_{A/B_i}), as well as the coordinates of the events that limit it (x_{A/B_i} and $x_{A/B_{i+1}}$), are calculated by the simulation. This image is a simplified representation for explicative purposes, as in the developed simulations a particle track across the sensitive volumes (gas regions of detectors A and B) is typically composed by thousands of steps of variable lengths.

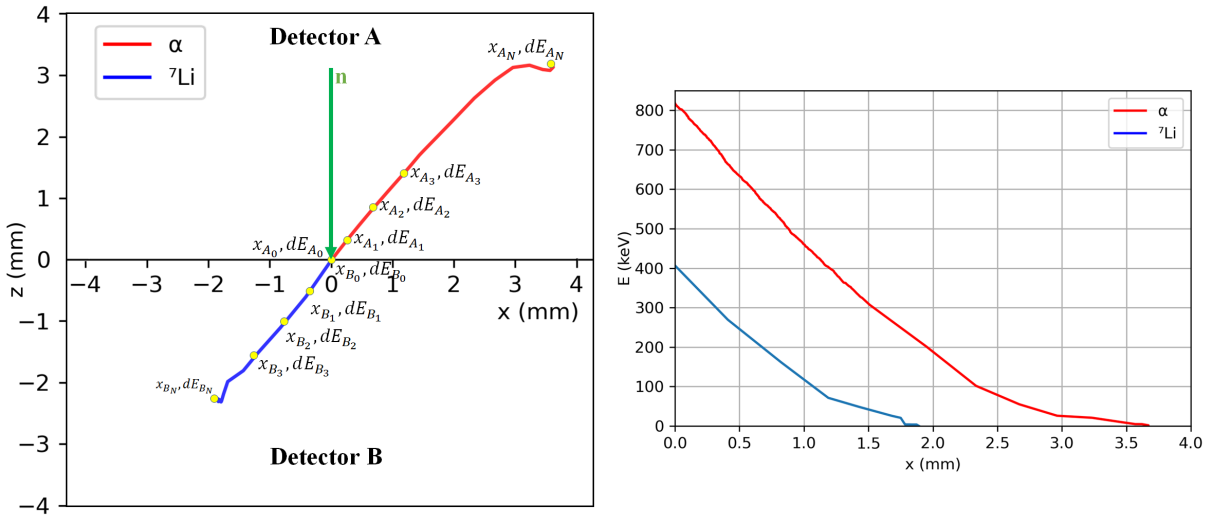

Figure 5.27: Left: Step information of the tracks of a ^{7}Li and α particles emitted upon a neutron capture in the coincidence detector, obtained from GEANT4 simulation. Right: Energy of the particles along the x-projection of their trajectories.

The energy lost by a secondary particle to ionizations in the gas is not linear over the particle trajectory. In the particular case portrayed in Fig. 5.27-left, both secondary particles lose more energy at the beginning of their tracks, and this value (dE/dx) gradually decreases as the particles approach the end of their tracks. This is evidenced by the slope of the plots of Fig. 5.27-right, representing the remaining energy of each particle (E) across the x-projection of their path (x), which flattens as x increases. However, as seen in Fig 5.5, this is not always the case. Specifically, α particles produced near the surface of the neutron converter escape the gas with most of their initial energy, and in such cases a distinctive Bragg peak occurs closer to the end of the particle trajectory, where a larger fraction of energy is deposited.

Because of the high variability of the secondary particles energy deposition in the gas, to accurately predict how charges would be collected by the readout of the detector for a given neutron capture, it is fundamental to take into consideration the energy deposition along every step of the particles track. With that information, an unidimensional estimation of the neutron capture interaction site, derived from the position of the collected charges, would be given by an average of the x-coordinates of the events that compose the particle track, weighted by the energy deposited on each step. This consists of a simplified model that neglects the discrete nature of the readout (composed of individual wires, strips or pads) and the diffusion and absorption of electrons as they drift towards

the electrodes. Hence, if we consider x_A and x_B the x-coordinate estimations of the neutron capture site by detectors A and B, respectively, they would be given by:

$$x_A = \frac{\sum_{i=0}^{N} x_{A_i} dE_{A_i}}{\sum_{i=0}^{N} dE_{A_i}} \quad ; \quad x_B = \frac{\sum_{i=0}^{N} x_{B_i} dE_{B_i}}{\sum_{i=0}^{N} dE_{B_i}} \tag{5.4}$$

in which $\sum_{i=0}^{N} dE_{A_i} = E_A$ and $\sum_{i=0}^{N} dE_{B_i} = E_B$, i.e., the total energy deposited by the secondary particle in the gas region of detectors A and B, respectively. In a conventional thick boron detector, which only detects one of the secondary particles in each event, equations (5.4) would correspond to the neutron capture site estimation for each neutron detection:

$$x_{\text{thick}} = \frac{\sum_{i=0}^{N} x_i \, dE_i}{\sum_{i=0}^{N} dE_i} \tag{5.5}$$

As perceptible by the scheme of Fig. 5.27, because of the direction in which the secondary particles are emitted, the x-coordinate of the neutron interaction sites will be overestimated to the right side ($x_A > 0$) by detector A, and to the left by detector B ($x_B < 0$). The inverse scenario could also occur for different a neutron detection. From Fig. 5.27, we can also infer that the smaller the angle between the neutron detection layer and the initial trajectory of the secondary particles is, the greater the error on the neutron capture site estimation will be. On the other hand, if the secondary particles were emitted perpendicularly to the detection layer, their energy would be deposited over a tiny x-projection range, which would make for a more accurate unidimensional estimation of the neutron capture site. In a conventional boron coated thick detector, these overestimations are balanced out by statistical accumulation of many neutron captures, since the secondary products are isotropically emitted. However, for the coincidence detector, the overestimations of a single neutron capture can be balanced out by crossing the information of x_A and x_B, which are correlated by the fact that the secondary particles are emitted along the same line. One possible option would be to calculate the arithmetic mean of the estimated positions of each detector, i.e., $x_{\text{coinc}} = (x_A + x_B)/2$. But the fact that in a gaseous detector operating as a proportional counter the information of the total energy deposited by each secondary particle is accessible, it can be used to make a better prediction of the neutron interaction site. Higher energy particles reaching the gas will have longer trajectories, and consequently the described overestimation effect will be more significant. Additionally, the energies that the two secondary particles deposit in the gas are correlated: the greater one is, the minor the other will be. This is due to the complementary losses in the detection layer: if one particle reaches the gas with a large fraction of its initial energy, it would imply that the neutron capture occurred relatively close to the converter-gas surface limit. Consequently, the other secondary particle will have to traverse a substantial thickness of converter and substrate materials, and as a result reaches the opposing gas region with correspondingly less energy and a matching shorter track. Due to this shorter track, its energy deposition will be more concentrated in the region closer to the actual neutron capture interaction position than the opposing

longer particle with a longer track. Therefore, more weight can be attributed to the neutron capture site estimation of the particle with a shorter track, i.e., which deposited less energy in the gas. Weighting in these factors for the estimation of the neutron capture site, we can write:

$$x_{\text{coinc}} = \frac{x_A E_B + x_B E_A}{E_A + E_B} \tag{5.6}$$

where the estimation of the neutron capture site by each secondary particle is weighted by the energy of the other one, detected in the opposing gas region. Due to the mentioned energy deposition correlation, equation (5.6) assures that the secondary particle which has a longer track, has less weight in the overall neutron capture estimation site than the particle which has a shorter track, and consequently yields a neutron capture site closer to the real one. As will be further discussed in the next section, equation (5.6) has the potential to produce better results than the simple arithmetic average of x_A and x_B. For the specific neutron capture event, which output of the simulation is presented in Fig. 5.27, the values calculated were $x_A = 1.358$ mm, $x_B = -0.908$ mm and $x_{\text{coinc}} = -0.155$ mm. Taking into account that the neutron capture occurred at $x = 0$ mm, it is verified that x_A and x_B are slightly shifted respectively to the right-end and left-end of the x-axis, as expected, and x_{coinc} results in an estimation closer to the real value. If we considered detector A or B to be a conventional thick boron detector, the final neutron capture site estimations for this particular interaction would respectively be x_A and x_B, and therefore less accurate than the one obtained with the coincidence detector.

If instead of using equation (5.6), x_{coinc} was calculated by taking the arithmetic mean of x_A and x_B, it would yield $x_{\text{avg}} = 0.225$ mm, which, despite being a better estimation than what would be obtained by a thick detector, whether detector A or detector B, it is not as accurate as the value obtained by the energy weighting method.

5.6 Spatial Resolution Simulations

Since the main motivation for the development of the coincidence detector is to improve the spatial resolution in PSND, it is fundamental to compare the improvement potential in the neutron capture position estimation of this detector in regard to conventional thick boron coating detectors. To do this, Monte Carlo simulations with GEANT4 were developed to compare the position reconstruction uncertainty between the two.

The thick detector geometry used for comparison consisted of a 3 μm $^{10}B_4C$ conversion layer, with the neutron beam interacting in back-scattering mode. The converter was on top of a 0.5 mm aluminium substrate, but seeing that the sensitive region defined in the simulation was the gas volume on top of the converter (analogous to detector A in the scheme of Fig. 5.27), the substrate geometry and material has a negligible impact in the simulation. The 3 μm coating thickness was selected because, as discussed in section 5.1, it corresponds to the saturation limit of detectable neutron captures, meaning that the results obtained for this value can, in principle, be extrapolated for superior coating thickness.

For the coincidence detector, all the substrate and coatings layout possibilities previously exposed were considered, namely the 0.4 μm aluminium, 0.5 μm Mylar, and 0.9 μm Mylar substrates, for one-sided and symmetric coatings. The common factor was the total coating thickness, which was found to be optimal in terms of efficiency for 1

μm. The conversion material in every scenario was 99% enriched $^{10}B_4C$, and the filling gas Ar:CO2 (90%:10%) at atmospheric pressure.

To compare the spatial resolution of both detectors, a perpendicularly incident infinitely collimated thermal neutron beam at (x,y) coordinates (0,0) was used. The total number of incident neutrons was 10^6. The estimation of the neutron interaction site for each detected neutron was calculated by weighting the energy deposited in the gas along the trajectory of each particle in the x-projection of the track, as described in equations (5.4) and (5.5). To calculate the position determined by the coincidence detector, equation (5.6) was additionally used.

By accumulation of several neutron captures occurring at the same (x,y) coordinates, each one resulting in a neutron capture interaction site estimation, it is possible to draw a histogram of the obtained positions. For the coincident neutron, only coincident events were considered, i.e., neutron captures in which both secondary particles deposited an energy superior to the gamma discrimination threshold in the opposing regions of the gas (detectors A and B), which was set as 100 keV. The same threshold was used for the thick detector

Fig. 5.28 compares the histogram of a coincidence detector deploying a 0.9 μm Mylar substrate (for both symmetric and one-side coating deposition), with that of a conventional thick boron coated detector. Each histogram was fitted with a Gaussian function $g(x) = a \cdot e^{-\frac{(x-\mu)^2}{2\sigma^2}}$, in which a is the peak amplitude, μ the centroid and σ its standard deviation. The full width at half maximum (FWHM), is related to σ by $\text{FWHM} = 2\sqrt{2\ln 2}\sigma \approx 2.355\sigma$. The centroid of the Gaussian function (μ) can be used to quantify the accuracy of the neutron capture site estimation, i.e., its proximity to the real value, while the FWHM can be used to quantify its precision, i.e., the uncertainty of the estimation, which is related to the spatial resolution.

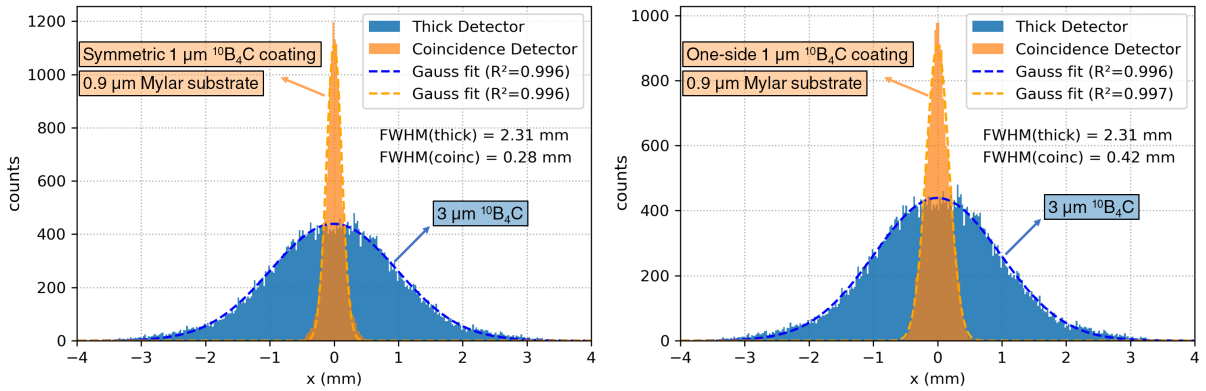

Figure 5.28: Estimated spatial resolution, limited only by the range of the ^{10}B neutron capture reaction products in Ar:CO2 (90%:10%) at atmospheric pressure, of a conventional thick boron gaseous detector (3 μm $^{10}B_4C$ coating) and of the coincidence detector with 1 μm $^{10}B_4C$ coating deposited on a 0.9 μm Mylar substrate with a symmetric deposition (left) and one-sided deposition (right).

From this figure, it is notorious the improvement of the estimated spatial resolution of the coincidence detector, quantified by the FWHM of the neutron interaction site estimation distribution. While the thick detector results in a FWHM = 2.31 mm, the coincidence detector with a symmetric coating has a FWHM = 0.28 mm, which represents an improvement by a factor of 8.25. For the one-side coating layout, FWHM = 0.42 mm

is obtained, resulting in an improvement by a factor of 5.5 in comparison to the thick detector. Therefore, we can also conclude that the symmetric coating can intrinsically perform 1.5 times better than the one-side coating in terms of position resolution.

A significant improvement of the FWHM of the neutron capture x-position, relative to the thick detector, was obtained for the all considered geometries of the coincidence detector (Fig. 5.29-right). The accuracy of the neutron capture interaction x-position estimation (Fig. 5.29-left), i.e., its closeness to $x = 0$, is similar for every considered geometry, given that a large number of events are sampled. As for the FWHM, relevant disparities are observed for the several geometries. Most noticeably, regardless of the thickness and material of the substrate, the symmetric $^{10}B_4C$ coating reaches inferior FWHM values than the one-side coating. This is an additional motivation to prefer this converter deposition layout in the practical implementation of the detector. The simulation results also show that the 0.4 μm aluminium and the 0.5 μm Mylar substrates are similar for each coating layout in terms of FWHM. The 0.9 μm Mylar substrate, on the other hand, reaches an inferior FWHM value. This is explained by the fact that an increased substrate thickness, while causing a detection efficiency reduction (Table 5.3), also makes for smaller secondary particle tracks in the gas, which favours the neutron interaction site estimation.

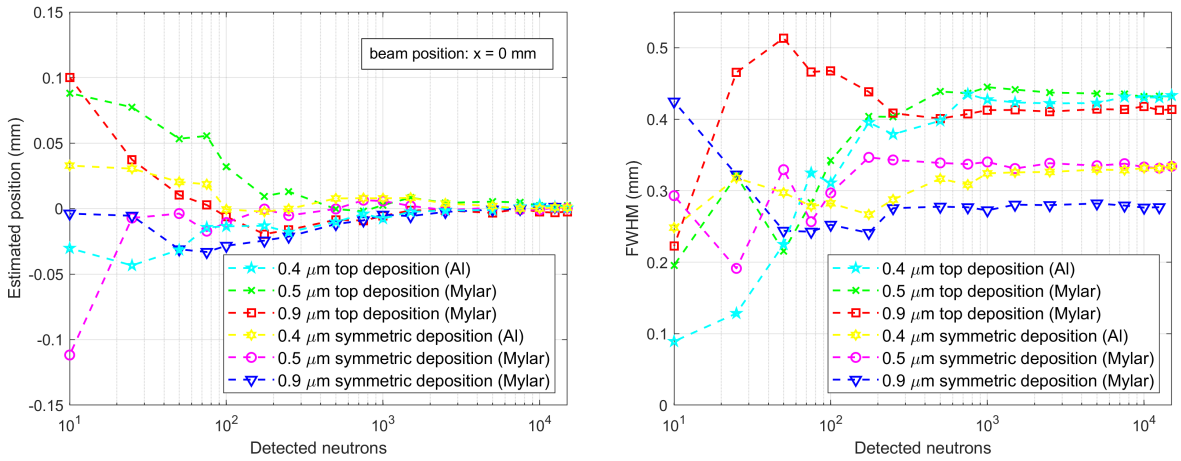

Figure 5.29: Results of a Gaussian fit to the histograms of the neutron capture x-position estimation, for different geometries of the coincidence detector: centroids (left) and FWHM (right).

The convergence of these parameters is also similar. The convergence factor relates the variability of a given parameter as a function of the statistics acquired, in this case, the number of detected neutrons. In experiments that involve neutron irradiation, this can be a particularly relevant factor to consider, since it is related to the required beam time exposure in a given experiment, which is generally a highly solicited and expensive resource. Shorter irradiation times also make for less noise contamination of the signal and a stable detector operation over the acquisition period.

It is important to notice that in Fig. 5.28 the coincidence detector was compared to what can be considered an infinitely thick detector, for the same neutron exposure, i.e., the same number of primary neutrons generated for each simulation. Due to the higher detection efficiency of a thick coating detector, more statistics is used in the estimation of the neutron capture coordinates, which benefits it. However, most

applications use a cascade of several detection elements, and since the optimal thickness to optimize detection efficiency decreases as the number of stacked detection layers increases, neutron detectors that deploy this strategy use thinner coatings, typically around 1 μm [37, 97, 105, 109, 114, 126, 171, 175]. In this case, if each detection layer has its own independent readout system, less statistics will be involved in the determination of the neutron interaction site position, which leads to a decrease of its precision. The comparison of the performance between the coincidence detector (symmetric coating on a 0.9 μm Mylar substrate) and a thick detector, both equipped with a 1 μm $^{10}B_4C$ layer, is shown in Fig. 5.30. Although both detectors have a total ^{10}B$_4$C thickness of 1 μm, because the coincidence detector only takes into consideration the neutron captures that are coincidently detected by detectors A and B, it will collect a lower number of events for the same irradiation exposure. Referring back to Table 5.3, the detection efficiency of a conventional 1 μm detector is approximately 3.1%, while for the coincidence detector regarded it is only about 1.4%. This implies that the number of events recorded the thick detector is more than the double of the ones recorded with the coincidence detector. Yet, the FWHM parameter for the latter is improved by roughly a factor of 10, as the position resolutions of the thick and coincidence detectors are respectively FWHM = 2.83 mm and FWHM = 0.28 mm, for the same 1 μm thickness of ^{10}B$_4$C.

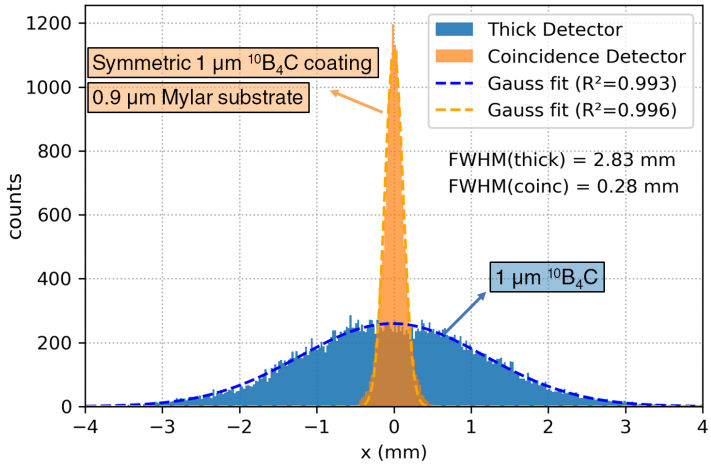

Figure 5.30: Estimated spatial resolution, limited only by the range of the ^{10}B neutron capture reaction products in Ar:CO2 (90%:10%) at atmospheric pressure, of a conventional thick boron gaseous detector (1 μm ^{10}B$_4$C coating) and of the coincidence detector with 1 μm ^{10}B$_4$C coating deposited on a 0.9 μm Mylar substrate with a symmetric deposition.

One additional benefit of the coincidence detector is the fact that it quickly converges to the stable values of the estimated neutron position and associated FWHM, as shown in Fig. 5.31, where these parameters are plotted as a function of the number of events detected with the thick and coincidence detectors.

The estimated neutron interaction site achieved for a thick detector and the coincidence detector is ultimately the same (although the former has a significantly higher spatial resolution, which is a drawback in PSND). However, as seen in Fig. 5.31-left, the coincidence detector shows less fluctuations over the number of detected neutrons, and converges significantly faster. As for the FWHM (Fig. 5.31-right), the coincidence detector not only achieves lower values, but they also stabilize for a significant inferior

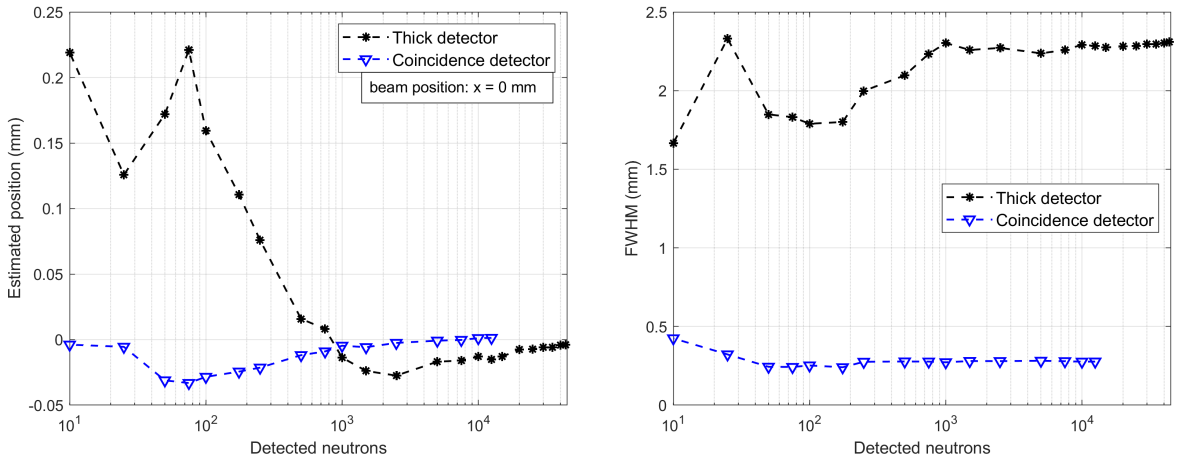

Figure 5.31: Convergence of the estimated neutron capture x-coordinate (left) and the associated FWHM (right) for the thick detector (3 μm $^{10}B_4C$ coating) and the coincidence detector with 1 μm $^{10}B_4C$ coating deposited on a 0.9 μm Mylar substrate with a symmetric deposition

number of detected neutrons. In fact, the simulation results show that while about 1000 neutron detections are necessary for the thick detector to reach and stabilize on its ultimate FWHM value, for the coincidence detector this number is roughly just 50 neutron captures, for which it already lands on a significantly lower FWHM value. Therefore, it is fair to say that the loss in detection efficiency by the coincidence detector is overcompensated by the fact that it can be more precise in terms of position resolution with significantly less neutron detections.

When comparing the response of both detectors for an equally low number of neutron detections, just 50, the thick detector is evidently outperformed by the coincidence detector (Fig. 5.32).

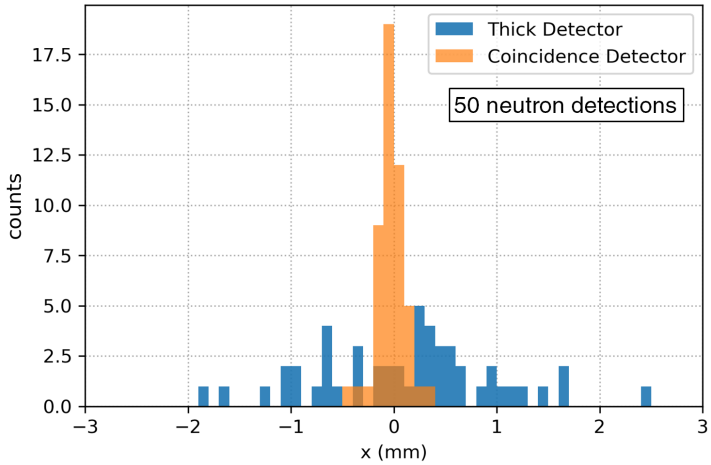

Figure 5.32: Estimated spatial resolution, limited only by the range of the ^{10}B neutron capture reaction products in Ar:CO2 (90%:10%) at atmospheric pressure, of a conventional thick boron gaseous detector (1 μm $^{10}B_4C$ coating) and of the coincidence detector with 1 μm $^{10}B_4C$ coating deposited on a 0.9 μm Mylar substrate with a symmetric deposition for 50 neutron detections.

In this scenario, the neutron x-position estimations with the thick detector can take values from −1.8 mm to 2.4 mm, while for the coincidence detector the range of possible values is much shorter, from −0.5 mm to 0.5 mm, centred around the position of the incoming beam ($x = 0$ mm). Therefore, the coincidence detector allows to obtain precise neutron capture site estimations even with a very low number of detected neutrons.

Drawing now attention to the two possible estimations of the neutron capture x-coordinate, discussed in the previous section - the arithmetic mean ($x_{\text{coinc}} = (x_A + x_B)/2$) and the energy weighted average ($x_{\text{coinc}} = \frac{x_A E_B + x_B E_A}{E_A + E_B}$) - their comparison for the coincidence detector composed by a 1 μm symmetric B_4C coating on a 0.9 μm Mylar substrate in a symmetric and one-sided layouts is presented in Fig. 5.33.

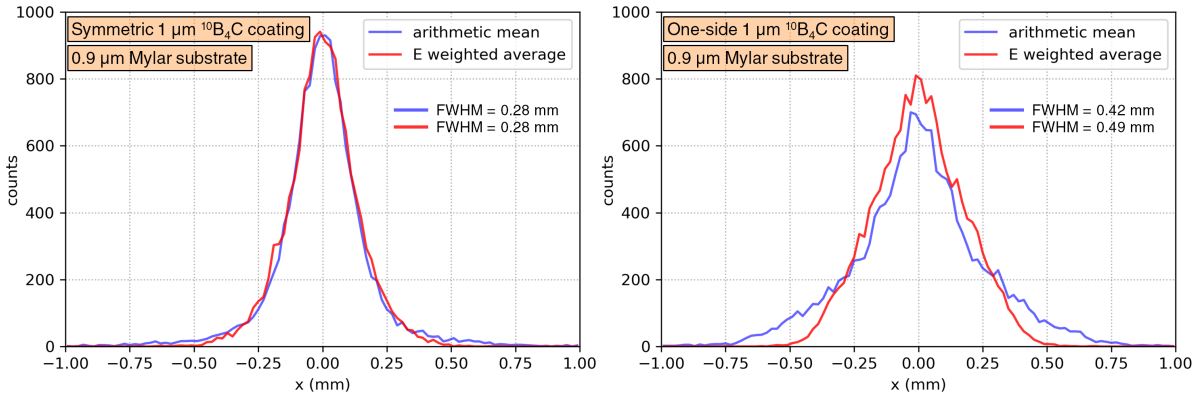

Figure 5.33: Comparison of the FWHM of the coincidence calculated by taking the arithmetic mean and the energy weighted average (equation (5.6)), for a symmetric (left) and one-side (right) deposition of 1 μm $^{10}B_4C$ coating on a 0.9 μm Mylar substrate.

A slight improvement of the FWHM is obtained by the energy weighted average formula for the one-side deposition, going from FWHM = 0.49 mm for the arithmetic mean to FWHM = 0.42 mm. However, for the symmetric coating, the two formulas produce very similar results, both yielding FWHM = 0.28 mm. This can be explained by the fact that this layout makes for a very balanced energy deposition across detectors A and B. As a result, for most events $E_A \approx E_B$, and for this condition equation (5.6) is approximately equal to the arithmetic mean.

5.7 Signal Readout

The initial approach to the experimental implementation of the coincidence detector is composed of two MWPCs (detector A and B). In each one, the wires are interconnected in a resistive chain, as means of obtaining a one-dimensional determination of the neutron interaction site by the charge division method. Although the wires of the MWPC could be connected to distinct electronic readout channels, making each an individual readout unit, that would add a significant layer of complexity to the front-end electronics system and a consequent cost increase. For that reason, linking the wires in a resistive chain was the preferred option. Using this method, only two channels per MWPC are required to determine the neutron interaction position in 1D, which substantially reduces costs and complexity. Despite being simpler and less expensive, it is also slower when compared to

using individual channels, which compromises the achievable detector counting rate [54]. Therefore, in future developments, the use of individual channels can be considered in case of applications in very bright neutron beams.

In the scheme of Fig. 5.34, it is depicted the operation principle of a MWPC with charge division readout. The MWPC consists of a set of anode wires uniformly spaced, connected by resistors of the same value. Each side of the resistive chain is connected to a preamplifier that collects the charge generated in gas ionizations upon a neutron detection, and are also used to polarize the wires with a positive high voltage provided by a HV source. When a neutron capture occurs, and the secondary particles interact with the gas, the anode wires accelerate towards them the primary electrons from the gas ionizations, and in the close proximity of the wires, the avalanche multiplication of electrons takes place, generating an electrical current. This current is split in inverse proportion to the resistance between the triggered wire(s) and the ground at both ends of the resistive chain. Because the resistors are chained in series and the wires are uniformly spaced, the resulting currents I_1 and I_2 carry the information of the position of the triggered wire(s).

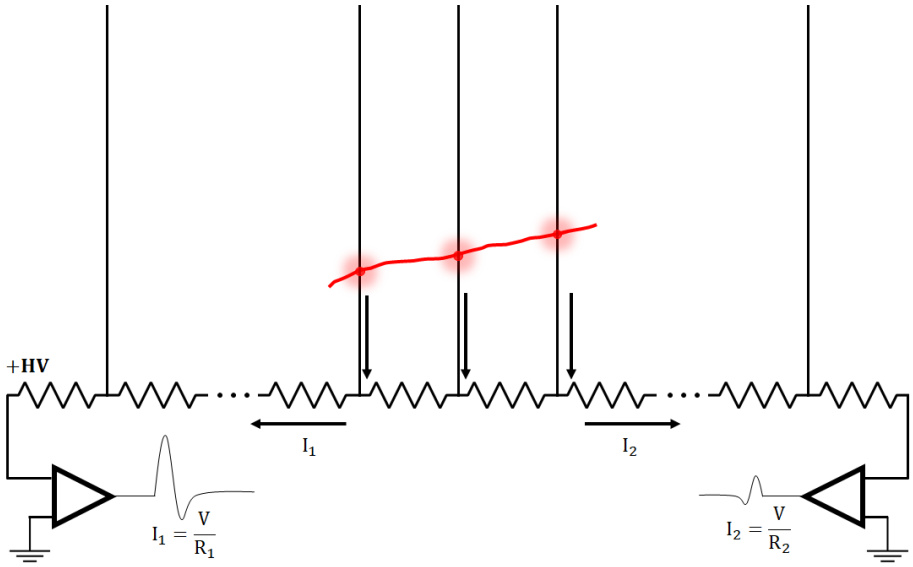

Figure 5.34: Operation principle of a MWPC with charge division readout. The red track represents a two-dimensional projection of a charged particle, and the red circles the avalanche multiplication of electrons that induce the original current on the wires. Each end of the resistive chain is connected to a charge sensitive preamplifier which converts the current signals into voltage pulses. By comparing the amplitudes of these pulses it is possible to estimate the position in which the original current was induced.

The interaction position in one dimension can be derived from:

$$x = \frac{I_2}{I_1 + I_2} L \tag{5.7}$$

where L is the length of the resistive chain, which corresponds to the width of the MWPC, i.e., the distance between the first and last wires. The currents I_1 and I_2 are collected by separate charge sensitive preamplifiers, which integrate the current signal and generate a voltage signal with amplitude proportional to the incoming charge. Therefore, equation (5.7) can be computed by considering I_1 and I_2 as the pulse amplitudes obtained

after this signal conversion. Seeing that the current intensity is given by Ohm's law: $I_{1/2} = \frac{V}{R_{1/2}}$, equation (5.7) can also be written as:

$$x = \frac{\frac{1}{R_2}}{\frac{1}{R_1} + \frac{1}{R_2}} L \iff x = \frac{1}{\frac{R_2}{R_1} + 1} L \tag{5.8}$$

where R_1 and R_2 are the sums of the individual resistors in the path between the ground and the point where the original current is split, and therefore depend on the position where the signal was generated. In relation to the scheme of Fig. 5.34, equations (5.7) and (5.8) assume the left-end of the resistive chain as the beginning of the coordinate system, i.e., $x = 0$. A simple analysis of this last equation shows its adequacy to determine the interaction position: if we consider $R_1 = R_2$, we obtain $x = L/2$, as expected, seeing that this condition implies that the interaction took place in the middle of the resistive chain. If $R_1 >> R_2$, the interaction must take place near the right-end of the resistive chain, and in fact we obtain $x \approx L$. In opposition, if $R_2 >> R_1$, the interaction must take place near the left-end of the resistive chain, and accordingly equation (5.8) yields $x \approx 0$.

The working principle of the coincidence detector requires the use of two MWPCs, on opposite sides of the detection layer, to reconstruct the neutron capture site in one-dimension. Its scheme and a photograph of the mounted structure is presented in Fig. 5.35.

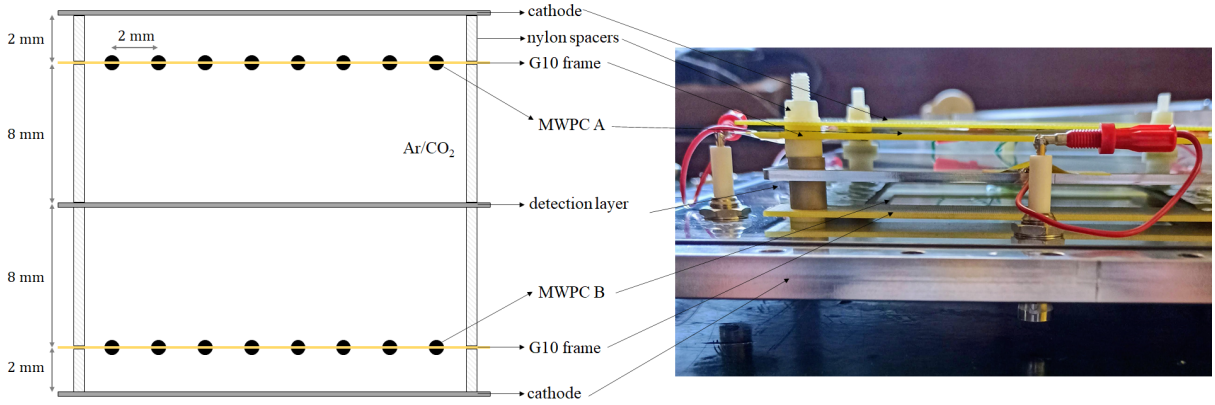

Figure 5.35: Left: Scheme of the coincidence detector, as developed for the first irradiation measurements. Right: Photograph of the mounted structure.

Each of the two MWPCs is composed of 39 wires, with a pitch of 2 mm between them, connected by 120 Ω resistors (Fig. 5.36). The first and last wire also have a soldered resistor before conducing the signal to the preamplifier input, making for a total of 40 resistors, and consequently a total resistance of 4.8 kΩ. Each wire is 100 mm long and made of gold-coated 50 μm diameter tungsten, resulting in a detection area of 100×100 mm^2. The wires and resistors were mounted on a G10 (fiber glass) frame with a series of small conductive pads at a 2.5 mm distance to apply the solder. Each wire was first soldered on one-side, and then stretched using a suspended weight which applied tension to the wire through gravity force, while soldering it on the other side.

While the bottom cathode is the conductive surface of the vessel in which the structure is inserted, the top cathode consists of a 100×100 mm^2 thick aluminium foil on a G10 frame, rather than the top inner surface of the vessel. This allows for flexibility to change the distance between the MWPC and the top cathode by increasing or decreasing the

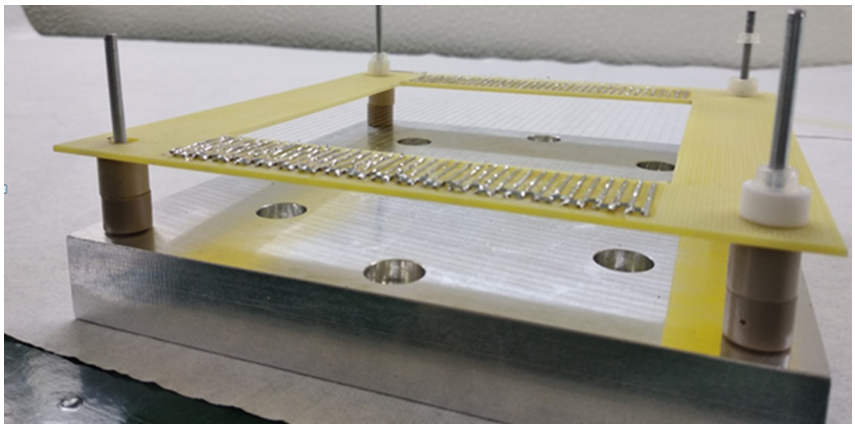

Figure 5.36: Photograph of one of the two MWPC assembled.

length of the nylon spacer between the two. In case of variation, it would have to be complemented with a similar change in the spacer between the bottom cathode and bottom MWPC, to preserve the symmetry of the electric field.

This structure is fixed inside a stainless-steel vessel, with lateral inlets and outlets on opposing sides to allow the gas to flow through the detector. The top of the vessel has an aluminium window for neutrons to enter with inferior scattering probability.

On a final note, it is important to notice that, although a MWPC with charge division was the selected readout mechanism for first implementation of the coincidence detector, its operation principle is still valid for other readouts that might prove to be advantageous, such as any combination of GEMs, strips and pads.

6 Conclusions and Future Work

Neutron science has been in continuous evolution for nearly a century. During the last decade, this evolution was marked by a severe shortage of ^{3}He, the massively deployed gas that was considered a golden standard for neutron detectors. The increasing deployment of neutron detectors in combination with the limited reserves of ^{3}He made it clear that a sustainable supply and demand balance for this gas is not a long-term possibility. With many scientific and homeland security applications deeply dependent on ^{3}He, and new neutron research facilities under construction or planned for construction, the scarcity of ^{3}He was an obstacle that threatened the maintenance and further development of neutron detectors. Solutions were urgently needed, and over the course of the last decade, intensive research and development of ^{3}He-free technologies for neutron detection has been carried by several groups around the world. Although the ^{3}He shortage crisis was a big catalyst, the development of new detectors was also driven by the need of exceeding the capability limits of ^{3}He proportional counters, namely in terms of counting rate and spatial resolution, to take full advantage of the neutron beams that will be provided by the new neutron research facilities.

In this thesis, two ^{3}He-free neutron detectors with unique characteristics were developed: the fine powder aerosol detector, and the coincidence detector. The detection principle of the first, although originally developed for neutron detection, also showed favourable results when applied in the detection of hard x-rays, if the medium for neutron conversion is replaced by a high-Z material.

In the fine powder aerosol for neutron detection, the capture reaction occurs with the ^{10}B isotope present in B_4C microparticles suspended in a proportional counter in continuous flow, thus forming an aerosol. Before the beginning of this thesis, proof-of-concept measurements were carried at PSI, which indicated the occurrence of neutron captures in the suspended particles, thus validating the potential of the detection concept proposed. The unique feature of this detector, when compared to other boron-based gaseous detectors, is the fact that both fission fragments emitted in a neutron capture reaction can escape the conversion medium and deposit a large fraction of their energy in the gas, extending the energy range of the detector response to higher values, which is an attractive feature to improve gamma-ray discrimination.

The first experimental results presented in this work relative to the fine powder aerosol detector consist of a study on the effect of the presence of the B_4C microparticles in the gas on the avalanche gain and on energy resolution, which are issues that are needed to be met in order to check the feasibility of this detection concept. Using a soft x-ray source (5.9 keV), the detector gain, energy resolution and intrinsic energy resolution were compared with and without the presence of the B_4C powder in the detector. A gain decrease by a factor of 36%, an energy resolution increase by 15% (absolute value) and an intrinsic

energy resolution increase by 17% (absolute value) were observed when dispersing the powder. The degradation of these parameters is explained by the rise of fluctuations of the avalanche multiplication of charges, due to inhomogeneities in the electric field created by the microparticles.

Strategies for the optimization of particle dispersion were also investigated. A homogeneous and continuous particle dispersion is essential for the long time operation of the detector, but it is compromised by the fact that particles have a natural tendency to agglomerate with each other, attach to the detector walls and getting trapped on the particle filters placed in the gas inlet and outlet of the detector. To optimize particle dispersion, a solenoid valves system was developed to periodically reverse the direction of the gas flow, which showed to be effective to unclog the particles saturating the particle filters. Additionally, through irradiation with alpha particles it was demonstrated that the periodical alternation of the flow direction does not affect the gas gain curve.

To prevent the attachment of the fine powder to the detector walls, the effect of surface polishing in the attachment of B_4C particles to stainless-steel was investigated, through image analysis of particles deposited on several surface samples with different degrees of polishing. A decrease in the attachment of B_4C fine powder with increasing surface smoothness was observed for high polishing levels, with the lowest values of area fraction with attached particles being achieved for the samples that were polished with sandpaper grit sizes above P2000, and showing little variation up to a grit of P6000. In light of these results, the inner walls of the detector were progressively polished up to P6000 grit sandpaper.

After these particle dispersion optimization efforts, irradiation measurements with thermalized neutrons from an ^{241}AmBe source were performed. By making consecutive short time acquisitions varying the gas flow conditions, a peak-like detector response was temporarily observed, compatible with what is expected from neutron captures occurring in suspended B_4C particles. However, the detector operation was severely limited by a current leakage that occurred for higher gas flow rates, which uninhibited the increase of the HV supply due to the occurrence of electrical discharges. This leakage current was attributed to the fact that the suspension of the B_4C powder was creating an electrically conductive path between the top of the anode wire, soldered to the SHV feedthrough, and the surface of the cathode flange. This issue was resolved by redesigning the top flange of the detector, increasing the distance between the flange surface and the conductive end of the SHV connector. Through irradiation with alpha particles, it was verified that the leakage currents were resolved and it was possible to operate the detector in stable conditions. After this, a new experimental campaign was carried, irradiating the detector with neutrons emitted from a cyclotron in the process of producing radioisotopes for pharmaceutical purposes. This time, however, the high energy peak expected from the simultaneous detection of both neutron capture secondary products was not observed, both with and without the use of the solenoid valves system to optimize particle dispersion.

Overall, after the detector developments and irradiation measurements performed, it is evident that the main obstacle for a stable operation of the detector for long time periods while featuring a peak in the PHS from the simultaneous detection of both fission fragments, is the difficulty to sustain a homogeneous dispersion of the powder due to its agglomeration and attachment susceptibility. Indeed, the visual tests of particle dispersion on an acrylic tube with the solenoid valves system showed that after several cycles alternating the gas flow direction, the number of suspended particles progressively decreases, up to a point in which no particle suspension is observed at all, after a couple

of minutes. Despite the limitations of this visual assessment, specifically the fact that the average particle diameter is on the micron scale, invisible to the naked eye, meaning that particles could be suspended in the tube for longer times without being visible, it still serves as a good indicator that the alternation of the gas flow direction through the solenoid valve system is not sufficient to guarantee an adequate long term dispersion of the powder.

The inner wall polishing of the detector also showed limited effectiveness: although a significant reduction of the particle attachment can be expected, if the detector is in operation for a long enough time, the number of particles attaching to the wall is still sufficient to produce a two-step plateau response characteristic of boron-lined detectors, capturing neutrons before they have the chance to reach the suspended particles of the powder, and reducing the number of suspended particles for neutrons to interact with.

In the future developments of this detector, the wall-effect may be attenuated by creating a gap between the bottom dispersion cone and the sensitive region of the detector. Indeed, the visual tests with the transparent tube showed that particle attachment to the walls was more preponderant on the bottom region, near the dispersion cone, as had also been predicted by the COMSOL particle tracing simulations. However, this might also be associated with an inferior concentration of suspended particles on the top region of the detector, meaning that a compromise between wall-effect and detection efficiency would have to be made.

Another possibility for the reduction of the wall-effect is to increase the detector diameter, which leads to an increase of the proportion between volume and wall surface area, even for collimated beams that traverse only a fraction of the detector volume, as was demonstrated in section 4.2.3. This measure can be conjugated with the installation of a field cage composed of several cathode wires surrounding the central anode wire. By applying a negative bias on these electrodes, a reversed electric field is established between the field cage and the wall, which prevents the primary electrons from neutron captures occurring in particles attached to the wall to drift towards the anode, and consequently from being detected. To minimize the fraction of insensitive volume, the ideal distance between the field cage wires and the cathode walls should be around $\sim$8 mm, corresponding to the unidimensional projection of the maximum range of the alpha particles emitted in the neutron capture reaction, as was concluded from the simulation results presented in Fig. 5.4. The field cage, however, introduces an additional problem: the attachment of particles to the electrodes as well as to the mechanical components required to fix them, which would still contribute to the wall-effect presence in the detector response. Nonetheless, an overall improvement can be anticipated, due to the significantly inferior surface area of the combined electrodes in comparison to the detector walls.

The potential for the fine powder aerosol detector to be applied in the detection of hard x-rays was also investigated, by replacing the B_4C particles with high-Z nanoparticles. Using Bi_2O_3 fine powder dispersed in Ar:CO_2 (95%:5%) gas, an increase by a factor of 3.6 in the detection efficiency for the 59.5 keV peak from an ^{241}Am gamma-ray source was measured. The next steps in the further development of this detector would be to test it for even higher photon energies, for which traditional gaseous detectors are progressively less efficient, which consequently can lead to an efficiency increase by a greater factor. Additionally, a multitude of nanoparticles composition and sizes can be studied and compared. This is because, in contrast to neutron detection applications which are constrained by the fact that only a few isotopes have a relevant neutron capture

cross-section, a wide range of high-Z materials can be used to increase the probability of photoelectric occurrence with the nanoparticles, to generate a signal in the detector.

The second neutron detector introduced in this work was the coincidence detector, based on a novel detection technique that aims to improve the intrinsic spatial resolution of gaseous neutron detectors with solid boron converters, by simultaneously detecting both reaction products emitted in the ^{10}B neutron capture reaction. The motivation for adopting this strategy is the fact that the range of the secondary reaction products in the gas is a major limiting factor of spatial resolution in PSND, which detect only one reaction product isotropically emitted per neutron capture. Because the ^{7}Li and alpha particles are emitted in-line and with opposite directions, by tracking both particles it is possible to pinpoint the neutron interaction site. In practice, this can be achieved using a thin boron layer coated on a thin substrate, allowing for both particles to escape the solid detection layer and deposit their energy in opposite sides of the surrounding gas, where they are detected by two independent MWPCs.

The detector design in terms of geometry, materials and substrate and neutron converter thicknesses was optimized based on GEANT4 simulation results. The optimal coating thickness to maximize the detection efficiency of coincident events was determined to be 1 μm for a boron-carbide coating. The obtained results also showed that the achievable spatial resolution can be improved by equally dividing the 1 μm coating thickness by both surfaces of the substrate, rather than depositing the full thickness on one side only.

Mylar and aluminium substrates of different thicknesses were analysed, both through simulations, to access their impact on the detector response, and experimentally, to compare their robustness and aptitude to be stretched on a frame for the coating process. Mylar proved to be easier to manipulate, and several 100×100 mm^2 frames were prepared for coating, with 0.9 μm and 0.5 μm thicknesses. A 0.9 μm Mylar frame was coated with enriched $^{10}B_4C$ at PSI by DC-magnetron sputtering. Although the coating adhered properly to the substrate, the Mylar foil lost some of its surface tension. However, it is presumably possible to restretch the coated substrate to regain its initial surface tension, with the cost of losing part of the original effective area.

Considering both detectors operating at atmospheric pressure, the simulation results indicate an improvement by a factor of 8.25 in spatial resolution for the coincidence detector with a symmetric 1 μm deposition of $^{10}B_4C$ on a 0.9 μm Mylar substrate, when compared to a conventional thick boron coating detector with a single 3 μm layer, that corresponds to the efficiency saturation limit. This improvement, however, takes only into consideration the limitation to spatial resolution that arises from the ranges of the secondary particles in the gas. In future work, it is important to account for the limitation in spatial resolution inherent to the charge collection by the MWPCs, to get a more realistic prediction of spatial resolution improvement. This can be done using the spatial distribution information of the primary charges obtained with GEANT4 as an input for a simulation software such as Garfield++, which focuses on the detailed simulation of electron drift in detectors, where the geometry and polarization of the readout electrodes can be defined, to generate a corresponding detector response.

Although the detection efficiency of the coincidence detector is inferior to that of a conventional thick boron coating detector, this is not necessarily a drawback in applications where the end goal is to have an accurate determination of neutron interaction sites. In fact, the simulation results showed that the coincidence detector can generate

a more precise neutron capture site estimation even for a substantially lower number of neutron detections. This also allows the coincidence detector to be exposed to higher neutron fluxes before reaching its counting rate limit. Nonetheless, this detection concept is compatible with the conventional strategies used to improve detection efficiency: stacking consecutive detection layers, tilting the detector to form a grazing angle with the incoming neutrons, or a combination of both.

Bibliography

[1] J. Chadwick. Possible existence of a neutron. *Nature*, 129(3252):312–312, 1932. doi: 10.1038/129312a0.

[2] N. Tsoulfanidis. *Measurement and detection of radiation*. CRC press, 2010.

[3] M. J. Berger, J. S. Coursey, M. A. Zucker, et al. ESTAR, PSTAR, and ASTAR: computer programs for calculating stopping-power and range tables for electrons, protons, and helium ions (version 1.2.3). 2005.

[4] C. Leroy and P. G. Rancoita. *Principles of radiation interaction in matter and detection*. World Scientific, 2011.

[5] J. F. Ziegler. Srim-2003. *Nucl. Instrum. Methods B*, 219:1027–1036, 2004. doi: 10.1016/j.nimb.2004.01.208.

[6] W. R. Leo. *Techniques for nuclear and particle physics experiments: a how-to approach*. Springer Science & Business Media, 2012.

[7] R. H. Dicke and J. Marshall. Inelastic scattering of protons. *Phys. Rev.*, 63:86–90, 1943. doi: 10.1103/PhysRev.63.86.

[8] G. F. Knoll. *Radiation detection and measurement*. John Wiley & Sons, 2010.

[9] M. J. Berger and J. H. Hubbell. XCOM: Photon cross sections on a personal computer. 1987. National Bureau of Standards, Washington, DC (USA).

[10] K. Nakamura. Review of particle physics. *J. Phys. G. Nucl. Part. Phys.*, 37(7A), 2010. doi: 10.1088/0954-3899/37/7A/075021.

[11] T. Jevremovic. *Nuclear principles in engineering*, volume 2. Springer, 2009.

[12] C. Salt, A. J. Lennox, M. Takagaki, J. A. Maguire, and N. S. Hosmane. Boron and gadolinium neutron capture therapy. *Russ. Chem. Bull.*, 53(9):1871–1888, 2004. doi: 10.1007/s11172-005-0045-6.

[13] F. Piscitelli. *Boron-10 layers, neutron reflectometry and thermal neutron gaseous detectors*. PhD thesis, University of Perugia, 2014.

[14] C. H. Lee, J. Son, T. H. Kim, S. Lee, and Y. K. Kim. Measurement of neutron energy spectrum emitted by Cf-252 source using time-of-flight method. In *Transactions of the Korean Nuclear Society Autumn Meeting*, 2016.

[15] E. F. Richard and J. K. Shultis. Radiation sources. In *Encyclopedia of Physical Science and Technology (Third Edition)*, pages 613–631. Academic Press, New York, third edition edition, 2003.

[16] ILL website. URL `https://www.ill.eu/`. Accessed: 2021-09-30.

[17] FRM II website. URL `https://www.frm2.tum.de/en/frm2/home/`. Accessed: 2021-09-30.

[18] PIK Reactor website. URL `http://www.pnpi.spb.ru/en/facilities/reactor-pik`. Accessed: 2021-09-30.

[19] ESS website. URL `https://europeanspallationsource.se`. Accessed: 2021-09-30.

[20] SINQ website. URL `https://www.psi.ch/en/sinq`. Accessed: 2021-09-30.

[21] ISIS website. URL `https://isis.stfc.ac.uk/`. Accessed: 2021-09-30.

[22] SNS website. URL `https://neutrons.ornl.gov/sns`. Accessed: 2021-09-30.

[23] CSNS website. URL `http://english.ihep.cas.cn/csns/`. Accessed: 2021-09-30.

[24] J-PARC website. URL `http://j-parc.jp/c/en/`. Accessed: 2021-09-30.

[25] M. Åberg et al. ESS Technical Design Report. Technical report, European Spallation Source, 2013.

[26] SINQ website: Accelerator and proton beam line. URL `https://www.psi.ch/en/bsq/proton-accelerator`. Accessed: 2021-09-30.

[27] J. W. G. Thomason. The ISIS spallation neutron and muon source—The first thirty-three years. *Nucl. Instrum. Methods A*, 917:61–67, 2019. doi: 10.1016/j.nima.2018.11.129.

[28] J. Galambos et al. Operations experience of SNS at 1.4 MW and upgrade plans for doubling the beam power. *Proceedings of IPAC*, 19:4380–4385, 2019. doi: 10.18429/JACoW-IPAC2019-FRXPLM1.

[29] J. Wei, S. Fu, and S. Fang. China Spallation Neutron Source accelerators: design, research and development. In *Proceedings of Eur. Part. Accel. Conf.* Brookhaven National Laboratory, Upton, NY (United States), 2006.

[30] S. Igarashi et al. Accelerator design for 1.3-MW beam power operation of the J-PARC Main Ring. *Prog. Theor. Exp. Phys*, 2021(3):033G01, 2021. doi: 10.1093/ptep/ptab011.

[31] W. E. Fischer. SINQ - The spallation neutron source, a new research facility at PSI. *Phys. B Condens. Matter*, 234-236:1202–1208, 1997. doi: 10.1016/S0921-4526(97)00260-3.

[32] N. J. Carron. *An introduction to the passage of energetic particles through matter.* CRC Press, 2006.

[33] J. S. Nico and W. M. Snow. Fundamental neutron physics. *Annu. Rev. Nucl. Part. Sci.*, 55(1):27–69, 2005. doi: 10.1146/annurev.nucl.55.090704.151611.

[34] F. M. Piegsa, M. Fertl, S. N. Ivanov, M. Kreuz, K. K. H. Leung, P. Schmidt-Wellenburg, T. Soldner, and O. Zimmer. New source for ultracold neutrons at the Institut Laue-Langevin. *Phys. Rev. C*, 90(1):015501, 2014. doi: 10.1103/PhysRevC.90.015501.

[35] C. F. Majkrzak and S. S. Malik. The production of cold and ultracold neutrons by a moving crystal lattice. *J. Appl. Crystallogr.*, 13(3):265–272, 1980. doi: 10.1107/S0021889880012046.

[36] T. W. Crane and M. P. Baker. *Passive Nondestructive Assay of Nuclear Materials*, chapter Neutron detectors, pages 379–406. United States Nuclear Regulatory Commission, 1991.

[37] G. Croci, G. Claps, C. Cazzaniga, L. Foggetta, A. Muraro, and P. Valente. GEM-based detectors for thermal and fast neutrons. *Eur. Phys. J. Plus*, 130(6), 2015. doi: 10.1140/epjp/i2015-15118-1.

[38] I. Sidelnik, H. Asorey, J. J. Blostein, and M. G. Berisso. Neutron detection using a water Cherenkov detector with pure water and a single PMT. *Nucl. Instrum. Methods A*, 876(February):153–155, 2017. doi: 10.1016/j.nima.2017.02.048.

[39] National Nuclear Data Center. URL `https://www.nndc.bnl.gov/sigma/`. Accessed: 2021-09-30.

[40] *Modern Neutron Detection*. Number 1935 in TECDOC Series. International Atomic Energy Agency, Vienna, 2020. ISBN 978-92-0-126520-3. URL `https://www.iaea.org/publications/14690/modern-neutron-detection`.

[41] K. D. Ianakiev, M. T. Swinhoe, A. Favalli, K. Chung, and D. W. Macarthur. 6Li foil scintillation sandwich thermal neutron detector. *Nucl. Instrum. Methods A*, 652 (1):417–420, 2011. doi: 10.1016/j.nima.2010.07.081.

[42] N. J. Rhodes. Scintillation detectors. *Neutron News*, 23(4):26–30, 2012. doi: 10.1080/10448632.2012.725331.

[43] A. Stoykov, J. B. Mosset, U. Greuter, M. Hildebrandt, and N. Schlumpf. A SiPM-based ZnS: 6LiF scintillation neutron detector. *Nucl. Instrum. Methods A*, 787: 361–366, 2015. doi: 10.1016/j.nima.2015.01.076.

[44] C. D. Bass, E. J. Beise, H. Breuer, C. R. Heimbach, T. J. Langford, and J. S. Nico. Characterization of a 6Li-loaded liquid organic scintillator for fast neutron spectrometry and thermal neutron detection. *Appl. Radiat. Isot.*, 77:130–138, 2013. doi: 10.1016/j.apradiso.2013.03.053.

[45] B. M. Fisher et al. Fast neutron detection with 6Li-loaded liquid scintillator. *Nucl. Instrum. Methods A*, 646(1):126–134, 2011. doi: 10.1016/j.nima.2011.04.019.

[46] G. Rusev, M. Jandel, M. Krtička, C. W. Arnold, T. A. Bredeweg, A. Couture, W. A. Moody, S. M. Mosby, and J. L. Ullmann. Cascade γ rays following capture of thermal neutrons on 113Cd. *Phys. Rev. C - Nucl. Phys.*, 88(5):6–9, 2013. doi: 10.1103/PhysRevC.88.057602.

[47] C. T. Hibdon and C. O. Muehlhause. Internal conversion of neutron capture γ-rays. *Phys. Rev.*, 88(4):943, 1952. doi: 10.1103/PhysRev.88.943.

[48] Y. Liu, Y. G. Yang, Y. Tai, and Z. Zhang. A capture-gated fast neutron detection method. *Chinese Phys. C*, 40(7):076201, 2016. doi: 10.1088/1674-1137/40/7/076201.

[49] D. Pfeiffer et al. First measurements with new high-resolution gadolinium-GEM neutron detectors. *J. Instrum.*, 11(5):P05011, 2016. doi: 10.1088/1748-0221/11/05/P05011.

[50] E. Aprile et al. Projected WIMP sensitivity of the XENONnT dark matter experiment. *J. Cosmol. Astropart. Phys.*, 2020(11):031, 2020.

[51] D. S. Akerib et al. The LUX-ZEPLIN (LZ) experiment. *Nucl. Instrum. Methods A*, 953:163047, 2020. doi: 10.1016/j.nima.2019.163047.

[52] G. Croci, C. Cazzaniga, M. Tardocchi, R. Borghi, G. Claps, G. Grosso, F. Murtas, and G. Gorini. *J. Instrum.*, page P04006. doi: 10.1088/1748-0221/8/04/P04006.

[53] A. Khaplanov, F. Piscitelli, J. C. Buffet, J. F. Clergeau, J. Correa, P. Van Esch, M. Ferraton, B. Guerard, and R. Hall-Wilton. Investigation of gamma-ray sensitivity of neutron detectors based on thin converter films. *J. Instrum.*, 8(10):P10025, 2013. doi: 10.1088/1748-0221/8/10/P10025.

[54] F. Piscitelli and others. The Multi-Blade Boron-10-based neutron detector for high intensity neutron reflectometry at ESS. *J. Instrum.*, 12(3):P03013, 2017. doi: 10.1088/1748-0221/12/03/P03013.

[55] J. Choi, J. Park, J. Son, and Y. K. Kim. Study of n/γ discrimination using 3He proportional chamber in high gamma-ray fields. *Nucl. Eng. Technol.*, 51(1):263–268, 2019. doi: 10.1016/j.net.2018.08.013.

[56] D. H. Beddingfield, N. H. Johnson, and H. O. Menlove. 3He neutron proportional counter performance in high gamma-ray dose environments. *Nucl. Instrum. Methods A*, 455(3):670–682, 2000. doi: 10.1016/S0168-9002(00)00532-5.

[57] W. Diethorn. A methane proportional counter system for natural radiocarbon measurements. Technical report, United States Atomic Energy Commission, Technical Information Service, 1956.

[58] E. Rossi. *Characterisation of the spatial resolution and the gamma-ray discrimination of helium-3 proportional counters.* Master's thesis, University of Milano-Bicocca, 2015.

[59] C. G. Shull. Early development of neutron scattering. *Rev. Mod. Phys.*, 67(4):753, 1995. doi: 10.1103/RevModPhys.67.753.

[60] N. Kardjilov, I. Manke, A. Hilger, M. Strobl, and J. Banhart. Neutron imaging in materials science. *Mat. Today*, 14(6):248–256, 2011. doi: 10.1016/S1369-7021(11)70139-0.

[61] G. Zaccai. Molecular dynamics in cells: A neutron view. *Biochim. Biophys. Acta. Gen. Subj.*, 1864(3):129475, 2020. doi: 10.1016/j.bbagen.2019.129475.

[62] M. P. Blakeley, P. Langan, N. Niimura, and A. Podjarny. Neutron crystallography: opportunities, challenges, and limitations. *Curr. Opin. Struct. Biol.*, 18(5):593–600, 2008. doi: 10.1016/j.sbi.2008.06.009.

[63] R. F. Barth, A. Coderre, M. G. H. Vicente, and T. E. Blue. Boron neutron capture therapy of cancer: Current status and future prospects. *Clin. Cancer Res.*, 11(11): 3987–4002, 2005. doi: 10.1158/1078-0432.CCR-05-0035.

[64] A. Klett. *Neutron Detection*, pages 759–790. Springer Berlin Heidelberg, Berlin, Heidelberg, 2012. ISBN 978-3-642-13271-1. doi: 10.1007/978-3-642-13271-1_31.

[65] United States Nuclear Regulatory Commission - Special Nuclear Material. URL `https://www.nrc.gov/materials/sp-nucmaterials.html`. Accessed: 2021-09-30.

[66] R. T. Kouzes. The 3He supply problem. Technical report, Pacific Northwest National Lab.(PNNL), Richland, WA (United States), 2009.

[67] S. S. Oakley. Radiation portal monitors: DHS's fleet is lasting longer than expected, and future acquisitions focus on operational efficiencies. Technical Report GAO-17-57, US Government Accountability Office, 2016.

[68] K. A. Guzman-Garcia, H. R. Vega-Carrillo, E. Gallego, J. A. Gonzalez-Gonzalez, A. Lorente, and S. Ibañez-Fernandez. 10B+ ZnS (Ag) as an alternative to 3He-based detectors for Radiation Portal Monitors. In *EPJ Web of Conferences*, volume 153, page 07008. EDP Sciences, 2017. doi: 10.1051/epjconf/201715307008.

[69] H. Johnston. Ultracold neutrons probe the particle-physics frontier. *Physics World - Astroparticle Physics*, 2011. URL `https://physicsworld.com/a/ultracold-neutrons-probe-the-particle-physics-frontier/`. Accessed: 2021-09-30.

[70] ILL Brochure. URL `https://www.ill.fr/fileadmin/user_upload/ILL/1_About_ILL/Documentation/ILL-General-brochure/Brochure-ILL-GB.pdf`. Accessed: 2021-09-30.

[71] Wolfram Research, ElementData, Wolfram Language function. URL `https://reference.wolfram.com/language/ref/ElementData.html`. Accessed: 2021-09-30.

[72] ESS website: ESS mandate. URL `https://europeanspallationsource.se/ess-mandate`. Accessed: 2021-09-30.

[73] K. H. Andersen et al. The instrument suite of the European Spallation Source. *Nucl. Instrum. Methods A*, 957:163402, 2020. doi: 10.1016/j.nima.2020.163402.

[74] A. J. Hurd and R. T. Kouzes. Why new neutron detector materials must replace helium-3. *Eur. Phys. J. Plus*, 129(10):1–3, 2014. doi: 10.1140/epjp/i2014-14236-6.

[75] W. K. Hagan. Caught by surprise: Causes and consequences of the helium-3 supply crisis. *House Committee on Science and Technology, Subcommittee on Investigations and Oversight*, 2010.

[76] R. Stone. Researchers rise to challenge of replacing helium-3. *Science*, 353(6294): 15–16, 2016. doi: 10.1126/science.353.6294.15.

[77] D. A. Shea and D. Morgan. The helium-3 shortage: Supply, demand, and options for congress. Technical report, Congressional Research Service Washington, DC, 2010.

[78] C. A. Slocum. Defining the helium-3 industry for private sector. Technical report, Arizona Oil and Gas Inc., 2016.

[79] A. Cho. Helium-3 shortage could put freeze on low-temperature research. *Science*, 326:778–779, 2009. doi: 10.1126/science.326_778.

[80] J. Niechciał et al. Operational Costs of He3 Separation Using the Superfluidity of He4. *Energies*, 13(22):6134, 2020. doi: 10.3390/en13226134.

[81] L. L. Lucas and M. P. Unterweger. Comprehensive review and critical evaluation of the half-life of tritium. *J. Res. Natl. Inst. Stand.*, 105:541–549, 2000. doi: 10.6028/jres.105.043.

[82] D. Kramer. For some, helium-3 supply picture is brightening. *Phys. Today*, 64(5): 20–23, 2011. doi: 10.1063/1.3591998.

[83] I. Stefanescu et al. Neutron detectors for the ESS diffractometers. *J. Instrum.*, 12 (01):P01019, 2017. doi: 10.1088/1748-0221/12/01/P01019.

[84] A. Ravazzani, A. Foglio Para, R. Jaime, M. Looman, M. Marín Ferrer, P. Peerani, and P. Schillebeeckx. Characterisation of 3He proportional counters. *Radiat. Meas.*, 41(5):582–593, 2006. doi: 10.1016/j.radmeas.2005.08.004.

[85] S. Agostinelli et al. Geant4—a simulation toolkit. *Nucl. Instrum. Methods A*, 506 (3):250–303, 2003. doi: 10.1016/S0168-9002(03)01368-8.

[86] B. Gebauer and B. Guerard. Detector Development in NMI3. *Neutron News*, 20 (1):22–25, 2009. doi: 10.1080/10448630802649528.

[87] V. Cristiglio, B. Giroud, L. Didier, and B. Demé. D16 is back to business: more neutrons, more space, more fun. *Neutron News*, 26(3):22–24, 2015. doi: 10.1080/10448632.2015.1057051.

[88] T. Unruh, J. Neuhaus, and W. Petry. The high-resolution time-of-flight spectrometer TOFTOF. *Nucl. Instrum. Methods A*, 580(3):1414–1422, 2007. doi: 10.1016/j.nima.2007.07.015.

[89] S. A. Korff and W. E. Danforth. Neutron measurements with boron-trifluoride counters. *Phys. Rev.*, 55(10):980, 1939. doi: 10.1103/PhysRev.55.980.

[90] A. P. Simpson, S. Jones, M. J. Clapham, and S. A. McElhaney. A review of neutron detection technology alternatives to helium-3 for safeguards applications. *INMM 52 Annual Meeting*, pages 1–10, 2011. doi: 10.1017/CBO9781107415324.004.

[91] S. Tavernier. *Experimental techniques in nuclear and particle physics*. Springer Science & Business Media, 2010.

[92] T. Wilpert. Boron trifluoride detectors. *Neutron News*, 23(4):14–19, 2012. doi: 10.1080/10448632.2012.725326.

[93] T. M. Persons and G. Aloise. Neutron detectors alternatives to using helium-3. Technical report, United States Government Accountability Office GAO-11-753, 2011.

[94] K. Zeitelhack. Search for alternative techniques to helium-3 based detectors for neutron scattering applications. *Neutron News*, 23(4):10–13, 2012. doi: 10.1080/10448632.2012.725325.

[95] L. M. S. Margato and A. Morozov. Boron-10 lined RPCs for sub-millimeter resolution thermal neutron detectors: conceptual design and performance considerations. *J. Instrum.*, 13(08):P08007, 2018. doi: 10.1088/1748-0221/13/08/P08007.

[96] L. M. S. Margato et al. Boron-10 lined RPCs for sub-millimeter resolution thermal neutron detectors: Feasibility study in a thermal neutron beam. *J. Instrum.*, 14 (01):P01017, 2019. doi: 10.1088/1748-0221/14/01/P01017.

[97] L. M. S. Margato, A. Morozov, A. Blanco, P. Fonte, L. Lopes, K. Zeitelhack, R. Hall-Wilton, C. Höglund, L. Robinson, S. Schmidt, and P. Svensson. Multilayer 10b-rpc neutron imaging detector. *J. Instrum.*, 15(6):P06007, 2020. doi: 10.1088/1748-0221/15/06/P06007.

[98] I. Stefanescu, Y. Abdullahi, J. Birch, I. Defendi, R. Hall-Wilton, C. Höglund, L. Hultman, D. Seiler, and K. Zeitelhack. Development of a novel macrostructured cathode for large-area neutron detectors based on the 10B-containing solid converter. *Nucl. Instrum. Methods A*, 727:109–125, 2013. doi: 10.1016/j.nima.2013.06.003.

[99] I. Stefanescu, Y. Abdullahi, J. Birch, I. Defendi, R. Hall-Wilton, C. Höglund, L. Hultman, M. Zee, and K. Zeitelhack. A 10B-based neutron detector with stacked MultiWire Proportional Counters and macrostructured cathodes. *J. Instrum.*, 8 (12):P12003, 2013. doi: 10.1088/1748-0221/8/12/P12003.

[100] D. Pfeiffer et al. The μTPC method: improving the position resolution of neutron detectors based on MPGDs. *J. Instrum.*, 10(04):P04004, 2015. doi: 10.1088/1748-0221/10/04/p04004.

[101] M. Köhli, K. Desch, M. Gruber, J. Kaminski, F. P. Schmidt, and T. Wagner. Novel neutron detectors based on the time projection method. *Phys. B Condens. Matter*, 551:517–522, 2018. doi: 10.1016/j.physb.2018.03.026.

[102] K. S. McKinny, T. R. Anderson, and N. H. Johnson. Optimization of coating in boron-10 lined proportional counters. *IEEE Trans. Nucl. Sci.*, 60(2):860–863, 2013. doi: 10.1109/TNS.2012.2224125.

[103] J. L. Lacy, A. Athanasiades, N. N. Shehad, R. A. Austin, and C. S. Martin. Novel neutron detector for high rate imaging applications. *IEEE Nucl. Sci. Symp. Conf. Rec.*, 1:392–396, 2002. doi: 10.1109/NSSMIC.2002.1239339.

[104] J. L. Lacy, A. Athanasiades, L. Sun, C. S. Martin, and G. J. Vazquez-Flores. Boron coated straw detectors as a replacement for 3He. *IEEE Nucl. Sci. Symp. Conf. Rec.*, pages 119–125, 2009. doi: 10.1109/NSSMIC.2009.5401846.

[105] J. L. Lacy, A. Athanasiades, C. S. Martin, L. Sun, and G. J. Vazquez-Flores. The evolution of neutron straw detector applications in homeland security. *IEEE Trans. Nucl. Sci.*, 60(2):1140–1146, 2013. doi: 10.1109/TNS.2013.2248166.

[106] Proportional Technologies Inc. website. URL `https://www.proportionaltech.com/pages/products`. Accessed: 2021-09-30.

[107] Z. Xie, J. Zhou, Y. Song, J. L. Lacy, L. Sun, Z. Sun, B. Hu, and Y. Chen. Experimental study of boron-coated straws with a neutron source. *Nucl. Instrum. Methods A*, 888:235–239, 2018. doi: 10.1016/j.nima.2018.01.090.

[108] J. Birch, J. C. Buffet, J. Correa, P. Van Esch, L. Hultman, A. Khaplanov, and F. Piscitelli. 10B4C Multi-Grid as an Alternative to 3He for Large Area Neutron Detectors. *IEEE Trans. Nucl. Sci.*, 60(2):871–878. doi: 10.1109/TNS.2012.2227798.

[109] K. Andersen et al. 10B multi-grid proportional gas counters for large area thermal neutron detectors. *Nucl. Instrum. Methods A*, 720:116–121, 2013. doi: 10.1016/j.nima.2012.12.021.

[110] M. Anastasopoulos et al. Multi-Grid detector for neutron spectroscopy: results obtained on time-of-flight spectrometer CNCS. *J. Instrum.*, 12(04):P04030, 2017. doi: 10.1088/1748-0221/12/04/P04030.

[111] F. Piscitelli. Novel boron-10-based detectors for neutron scattering science: Helium-3-free detectors for large and small-area applications: The Multi-Grid and the Multi-Blade prototypes. *Eur. Phys. J. Plus*, 130(2), 2015. doi: 10.1140/epjp/i2015-15027-3.

[112] J. C. Buffet, J. Correa, P. Van Esch, B. Guerard, A. Khaplanov, and F. Piscitelli. Study of a 10B-based multi-blade detector for neutron scattering science. *IEEE Nucl. Sci. Symp. Med. Imaging Conf. Rec.*, 02:171–175, 2012. doi: 10.1109/NSSMIC.2012.6551086.

[113] G. Mauri et al. The Multi-Blade Boron-10-based neutron detector performance using a focusing reflectometer. *J. Instrum.*, 15(03):P03010, 2020. doi: 10.1088/1748-0221/15/03/P03010.

[114] M. Henske, M. Klein, M. Köhli, P. Lennert, G. Modzel, C. J. Schmidt, and U. Schmidt. The 10B based Jalousie neutron detector – An alternative for 3He filled position sensitive counter tubes. *Nucl. Instrum. Methods A*, 686:151–155, 2012. doi: 10.1016/j.nima.2012.05.075.

[115] I. Stefanescu et al. Performance study of the Jalousie detector baseline design for the ESS thermal powder diffractometer HEIMDAL through GEANT4 simulations. *J. Instrum.*, 14(10):P10020, 2019. doi: 10.1088/1748-0221/14/10/p10020.

[116] F. Sauli. GEM: A new concept for electron amplification in gas detectors. *Nucl. Instrum. Methods A*, 386(2-3):531–534, 1997. doi: 10.1016/S0168-9002(96)01172-2.

[117] F. Sauli. The gas electron multiplier (GEM): Operating principles and applications. *Nucl. Instrum. Methods A*, 805:2–24, 2016. doi: 10.1016/j.nima.2015.07.060.

[118] G. Albani. *High-rate thermal neutron gaseous detector for use at neutron spallation sources.* PhD thesis, University of Milano-Bicocca, 2017.

[119] A. Muraro. *GEM based detectors for fast and thermal neutrons.* PhD thesis, University of Milano-Bicocca, 2018.

[120] G. Croci et al. Characterization of a thermal neutron beam monitor based on gas electron multiplier technology. *Prog. Theor. Exp. Phys.*, 2014(8):83H01–0, 2014. doi: 10.1093/ptep/ptu105.

[121] G. Albani et al. Neutron beam imaging with GEM detectors. *J. Instrum.*, 10(04): C04040, 2015. doi: 10.1088/1748-0221/10/04/c04040.

[122] G. Croci et al. GEM-based thermal neutron beam monitors for spallation sources. *Nucl. Instrum. Methods A*, 732:217–220, 2013. doi: 10.1016/j.nima.2013.05.111.

[123] H. Ohshita et al. Stability of neutron beam monitor for High Intensity Total Diffractometer at J-PARC. *Nucl. Instrum. Methods A*, 672:75–81, 2012. doi: 10.1016/j.nima.2011.12.087.

[124] G. Albani et al. High-rate measurements of the novel BAND-GEM technology for thermal neutron detection at spallation sources. *Nucl. Instrum. Methods A*, 957: 163389, 2020. doi: 10.1016/j.nima.2020.163389.

[125] C. J. Schmidt and M. Klein. The CASCADE neutron detector: A system for 2D position sensitive neutron detection at highest intensities. *Neutron News*, 17(1): 12–15, 2006. doi: 10.1080/10448630500514735.

[126] M. Köhli, F. Allmendinger, W. Häußler, T. Schröder, M. Klein, M. Meven, and U. Schmidt. Efficiency and spatial resolution of the CASCADE thermal neutron detector. *Nucl. Instrum. Methods A*, 828:242–249, 2016. doi: 10.1016/j.nima.2016.05.014.

[127] M. Klein and C. J. Schmidt. CASCADE, neutron detectors for highest count rates in combination with ASIC/FPGA based readout electronics. *Nucl. Instrum. Methods A*, 628(1):9–18, 2011. doi: 10.1016/j.nima.2010.06.278.

[128] J. L. Lacy, A. Athanasiades, N. N. Shehad, C. S. Martin, and L. Sun. Performance of 1 meter straw detector for high rate neutron imaging. *IEEE Nucl. Sci. Symp. Conf. Rec.*, 1:20–26, 2007. doi: 10.1109/NSSMIC.2006.356101.

[129] F. R. Scott, D. B. Thomson, and W. Wright. Thermal neutron capture cross sections of hydrogen, boron, and silver. *Phys. Rev.*, 95(2):582, 1954. doi: doi.org/10.1103/PhysRev.95.582.

[130] F. D. Amaro, C. M. B. Monteiro, J. M. F. dos Santos, and A. Antognini. Novel concept for neutron detection: proportional counter filled with 10B nanoparticle aerosol. *Sci. Rep.*, 7(1):41699, 2017. doi: 10.1038/srep41699.

[131] F. D. Amaro. *Ion back-flow reduction in gaseous detectors with the micro hole and strip plate*. PhD thesis, University of Coimbra, 2010.

[132] Y. Zhang, Y. Zhang, H. Gong, J. Yu, J. Zhao, Z. Zhang, and Y. Zhang. Microwave-assisted sol-gel synthesis of neutron-absorbed nano-sized 10B-enriched B4C powders. *J. Solgel Sci. Technol.*, 80(3):683–689, 2016. doi: 10.1007/s10971-016-4147-4.

[133] US Research Nanomaterials Boron Carbide Nanopowder Safety Data Sheet. URL `https://n.b5z.net/i/u/10091461/f/MSDS-NANOPOWDERS/US2140.pdf`. Accessed: 2021-09-30.

[134] Beckman Coulter Inc. *LS 13 320 laser diffraction particle size analyser instrument manual, 11800*.

[135] MDC Precision website. URL `https://www.mdcprecision.com/`. Accessed: 2021-09-30.

[136] S. Fargher, C. Steer, and L. Thompson. The use of 3D printing in the development of gaseous radiation detectors. *EPJ Web Conf.*, 170:01016, 2018. doi: 10.1051/epjconf/201817001016.

[137] F. M. Brunbauer, M. Lupberger, H. Müller, E. Oliveri, D. Pfeiffer, L. Ropelewski, L. Scharenberg, P. Thuiner, and M. V. Stenis. 3D printing of gaseous radiation detectors. *J. Instrum.*, 14(12):P12005. doi: 10.1088/1748-0221/14/12/P12005.

[138] COMSOL Multiphysics version 5.3a. URL `https://comsol.com/multiphysics/finite-element-method`. COMSOL AB, Stockholm, Sweden.

[139] SMC SYJ3000 Series product page. URL `https://www.smc.eu/en-eu/products/syj300-3-port-solenoid-valve-all-types~37358~cfg`. Accessed: 2021-09-30.

[140] Arduino website. URL `https://www.arduino.cc/`. Accessed: 2021-09-30.

[141] L. A. Oliveira and A. G. Lopes. *Mecânica dos Fluidos*. ETEP–Edições Técnicas e Profissionais, 3ª Edição, Lisboa, 2010.

[142] J. Tang and A. A. Busnaina. The effect of relative humidity on particle adhesion and removal. *J. Adhes.*, 74(1-4):391–409, 2000. doi: 10.1080/00218460008034539.

[143] P. G. C. Petean and M. L. Aguiar. Determining the adhesion force between particles and rough surfaces. *Powder Technol.*, 274:67–76, 2015. doi: 10.1016/j.powtec.2014.12.047.

[144] W. R. Bowen, N. Hilal, R. W. Lovitt, and C. J. Wright. A new technique for membrane characterisation: direct measurement of the force of adhesion of a single particle using an atomic force microscope. *J. Membr. Sci.*, 139(2):269–274, 1998. doi: 10.1016/S0376-7388(97)00255-X.

[145] M. Kappl and H. J. Butt. The colloidal probe technique and its application to adhesion force measurements. *Part. Part. Syst. Charact.*, 19(3):129–143, 2002. doi: 10.1002/1521-4117(200207)19:3⟨129::AID-PPSC129⟩3.0.CO;2-G.

[146] J. Drelich, G. W. Tormoen, and E. R. Beach. Determination of solid surface tension from particle-substrate pull-off forces measured with the atomic force microscope. *J. Colloid Interface Sci.*, 280(2):484–497, 2004. doi: 10.1016/j.jcis.2004.08.002.

[147] M. C. Thomas and S. P. Beaudoin. An enhanced centrifuge-based approach to powder characterization: Experimental and theoretical determination of a size-dependent effective Hamaker constant distribution. *Powder Technol.*, 306:96–102, 2017. doi: 10.1016/j.powtec.2016.10.017.

[148] G. R. Salazar-Banda, M. A. Felicetti, J. A. S. Gonçalves, J. R. Coury, and M. L. Aguiar. Determination of the adhesion force between particles and a flat surface, using the centrifuge technique. *Powder Technol.*, 173(2):107–117, 2007. doi: 10.1016/j.powtec.2006.12.011.

[149] K. .Á. V. Aracena, R. O. Uñac, I. Ippolito, and A. M. Vidales. Movement initiation of millimeter particles on a rotating rough surface: the role of adhesion. *Particuology*, 53:92–99, 2020. doi: 10.1016/j.partic.2020.02.004.

[150] M. Soltani and G. Ahmadi. Particle detachment from rough surfaces in turbulent flows. *J. Adhes.*, 51(1-4):105–123, 1995. doi: 10.1080/00218469508009992.

[151] Y. Jiang, S. Matsusaka, H. Masuda, and Y. Qian. Characterizing the effect of substrate surface roughness on particle-wall interaction with the airflow method. *Powder Technol.*, 186(3):199–205, 2008. doi: 10.1016/j.powtec.2007.11.041.

[152] S. Wanka, M. Kappl, M. Wolkenhauer, and H. J. Butt. Measuring adhesion forces in powder collectives by inertial detachment. *Langmuir*, 29(52):16075–16083, 2013. doi: 10.1021/la404014d.

[153] S. Ripperger and K. Hein. Measurement of adhesion forces in air with the vibration method. *China Particuology*, 3(01n02):3–9, 2005. doi: 10.1142/S1672251505000047.

[154] A. Kumar, T. Staedler, and X. Jiang. Role of relative size of asperities and adhering particles on the adhesion force. *J. Colloid Interface Sci.*, 409:211–218, 2013. doi: 10.1016/j.jcis.2013.07.039.

[155] J. Katainen, M. Paajanen, E. Ahtola, V. Pore, and J. Lahtinen. Adhesion as an interplay between particle size and surface roughness. *J. Colloid Interface Sci.*, 304 (2):524–529, 2006. doi: 10.1016/j.jcis.2006.09.015.

[156] Federation of European Producers of Abrasives. URL `https://fepa-abrasives.org/`. Accessed: 2021-09-30.

[157] R. A. Serway and J. W. Jewett. *Physics for scientists and engineers*. Cengage learning, Boston, 2018.

[158] WaKi Software GmbH 2020. URL `https://online-image-comparison.com/`. Accessed: 2021-09-30.

[159] CAEN N471A data sheet. URL `http://www.quantech-works.ro/pdf/CAEN/PowerSupply.pdf`. Accessed: 2021-09-30.

[160] CANBERRA Model 2004 Preamplifier data sheet. URL https://groups.nscl.msu.edu/nscl_library/manuals/canberra/2004.pdf. Accessed: 2021-09-30.

[161] Amptek MCA-8000D data sheet. URL https://www.amptek.com/products/multichannel-analyzers/mca-8000d-digital-multichannel-analyzer. Accessed: 2021-09-30.

[162] M. M. Bé, V. Chisté, C. Dulieu, E. Browne, V. Chechev, N. Kuzmenko, R. Helmer, A. Nichols, E. Schönfeld, and R. Dersch. Table of radionuclides (Vol.2 - A = 151 to 242). *Monographie BIPM-5*, 2004.

[163] Henriques C. A. O. et al. Neutral Bremsstrahlung emission in xenon unveiled. *Submitted for journal publication.*

[164] ICNAS website. URL https://www.uc.pt/en/icnas. Accessed: 2021-09-30.

[165] Cyclone KIUBE website. URL https://www.iba-radiopharmasolutions.com/cyclone-kiube. Accessed: 2021-09-30.

[166] IBA Radiopharma Solutions. The Cyclone KIUBE Site Requirement Guide.

[167] P. De Marcillac, N. Coron, G. Dambier, J. Leblanc, and J. P. Moalic. Experimental detection of α-particles from the radioactive decay of natural bismuth. *Nature*, 422 (6934):876–878, 2003. doi: 10.1038/nature01541.

[168] J. H. Hubbell, P. N. Trehan, N. Singh, B. Chand, D. Mehta, M. L. Garg, R. R. Garg, S. Singh, and S. Puri. A review, bibliography, and tabulation of k, l, and higher atomic shell x-ray fluorescence yields. *J. Phys. Chem. Ref. Data*, 23(2):339–364, 1994. doi: 10.1063/1.555955.

[169] Sigma-Aldrich Bismuth(III) Oxide Safety Data Sheet. URL https://www.sigmaaldrich.com/PT/en/sds/aldrich/202827. Accessed: 2021-09-30.

[170] O. Kirstein et al. Neutron Position Sensitive Detectors for the ESS. *PoS Proc. Sci.*, Vertex2014:029, 2014. doi: 10.22323/1.227.0029.

[171] K. A. Nelson, N. S. Edwards, N. J. Hinson, C. D. Wayant, and D. S. McGregor. A suspended boron foil multi-wire proportional counter neutron detector. *Nucl. Instrum. Methods A*, 767:14–18, 2014. doi: 10.1016/j.nima.2014.08.007.

[172] F. Piscitelli, A. Khaplanov, A. Devishvili, S. Schmidt, C. Höglund, J. Birch, A. J. C. Dennison, P. Gutfreund, R. Hall-Wilton, and P. Van Esch. Neutron reflectometry on highly absorbing films and its application to 10B4C-based neutron detectors. *Proc. R. Soc. A Math. Phys. Eng. Sci.*, 472(2185), 2016. doi: 10.1098/rspa.2015.0711.

[173] A. Muraro et al. Performance of the high-efficiency thermal neutron BAND-GEM detector. *Prog. Theor. Exp. Phys.*, 2018(2):1–17, 2018. doi: 10.1093/ptep/pty005.

[174] H. Yu, H. Gong, J. Li, Y. Wang, X. Wang, Y. Li, and K. Kang. A multiplex readout method for position sensitive boron coated straw neutron detector. *Nucl. Instrum. Methods A*, 797:324–329, 2015. doi: 10.1016/j.nima.2015.05.038.

[175] J. Zhou, Q. Xiu, X. Zhou, J. Zhou, L. Ma, C. J. Schmidt, M. Klein, Y. Xia, L. Zhu, C. Huang, G. Sun, B. Hu, Z. Sun, and Y. Chen. Highly efficient GEM-based neutron detector for China Spallation Neutron Source. *Nucl. Instrum. Methods A*, 953(2019): 163051, 2020. doi: 10.1016/j.nima.2019.163051.

[176] J. F. Clergeau, M. Ferraton, B. Guerard, A. Khaplanov, F. Piscitelli, M. Platz, J. M. Rigal, P. Van Esch, and T. Daulle. An information-theoretical approach to image resolution applied to neutron imaging detectors based upon individual discriminator signals. *IEEE Trans. Nucl. Sci.*, 64(1):735–742, 2017. doi: 10.1109/TNS.2016.2628964.

[177] S. Potashev, Y. Burmistrov, A. Drachev, S. Karaevsky, E. Konobeevski, and S. Zuyev. Two-dimensional solid state gaseous detector based on 10 B layer for thermal and cold neutrons. *J. Phys. Conf. Ser.*, 798(1):012160, 2017. doi: 10.1088/1742-6596/798/1/012160.

[178] F. S. Varley. Neutron scattering lengths and cross sections. *Neutron News*, 3(3): 29–37, 1992. doi: 10.1080/10448639208218770.

[179] D. S. McGregor, M. D. Hammig, Y. H. Yang, H. K. Gersch, and R. T. Klann. Design considerations for thin film coated semiconductor thermal neutron detectors - I: Basics regarding alpha particle emitting neutron reactive films. *Nucl. Instrum. Methods A*, 500(1-3):272–308, 2003. doi: 10.1016/S0168-9002(02)02078-8.

[180] J. M. Tarascon. Is lithium the new gold? *Nat. Chem.*, 2(6):510–510, 2010. doi: 10.1038/nchem.680.

[181] B. W. Montag, S. L. Bellinger, N. S. Edwards, J. Lage, K. A. Nelson, L. C. Henson, and D. S. McGregor. Recent progress in the commercialization of the Li Foil multi-wire proportional counter neutron detectors. *Radiat. Phys. Chem.*, 155:158–163, 2019. doi: 10.1016/j.radphyschem.2018.08.003.

[182] PubChem website: lithium fluoride. URL `https://pubchem.ncbi.nlm.nih.gov/compound/224478`. Accessed: 2021-09-30.

[183] C. Fleta et al. Fabrication and nuclear reactor tests of ultra-thin 3d silicon neutron detectors with a boron carbide converter. *J. Instrum.*, 9(04):P04010, 2014. doi: 10.1088/1748-0221/9/04/P04010.

[184] M. M. Yimamu. *Chemical vapour deposition of boron-carbon thin films from organoboron precursors*. PhD thesis, Linköping University, 2016.

[185] C. Höglund, K. Zeitelhack, P. Kudejova, J. Jensen, G. Greczynski, J. Lu, L. Hultman, J. Birch, and R. Hall-Wilton. Stability of 10B4C thin films under neutron radiation. *Radiat. Phys. Chem.*, 113:14–19, 2015. doi: 10.1016/j.radphyschem.2015.04.006.

[186] K. Ahmed, R. Dahal, A. Weltz, J. J. Q. Lu, Y. Danon, and I. B. Bhat. Solid-state neutron detectors based on thickness scalable hexagonal boron nitride. *Appl. Phys. Lett.*, 110(2):13–16, 2017. doi: 10.1063/1.4973927.

[187] A. Maity, S. J. Grenadier, J. Li, J. Y. Lin, and H. X. Jiang. Hexagonal boron nitride neutron detectors with high detection efficiencies. *J. Appl. Phys.*, 123(4), 2018. doi: 10.1063/1.5017979.

[188] K. Shirai. Electronic structures and mechanical properties of boron and boron-rich crystals (Part I). *J. Superhard Mater.*, 32(3):205–225, 2010. doi: 10.3103/S1063457610050059.

[189] GoodFellow website, Al foil. URL `http://www.goodfellow.com/E/Aluminium-Foil.html`. Accessed: 2021-09-30.

[190] GoodFellow website, Mylar foil. URL `http://www.goodfellow.com/E/Polyethylene-terephthalate-Film.html`. Accessed: 2021-09-30.

[191] PSI Sputtering Laboratory website. URL `https://www.psi.ch/en/lin/sputtering-lab`. Accessed: 2021-09-30.